

PROCEEDING



Jakarta
Indonesia
11 – 12 November 2015



Mechanical Engineering Department
Faculty of Engineering
Universitas Indonesia



About the Conference

The International Meeting on Advances in Thermofluids (IMAT) is an initiative to bring together academicians, research scientists and all interested parties from all over the world in a common platform to foster discussion, exchange ideas for the exploration of future research in the fields of fluid mechanics, heat transfer, thermodynamics, combustion and all topics related to thermal fluids.

IMAT is a series of conferences that is held annually on the rotational basis between three universities, namely Universiti Teknologi Malaysia (UTM), National University of Singapore (NUS) and Universitas Indonesia (UI).

Previous IMAT conferences are as follows:

- 1st IMAT - UTM Johor, Malaysia in 2008
- 2nd IMAT - Safari Park, Bogor, Indonesia in 2009
- 3rd IMAT - Furama Hotel, Singapore in 2010
- 4th IMAT - Avillion Hotel, Melaka, Malaysia in 2011
- 5th IMAT - Nirwana Resort, Bintan Island, Indonesia in 2012
- 6th IMAT - NUS, Singapore in 2013
- 7th IMAT - Swiss Garden Hotel & Residences, Kuala Lumpur, Malaysia in 2014

This year, on 11th - 12th November 2015, Universitas Indonesia was given the chance to organize the 8th IMAT. Selected papers are featured in Scopus indexed publication, IJTECH. More than 50 papers have been presented in the conference with authors from 7 countries. From the selected papers, 20 are published in IJTECH special edition in January 2016 while the remaining is published in the proceeding. IMAT 2015 is sponsored by The Ministry of Research, Technology and Higher Education, Republic of Indonesia.

Invited Speaker

- Prof. Kiyoshi Saito, Waseda University (Japan)
- Prof. Jong-Taek Oh, Chonnam National University, (South Korea)



Topics of interest (Thermodynamics, Heat Transfer, and Fluid Mechanics)

- Sustainable and Renewable Energy
- Green Energy and Green Technologies
- Energy Conversion and Clean Energy Technology
- Environmental Engineering
- Experimental Techniques and Instrumentation
- Combustion, Propulsion and Emissions
- Power Plants and Power Generation
- Energy, Exergy and Second Law
- Refrigeration and Air-conditioning
- Turbo Machinery: Turbines, Compressors, Engines etc
- Cryogenics
- Heat Transfer: Conduction, Convection and Radiation
- Electronic Cooling
- Heat Exchangers
- Measurement Techniques and Thermal Properties
- Desalination
- Heating and Drying
- Thermal Behavior of Manufacturing systems
- Thermal Management
- Experimental Fluid Dynamics
- Laminar and Turbulent Flow
- Compressible and Incompressible Flow
- Computational Fluid Dynamics
- Multi-phase Flow
- Boundary Layer and Free Surface Flows
- Flow Control and Diagnostics
- Flow-Induced Vibration
- High-Speed Flows
- Microfluidic and Nano Applications
- Pumps, Blowers and Fans
- Tribology



Advisory Board

UNIVERSITAS INDONESIA (UI)

Prof. Dr. Ir. Bambang Sugiharto, M.Eng
Prof. Dr. I. Made Kartika, Dipl.Ing.
Prof. Dr. Yanuar, M. Eng., M.Sc
Prof. Dr. Ir. Budiarmo, MSc
Prof. Dr.-Ing. Nandy Setiadi Djaya Putra
Prof. Yulianto Sulistyono Nugroho, M.Sc., P.hd
Prof. Dr. Ir. Harinaldi, M.Eng
Prof. Dr. Ir. M. Idrus Alhamid
Assoc. Prof. Dr. Budihardjo, Dipl. Ing
Assoc. Prof. Dr.-Ing Nasruddin, MSc

UNIVERSITI TEKNOLOGI MALAYSIA (UTM)

Prof. Ir. Dr. Azhar Abdul Aziz
Prof. Dr. Farid Nasir Ani
Assoc. Prof. Dr. Mazlan Abdul Wahid
Assoc. Prof. Dr. Normah Mohd Ghazali
Assoc. Prof. Dr. Nor Azwadi Che Sidek
Assoc. Prof. Dr. Nazri Kamsah

NATIONAL UNIVERSITY OF SINGAPORE (NUS)

Prof. Dr. Kim Choon Ng
Assoc. Prof. Dr. Christopher Yap
Assoc. Prof. Dr. Chua Kian Jon Ernes

KING ABDULLAH UNIVERSITY OF SCIENCE AND TECHNOLOGY (KAUST), SAUDI ARABIA

Dr. Muhammad Wakil Shazad

INTERNATIONAL ISLAMIC UNIVERSITY OF MALAYSIA (IIUM)

Prof. Dr. M.N.A. Hawlader



Faculty of Engineering Universitas Indonesia
Mechanical Engineering Department
Kampus Baru UI – Depok, 16424, Indonesia, Tel. +62 21 727 0032
11 – 12 November 2015, Jakarta, Indonesia



Conference Organizer

Chairman:

Ardiyansyah ST, M. Eng., Ph. D.

Secretary:

Sentot Novianto, ST., MT.

Member:

Dr. Agus S. Pamitran, ST., M.Eng.

Ir. Supriyadi, M. Sc

Ir. Arief Surachman, MT

Ir. Senoadi, MT



Table of Contents

Experimental Investigation on a Mixed Refrigerants Joule Thomson Refrigerator	1-5
Condensate Water Processing of Split-Unit Air Conditioning System on Commercial Building	6-9
Automatic Cooled Air Distribution for Vehicle Cabin	10-13
The Tribological Characteristics of Rubber Seed Oil using Four-Ball Tribotester	14-19
Experimental Study on a Cold Storage System with a Variable Speed Compressor	20-23
Biobutanol Production from the Fermentation of Oil Palm Frond Extract using <i>Clostridium acetobutylicum</i> (ATCC4259)	24-28
Superhydrophobic surfaces for convective heat transfer applications	29-33
Physical Characteristics of Pulverized EFB Briquettes Produced under Various Heating Temperatures	34-37
Analysis of different friction factor correlations on the frictional pressure drop of two-phase flow ammonia-cooled minichannel	38-42
Optimization of a single phase rectangular microchannel heat sink cooling system	43-48
Two-Phase Frictional Pressure Drop Minimization in the Laminar-Laminar Region of a Mini-channel	49-53
The Effect of Bio-Based Additives on Engine Performance and Emissions of Petrol and Diesel Engine	54-60
The Effect of Decontamination on Vehicle Cooling System	61-66
A review of Development of Test Rig for Organic Rankine Cycle	67-70
Investigation into the Selection of an Appropriate Piston Head Geometry for a Spark Ignition Engine Equipped Direct-Fuel Injector	71-75
Investigation of Cylinder Deactivation strategies for better fuel consumption using 1-D Simulation Method	76-81
Design and Experimental Analysis of Low Temperature Freezer Using Cascade Method	82-86
Flame Propagation and Burning Rates of Methane-Air in a Closed Combustion Vessel	87-91
Reduction of NO _x emission using Swirling Flameless Combustion	92-96
Self-preheated Flameless Combustion	97-107



IMAT 2015 PROGRAM

Wednesday, Nov 11, 2015

Time	Room	
8:00		Registration open
9:00	10:00	Kecapi
		Opening Ceremony
		Welcome speech from University of Indonesia
		Thermofluids Research Progress Presentation
		- University of Indonesia
		- Universiti Teknologi Malaysia
		- National University of Singapore
10:00	10:15	
		Coffee Break
10:15	12:00	
		Keynote Speech
		Prof. Jong Taek Oh
		Chonnam National University, South Korea
		Prof. Kiyoshi Saito
		Waseda University, Japan
12:00	13:00	
		Lunch Break
13:00	15:00	Kecapi 1/2/3
		Parallel Session 1A/B/C
15:00	15:15	
		Coffee Break
15:15	17:00	Kecapi 1/2/3
		Parallel Session 2A/B/C
17:00	19:00	
		Break
19:00	21:00	Kecapi
		Gala Dinner

Thursday, Nov 12, 2015

Time	Room	
8:00		Kecapi
		Registration open for tour
9:00	10:00	
		Award Ceremony
		Closing Ceremony
10:00	15:00	
		Technical Tour to Universitas Indonesia, OR
		Tour of Taman Mini Indonesia Indah



Parallel Sessions

Wednesday, Nov. 11, 2015

13:00 15:00 Kecapi 1 Parallel Session 1A

Paper ID	Title	Presenter	Affiliation
2015-IMAT-004	Automatic Cooled Air Distribution for Vehicle Cabin	Henry Nasution	Universiti Teknologi Malaysia, Skudai 81310, Johor, Malaysia
2015-IMAT-031	An Adsorption Equilibria Model for Steady State Analysis	Kim Choon Ng	Thuwal 23955-6900, Kingdom of Saudi Arabia
2015-IMAT-007	Effect of Regeneration Air Temperature on the Performances of a Desiccant Wheel	Haslinda Mohamed Kamar	Universiti Teknologi Malaysia, Skudai 81310, Johor, Malaysia
2015-IMAT-050	Optimization of Hydrogen Storage Capacity by Physical Adsorption on Open-ended Single-walled Carbon Nanotube as Diameter Function	Nasruddin	Universitas Indonesia, Depok 16424
2015-IMAT-033	Use of Double Condenser series in Refrigeration Systems to Improve the Performance of Spray Dryer in the study of thermodynamic Balance System	E. A. Kosasih	Universitas Indonesia, Depok 16424
2015-IMAT-051	Microscale Study of Hydrogen Adsorption on Carbon Nanotube	Nasruddin	Universitas Indonesia, Depok 16424
2015-IMAT-052	The Effect of Adsorbent Granular Size on Zeolite-Water Solar Adsorption Chiller for UI Area	Nasruddin	Universitas Indonesia, Depok 16424
2015-IMAT-002	Experimental Investigations on a Mixed Refrigerants Joule Thomson Refrigerator	Henry Nasution	Universiti Teknologi Malaysia, Skudai 81310, Johor, Malaysia
2015-IMAT-032	A review of Development of Test Rig for Organic Rankine Cycle	M.I. Alhamid	Universitas Indonesia, Depok 16424

13:00 15:00 Kecapi 2 Parallel Session 1B

Paper ID	Title	Presenter	Affiliation
2015-IMAT-010	Biobutanol Production by Fermenting Oil Palm Frond Extract Using Clostridium acetobutylicum (ATCC4259)	Azhar Abdul Aziz	Universiti Teknologi Malaysia, Skudai 81310, Johor, Malaysia
2015-IMAT-023	CONTROLLED MICROWAVE INDUCED PYROLYSIS OF WASTE RUBBER TYRES	Farid Nasir Ani	Universiti Teknologi Malaysia, Skudai 81310, Johor, Malaysia
2015-IMAT-024	Physical Characteristics of Pulverized EFB Briquettes Produced under Various Heating Temperatures	Hasan Mohd Faizal	Universiti Teknologi Malaysia, Skudai 81310, Johor, Malaysia
2015-IMAT-035	Investigation into the Selection of an Appropriate Piston Head Geometry for a Spark Ignition Engine Equipped With Direct-Fuel Injector	M Farid	Universiti Teknologi Malaysia, Skudai 81310, Johor, Malaysia
2015-IMAT-046	Flame Propagation and Burning Rates of Methane-Air in a Closed Combustion Vessel	Aminuddin Saat	Universiti Teknologi Malaysia, Skudai 81310, Johor, Malaysia
2015-IMAT-011	Single-cylinder 125 cc Stepped Piston Engine for Mobility and Portable Power Generation Applications	Azhar Abdul Aziz	Universiti Teknologi Malaysia, Skudai 81310, Johor, Malaysia
2015-IMAT-006	The Tribological Characteristic of Rubber Seed Oil using Four-Ball Tribotester	Abdul-Fattah	Universiti Teknologi Malaysia, Skudai 81310, Johor, Malaysia



13:00 15:00 Kecapi 3 Parallel Session 1C

Paper ID	Title	Presenter	Affiliation
2015-IMAT-027	Optimization of a single phase rectangular micro channels heat sink cooling system	Normah Mohd. Ghazali	Universiti Teknologi Malaysia, Skudai 81310, Johor, Malaysia
2015-IMAT-013	Superhydrophobic surfaces for convective heat transfer applications	Kok Hwa Yu	National University of Singapore, Singapore 1175676
2015-IMAT-025	Analysis of different friction factor correlations on the frictional pressure drop of two-phase flow ammonia-cooled minichannel	Normah Mohd. Ghazali	Universiti Teknologi Malaysia, Skudai 81310, Johor, Malaysia
2015-IMAT-048	Thermal performance of carbon nanotube nanofluids in solar microchannel collectors: An experimental study	Thierry Mare	Université de Rennes 1, France
2015-IMAT-040	Thermal Properties of Beeswax- CuO Nano-Phase Change Material as Thermal Energy Storage	Nandy Putra	Universitas Indonesia, Depok 16424
2015-IMAT-017	CFD Analysis of Slurry Flow in Anaerobic Digester	Ahmad Indra Siswantara	Universitas Indonesia, Depok 16424
2015-IMAT-016	CFD Simulation of Turbulent Flows in Proto X-3 Bioenergy Micro Gas Turbine Combustor Using STD k- ϵ and RNG k- ϵ Model for Green Building Application	Asyari Daryus	Universitas Indonesia, Depok 16424

15:15 17:00 Kecapi 1 Parallel Session 2A

Paper ID	Title	Presenter	Affiliation
2015-IMAT-047	Solar Air-conditioning System in University of Indonesia	Hajime Yabase	Waseda University, Shinjuku-ku, Tokyo, Japan
2015-IMAT-003	Condensate Water Processing of Split-Unit Air Conditioning System on Commercial Building	Henry Nasution	Universiti Teknologi Malaysia, Skudai 81310, Johor, Malaysia
2015-IMAT-037	Design and Experimental Analysis of Low Temperature Freezer Using Cascade Method	Sumeru Kasni	Politeknik Negeri Bandung 40012, Indonesia
2015-IMAT-030	The Effect of Decontaminants on Vehicle Cooling System	Zulkarnain Abdul Latiff	Universiti Teknologi Malaysia, Skudai 81310, Johor, Malaysia
2015-IMAT-041	Potential for Utilization of Solar Radiation Absorption Cooling System in Indonesia	Yusvardi	Tirtayasa Cilegon, Banten
2015-IMAT-008	Experimental Study on a Cold Storage System with a Variable Speed Compressor	Haslinda Mohamed Kamar	Universiti Teknologi Malaysia, Skudai 81310, Johor, Malaysia
2015-IMAT-018	Desalination Costing: An Improved Exergetic Method	Muhammad Wakil Shahzad	King Abdullah University of Science & Technology
2015-IMAT-052	Efficiency of Chlorine and Other Oxidants in treating sweater for Cooling Towers	Mohammed Al-Bloushi	King Abdullah University of Science & Technology
2015-IMAT-044	Electrical Rating of Concentrated Photovoltaic (CPV) Systems: Long Term Performance Analysis and Comparison with Conventional PV Systems	Muhammad Burhan	National University of Singapore, Singapore



15:15 17:00 Kecapi 2 Parallel Session 2B

Paper ID	Title	Presenter	Affiliation
2015-IMAT-036	Investigation of Cylinder Deactivation strategies for better fuel consumption using 1-D Simulation Method	M Farid	Universiti Teknologi Malaysia, Skudai 81310, Johor, Malaysia
2015-IMAT-012	Reduction of NOx emission using Swirling Flameless Combustion	Raid A. Alwan	Universiti Teknologi Malaysia, Skudai 81310, Johor, Malaysia
2015-IMAT-015	Production of Pyrolysed Oil from Crude Glycerol using Microwave Heating Technique	Cheng Tung Chong	Universiti Teknologi Malaysia, Skudai 81310, Johor, Malaysia
2015-IMAT-019	Characterization of Carbon Nanotubes Produced from Hydrocarbon-rich Flame	Cheng Tung Chong	Universiti Teknologi Malaysia, Skudai 81310, Johor, Malaysia
2015-IMAT-029	The Effect of Bio-Based Additives on Engine Performance and Emissions of Petrol and Diesel Engine	Zulkarnain Abdul Latiff	Universiti Teknologi Malaysia, Skudai 81310, Johor, Malaysia
2015-IMAT-043	Self-preheated Flameless Combustion	Seyed Ehsan Hosseini	Universiti Teknologi Malaysia, Skudai 81310, Johor, Malaysia
2015-IMAT-009	Effects of Electromagnetic Field on Fuel Consumption in Diesel Engine	Tatun H Nufus	State Polytechnic of Jakarta
2015-IMAT-005	Controlling Fire Growth in Electrical Cable Compartment by Reducing Oxygen Concentration	Yulianto Sulisty Nugroho	Kampus UI Depok 16424, Depok, West Jawa, Indonesia
2015-IMAT-036	Investigation of Cylinder Deactivation strategies for better fuel consumption using 1-D Simulation Method	M Farid	Universiti Teknologi Malaysia, Skudai 81310, Johor, Malaysia

15:15 17:00 Kecapi 3 Parallel Session 3B

Paper ID	Title	Presenter	Affiliation
2015-IMAT-026	Single Objective Optimization of the Darcy Friction Factor and the Frictional Pressure Drop of R22 and R290	Qais Abid Yousif	Universiti Teknologi Malaysia, Skudai 81310, Johor, Malaysia
2015-IMAT-028	Two-Phase Frictional Pressure Drop Minimization in the Laminar-Laminar Region of a Minichannel	Normah Mohd. Ghazali	Universiti Teknologi Malaysia, Skudai 81310, Johor, Malaysia
2015-IMAT-014	Void Fraction of Two-phase Flow Evaporation with Propane in Circular Horizontal Tube	S. Novianto	Universitas Indonesia, Depok 16424
2015-IMAT-049	Characteristics of vortex ring formation by Synthetic Jet Actuator in Different Cavity	E. A. Kosasih	Universitas Indonesia, Depok 16424
2015-IMAT-042	Experimental Study of Spherical Pins under Varying Load Condition using Pin-On-Disk Tribotester	N. Nuraliza	Universiti Teknologi Malaysia, Skudai 81310, Johor, Malaysia
2015-IMAT-021	The Effect of Plasma Actuator Placement towards Drag Coefficient Reduction on Ahmed Body as an Aerodynamic Model	Harinaldi	Universitas Indonesia, Depok 16424



Faculty of Engineering Universitas Indonesia
Mechanical Engineering Department
Kampus Baru UI – Depok, 16424, Indonesia, Tel. +62 21 727 0032
11 – 12 November 2015, Jakarta, Indonesia

8th International Meeting
On Advances in
Thermofluids
<http://imat.eng.ui.ac.id>

Proceeding

Experimental Investigation on a Mixed Refrigerants Joule Thomson Refrigerator

Ade Suryatman Margana^a, Kasni Sumeru^{a,b}, Azhar Abdul Aziz^b, Henry Nasution^{b,*}, Abioye^{c,d}

^a Department of Refrigeration & Air Conditioning
 Politeknik Negeri Bandung, Bandung 40012
 Tel : (022) 2013789 ext 254. Fax : (022) 2013889
 E-mail : sumeru84@gmail.com

^b Automotive Development Centre
 Faculty of Mechanical Engineering, Universiti Teknologi Malaysia, Johor 81310
 E-mail : azhar@fkm.utm.my, henry@utm.my

^c Faculty of Mechanical Engineering, Universiti Teknologi Malaysia, Johor 81310

^d Department of Mechanical Engineering, Abubakar Tafawa Balewa University, Bauchi, Nigeria
 E-mail : kunleabioye@yahoo.com

ABSTRACT

This paper presents an investigation on the Joule Thomson refrigerator for very low temperature using binary mixture, i.e. propane and nitrogen as refrigerant. Two or three stages of vapor compression refrigeration cycle are utilized to obtain temperature below -100°C. The present study developed a mixed gas Joule Thomson refrigerator using single compressor with binary mixtures, i.e., propane and nitrogen. The use of single compressor in Joule Thomson refrigerator reduces the cost and complexity. Also, because the Joule Thomson operates using a compressor for refrigeration system, as a result the working pressure of the system is similar to the pressure of refrigeration system with single compressor. The experiments were carried out using binary mixtures between propane and nitrogen with different concentration. The experimental results showed that the lowest temperature in the refrigerator was -80.0°C, it was attained when the binary mixtures of 95.4% and 4.6% (by mass) for propane and nitrogen, respectively. Although nitrogen has very low normal boiling point compared to propane, however an increase in the nitrogen concentration above 4.6% increases the discharge pressure and the evaporation temperature.

Keywords: Joule Thomson, binary mixture, propane, nitrogen.

1. INTRODUCTION

A refrigerator for very low temperature typically operates with very low pressure on the suction and high pressure in the discharge. It is a great challenge to create a refrigerator for very low temperature using single compressor with normal pressures, namely

approximately 1 to 3 bar and 15 to 20 bar for suction and discharge pressures, respectively. For cryogenic temperature application is widely used Linde-Hampson cycle. This cycle is utilized to liquefy the gases using nitrogen as working fluid. The operating of this cycle up to 200 bar, as a result, the construction and operation is complicated. A Joule Thomson refrigerator using mixed refrigerant is introduced to reduce the complexity of the Linde-Hampson cycle. Because the operating pressure of Joule Thomson refrigerator only under 20 bar and can use a compressor that is usually applied in the typical air conditioner.

Polbielniak was the first person who proposed a patent in USA in 1936 [1]. Furthermore, Kleemenko [2] was the first person who demonstrated the liquefying of LNG from nature gas using Joule Thomson refrigerator with mixed refrigerant. Venkatarathnam [3], Alexeev [4] and Lee et al. [5] continue the Kleemenko's work. Also, patents related to gas liquefying using Joule Thomson refrigerator proposed by Arman [6] and Kountz [7].

This paper develops a prototype of Joule Thomson refrigerator using binary mixture of nitrogen and propane as working fluid and investigates the system performances.

2. DESCRIPTION OF THE SYSTEM

Figure 1 shows the Linde-Hampson cycle in the T-s diagram using nitrogen as working fluid. The figure shows that the working pressures are 1 bar and 200 bar for the lowest and the highest pressures respectively. Compared to the conventional refrigeration system, such as freezers and air conditioners, this pressure is very high, because the highest pressure of the freezers and air conditioners only approximately 20 bar. Because the

high of the working pressure of Linde-Hampson, this cycle cannot use a compressor that is typically applied for the freezers and air conditioners. As a result the developing and operating of the Linde-Hampson is very complicated. Joule Thomson refrigerator is introduced to reduce the complications of Linde-Hampson cycle. Because the working pressures of Joule Thomson refrigerator are similar to the air conditioner as a result the compressor on this refrigerator can use the compressor applied on the air conditioners.

Figure 2 shows the Joule Thomson cycle in T-s diagram. The figure shows that the working pressures of this cycle 2 and 20 bar, is similar to the working pressures of an air conditioner using vapor compression refrigeration cycle. In the operation, the Joule Thomson refrigerator uses mixture refrigerants as working fluid.

Typically, the air conditioners and freezers use vapor compression refrigeration cycle (VCRC) in their operation. The evaporation temperature of air conditioners is approximately 5°C to 8°C, whereas the freezer is about -20 to -40°C. To achieve the evaporation temperature below -40°C usually utilize cascade system using two compressors for temperature -40°C to -60°C and three or four compressors for temperature -60°C to -100°C. The more amounts of the compressor, the more complex the operating and maintenance. Because the Joule Thomson refrigerator only uses one compressor, it will reduce the complexity of the system. Decreasing system complexity will reduce operational and maintenance costs. As a result, the use of Joule Thomson refrigerator for very low temperature application is promising for the future.

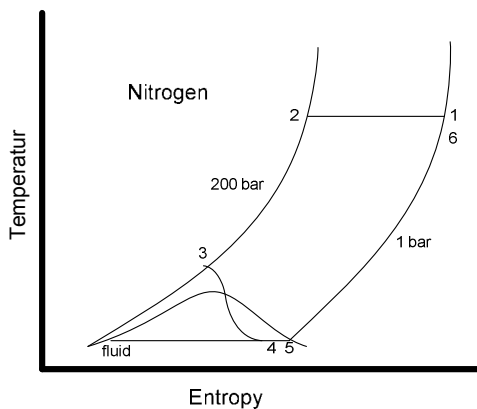


Figure 1: Linde-Hampson cycle uses nitrogen as working fluid

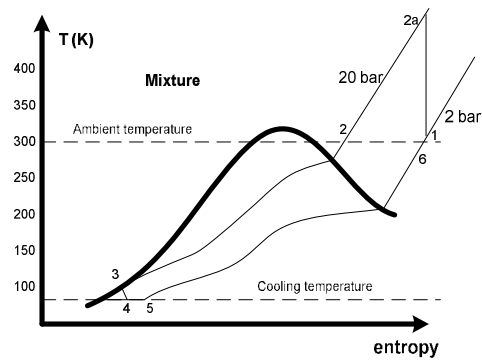


Figure 2: Joule Thomson cycle uses refrigerant mixture as working fluid

Figure 3 show the main components of the Joule Thomson refrigerator. There are five the main components in the Joule Thomson refrigerator, i.e., compressor, aftercooler, expansion device (TXV), evaporator and heat exchanger. Meanwhile, there are four the main components in the air conditioner, i.e., compressor, condenser, expansion device and evaporator, as shown in Figure 4.

Although the working pressures of the Joule Thomson refrigerator is similar to the air conditioner, however their working temperatures are different, especially on the evaporator.

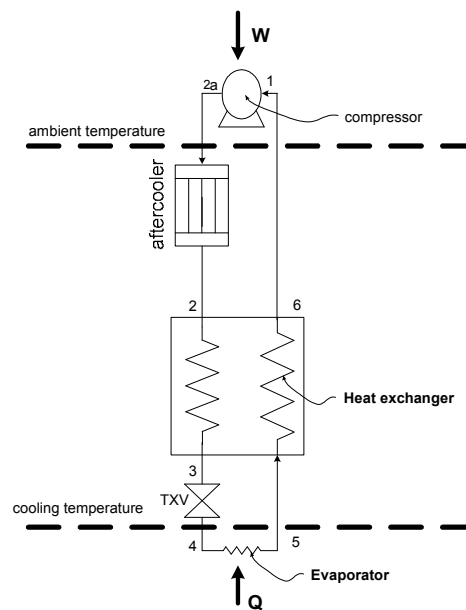


Figure 3: The main components of the Joule Thomson refrigerator

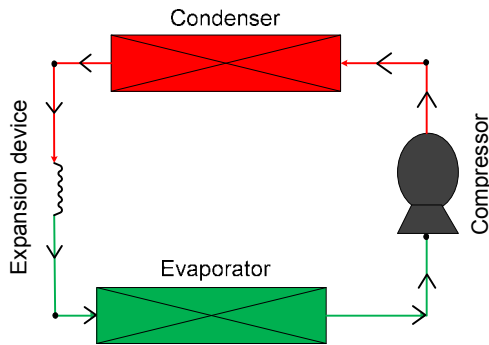


Figure 4: The main components of the air conditioner

3. METHODOLOGY

The Joule Thomson refrigerator was designed to achieve cryogenic temperature, that is below -150°C . In order to achieve the designed temperature, methane and ethane must be used as refrigerant. Because the both refrigerants are not used in the experiment, as a result the designed temperature has not achieved. In the experiment, two gases, i.e., propane and nitrogen were applied. Figure 5 shows the schematic diagram of the Joule Thomson refrigerator used in the experiment. The figure shows that an oil separator is placed after to the aftercooler. There are two outlets on the oil separator; one sends refrigerant vapor to the heat exchanger, the other will return oil to the compressor. In addition, the evaporator is placed in vacuum chamber to avoid heat transfer between the evaporator and ambient.

In order to investigate the system performances, six thermocouples to measure the temperature and five pressure gauges to measure the pressure were installed

in the system, as shown in Figure 5. The measured temperatures are:

1. Suction temperature
2. Discharge temperature
3. Inlet of the heat exchanger temperature
4. Outlet of the heat exchanger temperature
5. Outlet of the expansion device temperature
6. Outlet of the evaporator temperature

According to Figure 5, the outlet of the heat exchanger temperature is same with the inlet of the expansion device temperature. Likewise, the outlet of the expansion device temperature is same with the inlet of the evaporator temperature.

Furthermore, the measured pressures are:

1. Suction pressure
2. Discharge pressure
3. Inlet of the expansion device pressure
4. Outlet of the expansion device pressure
5. Outlet of the heat exchanger pressure

In this experiment, there are two gases refrigerant utilized in the Joule Thomson refrigerator with four different compositions. Table 1 shows the composition of mixed refrigerant used in the experiments.

Table 1: The refrigerant composition

Experiment	Nitrogen (%)	Propane (%)
1	0	100
2	4.6	95.4
3	8.2	91.8
4	12	88

According to Table 1, the first experiment was carried out on the system using 100% of propane. The subsequent experiments were carried out by mixing nitrogen for various compositions into the system, as shown in Table 1.

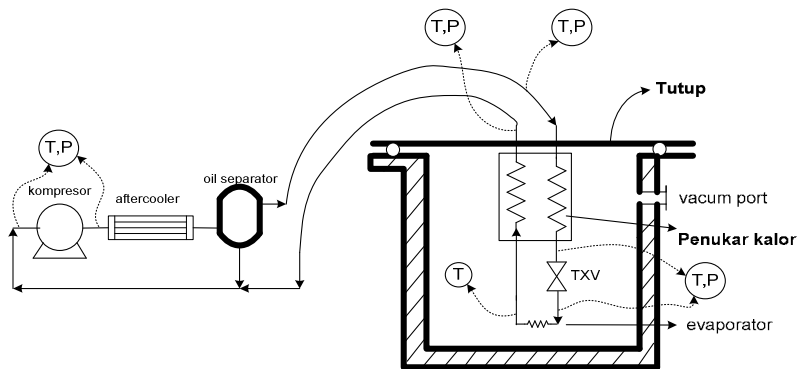


Figure 5: The schematic diagram of a prototype of Joule Thomson refrigerator and measurement points

4. RESULT AND DISCUSSION

Figure 6 illustrates the temperature profile on the evaporator of the Joule Thomson refrigerator for 60 minutes. The figure shows the evaporator temperature achieved -40°C at 20 minutes and also the minimum temperature is -57.2°C . Compared to the freezer using single compressor with propane (R290) as working fluid, these temperatures are much lower than that of the freezer. As a result, Joule Thomson is promising also to be utilized as a very low temperature freezer. The freezer using VCRC is widely used in the refrigerator. The VCRC refrigerator usually uses two compressors and three compressors for the evaporation temperature of -40°C and -80°C respectively.

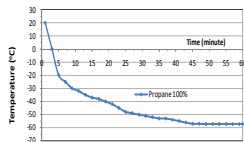


Figure 6: Evaporator temperature of the Joule Thomson refrigerator with propane 100%

Figure 7 illustrates the temperature profile of the evaporator of the Joule Thomson refrigerator using binary mixture for various compositions. The figure shows that the minimum temperature was achieved by the refrigerant composition propane 95.4% and nitrogen 4.6% (by mass), that is -80.0°C . When the percentage of nitrogen increases, the minimum temperature increases. Although the normal boiling point (NBP) of nitrogen much lower than that of propane, however by increasing the nitrogen above 95.4% will increase the evaporation temperature because result in high pressure on the compressor discharge. The more the amounts of nitrogen, the more the increase in evaporation temperature.

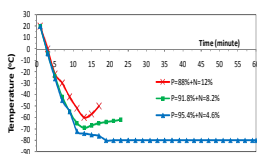


Figure 7: Evaporator temperature of the Joule Thomson refrigerator for various compositions of propane and nitrogen.

Likewise, based on the Figure 7, the cooling rate on the evaporator of Joule Thomson refrigerator using binary mixture (propane + nitrogen) is approximately $-15^{\circ}\text{C}/\text{minute}$. As a result, this refrigerator is also suitable for the fast cooling-down freezer.

5. CONCLUSION

A prototype of the Joule Thomson refrigerator using binary mixture (propane + nitrogen) has been developed. The experimental results showed that the minimum temperature was -80.0°C when the mixture composition was propane 95.4% and nitrogen 4.6% by mass. Although the NBP of nitrogen is much lower than that of propane; however the increase in the amounts of nitrogen into the system will increase the minimum temperature and increases the discharge pressure.

ACKNOWLEDGMENT

This study was supported financially by Politeknik Negeri Bandung was managed by UPPM and Post Doc RU, UTM. Cost Center Code : Q.J130000.21A2.02E30. In addition, the authors are also grateful to Automotive Development Centre, Faculty of Mechanical Engineering, Universiti Teknologi Malaysia for facilities and management support.

REFERENCES

- [1] W. J. Podbielniak, "Art of refrigeration", *U.S Patent 2,041,725*, 1936.
- [2] F. Nisenhoff, F. Patten, and S. A. Wolf, 1996, "... And what about cryogenic refrigeration" In proceeding of International Cryocooler Conference, June, 25-27, Waterville, USA, 1996.
- [3] Venkatarathnam, G., Sentil Kumar, P., and Srinivasa M.S., 2003, Experimental studies on fast cool down mixed refrigerant cascade refrigerator, *Proceeding of International Congress of Refrigeration, ICR0105*, Washington D.C.
- [4] A. Alexeev, A. Thiel, C. H. Haberstroh, and H. Quach, "Study of behavior in the heat exchanger of mixed gas Joule-Thomson cooler", *Journal of Advances in Cryogenic Engineering*, vol. 45, pp. 307-315, 2000.
- [5] J. Lee, G. Hwang, S. Jeong, B. J. Park, and Y. H. Han, "Design of high mixed refrigerant Joule-Thomson refrigerator for cooling HTS cable", *Cryogenics*, vol. 51, pp. 408-414, 2011.
- [6] B. Arman, D. P. Bonaquist, J. A. Weber, A. Ziemar, A. Ach, and M. A. Rashad, "Cryogenic rectification

- method for producing nitrogen gas and liquid nitrogen”,
US patent 6,125,656, 2000.
- [7] K. J. Kountz and M. B. Patrik, “Control method for
mixed refrigerant based natural gas liquefier”, *US Patent*
6,530,240, 2003.

Condensate Water Processing of Split-Unit Air Conditioning System on Commercial Building

Henry Nasution^{a,*}, Nurul Hanim Aubaidellah^a, Kasni Sumeru^a, Afiq Aiman Dahlan^a

^aAutomotive Development Center, Faculty of Mechanical Engineering
Universiti Teknologi Malaysia, 81310 UTM Johor Bahru, Johor, Malaysia
Tel : (07) 5535447. Fax : (07) 5535811
E-mail : henry@utm.my

ABSTRACT

A research to measure the condensate volume produced by the split unit air conditioning (AC) system on a commercial building was done where the measured volume was then used to determine the capacity of the water storage tank required to fill in the condensate. The selected building is Scholar's Inn UTM (SIUTM) in Johor which able to operate a maximum of 162 units of 1 Hp and 81 units of 1.5 Hp AC if the building is fully occupied. In this research, by maintaining the cooling load in the conditioned room, the condensate water produced by the split units was collected and measured to find the average to condensate production of the day. Based on the practical operating hours of SIUTM, at most a 12-hours operation per day is considered. With only depending on the relative humidity and the temperature of the day, the result obtained was compared to the previous research that using psychometric analysis to determine the condensate water produced in a hot and humid country. The results show that the condensate can be produced up to 4781 liter per day, 143430 liter per month and 1721160 liter every year and the condensate water having the value of pH at 7.17, TDS at 1.0 mg/liter and copper (Cu) of 1.1 mg/liter, which is acceptable values for raw water source. For drinking purposes, treatments such as reverse osmosis, distillation or ion exchange can be done.

Keywords

Condensate recovery, condensate water, water source, water quality

1. INTRODUCTION

Nowadays, air conditioning has become a necessity especially in building ventilation. For commercial buildings such as offices, malls and shopping centers they usually used central system.

The study on condensate water recovery just started not long time ago when sustainability becomes an important practice worldwide. Boulware [1] stated that due to quality issue, condensate water often ignored as a source of freshwater. It just gets into people's attention as drinkable and non-drinkable usage to cover the water shortage lately. In addition, the investigation

on water recovery also done in order to increase the coefficient of performance (COP) of the air conditioning system, as well as to increase the cost saving on operating the system [1-2].

As for the experiment on measuring the amount or volume of water produced from condensation from a split-unit air conditioning system, it can be done in many ways. Some of the ways are by collecting the condensate experimentally or through analytical model by taking the system cooling capacity into consideration.

A study on condensate water as water source was also performed by Al-Farayedhi et al. [3]. They have comparing between analytical model and experimental method results to investigate the condensate water as another water source from a vapour compression air conditioning system in hot and humid regions. Their investigation was focusing on the relationship between relative humidity and environment temperature with the amount of condensate water produced.

Barreira et al. [2] have done the thermoeconomic analysis and optimization of residential split-type using simulation-based optimization techniques. The research were focusing on the relationship between the COP of the system and the percentage of cost saving. As the COP increases, the percentage of cost saving also increases [2]. One of the ways to improve the COP is by utilizing the condensate captured from an air conditioning system, to be reuse back by the system. Typically, the condensate water from air conditioning units will just be drained away. Also, in a hot and humid climate, the amount of condensate produced is very significant and just become a waste. Therefore, it is very important to study the potential of water and energy sustainability by recovering the condensate water from air conditioning system [4].

Buildings such as apartment blocks will usually used split-unit types for individual comfort in each room. The Scholar's Inn of Universiti Teknologi Malaysia (SIUTM) is an apartment type building which provides on-campus lodging for anyone including UTM students, staff and also outsider. The building is using split-unit air conditioning system for space ventilation.

Just like the other split-unit system installation, the drainage of the condensate water will be installed too and somehow causing another problem to human comfort itself and also affecting the view of the building. Most of the piping will headed to the drain outside of the building. Improper piping installation sometimes distracting peoples lane. Furthermore, the water leaking from the broken pipe annoyed people and also causing moss problem in some part of the building. Economically, the drainage of condensate water is also a waste. From this problem, the ideas of designing the storage tank for the recovery of condensate water from the split-unit air conditioning system were carried out.

2. AIR CONDITIONING CONDENSATE RECOVERY

The water and the heat contained in the condensate can be used back for other purposes. This is called the condensate recovery. Instead of sent it to sewer drain, recovering condensate can help to significant savings of energy, chemical treatment and make-up water [2, 5].

Alliance for Water Efficiency [5] stated that the condensate water is essentially the same as distilled water which is having low mineral content and Total Dissolved Solids (TDS) level of near zero. Thus, it has to be removed to prevent damage to other equipments. Also, they stated that the collection of condensate from the air conditioning system can be used for various applications, depends on the amount produced.

The recovery of condensate water can be used as alternate water source for application such as:

- (a) The make-up water of cooling tower.
- (b) For irrigation purposes.
- (c) Evaporative cooler.
- (d) Industrial processes such as boiler feed water and heating system.
- (e) Cleaning applications.

The calculated total volume per day of condensate water is used to determine the capacity of the water storage tank. The volume of condensate water produced is defined as:

- (a) Average condensate produced (Q_1) in one hour (L/hour) for one unit:

$$Q_1 = \frac{\text{Volume of condensate water}}{4} \quad (1)$$

- (b) Total volume of condensate water per month (L/month):

$$Vol_{TN} = Q_1 \times N \times 12 \times 30 \quad (2)$$

- (c) Total volume of condensate water per year (L/year):

$$Vol_{TY} = Q_1 \times N \times 12 \times 365 \quad (3)$$

where N is number of split air conditioning unit in the building, 4 is hours of readings taken in a day, 12 is number of operation hours per day, 30 is number of days per month and 365 is number of days per year.

3. METHODOLOGY

The basic principle of obtaining the condensate produced by the split-unit air conditioner is by collecting it. The experimental work was done where the conditioned room was set to the temperature of 23°C and the condensate produced was measured for every 2 hours. The average production per hour is determined, by considering the relative humidity and outside temperature. Based on yearly occupancy rates of the building, the maximum condensate production was determined to be use as the water storage tank capacity.

To select the proper design for the water storage tank of the condensate water, several parameters need to be considered such as tank capacity, the materials of the water tank, position of the tank and how the piping system will be installed to the tank.

As for the piping system, it will be installed in inclined position so that the condensate water will flow by gravitational force only (Figure 1). Thus, no pump is needed to pump water down except one to be installed together with the tank.

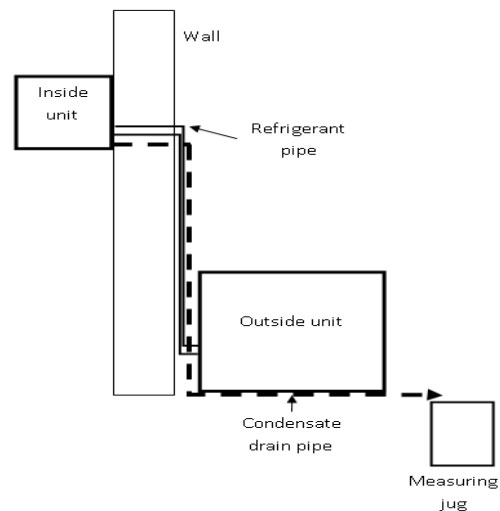


Figure 1: Experiment set up diagram

Water quality test also done in order to determine the possible use of the condensate such as for drinking purposes, raw water sources or even for watering plants. A sample of condensate collected was randomly picked to be tested in Chemical Analysis Laboratory of Faculty of Science in UTM. Due to some limitation, only three parameters tested which are water pH, total dissolved solid (TDS) and copper (Cu) content. These three parameters are significant since the pH define the acidity level of the condensate water, TDS reading shows the mineral content in the water while Cu content determine whether there are any Cu particles in the condensate due to the contact of the water with the cooling coil that made from copper.

4. RESULTS AND DISCUSSION

The experiment was done from 2.00 PM to 4.00 PM and 4.00 PM to 6.00 PM where it stated the highest temperature of the day with average high temperature of 31°C. For actual low temperature, it is usually happen during the night where the average low temperature is 24°C. Noted that during day and night the ambient temperature is different where at night, the ambient temperature is colder and lower than during the day thus the room temperature will also differ during the night. The lowest relative humidity ranges from 50% to 70% and highest which ranging from 74% up to 94%. Both relative humidity and temperature affect the volume of condensate water produced by the split-unit air conditioner.

Most of the occupants of SIUTM usually stay in the room during the night where they will operate the air conditioning unit. The experiment on collecting the condensate volume is however conducted during the day due to some restriction. Thus, the value of the results should be slightly different. The average volume of condensate produced per hour for 1.5 HP is 2.5 L/hour whereas for 1 HP is 2.2 L/hour. These results can be said as the minimum condensate volume produced by the air conditioner since the condition is high temperature and low relative humidity that slower the condensation process outside the cooling coil.

Table 1: Condensate water predicting

AC Unit (HP)	Room	Day (L)	Month (L)	Year (L)
1	81	2430	72900	886950
1.5	162	4276.8	128304	1773900
Total condensate water		6706.8	201204	2660850

In SIUTM, there are total of 93 rooms where 81 of them are air-conditioned and 12 without air-

conditioner. In one room there will be three units of air-conditioners; two of them are 1 HP and one 1.5 HP. Thus, the total 1.5 HP air-conditioners in the building are 81 units and the total 1 HP air-conditioners in the building are 162 units. Equation 2 and 3 is used to determine the monthly and yearly production rate of the condensate water (Table 1).

The piping system will only consider on how the condensate water will be directed to the storage tanks. In the SIUTM building, the air-conditioner split-unit types were installed in 243 units are located in different levels. Also, current condensate drain pipes only let the water flow to the drain below. To collect all these water, the existing pipes will be connected to each other by adding pipe junctions and collected in one bigger pipe before entering the storage tanks. Condensate water need to be flow smoothly through the drain pipe to prevent it from backflow and leak through the inside unit. Thus, the pipe will be in inclined arrangement where only gravitational force used to let the water flow downwards. Figure 2 shows the piping system need to be installed and add to the current drain pipe where it will let the condensate water flow from all the split-unit's compressor into one pipe and entering the water storage tank on the ground level. The inclination of the pipe is necessary in order to use the gravitational force instead of pump to collect the water.

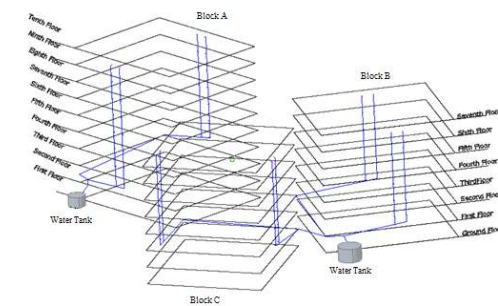


Figure 2: Piping and storage tank

Table 2 shows the condensate water has pH value of 7.17, in between the range of recommended raw water quality and drinking water quality standards by Ministry of Health Malaysia. pH value determine whether the water is acidic or alkali where in this case, it is acceptable. TDS consist of the dissolved of inorganic salts and small amount of organic matter in water. From the results, TDS value is 1.0 mg/liter, far below the drinking water standards by Ministry of Health Malaysia which is 1000 mg/liter. This is very low which is near zero and mineral free, thus makes it corrosive to most metals, especially steel and iron [5]. At higher levels, unpalatability, mineral deposition, excessive hardness and corrosion may occur. As for Copper (Cu) content, the result obtained is 1.055 mg/liter, slightly exceeding the standard made by

Ministry of Health Malaysia for both raw water and drinking water types at 1.0 mg/liter. At this level, the water will staining and has bitter taste but for health concern, the level is 1.3 mg/liter [6]. From these results, the condensate water can be used as raw water source and if it were to be used for drinking purposes, certain treatment procedure need to be done to remove or reduce the copper content from the water. The treatment options can be either reverse osmosis, distillation or ion exchange. Based on previous studies, Boulware [1] and many more found that the condensate water in most ways is exactly like rain. Condensate water by itself is distilled pure water, but it may require further treatment as it might get contaminated on the way [7]. Since the condensation process occurs outside the cooling coil surface which is made from copper, there might contain heavy metals from contact with the coil and air-conditioner equipment.

Table 2: Condensate water quality

Parameter	Condensate Water Quality	Recommended Raw Water Quality	Drinking Water Quality Standards
		Acceptable value	Maximum acceptable value
pH	7.17	5.5-9.0	6.5-9.0
TDS	1.0 mg/litre	1500 mg/litre	1000 mg/litre
Cu	1.1 mg/litre	1.0 mg/litre	1.0 mg/litre

5. CONCLUSION

Economically, the amount of condensate water produced by SIUTM building is too much to be waste. Based on the water quality test done, the collected condensate water can be used for as raw water material as well as for activities such as watering the plant, washing the car or even cleaning the floor since the properties is quite the same as distilled water. However for drinking purposes, some treatments need to be done to reduce or remove the copper contaminants in the water. Thus, the recovery of condensate water for SIUTM building is a good thing to be done where the volume of condensate water produced by the split-unit air conditioning system and the suggestion of water storage tanks already been made.

ACKNOWLEDGMENT

This work has been supported by the Ministry of Education Malaysia under Knowledge Transfer Program (R.J130000.7809.4L509) and Automotive

Development Center (ADC), Universiti Teknologi Malaysia

REFERENCES

- [1] Boulware B. Air conditioning condensate recovery. Environmental and Energy Management News. Pinchot University 2013; January 15.
- [2] Barreira EM, Negrao COR and Hermes CJL. Thermoeconomic analysis and optimization of residential split-type air conditioners. Appl Therm Eng 2013;50(1):629-636.
- [3] Al-Farayedhi AA, Ibrahim NI and Gandhidasan P. Condensate as a water source from vapor compression systems in hot and humid regions. Desalination 2014;349:60-67.
- [4] Licina D and Sekhar C. Energy and water conservation from air handling unit condensate in hot and humid climate. Energy and Build 2012;45:257-263.
- [5] Alliance for Water Efficiency. Promoting the efficient and sustainable use of water. Chicago. 2010.
- [6] Kissel DE, Vendrell PF and Atilas JH. Your household water quality: lead and copper. Household Water Quality Series 2003;Circular No. 858-10.
- [7] Guz K. Condensate water recovery. ASHRAE J 2005;47(6):54-56.

Automatic Cooled Air Distribution for Vehicle Cabin

Amirah Haziqah^a, Afiq Aiman Dahlan^a, Henry Nasution^{b,*}, Azhar Abdul Aziz^b

^aFaculty of Mechanical Engineering
Universiti Teknologi Malaysia, 81310 UTM Johor Bahru, Johor, Malaysia
Tel : (07) 5535447. Fax : (07) 5535811
E-mail : ahaziqahzulkifli@gmail.com

^bAutomotive Development Center
Universiti Teknologi Malaysia, 81310 UTM Johor Bahru, Johor, Malaysia
Tel : (07) 5535447. Fax : (07) 5535811
E-mail : henry@utm.my

ABSTRACT

Passenger's thermal comfort in vehicle cabin is the main priority in designing vehicle air-conditioning system. One of the parameters is the cabin air temperature. While other researchers are focusing on the temperature on the upper body, this research is focused on the air temperature for the whole body of the passengers inside vehicle cabin. Traditionally, drivers have to manually channel the cooled temperature according to their need. This paper discussed about the channeling of cooled air temperature throughout the passengers body automatically by controlling the gate so that temperature distribution in the vehicle cabin is according to the thermal comfort need by the passengers. The system is installed inside a hatchback vehicle and data is obtain from before and after the system installed. Results indicate that better thermal comfort temperature can be achieved throughout the driving.

Keywords

Thermal comfort, temperature distribution, intelligent vehicle cabin, HVAC

1. INTRODUCTION

The main challenge in designing vehicle air conditioning system is to develop an energy efficient system thus reducing the precious fossil fuel used by the vehicle. It is also helps in reducing the release of CO₂ emission to the environment. Many efforts by researchers have been made in various ways to decrease fuel consumption by the vehicle air conditioning system [1-6].

The temperature and thermal comfort in a vehicle cabin could be achieved by using proper controller. Matsui et al. [7] have made thermal analyses of a vehicle cabin by

using modern control theory and has determined the governing equations of the models by using statistical methods. Davis et al. [8] used fuzzy controlling system in building thermal modeling of a vehicle cabin. Wei and Dage [9] designed a control system for vehicle cabin based on intelligent methods.

Aeatrice et al. [10] analyze the thermal comfort of a vehicle cabin by analyzing the dynamic mode of a refrigeration cycle. Qi and Deng [11] applied a fuzzy controller system for thermal comfort modeling inside vehicle cabin where the inlet air volume rate is the only consideration for air temperature control. Farzaneh and Tootoonchi [12] used a fuzzy controller with temperature feedback to monitor the thermal comfort of passengers inside vehicle cabin.

The following are the contribution of this paper into the subject:

1. Control the blower speed using fuzzy controller.
2. Control cooled air distribution using fuzzy controller.

Air temperature inside a vehicle is not homogenous [13]. The air temperature inside vehicle cabin is expected to have higher temperature at head level compared to ankle level. Based on ASHRAE Standard 55, the vertical air temperature difference between head and ankle level is 3°C [14] while other study set the limit up to 6°C. Human are more sensitive to temperature variation than tolerable to humidity variation [15, 16].

2. FUZZY CONTROLLER

Fuzzy controller can be model for nonlinear relation between inputs and outputs. A controller is being applied to adjust the gate position for channeling the cooled air inside the vehicle cabin. Therefore, the difference between the upper body temperature and the lower body temperature is an input to the controller.

Another input signal for the controller is the temperature error between upper body and temperature setting. The error of input temperature is defined as:

$$error_{temperature} = T_{cabin} - T_{setting} \quad (1)$$

where $T_{setting}$ is the temperature setting by passengers and T_{upper} is the temperature of upper body of passenger inside vehicle cabin which changes by the existing air conditioning system. The error of temperature distribution is defined as:

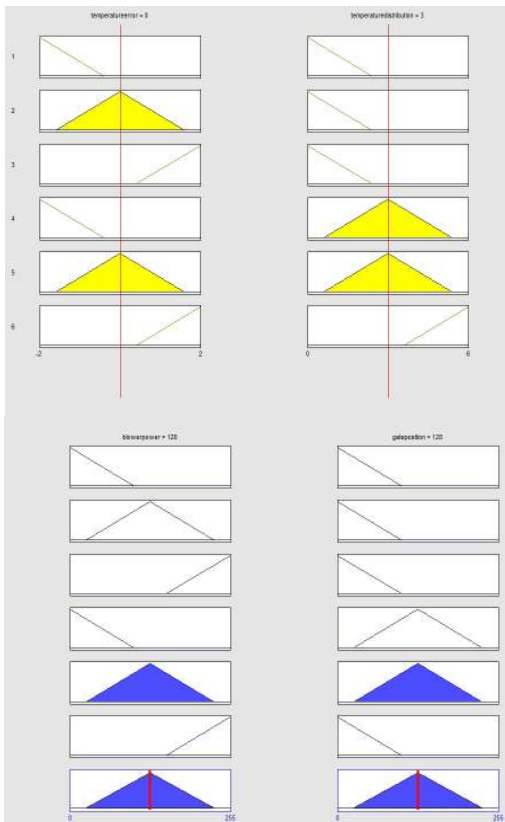
$$error_{distribution} = T_{upper} - T_{lower} \quad (2)$$

where T_{lower} the temperature of lower body of passenger inside vehicle cabin which changes by the existing air conditioning system. This section will discuss four stages of fuzzy controller system.

2.1 First step: fuzzification

The first step is to determine the physical inputs and set proper degree to inputs by membership functions. The system has six rules which are:

- (1) If the temperature error is small and temperature distribution is low, then the gate is upper and blower power is low.
- (2) If the temperature error is medium and temperature distribution is low, then the gate is upper and blower power is medium.



- (3) If the temperature error is large and temperature distribution is low, then the gate is upper and blower power is high.
- (4) If the temperature error is small and temperature distribution is medium, then the gate is half and blower power is low.
- (5) If the temperature error is medium and temperature distribution is medium, then the gate is half and blower power is medium.
- (6) If the temperature error is large and temperature distribution is high, then the gate upper and blower power is high.

As illustrated in Figure 1 and 2, the range of variation in variables can be shown as in the following number:

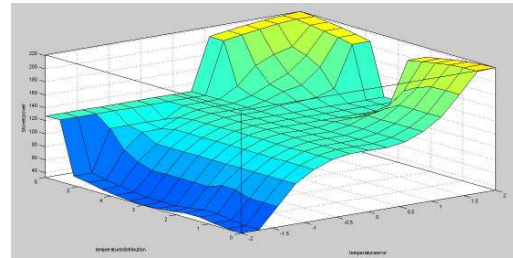


Figure 1: Fuzzy rule surface

Figure 2: Fuzzy rules

Range of temperature error variation: -2 to 2.
Range of temperature distribution error variation: 0 to 6.

2.2 Second step: fuzzy inference

When the inputs are fuzzificated, the degree for each section will found according to the stated rules. Min Max method is used for valuing the above the if-then rules stated above.

2.3 Third step: blend and make

Each fuzzy inference is transform to a certain command. The results of the defined rules will be implemented in this step.

2.4 Forth step: defuzzification

The fuzzy results drawn from previous steps is going through the defuzzification method where every rules are put together to show each rules attributed and blended where its membership function allocates a weight to each output.

3. METHODOLOGY

The air distribution system for the hatchback vehicle can be control by just rotate a lever that connected at center air conditioning cluster, shown in Figure 3. Therefore, a servo motor is placed and mounted so that

the required cooled air distribution can be achieved. This study will only consider the upper and lower body temperature.



Figure 3: Air conditioning console

This study is done at idle speed under direct sunlight with one passenger. The vehicle is using direct current electric compressor replacing the original belt-driven compressor. The direct current electric compressor is set at 1800 rpm using on/off controller. The experiment is done before and after the automatic cooled air distribution system is installed. The temperature setting is set at 23°C. The original blower speed is set at step 2.

The temperature of upper and lower body is taken by using LM35 temperature sensor and sent to a microcontroller and the data is saved to a connected computer. A DC motor driver is connected to the blower and the power supply is taken from the car battery. A PWM signal is sent by the microcontroller to the DC motor driver so that the blower speed can be control according to the fuzzy logic rules. A servo motor is used to control the lever of the gates so that the air can be distributed to the required space.

4. RESULTS AND DISCUSSION

Results in Figure 4 showed that by applying fuzzy controller to the cooled air distribution system, less time is needed to cool down the vehicle cabin to the temperature setting. This decreases the operation duration of the compressor that will lead to lower fuel consumption rate. The velocity of blower is also controlled according to temperature inside vehicle cabin, increasing thermal comfort. The temperature distribution of cooled air is also better controlled from head to foot according to ASHRAE recommendation. A more uniform variation of air temperature inside vehicle cabin could be achieved and the controller can reduce the temperature difference between inside air temperature and temperature setting and also upper body and lower body air temperature by regulating the blower power and the head foot gate in each moment.

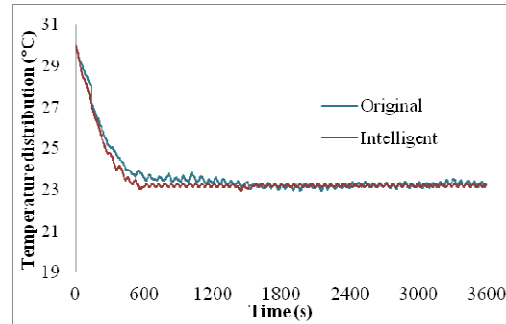


Figure 4: Temperature distribution against time(s)

5. CONCLUSION

Thermal comfort is the most comfort factors in a vehicle cabin for passengers. Vehicle cabin is complex and continuously varies after time. In this paper, the automatic cooled air distribution for passenger vehicle cabin help to increase the thermal comfort for passengers by distributing cooled air to the placed necessary either head or foot level by fuzzy controller. Results showed that through applying a fuzzy controller, less time was needed for the system to regulate the temperature of the vehicle cabin to the temperature setting. This decreases the operation time of compressor which substantially decreases the vehicle fuel consumption rate.

ACKNOWLEDGMENT

This work has been supported by the Ministry of Education Malaysia under Knowledge Transfer Programme (R.J130000.7809.4L509) as part of project titled “Intelligent and Energy Efficient Air Conditioning System for Automobiles”, Automotive Development Center, Universiti Teknologi Malaysia, and Zamalah Scholarship.

REFERENCES

- [1] Manzela AA, Hanriot SM, Cabezas-Gomez L, Sodre JR. Using engine exhaust gas as energy source for an absorption refrigeration system. *Appl Energy* 2010;2010(87):1141–8.
- [2] Sanaye S, Dehghandokht M, Fartaj A. Temperature control of a cabin in an automobile using thermal modeling and fuzzy controller. *Appl Energy* 2012;97:860–8.
- [3] Chua KJ, Chou SK, Yang WM. Advances in heat pump systems: a review. *Appl Energy* 2010;87:3611–24.
- [4] Fleming E, Wen S, Shi L, da Silva AK. Thermodynamic model of a thermal storage air conditioning system with dynamic behavior. *Appl Energy* 2013;112:160–9.
- [5] Zhao Y, Chen J, Xu B, He B. Performance of R-1234yf in mobile air conditioning system under different heat load conditions. *Int J Air-Cond Refrig* 2012;20:1250016.
- [6] Chih-Chiu S, Jau-Huai L. The performance of condenser under different vehicle speeds. *Int J Air-Cond Refrig* 2013;21:1350013.

- [7] Matsui K, Tabe T, Kakehi T, Ohba M. Automotive climate control. *IEEE Cont Syst Mange* 1986:20–4.
- [8] Davis LI, Sieja TF, Matteson RW, Dage GA, Ames R. Fuzzy logic for vehicle climate control. *3rd IEEE Int Conf Fuzzy Systems* 1994:530–4.
- [9] Wei KC, Dage GA. An intelligent automotive climate control system 1995:2977–82.
- [10] Aeatrice Gach B, Lang M, Riat JC. Fuzzy controller for thermal comfort in a car cabin. *SAE paper 1997-970107*.
- [11] Qi Q, Deng S. Multivariable control-oriented modeling of a direct expansion (DX) air conditioning (A/C) system. *Int J Refg* 2008. <http://dx.doi.org/10.1016/j.ijrefrig.2007.10.00>.
- [12] Farzaneh Y, Tootoonchi A. Controlling automobile thermal comfort using optimized fuzzy controller. *App Therm Eng* 2008;28:1906–17.
- [13] Temming, J. (1980). Comfort requirements for heating, ventilation and air conditioning in motor vehicles. *Human Factors in Transport Research* Edited By Dj Osborne, Ja Levis 2.
- [14] ANSI/ASHRAE Standard 55 (2004). *Thermal Environment Conditions for Human Occupancy*. Atlanta: American Society of Heating, Refrigerating, and Air-Conditioning Engineers, Inc.
- [15] Wan, J. W., Yang, K., Zhang, W. J., and Zhang, J. L. (2009). A new method of determination of indoor temperature and relative humidity with consideration of human thermal comfort. *Building and environment*, 44(2), 411-417.
- [16] Zhang, H., Huizenga, C., Arens, E. A., and Yu, T. (2005). Modeling thermal comfort in stratified environments. *Proceedings of Indoor Air 2005*, Beijing, 133 – 137.

The Tribological Characteristics of Rubber Seed Oil using Four-Ball Tribotester

Abdul-Fattah FN, Mohd Ariff M.A, Mohammed Hassan J[†], F.N. Ani*

*Faculty of Mechanical Engineering, Universiti Teknologi Malaysia,
81310 UTM Skudai, Johor, Malaysia.

[†]Electromechanical Engineering, University of Technology, Iraq

Tel : +607-5534715, Fax: +607-5566159

*Corresponding author: farid@mail.fkm.utm.my.

ABSTRACT

Malaysia, Indonesia and other South East Asia countries are known to be the producers of natural rubber that involves huge rubber plantation. Rubber latex is the main product from the cultivation of rubber plantation exists in the market for the manufacturing of rubber products. Beside the rubber products, an investigation was done on the seeds of the rubber trees for the purposes of bio-lubricant. Oil from the rubber seeds were extracted using Soxhlet extractor. The oil extraction rate and the solid to solvent ratio for the extraction process were obtained. The four ball tribotester was used for the determination of lubricant properties for the neat rubber oil. In this paper, the tribological characteristics of the rubber seeds oil as a neat bio-lubricant was investigated under different normal loads, and compared with commercial lubricant oil. All experimental works were conforming to ASTM D4172-B. The results exhibited that the rubber seeds oil has lower coefficient of friction under different loads, lower wear scar diameter of ball bearings and high value of flash temperature parameter under low loads compared to commercial lubricant oil. As a conclusion, the wear scar observation showed that the rubber seeds oil was capable to reduce wear at low loads but the wear condition become worse when the load increased, and the rubber seeds oil has high ability of anti-friction.

Keywords: *Rubber seeds oil, Normal load, Wear scar diameter, Coefficient of friction, Flash temperature parameter.*

1. INTRODUCTION

For many years, Malaysia is known as one of the producers of natural rubber that involves large cultivation of rubber plantation. Besides producing many types of rubber products such as tyres, sandals, gloves and others, its rubber seed oil could be used to turn into useful products. In this study, the rubber seed oil was investigated to study its lubricant

characteristics. Bio-lubricants, also known as bio-based lubricants are made from a variety of edible oils such as rapeseed, canola, sunflower, soybean, palm and coconut oils and the non-edible oils from jatropha, jojoba oils. The usage of bio-lubricants from non-edible oils can overcome the problems of food versus fuels, lubricants, environmental and economic issues related to edible vegetable. Non-edible oils are not suitable for human food due to the presence of some toxic components in the oils. The selection of non-edible oils as lubricants requires extensive characterisation works. Moreover, non-edible seed crops are expected to use lands that are largely unproductive and those that are located in poverty-stricken areas and in degraded forests. They can also be planted at field boundaries, fallow lands, and in public land such as along railways, roads and irrigation canals. Special attention has been paid to protecting the environment against pollution caused by the petroleum-based lubricants. A survey was conducted which found out that nearly 12 million tons of lubricant wastes were deposited into the environment every year [1].

As a result of increasing awareness of ecological pollution, biodegradable oil products are becoming an important alternative to conventional lubricants. Animal fat and vegetable oil are considered as substitutes for mineral-based oil as a lubricant. Found out that vegetable oils were used in the construction of monuments in ancient Egypt [2]. The advantages of choosing vegetable oil rather than lubricants from other sources are the fact that they are biodegradable and are less toxic when compared to petroleum-based oil. They are easy to produce and form a renewable source. In addition, when investigated the tribological behaviour of the two moving metals using biodegradable oil compared to mineral oil, they showed that the vegetable oils possess even a better lubricating ability than the current mineral or synthetic oils because they contain a large amount of unsaturated and polar ester groups components that favourably affected the conditions during reciprocating sliding [3]. Furthermore, the long-chain fatty acids present in

vegetable oil have better intrinsic boundary lubricant properties.

Vegetable oils show good lubricating abilities because they give rise to the low coefficients of friction. However, many researchers report that even when the coefficient of friction is low with vegetable oil as the boundary lubricant, the wear rate is high. Work on the investigation of the chemical attack on the surface by the fatty acid present in the vegetable oil [4]. They found out that the metallic soap film is rubbed away during sliding, and producing the non-reactive detergents increases wear.

Several researchers have tested vegetable oil for engineering applications. Included vegetable oil as a potential fuel in diesel engines [5,6], studied the potential of vegetable oil as hydraulic fluid [7,8] and the characteristics of palm oil as a metal forming lubricant [9, 10]. The research on vegetable oil as lubricant can be categorized into four (4) major groups, which (1) uses neat vegetable oil as a test lubricant [11,12], (2) uses vegetable oil emulsion [13,14] and (3) uses vegetable oil with additive [15,16,17] and (4) uses vegetable oil as an additive [18]. All of them found out that vegetable oil showed satisfactory results and has a bright future to be used widely in engineering applications. However, some factors such as the oxidation of vegetable oil must be taken into consideration. This study is to investigate the coefficient of friction and wear performance of rubber seeds oil with different normal loads by use a four-ball tribotester.

2. EXPERIMENTAL METHOD

Raw rubber seeds were collected from rubber plantation and were manually de-hulled to separate the kernels from the shells. After cleaning the rubber seed kernels, it was ground to smaller particles and was placed on a tray. It was dried in the oven at 105°C for 4 hours. After the drying process, the rubber seed particles were placed in the air tight container for extraction process.

2.1 Oil Extraction Apparatus

The extraction of rubber seeds oil from the rubber seed kernel particles was done using Soxhlet extractor. An amount of rubber seed particles was placed into the paper thimble which was placed in the Soxhlet extractor. N-hexane as the solvent is pour into the round bottom flask. The Soxhlet extractor was heated to temperatures of 70°C, which is above the boiling temperature of n-hexane. The vapours of n-hexane evaporate from the round bottom flask and flow into the Soxhlet chamber where it was condensed by the cooling temperature of the condenser. The condensed n-hexane liquid was drop into rubber seed

particles and extracts the rubber seeds oil and flow back into round bottom flask with the rubber seeds oil.

After the extraction process of rubber seeds oil has been done, the separation the n-hexane from the rubber seeds oil need to be separated. Rotary evaporator was used to separate the n-hexane from the rubber seeds oil.

2.2 Tribotester Apparatus

A four-ball wear tester is shown in Figure 1 and the machine having acquired the status of an established institution in the fundamental investigation of characteristics of the lubricants [19]. This instrument uses four balls, three balls at the bottom and one ball on the top. The three-bottom balls are held firmly in a balls pot containing the lubricant being tested and pressed against the top ball.



Figure 1: Photograph of a four-ball tribotester machine. The standard balls used in this experiment are made from AISI E-52100 chrome alloy steel, with the following specifications: diameter 12.7 mm; extra polish (EP) grade 25; hardness 64–66 HRC (Rockwell C Hardness). Four new balls were used for each test. Each time before starting a new test, the balls were cleaned with acetone and wiped dry using a fresh lint-free industrial wipe.

The top ball is made to rotate at the desired speed while the bottom three balls are pressed against it. The important components are the oil cup assembly, collet, and ball bearings. The surfaces of the components were cleaned with acetone before conducting each test. In this study, wear test was carried out at (392.4, 500,

600, 700 and 800 N) normal load and at 1200rpm for 1 hour at lubricant temperature 75°C.

2.3 Lubricants

The lubricants used for this experiment was the rubber seeds oil (RS100). The results obtained from experiments using the rubber seeds oil (RS100) were compared with the results from the experiment which used commercial mineral oil SAE 10W-30(E100). Each trial tested 10 ml of the lubricant.

2.4 Test procedures

To set up the steel balls, the balls pot and the steel balls were thoroughly cleaned using acetone and wiped dry using a fresh lint free industrial wipe. No trace of solvent should have remained when the lubricant was introduced and the parts were assembled. The steel ball bearings were placed into the balls pot assembly and the assembly was tightened using a torque wrench in order to prevent the bottom steel balls from moving during the experiment. The top, spinning ball was locked inside the collet and tightened onto the spindle, then the test lubricant was introduced into the balls pot assembly. The researcher observed that the oil level filled all the voids in the test cup assembly.

The assembled balls pot components were installed onto the non-friction disc in the four-ball machine and the test load was applied slowly to avoid shock loading. Next, the lubricant being tested was heated to 75 °C by the tribotester's built-in heater. When the set temperature was reached, the researcher would start the drive motor which had been set to drive the top ball at a desired speed. After one hour, the heater was turned off and the oil cup assembly was removed from the machine. The test oil was drained off from the oil cup and the ball bearings were wiped using a fresh lint free industrial wipe.

2.4.1 Wear Scar Diameter

The wear scar diameter of each of the three bottom test balls was measured to determine the lubricity performance of the test lubricant. The wear scar was evaluated by a computer running optical and scanning electronic microscope (high resolution) software and from the captured photomicrograph. Using this process, the wear scar diameter was determined for each of the three fixed balls. In general, the larger wear scar diameter, the more severe the wear.

2.4.2 Friction Torque and Coefficient of Friction

From the four-ball tribotester machine, the friction torque was recorded using specific data acquisition system. The friction torque for all test lubricants increased rapidly at the beginning of the test after 5–10 min, the friction torque data became a steady-state condition. The average of friction torque at the steady state condition was recorded and the friction

coefficient, as calculated according to IP-239, is expressed as follows:

$$\mu = \frac{T\sqrt{5}}{3Wr} \quad (1)$$

where μ is the friction coefficient, T is the frictional torque in kg mm, W is the applied load in kg and r is the distance from the center of the contact surface on the lower balls to the axis of rotation, which was determined to be 3.67 mm. The same calculation method was used by Throp [20].

2.4.3 Flash Temperature Parameter

The flash temperature parameter (FTP) is a single number that is used to express the critical flash temperature at which a lubricant will fail under given conditions. The FTP indicates less possibility of lubricant film to breakdown [21]. High value of FTP indicates high performance of the lubricant. The FTP can be measured by using the Equation below:

$$FTP = \frac{W}{(WSD)^{1.4}} \quad (2)$$

Where W is the applied load in kg and WSD is the wear scar diameter in mm.

3. RESULT AND DISCUSSIONS

3.1 Rubber Seeds Oil Yield

The weight of rubber seed particles and the oil yield was recorded to obtain the oil extraction rate of the rubber seed oil. The weight of rubber seeds particles used for the extraction is 20g and the weight of rubber seeds oil that was obtained from the extraction is 10.6 gm giving the oil yield extraction rate of 53%. The solid to solvent ratio for the extraction process is 1:7.5.

3.2 Lubrication Characteristics

The tribological characteristics of the rubber seeds oil (RS100) under different loads were investigated and characterized. The results provide a better understanding of worn surfaces of ball bearings with the rubber seeds oil using oil analysis such as WSD, COF and FTP. These results were compared with commercial mineral engine oil (E100).

3.2.1 Wear Scar Diameter

After the experiments, the wear scar diameter (WSD) on the three ball-bearings, which were fitted into the oil cup, was observed and measured using a computer running optical and scanning electronic microscope

(high resolution). The average value of the wear scar diameter were taken and plotted as shown in Figure 2.

From these values it can be concluded that the wear scar diameter of all lubricant samples increases as the normal load increases. The rubber seeds oil (RS100) showed a smaller value of wear scar diameter compared with the mineral oil at a lower value of load (484.4 μm at 392.4N) as compared with 546.4 μm at 392.4N for the mineral engine oil.

At higher loads, the rubber seeds oil has shown high values of wear scar diameter (964.7 μm at 800N) than the value of 871.1 μm at 800N using mineral oil. The behavior was due to the chemical attack on the surface by the fatty acid from rubber seeds and the metallic soap film was removed and scrubbed away during the sliding motion under high load, leading to the production of the non-reactive detergents that increased the wear.

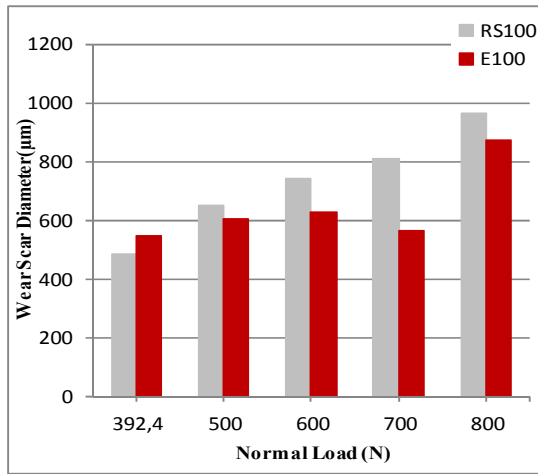


Figure 2: Wear scar diameter of oil samples under different loads.

3.2.2 Friction Torque

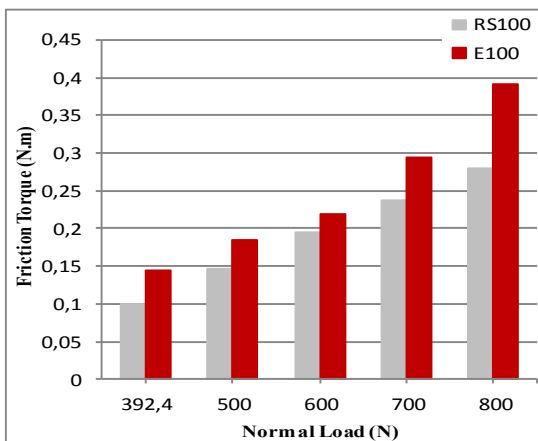


Figure 3: Friction torque value of oil samples under different loads.

In studying the friction performance of the rubber seeds oil under normal load (392.4 - 800 N), all experiments were conducted keeping the rotational speed at 1200 rpm and the bulk oil temperature at 75 °C for one hour. The results of the friction torque test were plotted and illustrated in Figure 3. This figure shows a similar pattern of friction torque increment when the normal load increases for the both oil samples (rubber seeds oil and mineral oil).

From Figure 3 could be seen also, the rubber seeds oil has lower values of friction torque compared with mineral engine oil under different loads.

3.2.3 Coefficient of Friction

The coefficients of friction values for the rubber seeds oil and mineral oil, under each experimental condition was calculated and tabulated and the results were analyzed from the graphs which are shown in Figure 4. Rubber seeds oil samples give the lower value of coefficient of friction as compared to coefficient of mineral lubricant. Results of the coefficient of friction in the Figure 4 shows also, the increased of load led to increase of the value of coefficient of friction for both oil samples. Lower value for the coefficient of friction was obtained of the rubber seeds oil at 0.0563 under 392.4N as compared with 0.0814 under same load for the mineral engine oil.

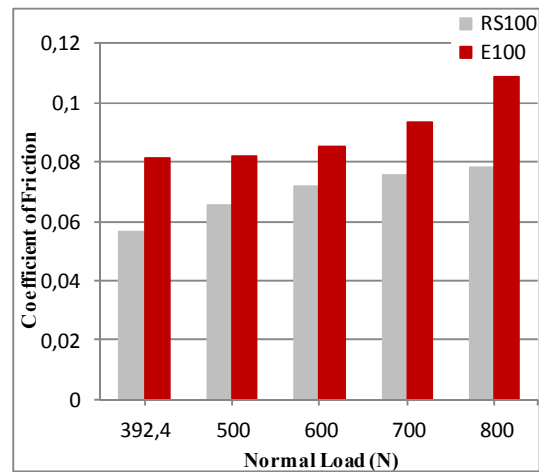


Figure 4: Coefficient of friction value of oil samples under different loads.

3.2.4 Flash Temperature Parameter

Flash temperature parameter is calculated and tabulated for rubber seeds oil and mineral oil under different normal loads as shown in Figure 5.

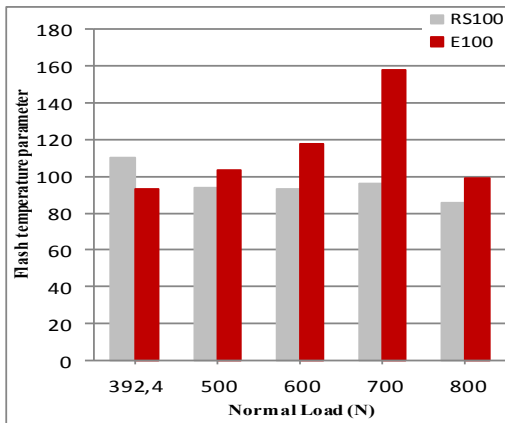


Figure 5: Flash temperature parameter value of oil samples under different loads

For the rubber seeds oil, the highest FTP value occurred at 392.4N was 110.2 as compared with 93.211 for the mineral engine oil under same normal load. Figure 5 show, under low loads, the rubber seeds oil give a higher value of the FTP and under high value of loads, the rubber seeds oil show lower value of FTP as compared with the FTP values of mineral engine oil. The reason is that, under lower value of loads, the rubber seeds oil caused reduction in the possibility for lubricant film to breakdown and increases the lubricity performance as compared to the mineral engine oil. Higher value of flash temperature parameter was obtained of the mineral oil 158.2 under 700N as compared with 96 under the same load of the rubber seeds oil.

4. CONCLUSIONS

The tribological behaviour characteristic of the rubber seeds oil was evaluated using the four-ball tribotester machine under varies normal loads. All the results were compared mutually with mineral oil. The evaluation results can be summarized as follows:

1. The friction coefficient obtained from the rubber seeds oil was the lowest compared to mineral engine oil, for both low and high normal load conditions. The friction coefficient for both lubricating oils increased as the applied load was increases.
2. The wear resulted from those lubricated with rubber seeds oil showed a better result under lower normal load. In contrast, at the higher normal load, the wear dominated by those lubricated with rubber seeds oil was higher compared to mineral engine oil.

3. Could be concluded that rubber seeds oil shows a better anti-friction performance compared to mineral oil in term of friction coefficient and wear at lower load. Therefore, rubber seeds oil has possibility to be used as lubricant of mating components.

ACKNOWLEDGEMENT

The authors are grateful to the Ministry of Higher Education Malaysia for the RU Grant, Vot 4L653 and Research Management Centre, Universiti Teknologi Malaysia for the financial and management support of this study.

REFERENCES

- [1] Delgado, M.A., Quinchia, L.A. and Galegos, C. "Viscosity modification of different vegetable oil with EVA copolymer for lubricant applicants". *Industrial Crops and Products*, vol.32, pp.607–612,2010.
- [2] Nosonovsky, M. "Oil as a lubricant in the ancient Middle East", *Tribology Online*, vol. 2, no. 2, pp. 44–49,2000.
- [3] Kalin, M. and Vizintin, J.A. "Comparison of the tribology behaviour of Steel/steel, steel/DLC and DLC/DLC contacts when lubricated with mineral and biodegradable oil", *Wear*, vol.261, pp. 22–31, 2006.
- [4] Golshokouh, I., Syahrullail, S., Ani, F.N. and Masjuki, H.H. "Investigation of Palm Fatty Acid Distillate Oil as an Alternative to Petrochemical Based Lubricant". *MPOB Journal*, 2013.
- [5] Bari, S., Lim, T.H. and Yu, C.W. "Effect of preheating of crude palm oil (CPO) on injection system, performance and emission of a diesel engine". *Renewable Energy*, vol. 27, pp. 339–351, 2002.
- [6] Abdullah M.A., Ani F.N., Masjuki H.H. Performance and Emission of a Common Rail Passenger Car Engine Fuelled with Palm Oil Biodiesel, *Applied Mechanics and Materials*. 564 (2014) 66-71.
- [7] Wan Nik, W.B., Ani, F.N. and Masjuki, H.H. Thermal stability evaluation of palm oil as energy transport media, *Energy Conservation and Management*, 46 (2005) 2198-2215.
- [8] Wan Nik W.B., Ani F.N., Masjuki H.H., Rheology of bio-edible oils according to several rheological models and its potential as hydraulic fluid. *Ind Crops and Prod*, 22 (2005) 249-255.
- [9] Syahrullail, S., Nakanishi, K. and Kamitani, S. "Investigation of the effects of frictional constraint with application of palm olein oil lubricant and paraffin mineral oil lubricant on plastic deformation by plane

- strain extrusion”, *Journal of Japanese Society of Tribologists*, vol. 50, no. 12, pp. 877–885, 2005.
- [10] Syahrullail, S., Zubil, B.M., Azwadi, C.S.N. and Ridzuan, M.J.M. “Experimental evaluation of palm oil as lubricant in cold Forward extrusion”, *International Journal of Mechanical Sciences*, vol. 53, pp.549–555, 2011.
- [11] Ing, C.T., Mohammed Rafiq, A.K., Azli, Y. and Syahrullail, S. “The effect of temperature on the tribological behavior of RBD palm stearin”, *Tribology Transactions*, vol. 55, no.5, pp. 539–548, 2012.
- [12] Maleque, M.A. and Masjuki, H.H. “Investigation of the anti-wear characteristics of palm oil methyl ester using a four-ball tribometer test”, *Wear*, vol.206, pp.179–186, 1997.
- [13] Nor Hayati, I., Yaakob, B.C.M., Chin, P.T. and Idris, N.A. “Thermal behavior of concentrated oil-in-water emulsions based on soybean oil and palm kernel olein blends”, *Food Research International*, vol. 42, pp. 1223–1232, 2009.
- [14] Husnawan, M., Masjuki, H.H., Mahlia, T.M.I. and Saifullah, M.G. “Thermal analysis of cylinder head carbon deposits from single cylinder diesel engine fueled by palm oil–diesel fuel emulsions”, *Applied Energy*, vol. 86, pp. 2107–2113, 2009.
- [15] Choi, U.S., Ahn, B.G., Kwon, O.K. and Chunt, Y.J. “Tribological behaviour of some antiwear additives in vegetable oils”, *Tribology International*, vol. 30, no.9, pp. 677–683, 1997.
- [16] Thiam, L.C. and Subhash, B. “Effect of catalyst additives on the production of biofuels from palm oil cracking in a transport riser reactor”, *Bioresource Technology*, vol.100, pp. 2540–2545, 2009.
- [17] Jabal M.H., F.N. Ani, S, Syahrullail. “The Tribological Characteristic of the Blends of RBD Palm Olein with Mineral Oil using Four-ball Tribotester”, *Jurnal Technology*, vol. 69, no. 6, pp.11-14, 2014.
- [18] Maleque, M.A., Masjuki, H.H. and Haseeb, A.S.M.A. “Effect of mechanical factors on tribological properties of palm oil methyl ester blended lubricant”, *Wear*, vol.239, pp. 117–125, 2000.
- [19] Golshokouh, I., Golshokouh, M., Ani, F.N., Kianpour, E. and Syahrullail, S. “Investigation of Physical properties for jatropa oil in different temperature as lubricant oil”. *Life Science Journal*, vol.10, pp.110-119, 2013.
- [20] Thorp, J.M. “Four-ball assessment of deep drawing oils”, *Wear*, vol. 33, pp. 93–108, 1975.
- [21] H.H. Masjuki, M.A. Maleque. “Investigation of the anti-wear characteristics of palm oil methyl ester (POME) contaminated with lube oil using a Four-ball machine of IP239 standard”, *Wear*, vol.206, pp.179-186, 1997.

Experimental Study on a Cold Storage System with a Variable Speed Compressor

Nazri Kamsah^a, Haslinda Mohamed Kamar^b, KASNI Sumeru^c, and Tandil Sutandi^d

^aFaculty of Mechanical Engineering
Universiti Teknologi Malaysia, Johor Bahru, Malaysia
Tel : (+607) 5534749. Fax : (+607) 5566159
E-mail : nazrikh@mail.fkm.utm.my

^bFaculty of Mechanical Engineering
Universiti Teknologi Malaysia, Johor Bahru, Malaysia
Tel : (+607) 5534748. Fax : (+607) 5566159
E-mail : haslinda@mail.fkm.utm.my

^cDepartment of Refrigeration & Air Conditioning
Gegerkalong Hilir Ciwaruga, Bandung 40012, Indonesia
E-mail : sumeru84@gmail.com

^dDepartment of Refrigeration & Air Conditioning
Gegerkalong Hilir Ciwaruga, Bandung 40012, Indonesia
E-mail : ade.tandi@gmail.com

ABSTRACT

Selection of a compressor for a refrigeration system is generally done based on a peak load operating condition. The energy consumed by the compressor can potentially be reduced by regulating the compressor speed using an inverter. This experimental study investigates energy saving and performance enhancement potentials in an experimental cold-storage system when the electric frequency supply is reduced from 45 to 25 Hz, with a 5 Hz interval. The system is equipped with a compressor with a power rating of 3 HP (2.25 kW) and R22 was used as the refrigerant. The cooling load of the system was provided using an electric heater placed at the bottom of the cold storage chamber. Results show that the power input to the compressor was reduced when the electric frequency supply was decreased. The highest reduction in the compressor power input occurred when the electric frequency was decreased from 45Hz to 40Hz. The results also show that the coefficient of performance (COP) of the cold storage system was improved when the electric frequency supply was decreased. The largest COP improvement occurred when the frequency was decreased from 30 Hz to 25 Hz.

Keywords

Variable speed compressor, energy saving, inverter, cold storage system, COP

1. INTRODUCTION

There are four basic components in a vapor-compression refrigeration cycle (VCRC): a compressor, a condenser, an evaporator and an expansion device. In a small air-conditioning system the compressor typically consumes nearly 90% of total energy input while in a central-type system the compressor consumes approximately 72% of the total energy input [1, 2]. A thermostatic expansion valve (TXV) is traditionally used to regulate the degree of superheating and cooling capacity of the system [3]. The device also regulates the evaporating pressure and the refrigerant mass flow rate. The opening of the TXV depends on the cooling load demand. However, the degree of superheating and refrigerant mass flow rate cannot be controlled independently.

In a refrigeration system the compressor capacity is usually chosen to meet the peak cooling load demand, which is a combination of internal and external cooling load. The internal cooling load could reach the peak value at any time, but the external cooling load very rarely occurs because the sun position always change with time. Hence it is desirable to have a control strategy that can regulate the speed of the compressor so that the system is able to respond to partial load working conditions. Since a large portion of the energy supply is consumed by the compressor, regulating its speed could potentially lead to saving in energy consumption of the refrigeration system [4, 5].

At the peak load condition the compressor works at the nominal frequency of the electrical power supply. At part load conditions, the frequency of the electrical power supply to the compressor can be reduced, which in turn, would reduce the compressor speed. The aim of this experimental study is to investigate the energy saving and performance enhancement potentials of an experimental cold-storage system by regulating the electric frequency supply to the compressor.

2. EXPERIMENTAL APPARATUS

Figure 1 shows a schematic diagram of the experimental cold-storage system employed in this study. It comprises of a cooling compartment measuring 1.5m (L) x 1.5m (W) x 2.2m (H). The evaporator coil is located at the top of the cooling compartment while an electrical heater, which is used as a source of cooling load, is located near the bottom of the compartment.

The vapor-compression refrigeration system consists of a reciprocating compressor, an air-cooled condenser, a liquid receiver, an evaporator and a thermal expansion valve (TXV). Refrigerant-22 was used as the working fluid. The compressor has a nominal capacity of 3 HP (2.25 kW). The compressor speed was varied using a modulated source inverter by regulating the frequency of the electrical power supply, namely at, 25, 30, 35, 40 and 45 Hz. The three-phase main electrical power supply (380V, 50 Hz) was converted to DC voltage supply using an inverter. A schematic diagram of the inverter and the compressor is shown in Figure 2.

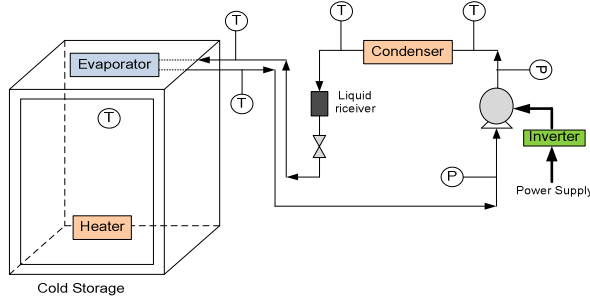


Figure 1: Schematic diagram of an experimental cold storage system.

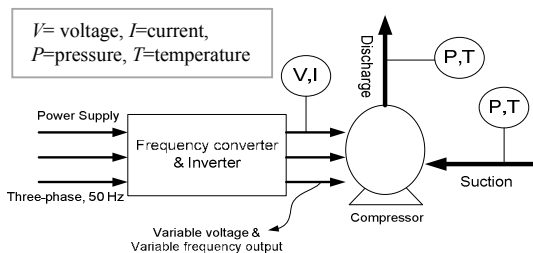


Figure 2: Schematic diagram of an experimental cold storage system.

To evaluate the performance of the cold storage system, four parameters were measured namely temperature (T), pressure (P), voltage (V) and electric current (I). The voltage and electric current were used to determine the power input of the compressor. The cooling load was provided by the electric heater with power rating of 1.5 kW. During the experiments the air temperature inside the cooling compartment was maintained at -5°C . The performance of the cold-storage system is expressed in terms of the coefficient of performance (COP), defined as,

$$\text{COP} = \frac{\text{Cooling capacity}}{\text{Compressor power input}} \quad (1)$$

The cooling capacity of the system was determined based on the enthalpy values at the inlet and outlet of the evaporator, which are obtained from the pressure-enthalpy ($p-h$) chart for R22 refrigerant. The input power reduction and COP improvement due to the variation in the electric frequency are determined using Eq. (2) and Eq. (3), respectively while the compression ratio (CR) is defined by Eq. (4), as follows:

$$P_{\text{reduction}} = \frac{P_n - P_{n-1}}{P_n} \quad (2)$$

$$\text{COP}_{\text{improved}} = \frac{\text{COP}_{n-1} - \text{COP}_n}{\text{COP}_{n-1}} \quad (3)$$

$$\text{CR} = \frac{P_{\text{discharge}}}{P_{\text{suction}}} \quad (4)$$

where P_n is the compressor input power at a given electric frequency supply and P_{n-1} is the input power at the reduced frequency. Similarly, COP_n is the coefficient of performance of the experimental cold-storage system at a given electric frequency and COP_{n-1} is the corresponding value at the reduced frequency. Also, $P_{\text{discharge}}$ is the discharge pressure while P_{suction} is the suction pressure of the compressor.

3. RESULTS AND DISCUSSION

Figure 3 shows the variation of compressor suction pressure, discharge pressure and compression ratio of the cold storage system with the electric frequency supply. It is seen that the compressor discharge pressure continuously increases when the electric frequency was decreased from 45 Hz to 25 Hz. However, the magnitudes of the pressure increment can be considered small. Since temperature and pressure are dependent properties of the refrigerant, the increase in the compressor discharge pressure also causes the refrigerant temperature at the compressor exit to increase. The figure also shows that the suction pressure of the compressor continuously increases when the electric frequency supply was regulated from

45 Hz to 25 Hz. This leads to the superheating of the refrigerant at the evaporator outlet. To maintain the cooling load at a constant value, the mass flow rate of the refrigerant will have to be decreased. This can only be attained by reducing the compressor speed. Figure 3 also shows that, the compression ratio of the compressor also decreases when the electric frequency supply is reduced.

Figure 4 shows the variation of compressor power input and coefficient of performance (COP) of the cold-storage system with electric frequency supply. It can be observed that, the compressor input power decreases from 1.37 kW to 1.13 kW as the electric frequency supply was reduced from 45 Hz to 30 Hz. There are no changes in the compressor input power when the frequency supply was decreased from 30 Hz to 25 Hz. The highest reduction in the compressor power input, i.e. from 1.37 kW to 1.2 kW (about 12.4%) occurs when the electric frequency was reduced from 45 Hz to 40 Hz. The total reduction in the compressor input power is about 18%. The COP of the system is inversely proportional to the compressor power input. As the power input decreases as a result of reduction in electric frequency supply, the COP of the system increases. This finding agrees well with the results of a similar study reported by Aprea *et al.* [6]. The highest COP improvement occurs when the electric frequency supply was reduced from 30 Hz to 25 Hz.

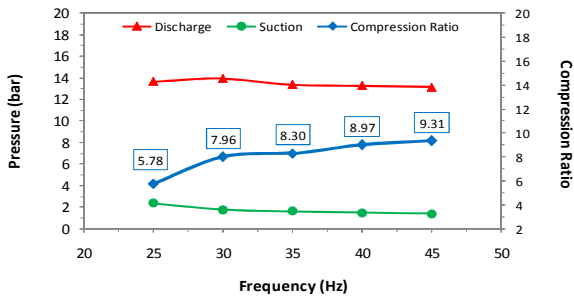


Figure 3: Variation of compressor suction pressure, discharge pressure and pressure ratio with electric frequency supply.

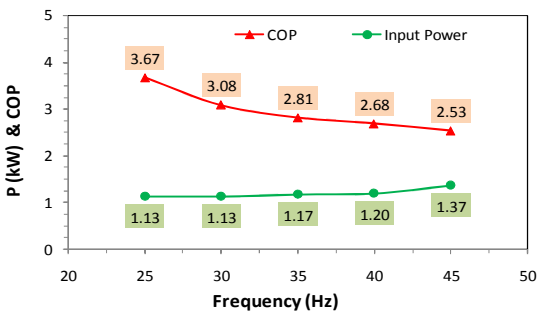


Figure 4: Variation of compressor power input and COP of the system with electric frequency supply.

Figure 5 shows the variation of percent reduction in the compressor power input and system COP with electric frequency supply. It can be observed that the COP of the system can potentially be improved by about 5.6% if the electric frequency supply was reduced from 45 to 40 Hz and by about 8.8% when the frequency supply was further reduced to 30 Hz. The highest COP improvement of 16% can be achieved when the frequency supply was reduced from 45 Hz to 25 Hz. It can also be observed that the largest reduction in compressor power input of about 12.4% can be achieved when the electric frequency supply was reduced from 45 Hz to 40 Hz.

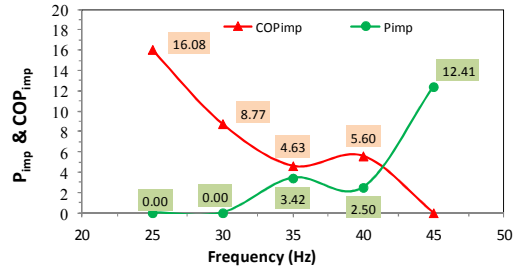


Figure 5: Variation of percentage reduction in compressor input power and system COP with electric frequency supply.

The percent power input reduction is only about 3.42% when the electric frequency supply was reduced from 35 Hz to 30 Hz. The results also show that there is no further reduction on in the compressor power input when the frequency supply was further reduced to 25 Hz.

4. CONCLUSION

An experimental study on the effects of reducing electric frequency supply on the compressor power input and COP of a lab-scale cold storage system was presented. Results show that the compressor input power can be reduced by about 12% when the electric frequency was regulated from 45 Hz to 40 Hz. In addition, the COP of the system can potentially be increased by about 16% when the electric frequency was reduced to 25 Hz.

ACKNOWLEDGMENT

The authors are grateful to the Universiti Teknologi Malaysia for providing the funding under a vot number of 06H75. The authors are also grateful to the Ministry of Higher Education (MOHE) Malaysia for providing a research funding under a vot number of 4F645. The grants were managed by the Research Management Centre of the Universiti Teknologi Malaysia, Johor Bahru, Johor, Malaysia.

REFERENCES

- [1] K. Tojo, M. Ikejawa, M. Shiibayasi, N. Arai, N. Uchikawa, A scroll compressor for air conditioner, Proceeding of International Compressor Engineering Conference, Purdue University, pp. 496-503 (2015).
- [2] H.H. Masjuki, T.M.I. Mahlia, I.A. Choudary, Potential electricity saving by implementing minimum energy efficiency standards for room air conditioners in Malaysia, Energy Convers. Manage. 42 (2001) 439-450.
- [3] L. Hua, S.K. Jeong, S.S.You, Feedforward control of capacity and superheat for variable speed refrigeration system, Appl. Therm. Eng. 29 (2009) 1016-1074.
- [4] Y.B. Yang, M.D. Wu, Y.C. Chang, Temperature control of the four-zone split inverter air conditioners using LMI expression based on LQR for mixed H₂/H_∞, Appl. Energy 113 (2014) 912-923.
- [5] R. Karunakaran, S. Iniyan, R.Goic, Energy efficiency fuzzy based combined variable refrigerant volume and variable air volume air conditioning, App. Energy87 (2010) 1158-1175.
- [6] C. Aprea, R. Mastrullo, C. Renno, Fuzzy control of the compressor speed in a refrigeration plant, Int. J. Refrig. 27 (2004) 639-648.

Biobutanol Production from the Fermentation of Oil Palm Frond Extract using *Clostridium acetobutylicum* (ATCC4259)

^aAzhar Abdul Aziz, ^bAbubakar Sadiq Aliyu, ^cAdibah Yahya and ^dZulkanain Abdul Lattiff

^aAutomotive Development Centre (ADC),
Faculty of Mechanical Engineering,
Universiti Teknologi Malaysia (UTM),
81310 Skudai, Johor Bahru, Malaysia
azhar@fkm.utm.my

^bDepartment of Mechanical Engineering,
Kaduna Polytechnic,
P.M.B 2021, Kaduna, Nigeria
asalihu2@yahoo.com

^cFaculty of Bioscience and Biomedical Engineering,
Universiti Teknologi Malaysia (UTM),
81310 Skudai,
Johor Bahru, Malaysia
adibah@fb.utm.my

^dAutomotive Development Centre (ADC),
Faculty of Mechanical Engineering,
Universiti Teknologi Malaysia (UTM),
81310 Skudai, Johor Bahru, Malaysia
zkarnain@fkm.utm.my

ABSTRACT

The recent global energy crisis has attracted interest in producing an alternative sustainable fuel from clean, renewable, abundant and yet untapped resource via biological processes. Oil palm frond (OPF) has the potential for Biobutanol production. In this study, batch fermentation tests were carried out in terms of metabolite, cell production and sugar conversion for the production of biobutanol using clostridium acetobutylicum (ATCC4259) with and without organic nitrogen supplement. The kinetic cell growth, solvent and acids production at PH 6.0 were examined. In general, clostridium acetobutylicum (ATCC4259) strain was capable of converting sugar in OPF extract to solvent and acids. The result showed the maximum acetone, butanol and ethanol concentration of 1.94, 0.015 and 7.09 g/L respectively at an initial glucose concentration of 50g/L. Furthermore, sugar utilization and growth were the controlling factor for solventgenesis as observed by the dominant production of acid as compared to solvent. These results indicate the OPF extract has potential for biobutanol production.

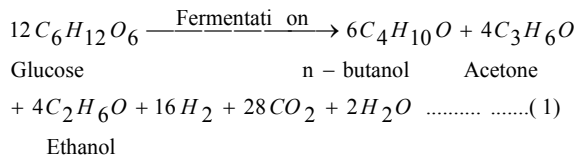
Keywords: *Alternative fuel, Bio-butanol production, Clostridium acetobutylicum, Mix acid fermentation, Oil Palm Frond.*

1. INTRODUCTION

Biobutanol production by fermentation has drawn increasing attention worldwide for two reasons; energy security implying the production from renewable agricultural waste at cost-effective price and climate

change [1, 2]. Therefore, the economics of biobutanol fermentation are greatly influenced by the raw materials where oil palm plantation waste could be a good option for reducing cost [3]. Although, oil palm trees have a life span of 30 years they have only 10-25 years of economic fruit production [3]. Currently, Malaysia is the world's second largest palm oil producer generating approximately 80 million tonnes of dry solid biomass from the oil palm industry, with a figure likely to reach 10 million tonnes by the year 2020 [4]. The oil palm fronds are collected during pruning and replanting activities with an average generation rate of 9.8 t-dry/ha-plantation/year and 14.9 t-dry/ha-replantation/year, respectively as shown in Table 1. Thus, oil palm frond utilization as fermentable sugar for biobutanol production is highly beneficial due to its renewability, low cost and availability in Malaysia [5, 6]. Oil Palm Frond can be squeezed to obtain liquid extract that contain readily fermentable sugars (Table 2), and rich in nitrogen, minerals and vitamins A.

The growth and metabolism of *Clostridium acetobutylicum* (ATCC4259) depends on the medium composition and the culture age [8]. *Clostridium acetobutylicum* (ATCC4259) is among the solvent genic clostridia that produce two major types of products, solvent (acetone, butanol, and ethanol, ABE) and gases (carbon dioxide and hydrogen) with the intermediate fermentation products being organic acids (acetic acid and butyric acid). The metabolism reaction of the fermentation is as represented in Equation 1.



Butanol production process in ABE fermentation can therefore be divided into acid production phase (acidogenesis) and the solvent production phase (solvent genesis) [10]. In the acid production phase, the growth is accompanied by the production of organic acids (acetate, butyrate) and hydrogen. In the solvent phase, the organic acids generated in the earlier phase are converted to produce acetone, ethanol and butanol. It is noteworthy, that the formation of butyric acid during the acidogenic phase is important for maintenance of the redox equilibrium, although the glucose obtained from OPF is used at substrate for the production of bioethanol [11]. However, fermentation of OPF extract to produce biobutanol has not fully been explored.

Table1: Oil palm biomass generation rate from plantation site [9].

Site	Residue type	Unit rate	Representative generation rate
Plantation	Oil palm Trunk generated at replanting.	t-dry/ha replantation/year	62.8
	Fronds generated at replanting	-	14.9
	FronD (pruned)	t-dry/ plantation /year	9.8

Hence, the batch fermentation analysis were carried out in terms of metabolite, cell production and sugar conversion for the production of biobutanol using *Clostridium acetobutylicum* (ATCC4259) with and without organic nitrogen supplement .

Table 2: Sugar content in OPF extract

Type of Sugar	Concentration (g/L)
Glucose	49.50
Fructose	3.96
Xylose	16.84

2. MATERIALS AND METHOD

2.1 Raw Materials

Oil palm frond petiole was obtained from several local palm plantations in Johor Bahru, Malaysia. The OPF

extract was obtained by pressing the petiole using a conventional press machine. The glucose content in OPF extract used in this study is 50g/L.

2.2 Microorganism.

In this study, *Clostridium acetobutylicum* ATCC4259 (purchased from American Tissue Collection Centre, USA) was used for butanol fermentation. In order to germinate the spores of *C. acetobutylicum*, spore culture was heat shocked for 90 seconds at 90°C and transferred under anaerobic condition to fresh pre-culture medium, RCM2107 (Reinforced Clostridium Medium, Oxoid) at 37°C for 24 hours.

2.3 Medium

The medium used to grow *Clostridium acetobutylicum* ATCC4259 consisted of (g/L) : yeast extract (1); KH₂PO₄ (0.5); K₂HPO₄ (0.5); Ammonium acetate (2.2); NaCl (0.5); MgSO₄.7H₂O (0.2); MnSO₄.7H₂O (0.01); A 4.0 mL/L vitamin solution consisting of 1.0 mg/L P-amino benzoic acid; 0.01mg/L biotin and 1.0 mg/L Thiamin were also added into the medium.

2.4 Fermentation

Batch fermentation was carried out using 130mL serum bottles. Two types of media M1(OPF juice) and M2 (OPF juice + yeast extract) were prepared under strictly anaerobic condition according to the Hungate Technique [12] by sparging the medium with oxygen-free N₂. Vitamin and mineral solutions which were also prepared and filter sterilized prior to add into the two media. The experiment was carried out to investigate growth and solvent production by *C. acetobutylicum* ATCC4259 in two types of media, with initial glucose concentration ranging from 45-50 g/L. In all experiments, the pH of the media was adjusted to pH 6 using 3M NaOH. Batch culture was initiated by inoculating 10 mL (10%vol/vol) of vegetative cell that was previously grown in RCM2107 medium. The cultures were incubated at 37°C for up to 3 days

2.5 Analytical Procedure

Samples (1.5 mL) were withdrawn at 4 hour intervals. Cell concentration was estimated by optical density measurement at 600 nm using a T60 Visible spectrophotometer while the pH was measured using a pH meter (Model Agilent Technologies). Other analysis were carried out using cell-free supernatants obtained by centrifugation at 10,000 rpm for 10 minutes. Concentration of the solvents ethanol (E), acetone (A), butanol (B) and acids (acetic and butyric) were analyzed using a gas chromatography (Model 6890N, Agilent Technologies, USA) equipped with a flame ionization detector (FID). The separation of ABE and organic acids was achieved by using a capillary polyethylene glycol (PEG) column (HP-INNO wax, Agilent Technologies) and helium as a carrier gas. The column temperature was initially held at 35°C, programmed with the following increments; 10°C/min

to 11°C, 20°C /min to 155°C, 40°C/min to 200°C held for minute, and the final temperature of 250°C was held for 2 minutes. The temperature of the detector and injector were maintained at 300°C and 250°C respectively. The peak area of the respective compounds was quantified based on 1% standard prepared. The gas chromatogram is as indicated in Fig.1.

3. RESULTS AND DISCUSSION

The ability of *Clostridium acetobutylicum* to use oil palm frond fiber for solvent fermentation has been reported [11]. Batch fermentation of solvent (acetone-butanol-ethanol) by clostridium using glucose as carbon source can be divided into two phases, acidogenic and solventogenic phase [13]. During acidogenic phase, hydrogen, carbon dioxide, acetic acid and butyric acid was produced and cause reduction of pH. Solvent was produced from the conversion of acid during solventogenic phase. Similar process was however, observed in batch fermentation of oil palm frond extract to solvent as indicated in equation 1. The pH of both media M1 and M2 decreased from initial value of 6.0 to 4.9. The shift from acid to solvent formation required low pH when grown on glucose as carbon source as previously reported [14, 15].

Findings from this study indicated that pH range from 4.9 to 6 during acetogenic phase, resulted in dominant acid production as compared to solvent (Fig. 2 and 3). This result is in agreement with direct fermentation of gelatinized sago starch to acetone-butanol-ethanol by *Clostridium acetobutylicum* [14] and a study on utilization of Jerusalem artichoke to solvent [16]. They both suggested that fermentation controlled at low pH during acidogenic phase favoured solvent production, while acid accumulation was enhanced at high pH. Furthermore, sugar utilization and growth rate were the controlling factor for solventogenesis. Hence pH condition seemed appropriate to limit acid accumulation and enhanced solvent production. The maximum cell density obtained in batch fermentation using medium (M1) and (M2) were 0.987 and 0.887 respectively, measured at 600nm.

The relationship between cell growth and glucose consumption for medium M1 and M2 were shown in Fig. 4 and Fig. 5, indicate that rapid growth of *C. acetobutylicum* ATCC4259 was directly associated with glucose consumption. Active fermentation of glucose has resulted to the significant decrease of pH from 6.0 to 4.9 due to the accumulation of mixed acids (acetic acid and butyric acid), produced during the active growth phase of the bacteria.

At the end of fermentation process, *C. acetobutylicum* ATCC4259 produced 0.015g/L and 0.013g/L of butanol using medium M1 and M2 respectively. In general, medium M1 produced higher butanol and acetone than M2 after the third day of fermentation (Fig. 6). After 48 hours of fermentation, the

concentration of ethanol was still higher than acetone and butanol and this did not follow the usual ratio ABE i.e. 3:6:1. (Fig. 3 and 4). Optimization of important factors affecting the fermentation will significantly increase butanol production. Studies of butanol production in a bioreactor will ease the controlling of important functional units during fermentation for butanol production.

Table3: Composition of micro elements in OPF liquid Extract.

Micro elements	Symbols	Composition in (mg/L)
Nitrogen	N	1077
Phosphorus	P	89.5
Potassium	K	2459
Iron	Fe	6.0
Calcium	Ca	529
Magnesium	Mg	1590
Zinc	Zn	2.7
Copper	Cu	0.3
Sodium	Na	1440
Sulphate	SO ₄	9480

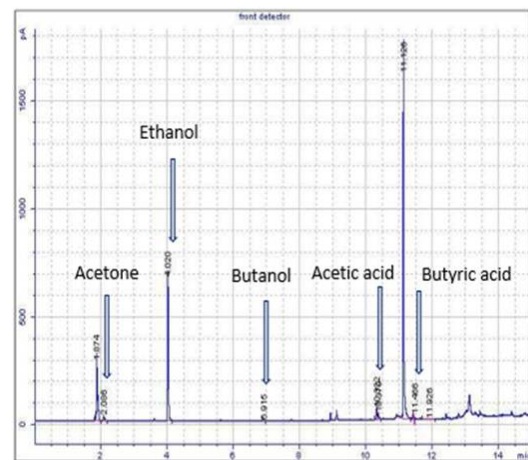


Figure 1. Gas chromatogram indicating solvents and acids in OPF liquid extract medium.

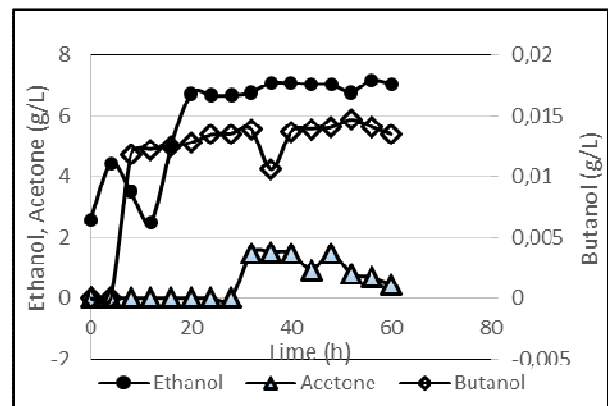


Figure 2. Solvent fermentation by *C. acetobutylicum*

ATCC4259 in M1 medium.

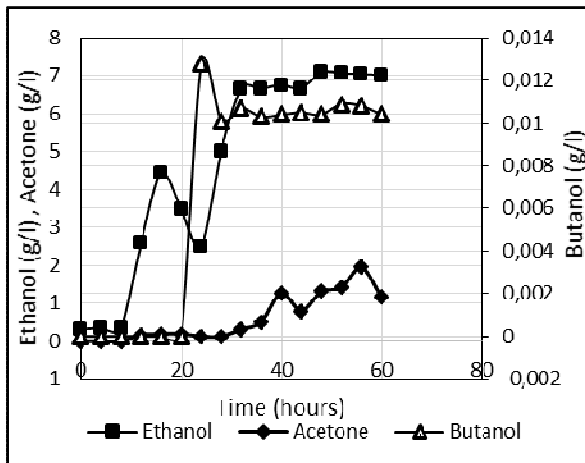


Figure 3. Solvent fermentation by *C. acetobutylicum* ATCC4259 using OPF extract as carbon source (medium M2, OPF+Yeast Extract).

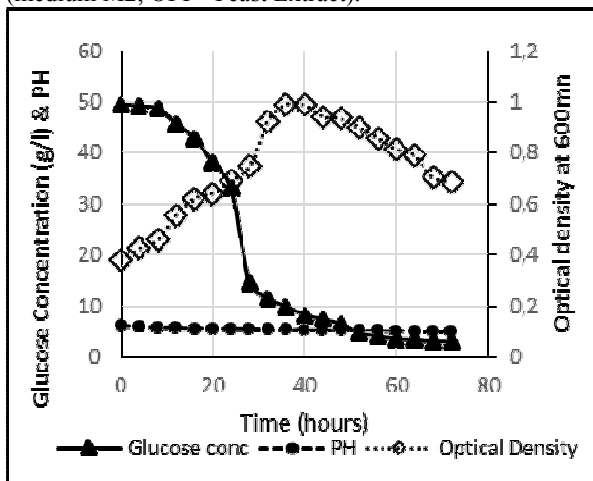


Figure 4. Cell growth, Glucose consumption and pH for medium M1 (OPF only).

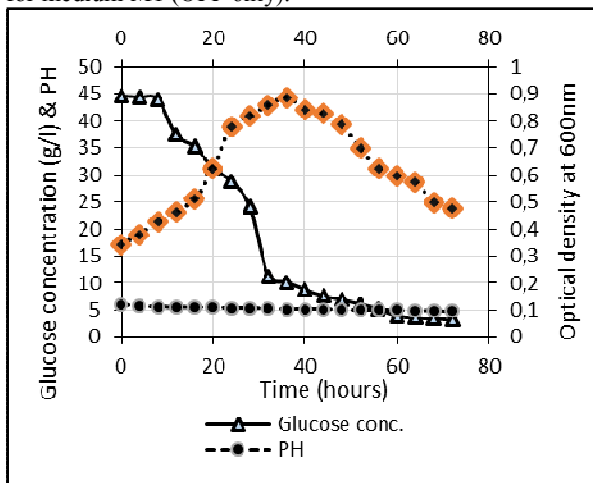


Figure 5. Cell growth, Glucose consumption and pH for medium M2 (OPF+ Yeast Extract).

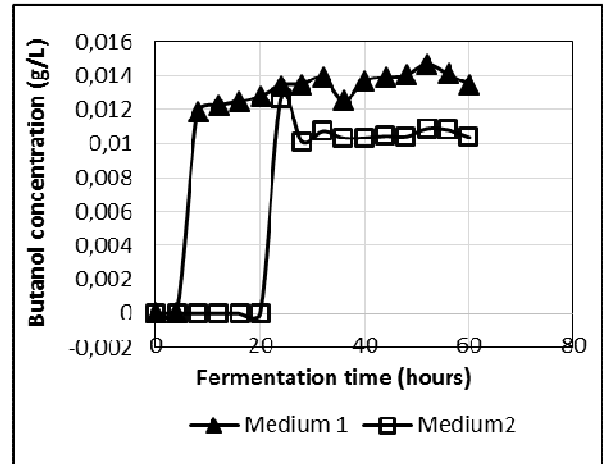


Figure 6. Butanol production profile by *C. acetobutylicum* ATCC4259 in medium 1 (M1) and medium 2 (M2).

4. CONCLUSION

From this study, it was found that *C. acetobutylicum* ATCC4259 was able to utilize the oil palm frond extract as the sole source of carbon and energy for growth and solvent production. The maximum total solvent concentration of 9.05g/L obtained in this study demonstrated that oil palm frond extract can be used as an inexpensive raw materials for ABE production. The OPF extract that is rich in minerals, carbon and nitrogen able to support microbial metabolism for solvent production with minimal amendments, thus potentially contributes to sustainable production of ligno-biomass solvent in the chain of bio-refinery processes.

ACKNOWLEDGEMENT

The authors wish to thank *Universiti Teknologi Malaysia*, for the initial funding extended to them in 2013 to 2014 (ref. No. QJ1300002514.06H96). They would also like to express their utmost gratitude to Ministry of Science Technology and Innovation, Malaysia (MOSTI) for currently supporting this project through another research grant, Ref No.: R. J130000.7909.4S111.

REFERENCES

- [1] P. Dürre, "New insights and novel developments in clostridial acetone/ butanol/ isopropanol fermentation," *Appl. Microbiol. Biotechnol.*, vol. 49, pp. 639-648, 1998.
- [2] N. Qureshi, B. C. Saha, B. Dien, R. E. Hector, and M. A. Cotta, "Production of butanol (a biofuel) from agricultural residues: part 1- Use of barley straw hydrolysate.," *Biomass Bioenergy*, vol. 34, pp. 559-565, 2010.
- [3] A. H. Norhazimah, M. Asmadiyahana, and M. Faizal Che Ku, "Feasibility of Acetone-Butanol-Ethanol Production from the

- Fermentation of Oil Palm Trunk Juice," *Research Journal of Chemistry and Environment*, vol. 17, pp. 66-69, 2013.
- [4] C. M. H. Che Maail, H. Ariffin, M. A. Hassan, U. K. Md Shah, and Y. Shirai, "Oil Palm Frond Juice as Future Fermentation Substrate: A Feasibility Study" *Biomed Research International*, vol. 2014, pp. 1-8, 2014.
- [5] C. K. Lee and F. A. Abdul Hakim, "A potential for Bioethanol production," *International Journal of Scientific and Research Publications*, vol. 4, pp. 1-7, 2014.
- [6] A. S. Aliyu, A. A. Azhar, Y. Adibah, and A. L. Zulkainain, "Potential of Oil Palm Frond liquid extract and fiber as feedstock for Biobutanol production," *Jurnal Teknologi(Science and Engineering)*, vol. 72, pp. 1-6, 2015.
- [7] A. Kosugi, R. Tanaka, K. Magara, Y. Murata, T. Arai, O. Sulaiman, *et al.*, "Ethanol and lactic acid production using sap squeezed from old palm trunks felled for replanting," *Journal of Bioscience and Bioengineering*, vol. 110, pp. 322-325, 2010.
- [8] F. Monot, J. M. Engasser, and H. Petitdemange, "Influence of PH and undissociated butyric acid on the production of acetone and butanol in batch cultures of *Clostridium acetobutylicum*," *Applied Microbiology Biotechnology*, vol. 19, pp. 422-426, 1984.
- [9] H. Ahmed and R. Aljuboori, "Oil palm Biomass residue in Malaysia: Availability and Sustainability," *Universiti Teknologi PETRONAS*, 31750 Tronoh, perak, Malaysia ijbr.utp.edu.my, 2013.
- [10] S. P. Lee, J. H. Park, S. H. Jang, L. K. Nielsen, J. Kim, and K. S. Jung, "Fermentatlv Butanol Production by Clostridia," *Journal Biotechnology and Bioengineering*, vol. 101, pp. 209-228, 2008.
- [11] S. H. Lim, I. Darah, and C. O. Ibrahim, "Oil Palm Frond for the Production of Bioethanol," *International Journal of Biochemistry and Biotechnology*, vol. 1, pp. 7-11, (2012).
- [12] T. L. Miller and M. J. Wolin, "Aserum bottle modification of the Hungate technique for culturing obligate anaerobes.," *Journal of Applied Microbiology*, vol. 27, pp. 985-987, 1976.
- [13] D. T. Jones and D. R. Woods, "Acetone-Butanol Fermentation Revisited," *Micribiol Rev.*, vol. 50, pp. 484-524, 1986.
- [14] M. S. Madihah, A. B. Ariff, M. S. Khalil, A. A. Suraini, and M. I. A. Karim, "Anaerobic fermentation of gelatinized sago starch-derived sugars to acetone-1-butanol-ethanol solvent by *Clostridium acetobutylicum*," *Folia Microbiologica*, vol. 46, pp. 197-204, 2001.
- [15] M. Gottwald and J. C. Gottscalk, "The internal pH of clostridium acetobutylicum and its effect on the shift from acid to solvent formation.," *Archieve Microbiology*, vol. 143, pp. 42-46, 1985.
- [16] R. Marchal, D. Blanhet, and J. P. Vandecasteele, "Industrial optimization of acetone-butanol-ethanol fermentation: a study of the utilization of Jerusalem artichoke.," *Journal of Applied Microbiology Biotechnology*, vol. 23, pp. 92-98, 1985.

Superhydrophobic surfaces for convective heat transfer applications

K. H. Yu^{a,b}, C. J. Teo^a, B. C. Khoo^a

^aDepartment of Mechanical Engineering,
National University of Singapore,
Singapore 117576, Singapore.

^bSchool of Mechanical Engineering,
Engineering Campus, Universiti Sains Malaysia,
14300 Penang, Malaysia.

ABSTRACT

The unique non-wetting property of superhydrophobic surfaces poses a broad range of potential applications (e.g. self-cleaning, anti-icing, fluid control, etc.), but its prime benefit is notably attributed to the reduction in the flow frictional resistance. Inspired by the unique water-repellent surface properties of the lotus leaf, the hydrophobicity of such surfaces can be mimicked on artificial textured surfaces which contain protruding structures at the micron-/submicron-scale. While the use of such surfaces could substantially increase the mass flow rate through narrow channels/tubes, these surfaces could provide enhanced liquid circulations in microfluidic systems for thermal management applications. Our recent work focuses on the manipulation of geometric parameters in enhancing the thermal-hydraulic performance in devices containing microchannels patterned with textured superhydrophobic surfaces. Investigations on hydrodynamic and thermal transport properties over such surfaces reveal a substantial dependence on factors including the shear-free fraction, pattern width to channel height ratio, liquid-gas interface curvature, etc. By employing such surfaces, the presence of slip and the concomitant decrease in the flow resistance offer a great potential in overcoming the pumping power limitation and also enhancing the thermal-hydraulic performance in thermal transport applications.

Keywords

Laminar heat transfer, Superhydrophobic, Longitudinal grooves, Microchannels

1. INTRODUCTION

The rapid growth in the microelectronics technology towards faster processing speeds has presented a great challenge in thermal management, especially when dealing with high heat flux removal. As the multi-chip modules are integrated with smaller and closely mounted electronic chips, this gives rise to a higher heat flux density on the chip and module levels. With the rising heat flux demands, forced convection liquid

cooling has become a promising avenue for the thermal management of such systems. For the same thermal load, the superior thermal properties (e.g., high specific heat, density and thermal conductivity) of liquids relative to air allow a lower mass flow rate to be employed in cooling systems. Air can be replaced by a dielectric liquid for direct immersion cooling such that direct contact of the liquid with the back of the chip is permitted. For an indirect liquid cooling system where a physical wall is placed between the liquid and the chip, water (a non-dielectric) can be used as the liquid coolant. As downsizing leads to a higher surface-to-volume ratio, such narrow channels and tubes are ideal choices in handling high heat flux dissipation. The potential of such heat exchangers has been explored analytically, experimentally and numerically by numerous researchers over the years [1, 2] for assessing the heat removal capability within these devices. However, the heat transfer enhancement under pressure-driven flows is typically achieved at the expense of a pressure drop penalty which can be substantially large for flow in microscale devices, thereby limiting the heat transfer enhancement for a given pumping power. This has thus become a huge bottleneck in the practical implementation of microfluidic cooling systems.

To address this problem, one promising technology which has attracted considerable interests in recent years involves the flow through microchannels patterned with superhydrophobic surfaces. Such surfaces are potentially capable of reducing the flow resistance, or equivalently, the mass flow rate can be increased for a given pressure gradient. Maintaining a dewetted (Cassie state) condition as illustrated in Figure 1, the wetting of the groove is averted, leaving air pockets filling up the gap beneath the liquid interface. In between these small-sized structures, an approximately shear-free liquid-gas interface can be supported which allows liquid to slip over it. As a result, a reduction in viscous skin friction drag experience by the liquid flow can be potentially achieved as the direct contact and shearing effects between the solid surface and the flowing liquid are reduced.

The effects of the surface wettability on heat transfer performance in microchannels have received

considerable attention. Experimental investigations reveal that there exists a drop in heat transfer performance when hydrophobic features are employed, with reductions of up to 8% for the heat transfer coefficient [3] and 18% for the heat transfer rate [4], as compared to a plain microchannel. Apart from experimental works, numerical investigations were explored by Maynes and co-workers for axially constant temperature [5] and constant heat flux [6] conditions. Focusing on the transverse grooves, the thermal transport over a periodic array of alternating ribs and grooves shows that the rib and cavity averaged Nusselt number declines with respect to relative cavity length. However, the overall thermal-hydraulic performance could be enhanced, owing to a greater benefit from the reduced hydraulic resistance.

The present study mainly focuses on two aspects: First, the thermal conduction resistance of the superhydrophobic surfaces, owing to the two distinctly different values of thermal conductivity for gas and

liquid; and second, the trade-off between heat transfer and pumping power. In the following sections, the numerical formulations are presented along with the appropriate boundary conditions. Under uniform peripheral wall temperature and uniform axial heat flux conditions (H1 boundary condition), the hydrodynamic and thermal characteristics are evaluated in the following dimensionless forms: friction factor-Reynolds number product (fRe) and Nusselt number (Nu), as defined in the next section. The trade-off between heat transfer and pumping power is evaluated in terms of the area goodness factor, defined as the ratio of the Colburn j factor (j) and the friction factor (f). Based on the standard definition of area goodness factor $(j/f) = Nu Pr^{-1/3} / fRe$, the enhancement ratio is quantified by $(j/f)/(j/f)_0 = (Nu/fRe)/(Nu_0/fRe_0)$, with Nu_0 and fRe_0 corresponding to baseline values.

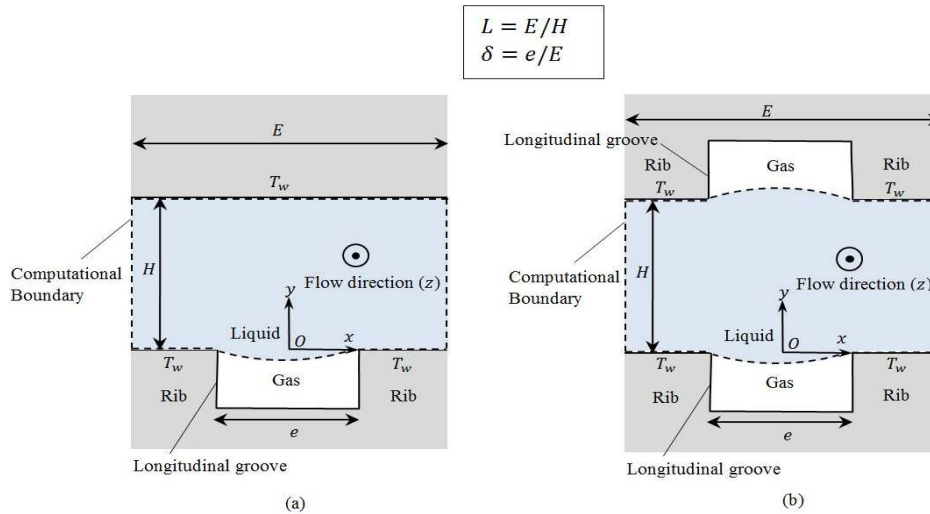


Figure 1: Schematic illustration of flow geometry for a single groove-rib unit patterned with longitudinal gas-filled groove on a) one wall (i.e., lower wall); b) both walls, under uniform peripheral wall temperature and uniform axial heat flux conditions

2. NUMERICAL FORMULATION

The flow configuration and the coordinate system for one repeating groove-rib unit with longitudinal superhydrophobic grooves patterned along the lower wall and both the upper and lower walls in a straight channel are illustrated in Figure 1a and Figure 1b, respectively. The groove-rib unit is characterized by the size of groove e and rib $(E - e)$, with channel height denoted by H . Based on these definitions, geometric parameters are designated as the shear-free fraction $\delta = e/E$ and the ratio of groove-rib spacing to channel height $L = E/H$, as employed throughout this study. Under a continuous unidirectional laminar flow condition, the liquid is assumed to maintain a non-wetting (hydrophobic) condition with the liquid and

gas phases separated by a liquid-gas interface. A dewetted Cassie state is assumed and the contact line is assumed to be pinned at the sharp corners of the ribs. The Capillary number is assumed to be sufficiently small and thus, the interface is assumed to have a constant curvature. The angle θ , known as the interface protrusion angle, is employed to represent the geometrical shape of the curvature, as illustrated in Figure 2.

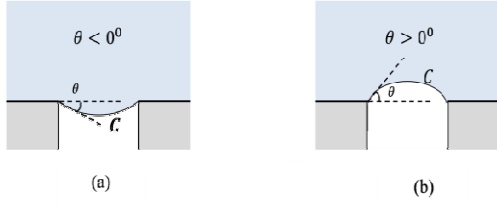


Figure 2: Liquid-gas interface in the form of: a) convex curvature; b) concave curvature

2.1 Governing equations

For a pressure-driven Poiseuille flow under both hydrodynamically and thermally fully-developed conditions, the Partial Differential Equations which govern the normalized streamwise velocity \tilde{w} and normalized temperature \tilde{T} are expressed as

$$\frac{\partial^2 \tilde{w}}{\partial \tilde{x}^2} + \frac{\partial^2 \tilde{w}}{\partial \tilde{y}^2} = -1, \quad (1)$$

$$\frac{\partial^2 \tilde{T}}{\partial \tilde{x}^2} + \frac{\partial^2 \tilde{T}}{\partial \tilde{y}^2} = -\tilde{w}, \quad (2)$$

where the normalized spatial coordinates with respect to channel height, x/H and y/H are labeled \tilde{x} and \tilde{y} . Deduced from the differential equations, the pertinent non-dimensional variables (\tilde{w} and \tilde{T}) are given by

$$\tilde{w} = w\mu/[H^2(-dp/dz)], \quad (3)$$

$$\tilde{T} = -\frac{k\mu(T_w - T)}{\rho c_p H^4} \frac{\partial T}{\partial z}, \quad (4)$$

where $|dp/dz|$ is the magnitude of the externally applied streamwise pressure gradient and T_w denotes the wall temperature. The thermophysical and transport properties, i.e. density ρ , dynamic viscosity μ , thermal conductivity k and specific heat c_p are all assumed to remain constant.

The following boundary conditions are imposed as follows:

- i) No slip along the solid surfaces: $\tilde{w} = 0$.
- ii) Shear-free along the liquid-gas interface: $\hat{n} \cdot \nabla \tilde{w} = 0$.
- iii) Uniform wall temperature along solid surfaces: $T_w = \text{constant}$.
- iv) Adiabatic condition along the liquid-gas interface: $\hat{n} \cdot \nabla \tilde{T} = 0$.
- v) Periodicity condition along the x -direction for normalized velocity and normalized temperature: $\frac{\partial \tilde{w}}{\partial \tilde{x}} = 0$ and $\frac{\partial \tilde{T}}{\partial \tilde{x}} = 0$.

Under the aforementioned conditions, results describing the hydrodynamic and thermal characteristics are evaluated in terms of the friction

factor-Reynolds number product and the Nusselt number, given as follows:

$$fRe = \epsilon \left(\frac{1}{S} \int_{S_w} \frac{\partial \tilde{w}}{\partial \tilde{n}} dS_w \right) / \left(\frac{1}{A} \int_A \tilde{w} dA \right), \quad (5)$$

$$Nu = \frac{2}{T_m} \left(\frac{1}{S} \int_{S_w} \frac{\partial \tilde{T}}{\partial \tilde{n}} dS_w \right) \quad (6)$$

where $\partial \tilde{w} / \partial \tilde{n}$ and the $\partial \tilde{T} / \partial \tilde{n}$ are, respectively, the local normalized velocity and the normalized temperature gradients normal to the solid surface S_w . The normalized unit vector normal to the solid surfaces is denoted by $\tilde{n} = \mathbf{n}/H$. The normalized bulk temperature difference is defined as $T_m = \int_A \tilde{w} \tilde{T} dA / \int_A \tilde{w} dA$ averaged over the normalized flow cross-sectional area A .

3. RESULTS AND DISCUSSION

The normalized governing equations along with the imposed boundary conditions are solved using a finite-element based Poisson equation solver which employs unstructured 2D triangular elements. A sufficiently large number of elements (approximately 500,000) is used to ascertain the accuracy of the obtained streamwise flow and thermal fields.

3.1 Normalized thermal slip length for small values of L

The effective hydrodynamic and thermal slip lengths are computed to describe the macroscopic (effective) slip velocity \tilde{w}_{eff} and temperature jump \tilde{T}_{eff} along superhydrophobic surfaces, given by

$$\tilde{\lambda}_h = \tilde{w}_{\text{eff}} / (d\tilde{w}_{\text{eff}}/d\tilde{n}), \quad (7)$$

$$\tilde{\lambda}_t = \tilde{T}_{\text{eff}} / (d\tilde{T}_{\text{eff}}/d\tilde{n}). \quad (8)$$

where $\tilde{\lambda}_h (= \lambda/H)$ and $\tilde{\lambda}_t (= \lambda_t/H)$ represent the normalized effective hydrodynamic and thermal slip lengths, respectively. In Figure 3, the numerical results for small values of L are plotted together with the analytical solution, given by [7]

$$\frac{\tilde{\lambda}_t}{\tilde{E}} = \frac{1}{\pi} \ln \left(\sec \left(\frac{\delta\pi}{2} \right) \right). \quad (9)$$

There is excellent agreement between the numerical and analytical solutions, thus alluding to the accuracy of the numerical simulations. For a fixed normalized groove-rib periodic spacing \tilde{E} , an increase in the value of δ gives rise to a corresponding increase in $\tilde{\lambda}_t$. By maintaining a fixed value of \tilde{w}_{eff} , this implies that the value of $|T_w - T_{\text{eff}}|$ tends to rise when the relative groove spacing increases.

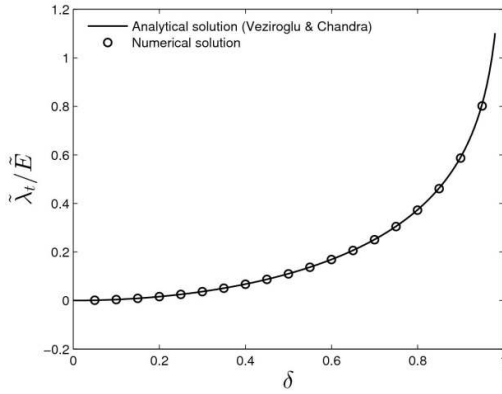


Figure 3: The normalized effective thermal slip length per normalized groove-rib spacing $\tilde{\lambda}_t/\tilde{E}$ as a function of shear-free fraction δ .

3.2 Effects of shear-free fraction

For flow through a microchannel patterned with longitudinal superhydrophobic grooves on both walls, the local Nusselt number distributions along the lower wall are plotted for different values of shear-free fraction in Figure 4 for $L = 0.02$. As can be deduced from Figure 4, Nu_x is approximately equal to or greater than the baseline value of $Nu_0 (= 8.235)$ along the solid surface ($\delta L/2 \leq x \leq L/2$). This suggests that there exists a local enhancement along the rib surface as compared to the classical no-slip scenario. For a given shear-free fraction δ the local enhancement is spatially dependent. For all values of δ investigated, there exists a peak at the edge of the rib, where the local velocity gradient is maximum.

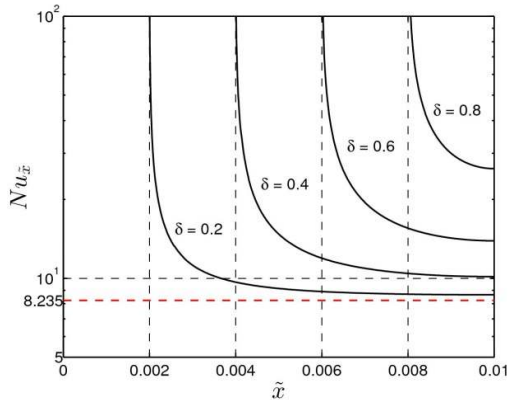


Figure 4: Distribution of Nu_x as a function of \tilde{x} at the lower wall for $L = 0.02$.

The results for the mean Nusselt number Nu plotted against the shear-free fraction δ for different values for L are shown in Figure 5. As can be observed in this figure, the Nusselt number decreases monotonically from the upper limit of $Nu = 8.235$ at $\delta \rightarrow 0$ as δ increases for all values of L investigated. Based on the definition for the Nusselt number, a decline in Nu can

be regarded as a reduction in the overall heat transfer performance. Maintaining a fixed value of L , this reduction is influenced by the size of the shear-free interface which is directly associated with the loss in the heating surface area. Likewise, the numerically obtained friction factor-Reynolds number product exhibits the same pattern as demonstrated in Figure 6, with $fRe = 24$ corresponding to the upper limit.

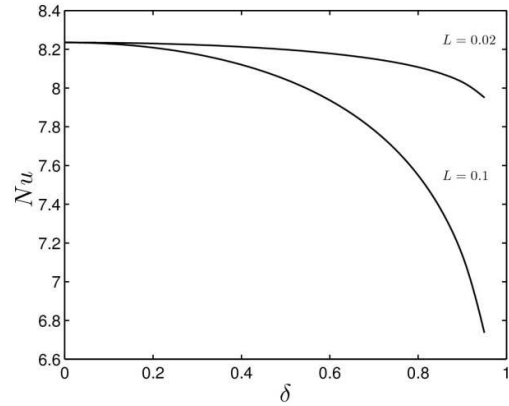


Figure 5: The averaged Nusselt number as a function of δ at different values of L . Flow over superhydrophobic longitudinal grooves patterned on both walls is considered

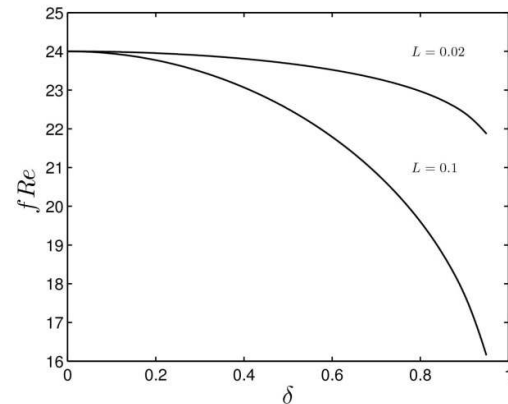


Figure 6: The averaged friction factor-Reynolds number product at different values of L

Quantified in terms of the overall performance, the enhancement ratio presented in Figure 7 shows favorable results within the range of δ values examined. Corresponding to the no-slip and constant axial heat flux conditions, the values for fRe_0 and Nu_0 are 24 and 8.235, respectively. The effect of shear-free fraction on the enhancement ratio is examined for small values of L . As can be deduced from Figure 7, the computed enhancement in terms of the relative area goodness factor for Poiseuille flow in microchannels patterned with superhydrophobic longitudinal grooves is found to be equal or above unity with an increasing trend as δ increases. As can be seen, configurations with larger L yield a greater enhancement ratio as compared to smaller values of L . For the same values

of L and δ , the numerically predicted $(j/f)/(j/f)_0$ ratio yields greater enhancements for flow configurations with superhydrophobic surfaces patterned on both walls than on a single wall, as demonstrated in Figure 7. Numerical simulations predict that the enhancement ratio could reach as high as 1.13 and 1.2155 at $L = 0.1$ for flow scenarios involving longitudinal superhydrophobic grooves patterned on single wall and both walls, respectively.

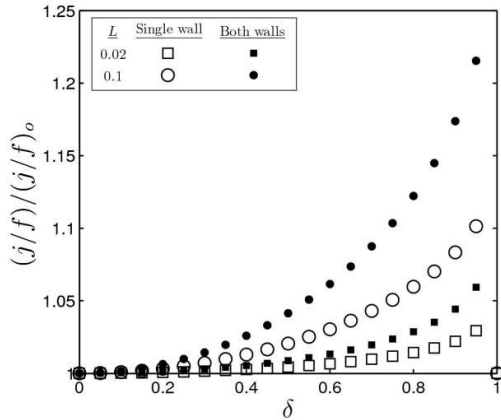


Figure 7: Variation of $(j/f)/(j/f)_0$ as a function of δ for small L ($L = 0.02$ and 0.1)

3.3 Effects of meniscus curvature

Figure 8 shows the results corresponding to the $(j/f)/(j/f)_0$ ratio for different interface protrusion angles with shear-free fractions δ ranging between 0.1 and 0.9. For small values of L , the $(j/f)/(j/f)_0$ ratio increases monotonically as the liquid-gas interface protrudes towards the liquid phase, corresponding to positive values of θ . However, when the interface bows away from the liquid phase, the $(j/f)/(j/f)_0$ ratio falls as compared to the result produced by the flat interface. For all values of δ investigated, the enhancement ratios consistently stay above unity.

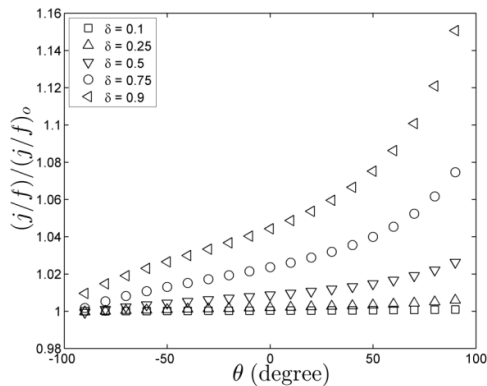


Figure 8: Variation of $(j/f)/(j/f)_0$ as a function of interface protrusion angle θ for various shear-free fractions δ . Flow over longitudinal grooves patterned on both walls with $L = 0.02$ is considered.

4. CONCLUSION

By employing superhydrophobic longitudinal grooves, the presence of heat conduction resistance along the wall and the reduction in thermal transport performance have been demonstrated. However, the degraded heat transfer performance can be offset by a greater benefit arising from the reduced hydraulic resistance to yield a positive overall thermal-hydraulic performance. As demonstrated, the results presented in this paper lead to the suggestion that longitudinal superhydrophobic grooves can be used advantageously for heat transfer applications.

REFERENCES

- [1] M.A. Ebadian, C.X. Lin, A review of high-heat-flux heat removal technologies, *Journal of Heat Transfer*, 133(11) (2011) 110801.
- [2] G.L. Morini, Single-phase convective heat transfer in microchannels: A review of experimental results, *International Journal of Thermal Sciences*, 43(7) (2004) 631-651.
- [3] S.-S. Hsieh, C.-Y. Lin, Convective heat transfer in liquid microchannels with hydrophobic and hydrophilic surfaces, *International Journal of Heat and Mass Transfer*, 52(1-2) (2009) 260-270.
- [4] G. Rosengarten, C. Stanley, F. Kwok, Superinsulating heat transfer surfaces for microfluidic channels, *International Journal of Transport Phenomena*, 10 (2008) 293-306.
- [5] D. Maynes, B.W. Webb, J. Davies, Thermal transport in a microchannel exhibiting ultrahydrophobic microribs maintained at constant temperature, *Journal of Heat Transfer*, 130(2) (2008) 022402.
- [6] D. Maynes, B.W. Webb, J. Crockett, V. Solovjov, Analysis of laminar slip-flow thermal transport in microchannels with transverse rib and cavity structured superhydrophobic walls at constant heat flux, *Journal of Heat Transfer*, 135(2) (2013) 021701.
- [7] T.N. Veziroglu, S. Chandra, Thermal conductance of two-dimensional constrictions, in: J.T. Bevens (Ed.) *Thermal Design Principles of Spacecraft and Entry Bodies*, American Institute of Aeronautics and Astronautics, 1969, pp. 591-615.

Physical Characteristics of Pulverized EFB Briquettes Produced under Various Heating Temperatures

Hasan Mohd Faizal^a, Z. A. Latiff^b, Muhammad Amin Bin Mohd Iskandar^c

^aAutomotive Development Centre,
Faculty of Mechanical Engineering,
Universiti Teknologi Malaysia,
81310 UTM Johor Bahru, Johor
Tel: (607)5534852
E-mail : mfaizal@mail.fkm.utm.my

^bAutomotive Development Centre,
Faculty of Mechanical Engineering,
Universiti Teknologi Malaysia,
81310 UTM Johor Bahru, Johor
E-mail: zkarnain@mail.fkm.utm.my

^cFaculty of Mechanical Engineering,
Universiti Teknologi Malaysia,
81310 UTM Johor Bahru, Johor

ABSTRACT

Physical characteristics of empty fruit bunch (EFB) briquettes produced under various heating temperatures were investigated experimentally. Empty fruit bunch (EFB) fibers were firstly grinded and sieved into pulverized form with the particle size of $<300 \mu\text{m}$. It was then compressed at the pressure of 7 MPa and under heating temperatures of 150-210 °C. The density of the briquettes was determined by using stereometric method while the compressive strength was determined by using machine Instron 600dx. It was found that density of briquettes produced is not really affected by the heating temperature. However, the compressive strength is improved when the heating temperature is increased. Overall, it can be said that the values of strength of all briquettes are sufficient to resist mechanical disintegration.

Keywords

Example:
EFB briquettes, continuous heating, pulverized EFB

1. INTRODUCTION

Nowadays, the climate change has driven towards the utilization of renewable energy sources such as solar, wind, hydro and biomass, without sole dependence on fossil fuel [1]. In Malaysia, biomass is one of the most important renewable energy, and it can be obtained mainly from palm oil plantation. During the extraction of palm oil from fresh fruit bunches, several types of biomass simultaneously produced such as shell, mesocarp fibre and empty fruit bunch (EFB). Among them, the production rate of EFB is the highest (~18

million tonnes/year), followed by fibre (~9 million tonnes/year) and shell (~4 million tonnes/year) [2].

Therefore, in this study, the use of EFB is emphasized for making solid fuel through briquetting process. Briquetting is known as a compaction of biomass residues into a small log with a diameter between 30mm and 100mm, and with any length [3]. The advantage of briquetting is it can improve the storage, thus the cost for transportation can be reduced. Briquettes are usually used for both domestic and industrial section including fireplaces, stoves and boiler for steam and hot water generation.

The effectiveness of briquetting process can be determined through the testing of strength and durability for the briquettes produced [4]. Examples of important parameter that show the strength of certain briquette are compressive strength, impact resistance, and shear strength. Meanwhile, the durability of the briquette depends on abrasion resistance and water resistance.

The palm biomass briquette has been introduced by Husain et al. (2002) [5]. The briquette contained mesocarp fibre and shell (weight ratio 60:40) and the binder used was starch. They found that the compressive strength of the briquettes produced was around 2.56 MPa, and is considered sufficient to resist mechanical disintegration. In the other study done by Nasrin et al. (2008), briquettes that contained pulverized empty fruit bunch (EFB) have been introduced [6]. In this case, they found that the addition of sawdust could improve the compressive strength of the briquettes, that was around 7.9 MPa.

In 2010, Faizal et al have introduced briquettes that contain EFB fibre and mesocarp fibre (weight ratio 60:40) [7]. It was found that the physical characteristics of the briquettes produced were competitive with characteristics of the local practiced briquettes that contain mesocarp fibre and shell (weight ratio 60:40). They have concluded that compressive strength of the introduced briquettes increases with an increase in compaction pressure during briquetting. Meanwhile, in 2013, Chin and Shiraz have conducted the test of impact resistance and they found that the addition of paper to briquettes that contain palm kernel shell and palm fibre (weight ratio 60:40) could improve the strength of the briquettes [8].

In 2014, Arzola et al. have demonstrated that a reliable strength of pellet with a mixture of palm kernel shell and mesocarp fibre (weight ratio 40:60) can be obtained when the moisture content is 10% and binder content is 4% [9]. Based on the researches as mentioned previously, it can be concluded that the physical characteristics of palm biomass briquettes strongly influenced by type of binder, briquetting pressure and moisture content.

In the present study, physical characteristics of briquettes that contain 100% pulverized EFB was investigated fundamentally in terms of relaxed density and compressive strength. The effect of temperature on the physical characteristics will be discussed in this paper since such subject is still less explored for palm biomass briquettes.

2. METHODOLOGY

2.5 Preparation of Raw Materials

The raw material (empty fruit bunch (EFB) fibres) was collected from Kilang Sawit Felda Lok Heng, Johor. Then, the fibres were grinded into powder form and was sieved to particle size of $<300 \mu m$. Before briquetting, there are common procedures to perform proximate analysis and to determine calorific value in prior to briquette production. The proximate analysis was performed for the EFB powder based on standards as shown by table 1 below. Meanwhile, gross calorific value was determined by using bomb calorimeter model LECO AC350 located at Plant and Automotive Laboratory, Faculty of Mechanical and Manufacturing Process, Universiti Tun Hussien Onn Malaysia (UTHM).

Table 1: Standard used for Proximate Analysis

Properties	Standard Used
Moisture Content	ASTM D3173
Volatile Matter	ASTM D3175
Ash Content	ASTM D3174

It was found that the gross calorific value of raw material is about 16100 kJ/kg. Meanwhile, the results of proximate analysis are shown in table 2 below.

Table 2: Results of Proximate Analysis

Properties	Percentage [%]
Moisture Content	~7
Volatile Matter	~75.5
Ash Content	~3.5
Fixed Carbon	~14

In the present study, the combustion properties are not yet discussed. The emphasis is given more on the basic physical characteristics of the briquettes to know the potential of pulverized EFB to be developed as binderless briquette without any synthetic binder.

2.6 Briquetting Process

For briquetting process, a die set made of stainless steel as shown by figure 1 below was used. It consists of plunger, die wall and base. For heating purpose, the die wall was covered with steel coil heater and was insulated during briquetting. Meanwhile, to control the heating temperature, a thermocouple and the steel coil heater were connected to a temperature controller. The horizontal distance between the thermocouple sensor and the inner wall of the die part was set about 3 mm. To apply load during briquetting process, die set that was placed at machine Instron 600dx.

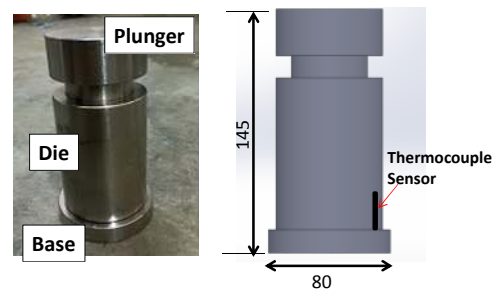


Figure 1: Die set for briquetting

The briquetting process was performed at constant pressure of 7 MPa, under various heating temperatures of 150°C to 210°C. Firstly, the pulverized EFB was filled in the die and was compressed without heating for 30 minutes. After that, the die set filled with EFB was heated simultaneously with desired temperature for 30 minutes. After the heating process was complete, it was left at room temperature for cooling process. The amount of pulverized EFB (powder form) that was used to make each briquette was set around 45g.

The briquettes produced were then left under ambient condition for around 1 week to obtain stability and

rigidity, before determination of relaxed density and being tested for compressive strength.

2.7 Determination of Relaxed Density

After the briquettes produced were dried under ambient condition for one week, the density of the briquette was measured using a stereometric method as used by Rabier et al. (2006) [10]. The volume of the briquette was measured using calipers and then the briquette was weighted. The density can be obtained by dividing the mass with volume of the measured briquette.



Figure 3: Image of briquette produced

2.8 Test of Compressive Strength

The test of compressive strength was performed by using Instron 600dx machine, as shown by figure 2 below. The Instron machine is located at Strength Laboratory, Faculty of Mechanical Engineering, UTM Skudai.

Firstly, the briquette was placed on the metal plate of the machine. Then the distance between upper and lower plate of the machine was reduced with a speed of 1.3 mm/min. The compression process continuously occurs until a crack could be observed on the briquette surface.



Figure 2: Test of compressive strength using Instron machine

3. RESULTS AND DISCUSSION

Figure 3 below shows the image of a 100% pulverized EFB briquette produced under temperature of 210°C. It can be observed that the surface of the briquette was very smooth. Therefore, it can be said that the binderless briquette without any synthetic binder was successfully produced in the present study. Here, the presence of natural lignin during the heating process really plays a significant role in the formation of the briquette.

Figure 4 below shows the result of relaxed density of the briquettes produced. The figure elucidates that the relaxed density of the briquette is not really affected by the heating temperature as the density remains almost the same for various heating temperatures. The values of density are within the range of 1200 to 1250kg/m³, thus could reduce the transportation and handling cost due to the increase in energy density.

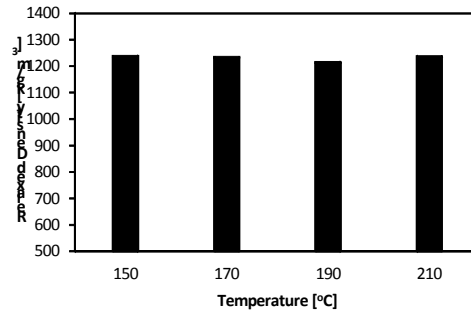


Figure 4: Relaxed density for various heating temperatures

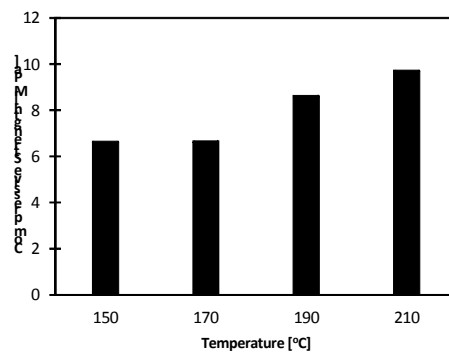


Figure 5: Compressive strength of briquettes produced under various heating temperatures

Figure 5 shows the result of compressive strength of the briquettes produced. The figure shows that the compressive strength increases with an increase in heating temperature. Therefore, it can be said that more lignin is produced when the temperature is increased,

thus could improve the compressive strength of the briquettes. Overall, it can be said that all values of compressive strength are competitive with the commercial briquette [6] and sufficient to resist against mechanical disintegration.

Based on figure 5 and 6, it can be said that the presence of lignin plays a significant role to improve the compressive strength of the briquettes produced, but does not really influence the value of relaxed density within the temperature range of the present study.

4. CONCLUSIONS

In the present study, the briquettes that contained 100% pulverized empty fruit bunch (EFB) have been successfully produced without any synthetic binder. Then, the physical characteristics of pulverized empty fruit bunch (EFB) briquettes have been investigated experimentally in terms of relaxed density and compressive strength.

Within the temperature range of the present study, it can be said that heating temperature does not really affect the relaxed density of briquettes. However, the heating temperature plays a significant role in improving the compressive strength of the briquettes produced.

Based on the results of physical characteristics in the present study, it can be said that the 100% pulverized EFB briquette is competitive with the commercial standard and local practiced briquette that contains mesocarp fibre and shell.

ACKNOWLEDGMENT

The authors acknowledge the Ministry of Education Malaysia and Universiti Teknologi Malaysia for giving cooperation and full of support in this research activity. The authors wish to thank Research Management Center (RMC) for Potential Academic Staff grant (Q.J130000.2724.01K44) from Ministry of Education Malaysia and Universiti Teknologi Malaysia. The authors also acknowledge Kilang Sawit Felda Lok

Heng, Kota Tinggi, Johor for giving full of cooperation in this research study by supplying raw materials (EFB fibres).

REFERENCES

- [1] Mekhilef Saad, Barimani Meghdad, Safari Azadeh and Salam Zainal, "Malaysia's renewable energy policies and programs with green aspects", *Renewable and Sustainable Energy Reviews*, Vol. 40, pp. 497-504, 2014.
- [2] Aljuboori ,A.H.R., "Oil Palm Biomass Residue in Malaysia: Availability and Sustainability", *International Journal of Biomass & Renewables*. Vol 2, No.1, pp. 13-18, 2013.
- [3] Cattaneo, D., "Briquetting-A Forgotten Opportunity", *Wood Energy*. Vol. 2, pp. 40-42, 2003.
- [4] Kaliyan, N., Morey R. V., "Factors Affecting Strength and Durability of Densified Biomass Products", *Biomass and Bioenergy*. pp. 1-23, 2008.
- [5] Husain, Z., Zainac, Z. and Abdullah, Z., "Briquetting of Palm Fibre and Shell from the Processing of Palm Nuts to Palm Oil", *Biomass and Bioenergy*, Vol. 22, pp. 505-509, 2002.
- [6] Nasrin, A.B., Ma, A.N., Choo, Y.M., Mohamad, S., Rohaya, M.H., Azali, A. and Zainal, Z. "Oil Palm Biomass as Potential Substitution Raw Materials for Commercial Biomass Briquettes Production", *American Journal of Applied Sciences*, Vol. 5, No.3, pp. 179-183, 2008.
- [7] Faizal, H.M., Latiff, Z.A., Mazlan, A. W. and Darus A. N., "Physical and Combustion Characteristics of Biomass Residues from Palm Oil Mills", *New Aspects of Fluid Mechanics, Heat Transfer and Environment Conference Proceedings*, pp. 34-38, 2010.
- [8] Chin, Y.S. and M. Shiraz, A., "A Study of Biomass Fuel Briquettes from Oil Palm Mill Residues", *Asian Journal of Scientific Research*, Vol. 6, No. 3, pp. 537-545, 2013.
- [9] Arzola, N., Gomez, A. and Rincon, S., "Experimental Study of the Mechanical and Thermal Behavior of Pellets Produced from Oil Palm Biomass Blends", *Global NEST Journal*, Vol. 16, No .1, pp. 179-187, 2014.
- [10] Rabier, F., Temmerman, M., Bohm, T., Hartmann, H., Jensen, P.D., Rathbauer, J., Carrasco, J. and Fernandez, M., "Particle Density Determination of Pellets and Briquettes", *Biomass and Bioenergy*. 30: 954-963, 2006.

Analysis of different friction factor correlations on the frictional pressure drop of two-phase flow ammonia-cooled minichannel

Muhammad Syafiq Shaari^a, Normah Mohd. Ghazali^{b*} and Hishamuddin Jamaludin^c

¹Faculty of Mechanical Engineering, University of Technology Malaysia,
Johor Bahru 81310, Malaysia

Email :^asyafiqshaari262@gmail.com,^bnormah@fkm.utm.my,^chishamji@fkm.utm.my

ABSTRACT

Friction factor is one of the major parameters that affect the frictional pressure drop in a mini channel of a compact heat exchanger. There have been many studies on the correlations for the friction factor, both in implicit and explicit forms. Differences between the predicted and experimental pressure drop have been reported and these could possibly be due to the different correlations used. This paper reports the effects of using five different friction factor correlations, both in implicit and explicit forms, on the frictional pressure drop of an ammonia-cooled minichannel under optimized conditions. For turbulent flow in a smooth channel, optimization is completed for 0.9-mm and 3-mm channels with genetic algorithm. Results show that different friction factor correlations produced different values of the frictional pressure drop even under optimized conditions. All five correlations produced evenly distributed optimal solutions for the simultaneous optimization of the frictional pressure drop and heat transfer coefficients. Comparison of R22 and ammonia refrigerants showed that the latter produced a higher heat transfer coefficient at the cost of a higher frictional pressure drop under optimized conditions.

Keywords: friction factor, correlations, ammonia-cooled minichannel, optimization

1. INTRODUCTION

The thermal performance or efficiency of transferring heat in a heat exchanger basically depends on the type of refrigerant used. Lately, the demand for compact heat exchangers that addresses the concerns for more environmentally friendly refrigerants as well, have attracted research into the behaviour of natural refrigerants in small channels. As an alternative refrigerant, ammonia (NH₃) with its zero global warming effect and low ozone depleting potential [1] has been identified to replace R22, the current refrigerant identified as hazardous [2]. Since two-phase flow has a higher heat transfer capacity compared to the single-phase flow due to the latent heat content, for very high heat transfer requirement, like the compact heat exchanger, two-phase flow is the expected phase of the primary refrigerant. Unfortunately, the refrigerant that exists in a small channel has a higher possibility for a higher pressure drop to occur along its operating length. Since two phase flow has a higher heat transfer capacity, and the

frictional pressure drop contributes significantly to the total pressure drop, much research on the two-phase frictional pressure drop has been completed in recent years to look at the effects of the frictional pressure drop on the hydrodynamic performance of the refrigerant in a heat exchanger tube [3].

Two phase frictional pressure drop analysis can be modelled according to two approaches; the homogeneous and separated model. The homogeneous model as stated in Xuet *al.* [4] considered the two phase flow like a single phase in which the velocities are the same for both phases. Meanwhile, in the separated model, both phases have different velocities with their specific friction factor for every phase. In the frictional pressure drop analysis that have been done by past researchers, many parameters are involved that may affect the hydrodynamic performance of the refrigerant. Friction factor is one of parameters that influenced the frictional pressure drop. The earliest friction factor proposed is in an implicit form by Nikuradse [5] which covers smooth pipes followed by Colebrook [6] which considered the effect of roughness. These equations require an iterative numerical procedure and thus necessitate later researchers to come up with explicit versions, among which are those by Barr [7], Haaland [8], and Fang *et al.* [9], to name a few. To date, disagreements between the predicted frictional pressure drop developed from past experimental data and later experimental data vary. Differences in the refrigerants utilized, experimental conditions, flow regimes, and the correlations used probably contribute to the discrepancies. Thus, the effects of these five different friction factors are studied here under the minimized frictional pressure drop as the objective function. In addition, due to the desired high heat transfer coefficient which may be adversely affected by the minimization of the pressure drop, the simultaneous achievement of both the minimization of the frictional pressure drop and maximization of the heat transfer coefficient is attempted. The process is completed with genetic algorithm (GA), a stochastic approach that has recently become popular in the design optimization of process, components, and systems [10]. This type of study using GA on two-phase flow has not been reported before.

2. THEORY

The frictional pressure drop defined in the homogeneous model is [4]:

$$\left(\frac{\Delta p}{\Delta L}\right)_{tp} = \frac{G^2}{2D\rho_{tp}} f_{tp} \quad (1)$$

where G , D , ρ , and f are mass flux, channel diameter, fluid density, and the two-phase friction factor, respectively. The subscript tp denotes two-phase. The friction factor is determined from,

$$\frac{1}{\sqrt{f}} = 2 \log(Re\sqrt{f}) - 0.8$$

$$\frac{1}{\sqrt{f}} = -2 \log\left(\frac{Rr}{3.7} + \frac{2.51}{Re\sqrt{f}}\right)$$

$$f = \left(-2 \log\left(\frac{\varepsilon/D}{3.70} + \frac{4.518 \log\left(\frac{1}{7}Ke\right)}{Re\left(1 + \frac{1}{20}Re^{0.52}(\varepsilon/D)^{0.7}\right)}\right)\right)^{-2} \quad (4)$$

$$f = \left(-1.8 \log\left(\left(\frac{\varepsilon/D}{3.70}\right)^{1.11} + \frac{6.9}{Re}\right)\right)^{-2}$$

$$f = 0.25 \left[\log \frac{150.39}{Re^{0.98865}} - \frac{152.66}{Re}\right]^{-2}$$

The term Re is the Reynolds number and ε is the roughness of the inner surface of the channel. Equations (2) and (3) are in implicit forms introduced by Nikuradse [5] and Colebrook [6], respectively. The correlations of equations (4) through (6) are in explicit forms developed by Barr [7], Haaland [8] and Fang *et al.* [9], respectively. In the present study, the implicit friction factor is solved using the Newton-Raphson method with the two-phase viscosity, μ_{tp} , in the Reynolds number calculated using the McAdam *et al.* [11] correlation,

$$\frac{1}{\mu_{tp}} = \frac{x}{\mu_g} + \frac{1-x}{\mu_l} \quad (7)$$

x being the vapour quality and the two-phase density, ρ_{tp} , is commonly calculated with,

$$\frac{1}{\rho_{tp}} = \frac{x}{\rho_g} + \frac{1-x}{\rho_l} \quad (8)$$

In the single-objective optimization, equation (1) is minimized within a given range of parameters. In the double-objective optimization, minimization of equation (1) and maximization of a correlation for the heat transfer coefficient given by Kandlikar [12],

$$h_{tp} = \text{MAX} \{ h_{tp,NBD}, h_{tp,CBD} \}$$

are used as the objective functions, where,

$$h_{TP,NBD} = 0.6683Co^{-0.2}(1-x)^{0.8}h_{lo} + 1058.0Bo^{0.7}(1-x)^{0.8}F_{fl}h_{lo} \quad (9)$$

$$h_{TP,CBD} = 1.1360Co^{-0.9}(1-x)^{0.8}h_{lo} + 667.2Bo^{0.7}(1-x)^{0.8}F_{fl}h_{lo} \quad (10)$$

The term Co , Bo , h_{lo} and h_L , are the convective number, boiling number, and the Dittus-Boelter correlation given by,

$$Co = (\rho_g/\rho_l)^{0.5}((1-x)/x)^{0.8} \quad (11)$$

$$Bo = q_l(Gh_{fg}) \quad (12)$$

$$h_{lo} = 0.023Re_L^{0.8}Pr_L^{0.4}\frac{K_L}{D} \quad (13)$$

(3) Re_L is liquid Reynolds number while Pr_L is Prandtl number,

$$Re_L = \frac{(1-x)GD}{\mu_l} \quad (14)$$

$$Pr_L = \frac{\mu_l C_{p,l}}{K_L} \quad (15)$$

(5) The values of the parameters used and the properties of refrigerants investigated are listed in Table 1 and Table 2. The study was done for a 0.9 mm and a 3-mm (6)channel.

Table 1: Parameters used in the optimization

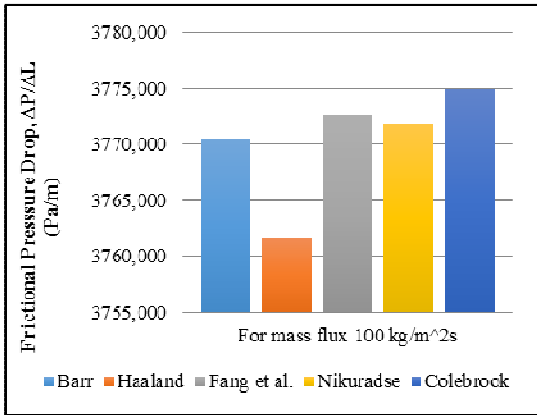
Parameter	Operating range
G (kg/m ² s)	100-600
D (mm)	0.9-3
Quality	0.38-1
T _{sat} (°C)	10
ε	0 (smooth)
q (kW/m ²)	60

Table 2: List of Ammonia and R22 Properties at saturation temperature 10°C [13].

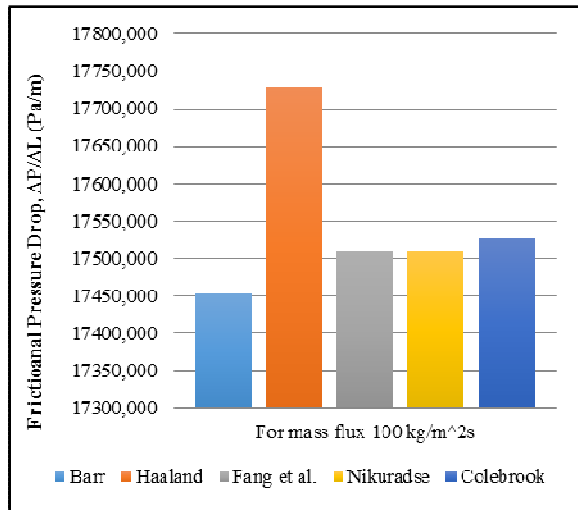
Refrigerant	Ammonia	R22
ρ_l (kgm ⁻³)	624.6	1246.7
ρ_g (kgm ⁻³)	4.8679	28.82
μ_l (Pa.s)	0.00015	0.00019
μ_g (Pa.s)	9.36×10 ⁻⁶	1.18×10 ⁻⁵
K_l (Wm ⁻¹ K ⁻¹)	0.52912	0.090247
h_{fg}	1228	196.4
$C_{p,l}$	4675	1199

3. RESULTS AND DISCUSSION

Figure 1 shows the comparison of the single-objective optimization with GA. There are differences between correlations under optimized conditions.



(a)



(b)

Figure 1: Frictional pressure drop with different friction factor correlations for (a) 0.9 mm inner diameter (b) 3.0 mm inner diameter

As generally expected, the frictional pressure drop for the smaller diameter channel is much higher than that in the larger diameter channel, more than four times higher. The Haaland [8] friction factor shows a higher value of frictional pressure drop among the correlations investigated. Although, the Colebrook, Barr, and Haaland correlations consider the channel surface roughness, for the case of a smooth channel when the corresponding term is dropped, the Haaland correlation gives a significant difference among all the correlations investigated. It is believed that the contribution from the flow condition, Reynolds number, plays a role in this effect. Fang *et al.* [9] correlation is among the latest friction factor proposed and it is claimed as the most accurate explicit single phase friction factor equation for turbulent flow in smooth pipes [4]. All correlations have been compared with Fang *et al.* [9] friction factor in terms of the percentage difference as shown in Figure 2. Interestingly, the implicit correlations show the smallest difference with about the same percentage difference for the small and large

diameter channels. The Nikuradse [5] correlation seems to agree well with the correlation given by Fang *et al.* [9]. This trend is also reported by Xu *et al.* [4] with a 0.02% mean absolute relative deviation of Fang *et al.* [9] compared with the Nikuradse [5] equation.

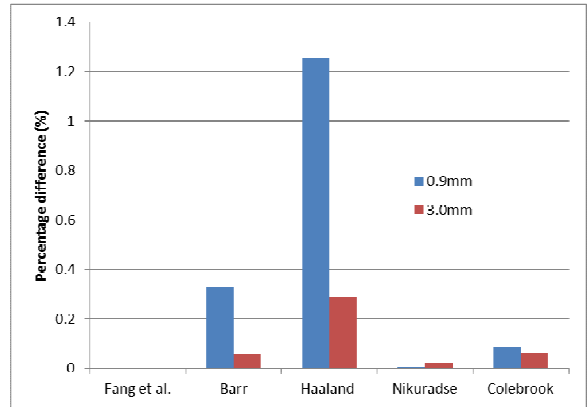


Figure 2: Percentage difference of friction factor correlations compared to Fang *et al.* (2011)

For both channel diameters, all correlations show a percentage difference of under 0.4% except for the Haaland [8] friction factor where it is shown above 1.2% for the smaller channel.

Figure 3 shows the outcome of the simultaneous optimization of the frictional pressure drop and heat transfer coefficient using the five correlations stated earlier. All correlations exhibit a fair distribution of optimal solutions.

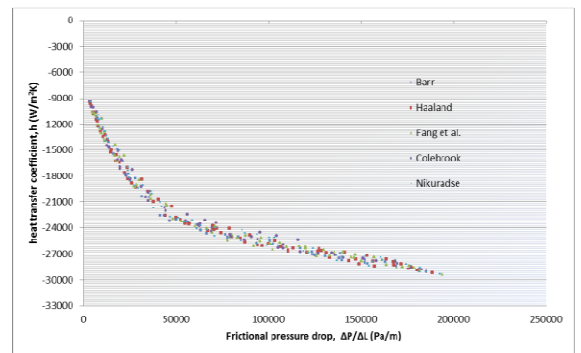


Figure 3: Result for frictional pressure drop and heat transfer coefficient of ammonia under same optimization using different friction factor correlations

Figure 4 shows the optimal solutions for R22 in comparison to ammonia using only the Fang *et al.* correlation [9]. The effects of mass flux on the frictional pressure drop and heat transfer coefficient are shown in Figure 5. GA optimization has shown that ammonia have a scattered solution for a given range of mass flux which is 300 until 600 $\text{kg/m}^2\text{s}$ while for R22 refrigerant, most solutions are located in the range mass flux of 300 to 400 $\text{kg/m}^2\text{s}$. As expected, frictional pressure drop increases with mass flux and it has also been observed by Maqbool [14]. For R22, most of the

mass flux is pointed at mass flux between 300 and 400 $\text{kg/m}^2\text{s}$ while most solution mass flux of ammonia is pointed at range 500 to 600 $\text{kg/m}^2\text{s}$. The trend is the same for both refrigerants where a higher mass flux produces a higher heat transfer coefficient. Pamitran *et al.* [15] stated that this is due to the increasing of convective boiling heat transfer contribution. These graphs also show at the same mass flux, it will have different magnitude of the frictional pressure drop and heat transfer coefficient.

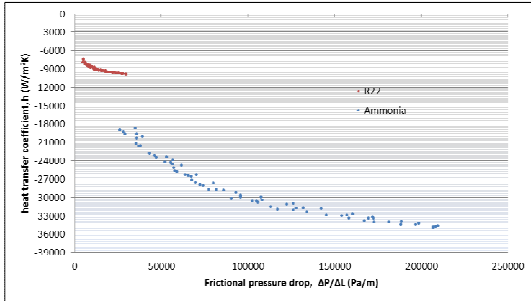
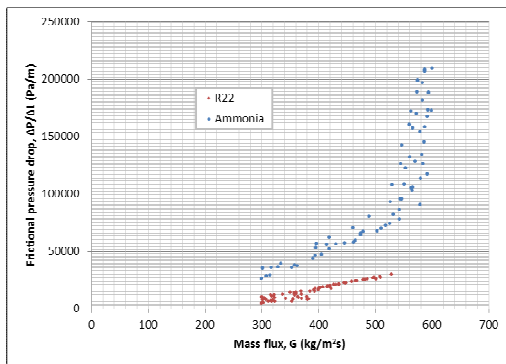
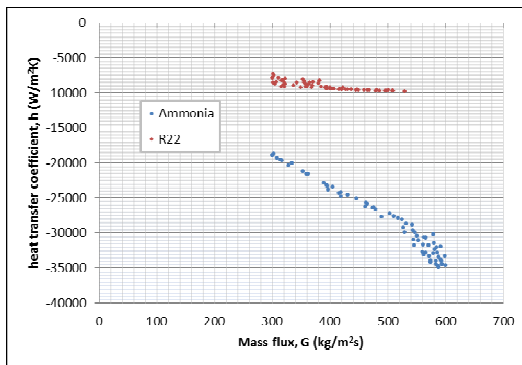


Figure 4: Comparison of ammonia and R22 under optimized conditions.



(a)



(b)

Figure 5: Solution and the effect of mass flux on frictional pressure drop and heat transfer coefficient

4. CONCLUSION

The effects of different friction factor on the optimized frictional pressure drop and heat transfer coefficient have been studied using 5 different friction factor correlations, both in implicit and explicit form. From

the investigations of the R22 and ammonia refrigerants in the 0.9-mm and 3-mm channels, the following conclusion can be seen:

1. For a smooth channel, Haaland [8] correlation is significantly different from the other correlations investigated.
2. For a smooth channel, the explicit Fang et al. [9] correlation is found to be closest to the earliest implicit Nikuradse [5] correlation as reported in a review by Xu et al. [4].
3. For consideration of surface roughness in the channel, the Barr [7] and Haaland [8] correlations are found to be closest to the implicit Colebrook [6] correlation.
4. Effect of heat transfer coefficient is always proportional to frictional pressure drop under the same optimized conditions.
5. R22 is a better refrigerant in the form of minimizing the frictional pressure drop. However, ammonia is a better refrigerant in the highest heat transfer coefficient.

ACKNOWLEDGEMENTS

The authors wish to thank the Ministry of Education for the Research University Grant (Vot 08H29) and Universiti Teknologi Malaysia for the grant and facilities to complete the research.

REFERENCES

- [1] J. Ricardo, D.S. Lima, J.M. Quiben, C. Kuhn, T. Boyman, R. Thome, "Ammonia two-phase flow in horizontal smooth tube: Flow pattern observations, diabatic and adiabatic frictional pressure drops and assessment of prediction methods.", *Int. J. Heat Mass Transfer*, vol.52, pp. 2273-2288, 2009.
- [2] C. Aprea and A. Greco, "An Experimental evaluation of the greenhouse effect in R22 substitution", Original Research Article. *Energy Conversion and Management*, vol. 39 (9), 1 July, pp. 877-887, 1998.
- [3] F. Illan-Gomez, A. Lopez-Belchi, J.R. Garcia-Cascale, Vera-Garcia, "Experimental two-phase heat transfer coefficient and frictional pressure drop inside mini-channels during condensation with R1234yf and R134a", *Int. Journal of Refrigeration*, vol. 51, pp. 12-23, 2015.
- [4] Y. Xu, X.D. Fang, Z.G. Su, Z.R. Zhou, W. Chen, "Evaluation of frictional pressure drop correlations for two-phase flow in pipes", *Nuc.Eng. Des.*, vol. 253, pp. 86-9, 2012.
- [5] J. Nikuradse, 1933 Laws of flow in rough pipes. *VDI Forschungsheft*, 361. In translation, *NACA TM 1292*, 1950.
- [6] C.F. Colebrook C.F, White C.M 1937 Experiments with fluid friction in roughened pipes. *PROC. R. Soc. A.* 161,367-378.
- [7] D.I.H. Barr, "Solutions of the Colebrook-White function for resistance to uniform turbulent flow", *Proc. Inst Civil Engrs.*, Part 2 71 529, 1981.
- [8] S.E. Haaland, "Simple and explicit formulas for the friction-factor in turbulent pipe flow", *Trans, ASME, JFE* 105 89, 1989.
- [9] X.D. Fang, Y. Xu, Z.R. Zhou, "New correlations of single-phase friction factor for turbulent pipe flow and evaluation of existing single-phase friction factor correlations", *Nuc.Eng. Des.*, vol. 241, pp. 897-902, 2011.

- [10] M.G. Normah, .T. Oh, B.C. Nguyen, K.I. Chai, A. Robiah, "Comparison of the Optimized Thermal Performance of Square and Circular Ammonia-cooled Microchannel Heat Sink with Genetic Algorithm", *Energy Conversion and Management*, DOI:10.1016/j.enconman.2015.02.008, 2015.
- [11] W.H. McAdams, W.K. Wood, R.L. Bryan, "Vaporization inside horizontal tubes-II-benzene-oil mixtures", *Trans. ASME* vol. 66, pp. 671-684, 1942.
- [12] S.G. Kandlikar, "A model for predicting the two-phase flow boiling heat transfer coefficient in augmented tube and compact heat exchanger geometries", *Journal of Heat Transfer*, vol. 113 (1), pp. 966-972, 1991.
- [13] NistWebBook, from <http://webbook.nist.gov/chemistry/fluid/>
- [14] M.H. Maqbool, *Flow boiling of ammonia and propane in mini channels*, Doctoral Thesis, Royal Institute of Technology, Stockholm, Sweden, 2012.
- [15] A.S. Pamitran, K.I. Choi, K.I., J.T. Oh, Nasruddin, "Evaporation heat transfer coefficient in single circular small tubes for flow natural refrigerants of C₃H₈, NH₃, and CO₂", *International Journal of Multiphase Flow*, vol. 37, pp. 794-801, 2011.

Optimization of a single phase rectangular microchannel heat sink cooling system

Husain Zaidan^{1, a}, Normah Mohd Ghazali^{1, b*} and Robiah Ahmad^{2, c}

¹Faculty of Mechanical Engineering, University Technology Malaysia: 81310, Johor Bahru, Johor, Malaysia

²UTM Razak School of Engineering and Adv. Techn., University Technology Malaysia

54100 Jalan Semarak, Kuala Lumpur, Malaysia

^ahusain_zaidan2000@yahoo.com, ^{b*}normah@fkm.utm.my, ^crobiah@ic.utm.my

ABSTRACT

A simple thermal resistance network model is developed to optimize the overall thermal performance of a single layer rectangular water-cooled micro-channel heat sink made from silicon which has a very high thermal conductivity. The object of this optimization is the minimization of the overall thermal resistance, firstly in series and secondly in series and parallel. The thermal resistance consists of the conduction resistance, convection resistance and bulk resistance due to the bulk temperature rise of the coolant. The conduction resistance is normally a small part of the overall resistance. The heat sink under consideration has a width and length of $W \times L = 1\text{cm} \times 1\text{cm}$. The thickness of the base of the micro-channel is $H_{\text{sub}} = 100[\mu\text{m}]$, and the depth of the micro channel $H_c = 365[\mu\text{m}]$. In the current study, minimization of the overall thermal resistance of a micro-channel heat sink is carried out using genetic algorithm (GA). The fin thickness w_w and the channel width w_c are the optimized variables under a fixed coolant volume flow rate. Results obtained agreed well with previous experimental studies.

Keywords

Micro-channel heat sink, optimization, thermal resistance, genetic algorithm

1. INTRODUCTION

The design optimization technique for the micro-channel heat sink (MCHS) has been rapidly developing in the last decade. The most important developments were guided by micro electromechanical systems (MEMS), very large-scale integration (VLSI) technologies, and devices associated with micron miniaturization. These developments have resulted in a growing demand for higher dissipation of heat flux from electronic devices. The problem is started with the temperature rise caused by the electronic devices which strongly influences the performance of these devices. Researchers have developed the MCHS as a potential solution to this problem. Research in this field was aimed at fabrication of an economically competitive system of micro channels having a high surface area to volume ratio for better

capabilities compared to the conventional cooling techniques to meet these requirements. The developments in this field started back in 1981 with Tuckerman and Pease [1] who worked experimentally on a single layer MCHS by mounting the single layer onto the back of a silicon wafer. They fabricated the MCHS with a 50 [μm] width and a 300 [μm] height. They discovered that the heat flux removable was at 790 [W/cm^2] and the maximum temperature difference between the substrate and inlet water at less than 71 [K] with the pressure drop at 31 [Pa], across the micro channels. In 1984, a second wave of a series of research groups had worked on modifying the introductory work of [1]. Goldberg [2] constructed and tested three air cooled MCHS with different fin thickness. The ratio, $W_{\text{fin}}/W_{\text{ch}}$, is normalized to unity and the air flow is restricted to laminar at 30[L/min]. The findings have shown that the design with the largest pressure drop and smallest channel width yields the smallest thermal resistance. Along with Goldberg, Mahalingam [3], constructed a MCHS using water and by attaching the channels to a square silicon substrate of 5 cm on the side. With a flux of 1100 [W], the thermal resistance yield of 0.03 [$^{\circ}\text{C}/\text{W}$] and 0.020 [$^{\circ}\text{C}/\text{W}$] were studied for flow rates of 12 [cm^3/s] and 63 [cm^3/s], respectively. The series of experimental work in 1981-1986 was followed by the first attempt of optimization conducted by Sasaki and Kishimoto [4] who optimized the channel dimensions of a finned heat sink constructed on a silicon chip for a given pressure drop. The developments were continued to include analytical and modelling approach. Samalam [5], established a quasi-two-dimensional differential equation to model the performance of a water-cooled silicon MCHS based on the assumption of a laminar flow. In 1990, Phillips [6] designed a system using water with both laminar and turbulent flow regimes at which fully developed scheme was achieved. In 1991, the first trial of computational techniques was carried out by Landram [7], who identified optimal configurations of heat sinks by using a computational scheme and thus the temperature profiles for the cooling fluid and the conductive heat sink were simultaneously determined. Knight *et al.* [8] later reported that at the optimal configuration, the thermal resistance for the Tuckerman and Pease device [1] could be reduced by 35% if turbulent flow is allowed. However, the required pumping power is almost five times

higher. The analytical work has led to very promising results regarding the heat flux, the pressure drop, and the temperature difference, and was compared to the work by [1, 2]. An advance step was carried out by Knight *et al.* [9], by extending their previous comparative study to include more studies to the work done by [1,2] and [6], introducing a non-dimensional thermal resistance model to determine the optimum design parameters for heat sinks. Another comparison was performed by Weisberg *et al.* [10], they analyzed the heat exchangers by solving numerically a conjugate heat transfer problem consisting of the simultaneous determination of the temperature fields in both the solid substrate and the fluid. A more advanced approach was done by Kim and Kim [11] who introduced a new MCHS by working on a porous medium model in which the pores could be considered as natural microchannel with a cylindrical shape departing from the conventional geometrical shapes [11]. The analytical solutions were obtained based on the modified Darcy model for fluid flow and the two equation model for heat transfer, their results of the thermal resistance compared with previous studies of [1] and [2].

More advanced studies with optimization by Shao *et al.* [12, 13] have shown that the heat flux of chip was found to be $278 \text{ [W/cm}^2\text{]}$ while the highest temperature in the chip could be kept below $42\text{[}^\circ\text{C]}$. More recent optimization studies have started in 2012 by Adham *et al.* [14] where potential improvement in the overall performance of a rectangular MCHS showed can be achieved with ammonia gas, the first time in this field. Using a multi-objective general optimization scheme with the thermal resistance model as an analysis method in combination with a nondominated sorting genetic algorithm (NSGA), it was found that a significant reduction in the total thermal resistance up to 34 % is attainable for an ammonia-cooled MCHS compared to an air-cooled MCHS under the same operating conditions. A very recent study by Adham *et al.* [15] utilized actual experimental data to look at the thermo hydrodynamic performance of liquid ammonia. The results show the potential of the powerful and possibly necessary combination of experimental data and analytical optimization scheme such as MOGA (multi objective genetic algorithm) to identify optimized parameters when there are conflicting multiobjectives such as the thermal resistance and pumping power.

Most previous work discussed which involved the thermal resistance model excluded the resistance due to the microchannel wall conduction and convection, assuming that with thin walls these resistances are negligible. In the current study, the thermal resistance network model is used to compare the outcomes when the wall resistance is included or neglected. With a constant heat flux, thermal resistance of a single layer MCHS is modelled; the resistances are in series for the analysis without the wall resistance and in series as well as in parallel to include the contribution of the wall resistance.

2. THERMAL RESISTANCE MODEL

A schematic of the single layer rectangular MCHS in the current study is shown in figure 1.

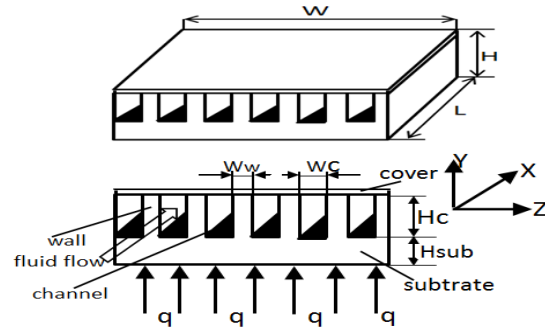


Figure 1: Schematic of a single layer rectangular MCHS.

A typical microchannel heat sinks consist of a substrate made from a material with a high level of thermal conductivity with several microchannels attached to each other on top of the substrate, here assumed to be silicon. To reserve the coolant flow, an adiabatic plate covers the top of the heat sinks. In this study, the heat flux generated by the electronic device was assumed uniformly applied on the heat sink bottom of the substrate and the coolant was assumed to enter the microchannel and flows parallel to the x -axis, parallel to the length of the micro channel (L); coolant passes through the micro channel and takes the heat away. The top surface ($y = H$) is insulated and adiabatic,

$$-k_s \left. \frac{dT}{dy} \right|_{y=0} = q_w \quad \text{and} \quad k_s \left. \frac{dT}{dy} \right|_{y=H} = 0$$

The dimensions of the heat sink under consideration are $W \times L = 1\text{cm} \times 1\text{cm}$. The thickness of the base of the micro-channel heat sink is H_{sub} , and the depth of the micro channel, H_c are kept constant. The channel width is w_c and separated by the wall width, w_w from the neighbouring channels; these parameters are the geometric parameters that influence the performance of a MCHS, selected to be optimized. The flow is assumed to be laminar and fully developed and is maintained by a fixed flow rate. Since the focus of the study is to optimize the micro channel geometry using genetic algorithm (GA), the results were compared against the experimental results of Tuckerman and Pease [1], which used water as the working fluid. The thermophysical properties of the working fluid are assumed to be constant at the reference temperature of 27°C . The computational zone which represents a half channel and half wall is shown in figure 2.

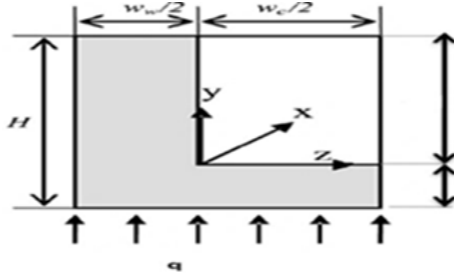


Figure 2: Schematic of computational cross-section

In the thermal resistance model where the channel walls are treated as fins, the heat transferred from the chip to the coolant refers to the three components, the conductive, convective and caloric fluid resistances heat transfer. The conductive thermal resistance, R_{cond} , is due to conduction through the substrate between the chip surface and micro channel base plane, defined as:

$$R_{cond} = \frac{t}{K_s A_{hs}} \quad (1)$$

Where $t = H_{sub}$, thickness of substrate, and A_{hs} is the area of the base of the heat sink. Upon simplification gives:

$$R_{cond} = \frac{t}{K_s LW} \quad (2)$$

Since the thickness of the substrate is fixed, R_{cond} is a constant. The convective thermal resistance, R_{conv} , is due to convection from the heat sink to the coolant, defined as:

$$R_{conv} = \frac{1}{h_{eff} A_{eff}} \quad (3)$$

where A_{eff} is the total effective area for the fin and h_{av} is the average convective heat transfer coefficient:

$$A_{eff} = nL (w_c + 2\eta H_c) \quad (4)$$

and

$$h_{av} = \frac{Nu K_f}{D_h} \quad (5)$$

The term n is the number of channels, $n = \frac{W}{W_w + W_c}$, and η is the efficiency of the fin, D_h the hydraulic diameter, K_f the fluid thermal conductivity, and Nu the Nusselt number. Nu can be expressed with [11]:

$$Nu = 2.253 + 8.164 \left(\frac{\alpha}{\alpha + 1} \right)^{1.5},$$

with

$$\alpha = \frac{h_c}{w_c}; \beta = W_w / W_c \quad (6)$$

Simplifying equation (3) gives:

$$R_{conv} = \frac{1}{h_{av} nL (w_c + 2\eta H_c)} \quad (7)$$

The caloric (capacitive) thermal resistance or fluid resistance is the resistance between the entrance and the exit of the MCHS, expressed as:

$$R_{fluid} = \frac{1}{\rho_f C_p G} \quad (8)$$

where ρ_f is the density of the fluid, C_p the specific heat and G is the volume flow rate. For laminar flow, the Reynolds number, $Re = \frac{\rho V D}{\mu} < 2300$. Two cases are investigated in this study. The first ignored the thermal resistance due to the presence of the thin walls of the micro channels (Model 1), whilst the second takes the wall resistance into consideration (Model 2).

Model 1:

For model 1, the schematic thermal resistance is shown in figure 3 where the resistances are in series.

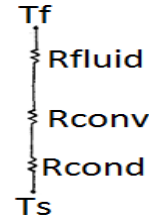


Figure 3: schematic thermal resistance in series

The thermal resistance due to the base is not included because it is the same for both models and the purpose of the present analysis is to look at the contribution of the resistance with and without the wall thermal resistance. The total thermal resistance for the serial model is:

$$R_{tot} = R_{cond} + R_{conv} + R_{fluid} \quad (9)$$

Since R_{cond} is a constant, the total thermal resistance of the single layer MCHS shown in figure 1 can be expressed by:

$$R_{tot} = R_{conv} + R_{fluid} \quad (10)$$

$$R_{tot} = \frac{1}{h_{av} nL (w_c + 2\eta H_c)} + \frac{1}{\rho_f C_p G} \quad (11)$$

Model 2:

The thermal resistance of the single layer is modelled as shown in figure 4. The modelling is described by a network of thermal resistances connected in series, parallel, and combination.

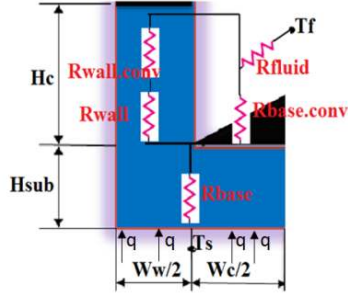


Figure 4: Series and parallel resistance network

Thus, the total thermal resistance of a half microchannel and wall “ R_{total} ” is solved below using a combination of series and parallel resistances:

$$R_{total} = R_{base} + \left(\frac{(R_{wall} + R_{wall.conv}) \times R_{base.conv}}{R_{wall} + R_{wall.conv} + R_{base.conv}} \right) + R_{fluid} \quad (12)$$

The thermophysical properties in the optimization process are listed in Table 1. Table 2 lists the dimensions used in this study and those from [1] and [8]. GA is then utilized to optimize the total thermal resistance for both models investigated.

Table 1: dimensions and thermophysical properties heatsink and coolant

Dimensions and properties	Values
Heat sink length ,L (m)	1×10^{-2}
Heat sink width ,W (m)	1×10^{-2}
Microchannel height, H_c (m)	5×10^{-4}
Material thermal conductivity (Si), k_{sil} (W/m ² °C)	148
Coolant thermal conductivity (water), k_w (W/m ² °C)	0.613
Density of the coolant , ρ (kg/m ³)	997
Dynamic viscosity of the coolant , μ (kg/m s)	8.55×10^{-4}
Flow rate, G (m ³ /s)	11
Specific heat of the coolant, c_p (J/Kg ² °C)	4179
Prandtl number, dimensionless, $Pr = \mu_f c_{p_f} / k_w$	5.83
Thickness of the substrate, H_{sub} (m)	1×10^{-4}
physical and engineering parameters for water , (°C)	27

The thickness of the MCHS base, $H_{sub} = 100 [\mu m]$ and the depth of the microchannel, $H_c = 365 [\mu m]$, are kept

constant during optimization. The channel width and wall are the design variables expressed as x_1 , x_2 respectively.

Table 2. Dimensions in the present study, [1,] and [8]

groups	Dimensionles	uckerman & Pease	nigh 1991	resent tudy
L(cm)	Heat sink length,		ame	ame
Heat sink width,W(cm)			ame	ame
Δp ,[kPa]	pressure drop,	06.8	ame	ame
Coolant		ater	ame	ame
Fin efficiency, η_f		.76	ame	ame
Fin Material		ilicon	ame	ame
Fin to channel thickness ratio, β			nrestricted	ame
Nusselt Number			nrestricted	nrestricted
Type of flow		aminar	ame	ame

3. GENETIC ALGORITHM (GA)

The main objective of this study is the minimization of the overall thermal resistance, $f_1(x)$, carried out using GA as an optimization tool. The upper and lower limits of the design variables are:

$$\begin{aligned} \text{Find } & x \\ \text{min } & F(x) = \min f_1(x) \\ & 5.7 \times 10^{-5} \leq x_1 \leq 10 \times 10^{-2} \\ & 5.7 \times 10^{-5} \leq x_2 \leq 10 \times 10^{-2} \end{aligned}$$

The design space is given in Table 3, the total thermal resistance, R_{total} is optimized to find the associated design variables using GA of MATLAB R2013a, as a single objective, $f_1(x)$.

Table 3: design variables limits

Design variable	Lower[m]	Upper[m]
w_c	5.7×10^{-5}	10×10^{-2}
w_w	5.7×10^{-5}	10×10^{-2}

The main data structures in the GA Toolbox are chromosomes, objective function values and fitness values. GA uses three main types of rules at each step to create the next generation from the current population. Selection rules select the individuals called parents that contribute to the population at the next generation, Crossover rules combine two parents to form children for the next generation and mutation rules apply random changes to individual parents to form children. The flow chart of the Genetic Algorithms shown in figure 5.

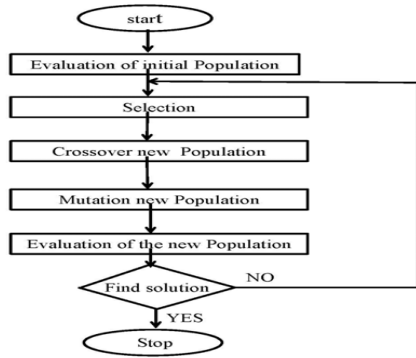


Figure 5: Flow chart Genetic Algorithms

4. RESULTS AND DISCUSSION

Comparison of the solutions obtained for Model 1 and Model 2 in the present study in the MCHS investigated against that of previous work is shown in Table 4. In previous studies of [1] and [8], the pressure drop across the inlet and exit of the micro channel is fixed at 206.8 [kPa], ($\beta = w_w/w_c = 1$), and ($\alpha = H_c/w_c = 6.4$) for a fully developed flow with a fixed Nusselt number ($N_u = 6$). The optimization here has managed a reduction in thermal resistance of 64% of that of [1] for Model 1 and 34% reduction for Model 2 with an almost equivalent pumping power requirement, this for the same flow rate. Inclusion of the resistances due to the walls raised the total resistance by 1.5 times compared to that without. This is quite significant if many MCHS units are combined for applications in VLSI systems.

Table 4: Comparison of present results and [1] and [8]

CALCULATED RESULTS	Tuckerman and Pease[1]	Knight 1991[8]	Present Study	
			Model 1	Model 2
n , of channels	88	83	88	88
Depth, H_c , [μm]	365	357	365	365
w_c , [μm]	57	60	57	57
w_w , [μm]	57	61	57	57
Reynolds Number	730	834	693	693
Flow Rate [cm^3/s]	11	12.4	11	11
Aspect Ratio, α	6.4	5.8	6.4	6.4
Nusselt Number	6	5.9	8	8
Pressure drop, Δp [kpa]	206.8	same	209	209
Pumping power, [W]	2.27	2.5	2.3032	2.30
Capacity Thermal Res, [$^{\circ}\text{C}/\text{W}$]	0.022	0.019	0.0109	0.010
Convective Thermal Res[$^{\circ}\text{C}/\text{W}$]	0.064	0.058	0.0264	0.053
Total Thermal Resistance, [$^{\circ}\text{C}/\text{W}$]	0.086	0.077	0.0306	0.057
Reduction in Thermal Resistance, ΔR		10.5%	64.41%	33.72%

These optimized outcomes indicate the ceiling for the possible highest level performance achievable if manufacturing technology can handle the fabrication specifically. And other losses are overcome.

Figure 6 and Figure 7, show that the thermal resistance for both models reaches a minimum after a small number of generation despite the change in the test, the behaviour confirmed that the optimization performer reach its optimum value in a short time. The GA parameters used to attain the presented outcomes are given in Table 5.

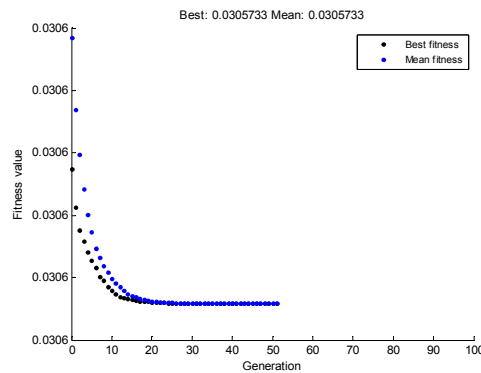


Figure 6. Best and mean values of the fitness function for

Model 1

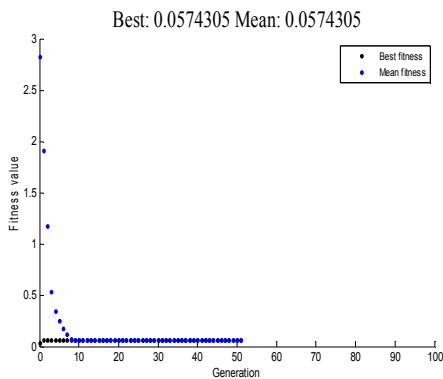


Figure 7. Best and mean values of the fitness function

Table 5. Genetic Algorithm Parameter

Parameters	Values
Fitness function	@single layer
Number of variables	2
Population type	Double vector
Population size	100
Creation function	uniform
Fitness function	Rank
Selection function	Roulette
Crossover function	0.7
Mutation function	Constraint dependent
Crossover fraction	Heuristic

5. CONCLUSION

The one-dimensional thermal resistance model for a MCHS has been aligned with the results from previous studies. The results are in agreement with the landmark experimental studies of Tuckerman and Pease [1] and that of Knight [8]. A significant reduction of the thermal resistance can be obtained under optimized conditions. The optimized thermal resistance obtained in this study is reduced by 35% from that of [1].

ACKNOWLEDGEMENT

The authors wish to thank Universiti Teknologi Malaysia for the facilities to complete the research.

REFERENCES

- [1] D. B. Tuckerman and R.F.W. Pease, "High-performance heat sinking for VLSI", IEEE Electron Device Letters, Vol. EDL-2, No. 5, pp. 126-9, 1981.
- [2] N. Goldberg, "Narrow channel forced air heat sink" IEEE Trans. Comp. Hybrids Manuf. Technol., vol. CHMT-7, pp.

- 154-159, Mar. 1984.
- [3] M. Mahalingam, "Thermal management in semiconductor device packaging," Proc. IEEE, vol. 73, pp. 1396-1404, Sept. 1985.
- [4] S. Sasaki and T. Kishimoto, "Optimal structure for micro-grooved cooling fin for high-power LSI devices," Electron. Lett. vol. 22, no. 25, pp. 1332-1334, 1986.
- [5] V.K Samalam, "Convective Heat Transfer in microchannels", Journal of Electronic Materials, Vol. 18, No. 5, 1989.
- [6] R. J. Phillips, "Micro-channel heat sinks," Advances in Thermal Modelling of Electronic Components and Systems, Volume 2. A. Bar-Cohen and A. D. Kraus, eds. New York: ASME, Ch. 3, 1990.
- [7] C. S. Landram, "Computational model for optimizing longitudinal fin heat transfer in laminar internal flows," Heat Transfer in Electron Equipment, vol. 171, pp. 127-134, 1991.
- [8] R. W. Knight, J. S. Gooding and D. J. Hall, "Optimal thermal design of forced convection heat sinks - analytical", Journal of Electronic Packaging, Vol. 113, No.3, pp 313-321, 1991.
- [9] R. W. Knight, D. J. Hall, S.J.Goodling, and Richard C. Jaeger, "Heat Sink Os, ptimization with Application to Microchannels", IEEE Trans. on Components, Hybrids, and Manufacturing Technology, vol. 15, No.5, 1992.
- [10] A. Weisberg, and H. H Bau, "Analysis of microchannels for integrated cooling" Int.J.heat mass transfer. Vol.35. No. 10, pp.2 465-2474, 1992.
- [11] J. Kim and D. Kim "Forced convection in microstructures for electronic equipment cooling", Journal of Heat Transfer ,Transacion of the ASME, Vol.121, pp639-645, 1999.
- [12] B.D. Shao, Z.W. Sun, and L.F. Wang, "Optimization design of micro channel cooling heat sink", International Journal of Numerical Methods for Heat & Fluid Flow, Vol. 17 No. 6, pp. 628-37, 2007.
- [13] B.D. Shao, L.F Wang, Li. Jianyun and Z.W. Sun, "Application of thermal resistance network model in optimization design of micro-channel cooling heat sink", International Journal of Numerical Methods for Heat Fluid Flow, Vol. 19 No. 3, pp. 535-45, 2009.
- [14] A.M. Adham, M.G. Normah and A. Robiah, "Optimization of an ammonia-cooled rectangular microchannel heat sink using multi-objective non-dominated sorting genetic algorithm (NSGA2)", Heat Mass Transfer (48), pp.1723-1733, 2012.
- [15] A.M. Adham, M.G. Normah and A. Robiah, "Multiobjective Optimization of Microchannels with Experimental Convective Heat Transfer Coefficient of Liquid Ammonia", Springer Inter. Publishing Switzerland IEA/AIE 2014, Part I, LNAI 8481, pp. 470-478, 2014.

Two-Phase Frictional Pressure Drop Minimization in the Laminar-Laminar Region of a Mini-channel

ShazwanFitriRazali^a, NormahMohd-Ghazali^a, RobiahAhmad^b, HishamuddinJamaludin^a

^aFac. of Mech. Engineering, UniversitiTeknologi Malaysia, 81310 Skudai, Johor, Malaysia
Tel: (60)75534577. Fax: (60)75566159
normahghazali@utm.my

^bUTMRazak School of Engineering & Advanced Tech., UTM Kuala Lumpur, Malaysia

ABSTRACT

The decreasing in sizes of heat exchanging devices is challenging the study of the performance of these refrigerants due to their differential behavior in small channels. This paper reports the study into the minimization of the two-phase pressure drop in the laminar-laminar region of a 1.5 mm minichannel. Four refrigerants were investigated at the saturation temperature of 10 °C; R22, R134a, CO₂, and R290, the latter two are natural refrigerants being considered as potentials to replacing R22 and R134a. Genetic algorithm (GA), a fast random search tool, is utilized to simultaneously minimize the frictional pressure drop and the Lockhart-Martinelli parameter, with the Chisolm constant, under optimized mass flux and vapor quality conditions. The optimization outcomes showed that CO₂ has the lowest frictional pressure drop in the low mass flux and quality region compared to R22 and R134a. Meanwhile, the optimized frictional pressure drop at the mass flux of 50 kg/m²s for R290 is 23% higher than that of R22 and 15% higher than that of R134a. The predicted minimized frictional pressure drop with GA shows promise in assisting researchers in the exploration of new refrigerants and their capabilities.

Keywords:

Natural refrigerants, two phase, frictional pressure drop, optimization.

1. INTRODUCTION

Since the Montreal Protocol [1], researchers have continuously looked for alternative refrigerants with a performance compatible with the current environmentally hazardous coolants generally in use in the air-conditioning and refrigeration industry. Global concerns over our environment together with the advancement of miniaturized heat exchangers have focused researchers' attention towards two-phase behavior of natural refrigerant applications in small channels. The advantages of large surface to volume ratio for higher heat removal, lower refrigerant charge, and higher heat transfer coefficients have made the mini/micro-channels desirable. However, experimental studies completed on correlations to predict the flow pattern that have been developed based on previous

experiments have shown a high degree of disagreements [2,3]. This is probably due to the different conditions of the parameters and various flow regimes applied to numerous newly developed refrigerants. This paper compares the results of the frictional pressure drop values of four refrigerants such as R-22, R134A, Propane (C₃H₈), and Carbon Dioxide (CO₂). Latest investigations show that natural refrigerants C₃H₈ and CO₂ are now being considered as an ultimate replacement to the hazardous R22 and R134A [4-6].

Genetic algorithm (GA) has proven to be a successful optimization method in dealing with different scopes of fields such as transportation, design and medicine [7]. The last couple of years have shown that GA has accomplished the optimization of conflicting objectives for single phase flows in micro-channels [8-11]. This study is part of a research project investigating the applicability of GA in minimizing the frictional pressure drop of two-phase flow in small channels. This paper reports the part of the optimization study completed assuming the separated flow model, that each of the liquid and vapor phase has its own velocity. A similar optimization work has been reported with the simpler homogeneous model using R290 [12] and results have been promising, showing the patterns as observed experimentally. It is hoped that the outcomes of the project can assist the refrigeration and the air-conditioning research community in identifying among potential coolants to replace the current R22 and R134A.

2. THEORY

The gravitational, acceleration, and frictional pressure drop contribute towards the total pressure drop. The frictional pressure drop in small mini-channels is considerably higher than that in the macrochannels. It is generally determined by using either one of the models; the homogeneous model or the separated model. In the homogeneous model, the two phases of liquid and vapour are assumed to move with the same velocity and act as a single phase considering the properties such as the density, viscosity and others. The separated flow model assumes that each phase behave as a separate entity, moving at different velocities. This model is further sub-divided into two categories based on the two-phase friction multiplier, ϕ . In this study the frictional pressure drop of the separated model

proposed by Lockhart and Martinelli and modified by Chisolm is used,

$$\left(\frac{\Delta P}{\Delta L}\right)_{TF} = \left(1 + \frac{C}{X} + \frac{1}{X^2}\right) \frac{(2f_f G^2 (1-x)^2)}{(\rho_f D)} \quad (1)$$

where G , ρ , D , and x are the mass flux, density, channel diameter, and vapor quality respectively. The subscript f stands for the liquid phase. The value of C is 5 for a condition of laminar-laminar flow as proposed by Chisolm [13] and the friction factor, f , is based on the Darcy's equation [14], given by,

$$f = \begin{cases} 16/Re, & Re < 2300 \\ 0.079Re^{-0.225}, & Re > 3000 \end{cases} \quad (2)$$

For the Reynolds number, Re , less than 2300, the flow is considered laminar while $Re > 3000$ is for turbulent condition. The Reynolds number for the liquid and vapor phase is determined differently,

$$Re_v = \left(\frac{Gx D}{\mu_v}\right) \quad (3)$$

for the vapor phase and

$$Re_l = \left(\frac{G(1-x)D}{\mu_l}\right) \quad (4)$$

for the liquid phase. The term X appearing in equation (1) is the Lockhart-Martinelli parameter given by,

$$X = \left[\frac{f_f}{f_g}\right]^{\frac{1}{2}} \left(\frac{1-x}{x}\right) \left(\frac{\rho_g}{\rho_f}\right)^{\frac{1}{2}} \quad (5)$$

The physical properties for each refrigerant are taken from NIST [15] at the saturation temperature of 10 °C. This is shown in Table 1.

Table 1: Physical properties of R-22, C₃H₈, R-134a and CO₂ at T_{sat} of 10 °C

Refrigerants	P, MPa	ρ_f , kg/m ³	ρ_g , kg/m ³	μ_f , 10 ⁻⁶ Pa·s	μ_g , 10 ⁻⁶ Pa·s
R22	0.68	1247	28.82	195.7	11.96
C ₃ H ₈	0.64	514.7	13.78	113.35	7.75
R134A	0.42	1261	20.23	234.87	11.09
CO ₂	4.50	861.1	135.2	82.56	16.06

Initial study of equations (1) and (5) indicates that each increases and decreases, respectively, as the vapour quality increases. As the two-phase flow develops with more liquid evaporating, higher heat transfer is expected due to the latent heat but at the expense of a higher frictional pressure drop. However, a total dry-out is undesirable. This is where the present research comes in, looking at parameters that could be controlled

to attain high vapour quality at low frictional pressure drop. Due to the opposite effects that equations (1) and (5) have on the vapour quality, they are suitable to be optimized with genetic algorithm (GA). The two equations are selected as the objective functions to be simultaneously minimized; the frictional pressure drop and the Lockhart-Martinelli parameter.

3. METHODOLOGY

A Genetic Algorithm (GA) double optimization approach using MATLAB toolbox [16] is utilized for the optimization of parameters to get the optimized pressure drop values for different refrigerants. The parameters and equations are typed as a code in MATLAB and executed in the MATLAB software. Two objectives are used in GA for the optimization. The first objective is the frictional pressure drop of equation (1) and the second objective is the Lockhart-Martinelli parameter, X of equation (5). The condition for laminar-laminar flow is used for the inputs at the saturation temperature of 10 °C for all refrigerants. The inner diameter of the smooth mini-channel is fixed at 1.5 mm while the mass flux, G , and vapor quality, x , is varied. The input conditions are shown in Table 2. Note that different range for the vapor quality had to be set so that the flow remains in the laminar-laminar region for this separated model, slightly more complex than the homogenous approach. Other than that, conditions for all refrigerants are the same for comparison purposes.

Table 2: Input parameters of the optimization

Laminar-laminar flow (Chisolm, $C = 5$)				
Range	R22	C ₃ H ₈	CO ₂	R134A
G (kg/m·s)	50 -150	50 -150	50 -130	50 -150
Quality	0.01 – 0.3	0.005 – 0.3	0.0005 – 0.00	0.005 – 0.3

4. RESULTS AND DISCUSSION

The Pareto front of the comparison between all refrigerants investigated is shown in Fig 1. The graph shows sets of solutions for both the optimized Lockhart-Martinelli parameter and the frictional pressure drop. Except for CO₂, the other refrigerants seem to have similar number of solutions under optimized conditions. The lowest frictional pressure drop is obtained for CO₂, followed by R-22, R-134A, C₃H₈. The optimized condition for CO₂ is at the lower end of the frictional pressure drop while the rest operates at 200 Pa/m and above. The Lockhart-Martinelli parameter is related to the vapor quality; it is zero at saturated vapor and largest at saturated liquid. The ratio of the vapor to liquid density for R22, R134A and C₃H₈ is of the same order of magnitude whilst that of CO₂ is 10% higher than that of R22. This is probably

the reason that the behavior of CO₂ observed here is different at any X .

The graphs of frictional pressure drop versus mass flux and quality are presented in Fig 2 and Fig 3. Most of the optimized mass flux is at 50 kg/m²s with CO₂ having the lowest pressure drop at this mass flux. The preset range for the vapor quality for CO₂ is much lower than the other refrigerants to have it operates under the laminar-laminar condition, its optimized condition is at the lower range. At higher vapor quality, C₃H₈ has a wide range of optimized mass flux operations but at the expense of increasing frictional pressure drop. This means that for C₃H₈, optimized operations at higher mass flux is possible if one is not concerned about the pumping power requirements to handle the higher pressure drop. Fig 3 shows the expected trend of increasing frictional pressure drop with increasing vapor quality. At any instant of a

particular quality, the frictional pressure drop is highest for propane and lowest for R22. As more vapors are formed, propane shows a larger drop in pressure. From these figures, it is not surprising that R134A is currently the short-term solution to R22 since its characteristic seems to be similar to R22.

Fig 4 shows a clearer relationship between the frictional pressure drop, quality, and mass flux for the particular refrigerant, CO₂. Note that the outcomes do not consider the system requirements with different refrigerants used. The study only examines their hydrodynamic behavior through comparisons of frictional losses during two-phase development under laminar-laminar conditions. This is important when new refrigerants are being explored and initial investigations into their performance, hydrodynamic or thermal, must be done prior to system requirement analysis.

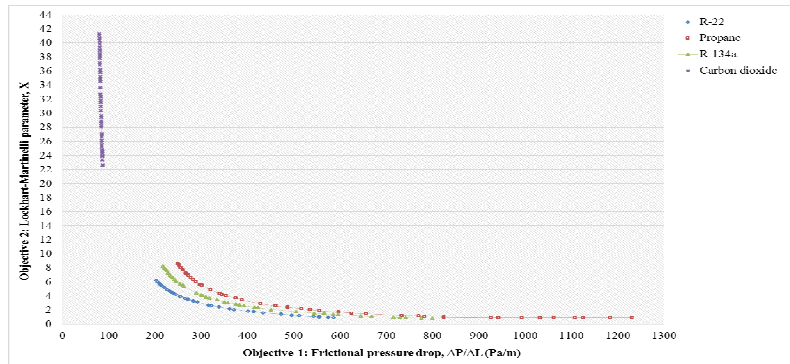


Figure 1: Pareto front of the double objective optimization

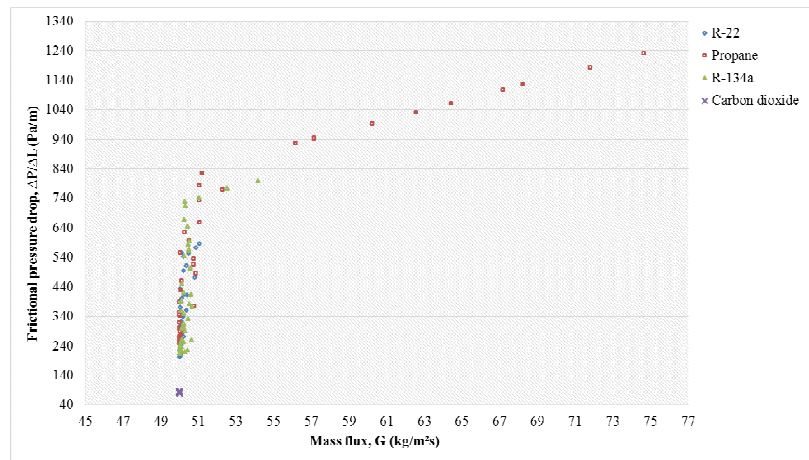


Figure 2: Frictional pressure drop versus mass flux

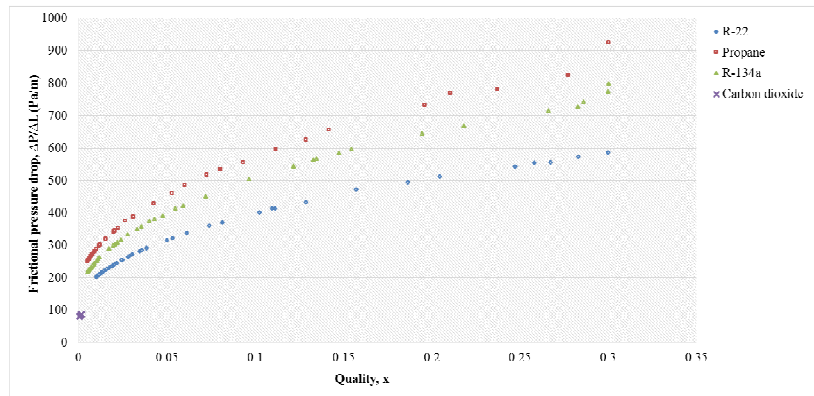


Figure 3: Frictional pressure drop versus quality

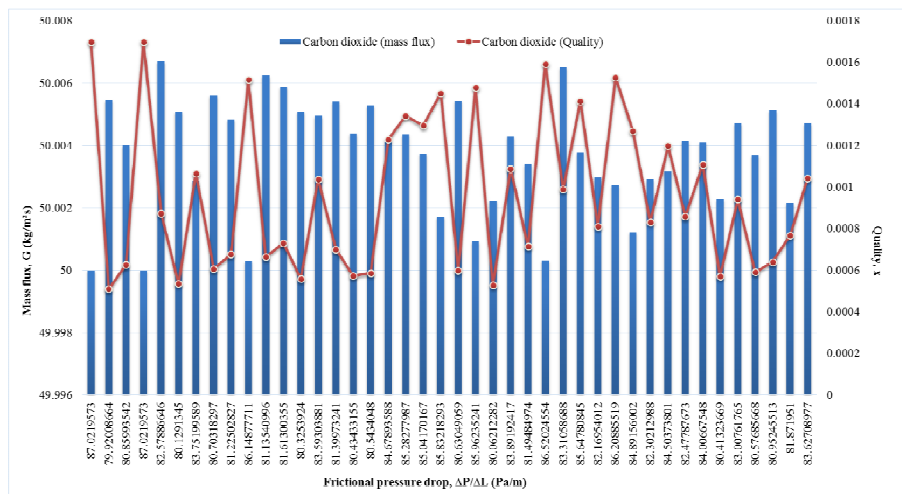


Figure 4: Mass flux and quality versus frictional pressure drop for CO₂.

5. CONCLUSION

Simultaneous optimization of the Lockhart-Martinelli parameter and frictional pressure drop has been completed on refrigerants R22 and R134A with their potential replacements, natural refrigerants C₃H₈ and CO₂. The outcomes showed the expected trend, that the frictional pressure drop increases with increasing mass flux and quality. The separated model under laminar-laminar conditions showed that CO₂ has the lowest frictional pressure drop under optimized conditions of mass flux and vapor quality. C₃H₈ may also be considered looking at its behavior here in comparison with R134A.

ACKNOWLEDGEMENT

The authors wish to thank the Research University Grant (GUP) 08H29 and Universiti Teknologi Malaysia for the funding and facilities to complete the research.

REFERENCES

[1] The Montreal protocol on substance that deplete the Ozone layer, 2000, <http://www.unep.orag/ozone>.
 [2] Y. Xu, X. Fang, X. Su, Z. Zhou, W. Chen, "Evaluation of frictional pressure drop correlations for two-phase flow in

pipes," *Nuclear Engineering and Design*, Vol. 253, pp. 86– 97, 2012.

[3] S.M. Kim and I.Mudawar, "Universal approach to predicting two-phase frictional pressure drop for mini/micro-channel saturated flow boiling", *International J. Of Heat and Mass Transfer*, vol. 58 pp. 718-734, 2013.

[4] A.S. Pamitran, K.I. Choi, J.T. Oh, P. Hrnjak, "Characteristics of two-phase flow pattern transitions and pressure drop of five refrigerants in horizontal circular small tubes", *International Journal of Refrigeration*, pp. 578-588, 2010.

[5] A.S. Pamitran, K.I. Choi, J.T. Oh, Nasruddin, "Evaporation heat transfer coefficient in single circular small tubes for flow natural refrigerants of C3H8, NH3, and CO2", *International Journal of Multiphase flow*, vol. 37 pp. 794-801, 2011.

[6] M.H. Maqbool, "Flow boiling of ammonia and propane in mini channels", *Energy Technology*, KTH industrial engineering and management: Stockholm, Sweden, pp. 107, 2012.

[7] P.R. Srivastava and T.H. Kim, "Application of Genetic Algorithm in Software Testing", *International Journal of Software Engineering and Its Applications*, vol. 3, pp. 87-96, 2009.

[8] A.M. Adham, N. Mohd-Ghazali, R.Ahmad, "Performance optimization of a microchannel heat sink using the Improved Strength Pareto Evolutionary Algorithm (SPEA2)", *J. of Engineering Thermophysics*, Vol. 24 (1) pp. 86-100, 2015.

[9] N. Mohd-Ghazali, J.T. Oh, B.C. Nguyen, K.I. Choi, R. Ahmad, "Comparison of the Optimized Thermal Performance of Square and Circular Ammonia-cooled Microchannel Heat Sink

with Genetic Algorithm”, *Energy Conversion and Management*, DOI:10.1016/j.enconman.2015.02.008,2015.

[10]N. Mohd-Ghazali, J.T. Oh, B.C. Nguyen, K.I. Choi, N.A. Zolpakar, R. Ahmad,“Multi Objective Optimization of Microchannels with Experimental Convective Heat Transfer Coefficient of Ammonia”, *Modern Advances in Applied Intelligence: Lecture Notes in Computer Science*, Vol. 8481, pp. 470-478, 2014.

[11]A.M. Adham, N. Mohd-Ghazali, R.Ahmad,“Optimization of an ammonia-cooled rectangular microchannel heat sink using multi-objective non dominated sorting genetic algorithm (NSGA2)”, *Heat and Mass Transfer*, vol. 48 (10), pp.1723-1733,2012.

[12]N.Mohd-Ghazali, A.S. Pamitran, S.Novianto, U.Khabibah, M.I. Alhamid, “Prediction of the optimized frictional pressure drop in a two-phase flow small-channel with genetic algorithm”, *Energy Procedia*, vol. 75, pp. 1431-1435, 2015.

[13]D. Chisholm, A theoretical basis for the Lockhart-Martinelli Correlation for Two-phase flow. *International Journal of Heat and Mass Transfer*, 10, 1997.

[14]C.Y. Yang, T.Y. Lin, Heat transfer characteristics of water flow in micro tubes. *Journal of Experimental Thermal and Fluid Science*, 32: pp. 432-439, 2007.

[15]<http://webbook.nist.gov/chemistry/>

[16] Matlab 2012a

The Effect of Bio-Based Additives on Engine Performance and Emissions of Petrol and Diesel Engine

Mohamad Ihsan Ahmad Zainuri^a, Zulkarnain Abdul Latiff^b,
Mohd Farid Muhamad Said^c, Azhar Abdul Aziz^d, Mohd Rozi Mohd Perang^e

Automotive Development Centre (ADC)
Faculty of Mechanical Engineering
Universiti Teknologi Malaysia
81310 Johor Bahru, Malaysia
Tel : (607) 5535447. Fax : (607) 5557097

^aihsanznr@gmail.com, ^bzulkarnain@fkm.utm.my, ^cmfarid@fkm.utm.my, ^dazhar@fkm.utm.my, ^erozi@fkm.utm.my

ABSTRACT

Fuel additives are additives that are added to fuel in small quantities to give improvement in terms of engine performance and emissions. Aftermarket fuel additives can be divided into two, chemical-based and bio-based. In this project, the effect of bio-based fuel additives on engine performance and exhaust emissions of a petrol and diesel engine is studied. The blending ratio is developed based on the instruction given on the bottle of the additives. The ratio of the fuel additives used for Vivo Racing (VR) is between 0.21% and 0.25%, Vivo Flawless (VF) is between 0.10% and 0.14% and Diesel Energy is between 0.14% and 0.18%. Constant throttle test had been done on both petrol and diesel engine. The results show that the fuel additives reduce brake power and brake specific fuel consumption while increasing brake thermal efficiency and reducing exhaust emissions. For brake power, VR0.24 is the best. For brake specific fuel consumption, the best are VR0.23 and VF0.11 for petrol and diesel engine respectively. For brake thermal efficiency, the best are VR0.24 and DE0.17. For HC composition, the lowest are VR0.25 and DE0.17. For CO composition, VR0.22 and DE0.14 are the lowest. As for NO_x, the lowest are VR0.25 and DE0.17.

Keywords

Fuel additives, engine performance, exhaust emissions

1. INTRODUCTION

Engine performance is one of the factors that differentiate engine capabilities from one to another. These capabilities are torque, power and fuel consumption. Nowadays, fuel consumption had been a major aspect in designing an engine because the earth's fuel supply is currently limited and decreasing day by day. In order to improve that area of engine performance, two methods can be done which are by mechanical or chemical means.

The method by mechanical is to improve the engine mechanically. For example, modifying the bore and

stroke an engine or add an aftermarket device to the engine like turbocharger and supercharger. This method can provide a huge amount of power and torque, but the cost is too expensive [1]. Meanwhile, by chemical means is to improve chemically like changing to high quality of lubricants or use aftermarket fuel additives. Fuel additives can be bought a lower price and be use instantly. But the problem is does the amount of fuel additives added into the fuel tank suites the amount of fuel that is already in the tank.

Therefore, in this study, aftermarket fuel additives have been tested on petrol and diesel engine in order to examine the effect of the additives on engine performance and exhaust emissions.

2. AFTERMARKET FUEL ADDITIVES

Aftermarket fuel additives are substances that were added to fuel in small quantities into the fuel tank. It is added to provide an improved performance in terms of power and fuel consumption. It is also reduce exhaust emissions from engines. Generally, aftermarket fuel additives can be divided into two groups which are chemical-based and bio-based.

2.1 Chemical and Bio-Based Fuel Additives

Chemical-based fuel additives are additives that are made of chemicals and minerals. The drawback of using chemical-based products is that they main contain harmful chemicals that could affect human's health.. Furthermore, the source of the chemical might be limited since it depends on the non-renewable resources.

Bio-based fuel additives are additives that are made of biomass such as plants or trees. Basically, bio-based products are advantageous in relation to depletion of resources. Bio-based could provide additional product functionalities, less resource intensive production and efficient use of all natural resources.

Vsafe's products are an example of bio-based fuel additives. This is due to the products made of plant that

is palm oil. Through the use of a new revolutionary method in refining and extracting palm oil, the company able to extract the special ingredients that create an extraordinary chemical effect when combined with any fuel.

3. EXPERIMENTAL SETUPS AND PROCEDURES

Experimental study is done on the fuel additives in terms of fuel properties, also effect on engine performance and exhaust emissions. The blending ratio between fuel additives and base fuel is developed based on the standard formula given on the products. As the fuel is blend, the properties might change and need to be analyzed. Fuels properties that are been focus are density and calorific value. This is because these two properties are crucial elements that affect the engine performance [2]. For engine performance, the effect on brake power, brake specific fuel consumption and brake thermal efficiency is considered. As for emissions, the study focuses on hydrocarbon (HC), carbon monoxide (CO) and nitrogen oxide (NO_x) composition.

Density test is done by measuring the weight of fuel in a piknometer. The weight is measured by using an electronic weighing machine. The volume of piknometer is constant which is 10.336 cm³. Calorific value is determined by igniting fuel samples in a bomb calorimeter. Bomb calorimeter is used to find the amount of heat energy produced by fuel during combustion. The unit for calorific value is kJ/kg.

Engine performance test is conducted on petrol and diesel engine. The test conducted is a constant throttle test where the engine speed is let constant at a high engine speed, then the speed is reduce by applying load [3,4]. The speed is reduced to the desired speed.

4. RESULTS AND DISCUSSIONS

4.1 Petrol Fuel Samples

Figure 1 shows the brake power against engine speed for Vivo Racing (VR) samples. Brake power decreases as the engine speed increases. Fuel sample with the highest brake power is VR0.24 with a maximum increase of 12.00% from base petrol. The lowest is VR0.23 with maximum decrease of 98.91%. Brake power is the net power produced by an engine. Higher brake power shows that the engine has a more power compared the lower ones.

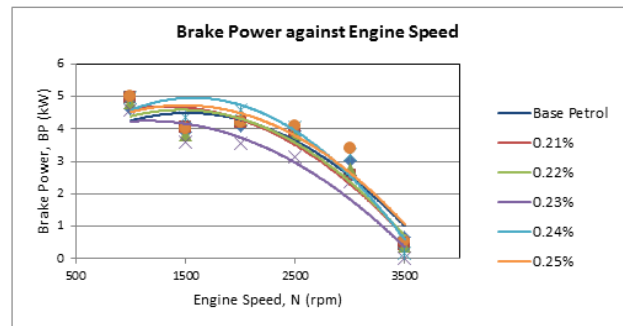


Figure 1: Brake power against engine speed (petrol)

Figure 2 shows the graph of brake specific fuel consumption (bsfc) against engine speed. Bsfc increases as engine speed increases. Fuel sample with the highest bsfc is VR0.21 with a maximum increase of 20.35% based on base petrol bsfc. The lowest is VR0.23 with a maximum decrease of 38.59%. Lower bsfc means that engine is running with same power but less fuel is consumed. Thus, lower bsfc leads to more fuel saved compared to a higher bsfc.

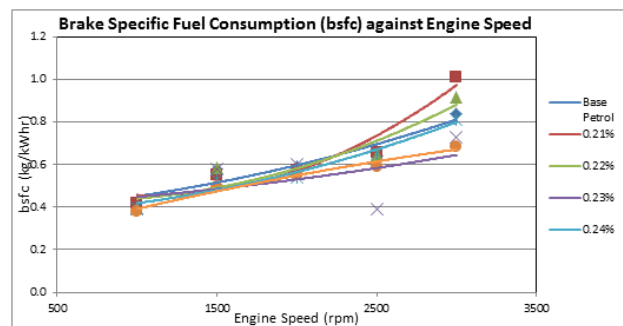


Figure 2: Brake specific fuel consumption against engine speed (petrol)

Figure 3 shows the brake thermal efficiency of each fuel samples against engine speed. As the engine speed increases, the brake thermal efficiency decreases. The results obtain show minor difference between all of the fuel samples. VR0.24 has the highest thermal efficiency with maximum increase of 12.34%. Meanwhile, the fuel sample with the lowest thermal efficiency is VR0.23 with a maximum decrease of 0.99%. Brake thermal efficiency indicates how much of heat energy converted to work. Generally, high brake thermal efficiency is beneficial since more heat energy is converted into work.

There are several reasons which affect the results. One of the reasons is calorific value. From previous study, it concluded that high calorific value gives high engine performance. This relates to the power produced by engine result from combustion of fuel. Based on the calorific value test results, the calorific value for VR0.24 and VR0.23 are 42693 J/g and 42238 J/g respectively. Hence, high calorific value results in high thermal efficiency.

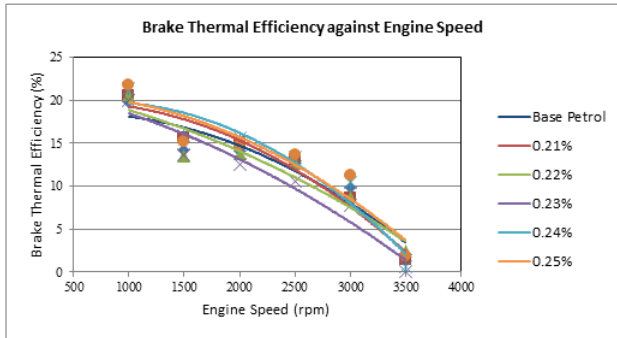


Figure 3: Brake thermal efficiency against engine speed (petrol)

Figure 4 shows the HC composition against engine speed where HC composition decrease as the engine speed increase. The composition is recorded in the unit of parts per million (ppm). All five samples that is added with fuel additives have minor difference between one to another but a major difference is visible between the samples and base petrol. The highest HC composition is from pure petrol while the lowest is V0.25 where it decreases maximum by 37.50% from base petrol.

HC composition indicates the amount of unburned hydrocarbon present in the exhaust system. These hydrocarbon produced because there is not enough of air to combust the fuel completely which leads to the formation of unburned hydrocarbon as product of the combustion. Less HC composition is better since it reduces power loss.

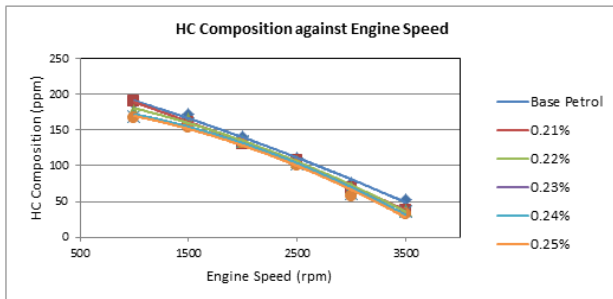


Figure 4: HC composition against engine speed (petrol)

Figure 5 shows the CO composition against engine speed. The trend of the graph shows that the lines fluctuate within the range of engine speed. Overall, all five samples added with Vivo Racing fuel additives have lower CO composition compared to base petrol. The lowest composition is from VR0.22 with maximum decrease of 24.20% from pure petrol. The least composition difference from pure petrol is VR0.24 where the minimum difference is 2.76%.

CO is produced due to the insufficient of air for carbon to react with. It usually occurs when the engine is operated with a fuel-rich air-fuel ratio. As fuel is burn, the elements of a fuel which is hydrogen (H) and

carbon (C) will react with to form products of combustion. But, when air is not enough, the fuel cannot have a complete combustion. Hence, CO is produced.

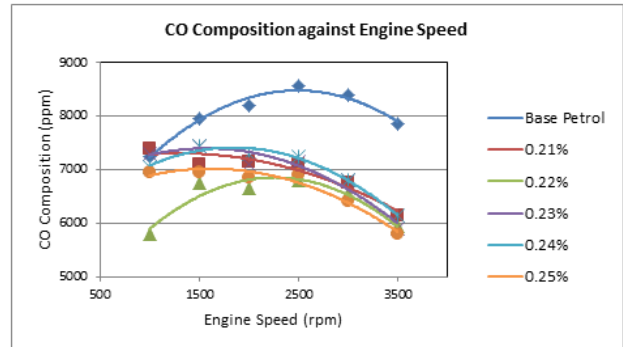


Figure 6, NO_x composition decreases as the engine speed increases. The difference between base petrol and other fuel samples can be seen at lower engine speed, but at higher engine speed, the composition is almost the same. Base petrol has the highest NO_x composition compared to the other fuels. The difference is 12.41% from the lowest point at 1500 rpm which is from VR0.23. The fuel sample with the lowest NO_x composition is VR0.25 which has a maximum decrease of 13.99% from base petrol.

NO_x produced as a result of combustion. For combustion to occur, a mixture of air and fuel is needed before a spark ignited the mixture. Basically, air that enters the combustion chamber consists of 80% nitrogen (N₂). Atmospheric nitrogen exists as a stable molecule at low temperature. However, at very high temperature inside the combustion chamber, the nitrogen become unstable and react with oxygen which produce nitrogen oxide (NO_x).

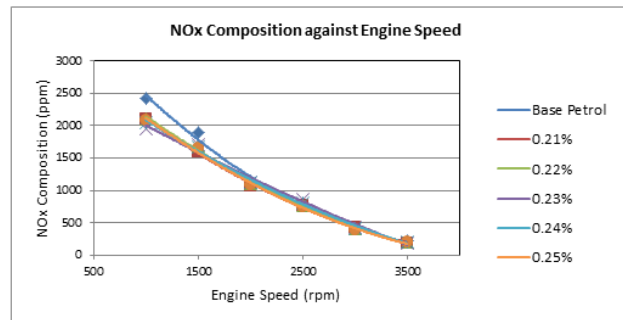


Figure 6: NO_x composition against engine speed (petrol)

4.2 Diesel Fuel Samples

Figure 7 shows brake power against engine speed for Vivo Flawless (VF) product. The lines show that brake power increases as engine speed increase. Base diesel has the highest brake power compared to other fuel

samples. The lowest brake power is from VF0.14 with a maximum decrease of 6.65%.

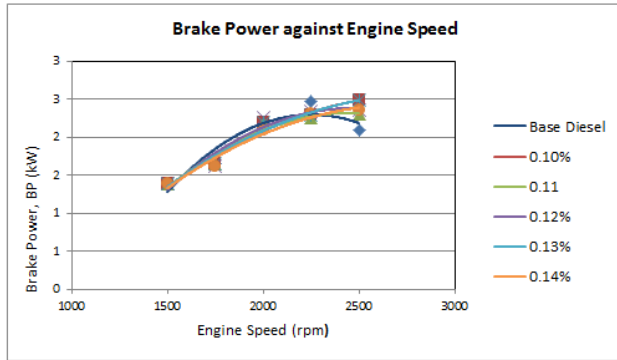


Figure 7: Brake power against engine speed (Vivo Flawless)

In Figure 8, brake power against engine speed for Diesel Energy (DE) product is shown. The pattern of the line is similar like in Figure 7. The highest brake power owns by base diesel. While the lowest brake power is VF0.18 with a maximum decrease of 53.33%.

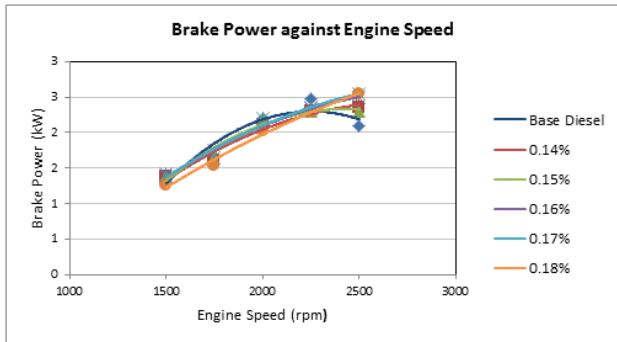


Figure 8: Brake power against engine speed (Diesel Energy)

Figure 9 and 10 show brake specific fuel consumption for VF and DE product. The line of the graph is a quadratic line where bsfc decrease to a minimum point and increase afterwards. For VF product, the highest bsfc owns by base diesel while the lowest bsfc owns by VF0.11. Bsfc of VF0.11 decreases 12.12%. As for DE product, DE0.18 has the highest bsfc with maximum increase of 4.40% from base diesel. While the lowest bsfc owns by DE0.17 with maximum decrease of 9.47%.

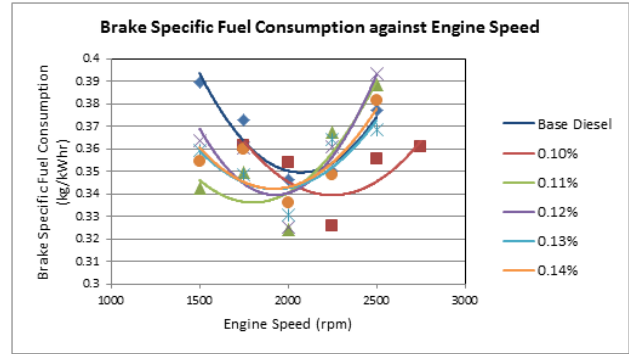


Figure 9: Brake specific fuel consumption against engine speed (Vivo Flawless)

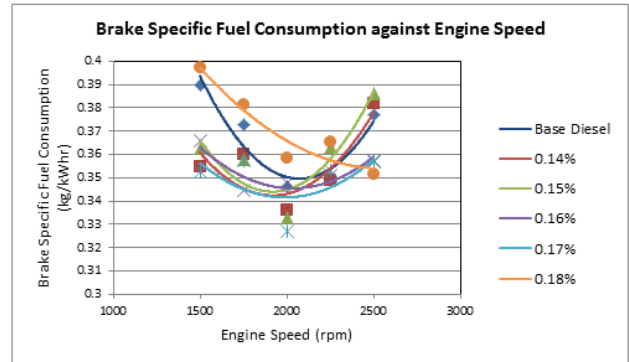


Figure 10: Brake specific fuel consumption against engine speed (Diesel Energy)

Figure 11 shows brake thermal efficiency against engine speed for Vivo Flawless product. The line of graphs is a quadratic like where the efficiency increase and decrease as the engine speed increase. The brake thermal efficiency of all samples has minor difference between one to another where the values are close to each other. The fuel sample with the highest brake thermal efficiency is VF0.10 with a maximum increase of 5.60% from base diesel. While the lowest brake thermal efficiency is from VF0.11 with a maximum decrease of 7.33%.

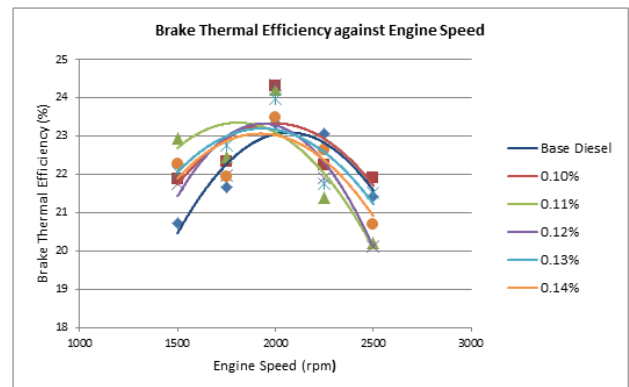


Figure 11: Brake thermal efficiency against engine speed (Vivo Flawless)

In Figure 12, the brake thermal efficiency against engine speed for Diesel Energy product is shown. The pattern of the graph is a quadratic line across the engine speed. Major difference is seen between DE0.17 and DE0.18 from other samples at engine speed of 2000 rpm. DE0.17 has the highest brake thermal efficiency among all samples. It increases 8.16% from base diesel. Meanwhile, DE0.18 has the lowest brake thermal efficiency which decrease 6.20% from base diesel.

Basically, the brake thermal efficiency of a diesel engine is higher compared to a petrol engine. This is due to the high compression ratio of a diesel engine. When comparing the thermal efficiency between diesel fuels, the most common factor is the calorific value of the fuel. Higher calorific value would give higher brake thermal efficiency under same condition of engine.

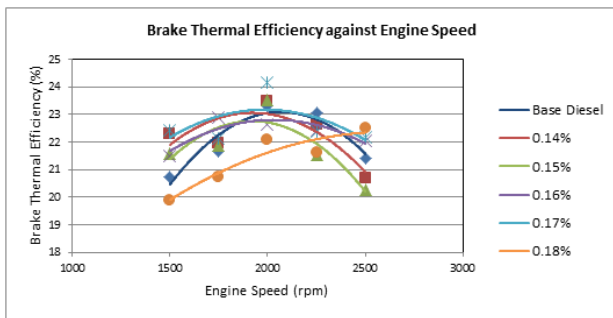


Figure 12: Brake thermal efficiency against engine speed (Diesel Energy)

Figure 13 shows the HC composition against engine speed where the graph is a quadratic line. Huge difference can be seen between all the samples where there are three samples that are far apart from the base diesel line. VF0.14 has the highest HC composition with an increase of 102.27%. Whereas, the lowest HC composition is VF0.13 which decreases 40.68% from base diesel.

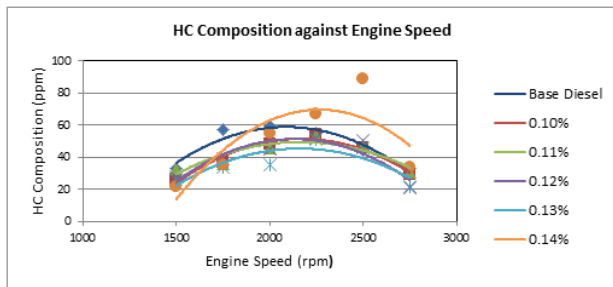


Figure 13: HC composition against engine speed (Vivo Flawless)

As illustrated in Figure 14, the graph is quite similar as in Figure 13 in terms of their pattern. The lines increase at lower engine speed and decrease at higher engine speed. DE0.14 has the highest HC composition

which is 102.27% from base diesel. While the fuel sample with the lowest HC composition is DE0.17 with a decrease of 57.89%.

HC composition is one of the undesired parameter in the exhaust gases. This is because it indicates the amount of the power loss by the engine since it is unburned fuel. Unburned fuel is produced due to the insufficient of air for the fuel to combust completely.

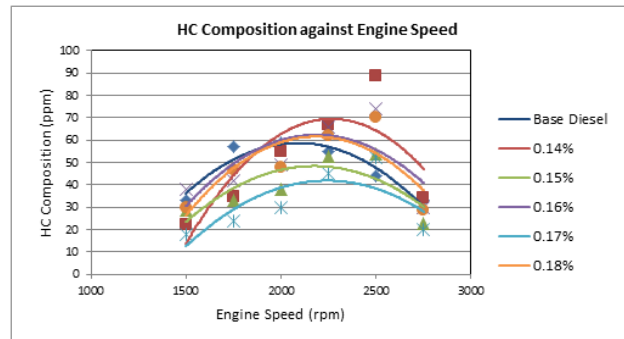


Figure 14: HC composition against engine speed (Diesel Energy)

In Figure 15, it shows the graph of CO composition against engine speed. The line of the graph is quadratic where the values of HC composition increase at lower engine speed till the middle and decrease afterwards. There are two samples that have higher CO composition compared to other samples which base diesel and VF0.13. VF0.13 has an increase of 8.07% from base diesel. While the fuel sample with the lowest CO composition is VF0.14 with a maximum decrease of 33.33%.

Meanwhile, Figure 16, shows the CO composition for Diesel Energy product. It has a similar pattern like in Figure 15. The highest CO composition recorded is from DE0.16 with a maximum increase of 21.74%. While the lowest CO composition is from DE0.14 with a maximum decrease of 33.33%.

Lower CO composition is better because it reduces the amount of poisonous carbon monoxide gases release from exhaust system of an engine. It also means that chemical energy can be minimize and fully utilize in the engine.

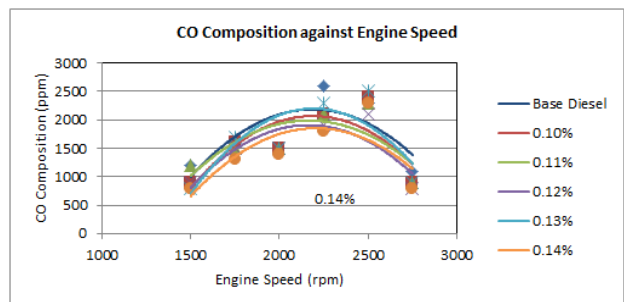


Figure 15: CO composition against engine speed (Vivo Flawless)

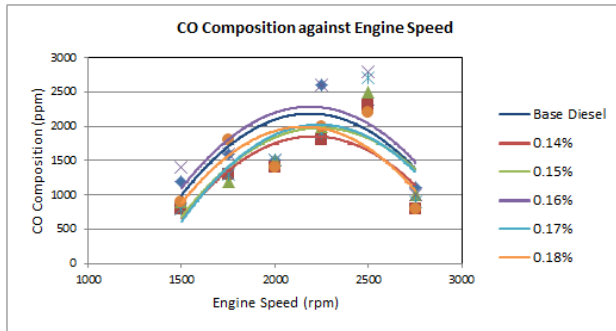


Figure 16: CO composition against engine speed (Diesel Energy)

Figure 17 shows the NO_x composition against engine speed of Vivo flawless product. The graph has quadratic lines where NO_x composition increase and decrease. Base diesel has the highest NO_x composition with an increase of 28.47% from VF0.12 which is situated in the middle between all the lines. While, VF0.14 has the lowest NO_x composition with a maximum decrease of 30.77% from base diesel.

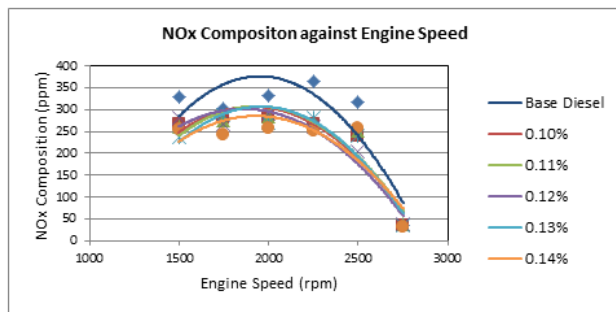


Figure 17: NO_x composition against engine speed (Vivo Flawless)

In Figure 18 the NO_x composition for Diesel Energy product is shown. The pattern of the graph is the same as in Figure 17 where the lines are quadratic lines. From the graph, base diesel has the highest NO_x composition with a difference of 45.32% based on DE0.17. As for the lowest NO_x composition, there are two samples with the lowest value which are at lower engine speed and higher engine speed. At lower engine speed, DE0.15 has the lowest NO_x composition with a maximum decrease of 61.89% from base diesel. Meanwhile, at higher engine speed, DE0.17 has the lowest NO_x composition with a maximum decrease of 45.32%.

NO_x composition for five samples that were added with fuel additives have decrease significantly from base diesel. NO_x are formed when the temperature inside the combustion chamber is high which means that the base diesel fuel has a high temperature during combustion compared to the other samples.

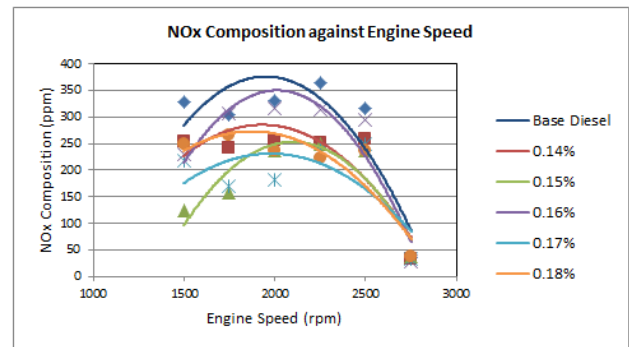


Figure 18: NO_x composition against engine speed (Diesel Energy)

5. CONCLUSION

Based on the experimental results for petrol and diesel engine, the effect of base fuel and blended fuel samples can be investigated in terms of engine performance and exhaust emissions. Generally, the blended fuel does not improve the brake power of the engines, however, it does reduce the brake specific fuel consumption and increase brake thermal efficiency. Furthermore, exhaust emissions such as HC, CO and NO_x are reduced. Details on which blending ratios give the best effect on engine performance and emissions are shown as follows:

1. For engine performance, fuel sample that gives the best result on brake power for petrol is VR0.24.
2. As for brake specific fuel consumption, the best are VR0.23 and VF0.11 for petrol and diesel engine respectively.
3. For brake thermal efficiency, the best fuel samples are VR0.24 and DE0.17.
4. For exhaust emission, HC composition for both engines, the lowest is VR0.25 for petrol fuel samples. As for diesel fuel samples, the lowest is DE0.17.
5. For CO composition, the lowest are VR0.22 and DE0.14.
6. Lastly, for NO_x composition, the lowest are VR0.25 for petrol, DE0.15 and DE0.17 for diesel.

ACKNOWLEDGMENT

The authors like to convey their thanks and gratitude to Vsafe Energy Sdn. Bhd for their support and assistance with this study and for their appreciation of the benefits to be gained from the research activities.

REFERENCES

- [1] Hua Zhao and Nicos Ladommatos (2001). *Engine Combustion Instrumentation and Diagnostics*. Warrendale, Pa: Society of Automotive Engineers, Inc.

- [2] Micheal Plint and Anthony Martyr (1998). *Engine Testing Theory and Practice*. Warrendable, Pa: Society of Automotive Engineers, Inc.
- [3] Heywood, John B. (1988). *Internal Combustion Engine Fundamentals*. United States; McGraw Hill.
- [4] Williard W. Pulkrabek (1999). *Engineering Fundamental of the Internal Combustion Engine*. Upper Saddle River, New Jersey: Prentice Hall.

The Effect of Decontamination on Vehicle Cooling System

Prisillia Wong Yuean Ning^a, Zulkarnain Abdul Latiff^b, Azhar Abdul Aziz^c,
Mohd Rozi Mohd Perang^d

Automotive Development Centre (ADC)
Faculty of Mechanical Engineering
Universiti Teknologi Malaysia
81310 Johor Bahru, Malaysia
Tel : (607) 5535447. Fax : (607) 5557097

^aprisilliawong@gmail.com, ^bzkarnain@fkm.utm.my, ^cazhar@fkm.utm.my, ^drozi@fkm.utm.my

ABSTRACT

This study analyzed the performance of the water pump and radiator under process of as-it-is condition, contamination, and decontamination among three types of radiator, namely used, new, and new coated radiators. Contamination process is completed by spraying the mixture of fine clay and water onto the radiator's surface for 30 layers. Decontamination process is done by Airestec Sdn Bhd, a local company. Internal analysis covers replacing the cooling fluid with used radiator water, tap water and tap water with additive to run experiments. As result, water pump displays similar trends for each set of experiment and air flow velocity, and its highest efficiency is 8.20 %. For external treatment, the effectiveness after decontamination process for new coated radiator, new radiator and used radiator are 43.60%, 31.42% and 30.16% respectively. While for internal treatment, tap water with additive, tap water and used radiator water exhibits 31.79%, 31.42% and 28.98% of effectiveness. As a conclusion, decontaminants towards radiator are effective to increase the performance of the radiator, but no impact on the efficiency of the water pump. For internal treatment, cooling fluid with additive help enhance the radiator performance in cooling system.

Keywords

Vehicle cooling system, radiator, effectiveness, contamination, decontamination

1. INTRODUCTION

Judgment on the level of performance or capability of a vehicle cooling system was not entirely rely on the label of brands and tags of price, but it's ability to effectively remove the unwanted heat which probably leaded to damage of mechanical components [1]. Particularly for most of the tropical countries which surrounding temperature is relatively high, the vehicle cooling system carries important responsibility to work on heat transfer via radiator of an engine in order to make sure that engine could operate under optimal temperature [2].

As refer to the sales of new vehicle in 2014, the number of new vehicles purchasing was increasing throughout the year. Since every single vehicle needed to rely on the cooling system to eliminate the excess heat from the engine, the demands for better reliability and longer life of engine cooling system definitely increased too. Related to the research, the study of the characteristic of components of engine cooling system undeniably became significant measure for future improvement.

From previous research study, the characteristics of main components in engine cooling system such as water pump and radiator were analyzed under real engine operating situation. For both research, water was selected as the cooling fluid to circulate the system, the temperature of the coolant, the speed of the vehicle operating, and the air velocity flowing in the radiator were taken into consideration. The efficiency of water pump and effectiveness of radiator were studied.

Accumulation of dirt, dust, and other contaminants in cooling system might result in insufficient cooling effect, and even catastrophic overheating [3]. Prolonged damage over the time leaded to engine core's severe damage as it is hard to observe when liquid cooling system goes wrong [3]. Thus, treatment used such as coating method of radiator could be a measure to minimize the problems of contamination.

In this project, the experiment will be conducted to observe the efficiency of pump and effectiveness of radiator using different radiators at varying vehicle travelling velocity under different radiator's conditions namely original condition, contaminated condition and decontaminated condition. Besides, the study will involve different types of cooling fluid for instance used radiator water, tap water and tap water with additive to identify whether there is a difference in performance of cooling effect.

2.0 EXPERIMENTAL RIG AND PROCEDURES

2.1 Experimental Test Rig

The simulator test rig used in the experiment work is displayed in Fig. 1. The simulator test rig consists of an electrical motor pump to circulate the water through the thermal storage, and direct the cooling fluid to reach flow meter. Cooling fluids flows through the radiator and back to the water pump. The water flow rate is controlled via controlling the valve. Bypass valve is installed for a more accurate flow control. Blower placed in front of the air box of the radiator and cooling fan mounted on the radiator are used to simulate the real air flow situation to allow heat transfer via medium of air.

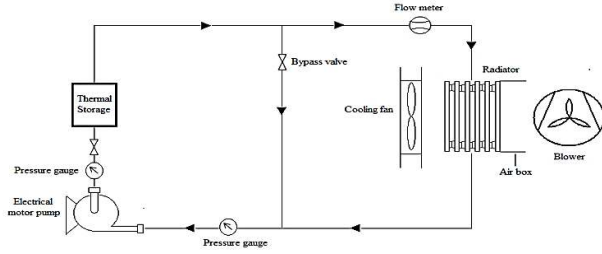


Figure 1: Schematic diagram of simulator test rig

2.2 Experimental Procedure

The experiment is mainly divided into two parts, external analysis which covers experimental works of investigating performance of water pump and different types of radiators at varying vehicle travelling velocity under different radiator's conditions, and internal analysis which includes experiments related to performance of radiators using different types of cooling fluid at varying vehicle travelling velocity. For external analysis, tap water is used as the cooling fluid to run all of the experiments, and three types of radiators involved are used radiator, new radiator and new coated radiator. During as-it-is condition, the simulator test rig is flushed and filled with tap water to ensure that pipes are full with tap water. The electrical motor pump is started and the heater is switched on. The temperature of tap water entering and leaving the radiator, and the temperature of air entering and leaving the fin of the radiator are recorded after the system reaches steady state.

The three radiators in as-it-is condition are then contaminated by using method of spraying the solution which is the mixture of water and clay onto the surface of the radiators. Decontamination process after completing the experiments of contaminated radiators involves releasing of multi-enzyme treatment cleaning for all three radiators and protective layer dip coating for used and new radiators. Experiments of contaminated radiators and decontaminated radiators are exactly the same with the procedure of experiments in as-it-is radiator condition.

The efficiency of the water pump can be calculated through the equation as shown in Equation 1:

$$\eta = \frac{\text{Output power}}{\text{Input power}} \times 100 \quad (1)$$

where output power is referred to the power of the water pump [4]. The output power of the water pump can be obtained via the equation shown in Equation. 2:

$$\text{Power} = \left[(P_{\text{gauge at delivery}} + P_{\text{atm}}) - (P_{\text{vacuum at suction}} + P_{\text{atm}}) \right] \times \text{Flowrate} \quad (2)$$

The effectiveness of the radiator which displayed in Equation 3 can be defined as the ratio of the rate of actual amount of heat transfer to the rate maximum possible heat transfer in a radiator [5]. The actual rate of heat transfer in a radiator is equal to the rate of heat transfer of coolant is shown in Equation 4 while the rate of maximum possible heat transfer is equal to the rate of heat transfer of air is shown in Equation 5. The reason is due to the specific heat capacity of coolant is higher than the specific heat capacity of air.

$$\varepsilon = \frac{\dot{Q}}{\dot{Q}_{\text{max}}} \quad (3)$$

$$\dot{Q} = \dot{m}_{\text{coolant}} (h_{\text{coolant, in}} - h_{\text{coolant, out}}) \quad (4)$$

$$\dot{Q}_{\text{max}} = \dot{m}_{\text{air}} (h_{\text{air, out}} - h_{\text{air, in}}) \quad (5)$$

where \dot{m}_{coolant} is the mass flow rate of coolant, \dot{m}_{air} is the mass flow rate of air, $h_{\text{coolant, in}}$ refers to enthalpy of coolant entering the radiator, $h_{\text{coolant, out}}$ equals to enthalpy of coolant leaving the radiator, $h_{\text{air, in}}$ is the enthalpy of air entering the radiator and $h_{\text{air, out}}$ represents the enthalpy of air leaving the radiator.

All experiments and temperatures are carried out under similar environmental condition. It may be noted here that all the data required includes temperatures of coolant entering and leaving the radiators are recorded at steady state condition.

3. RESULTS AND DISCUSSIONS

3.1 Efficiency of Water Pump

Figure 2 displays the efficiency of the water pump against flow rate. The efficiency of the water pump follows the same trend for each type of the radiator namely used radiator, new radiator, and new coated radiator under each condition as as-it-is situation, contamination, and decontamination at each air flow velocity which are 40 km/h, 50 km/h, 60 km/h and 70 km/h. As observed from Figure 2, the efficiency of the pump increases as the water flow rate increases until it reaches maximum performance level, which is

8.20% at 13 *lpm*. The efficiency of the pump decreases with increasing water flow rate after the peak of the efficiency. In other words, the contaminants on the surface of the radiators and the decontamination treatment applied do not affect the performance of the water pump for each of the experiment.

3.2 Effectiveness of Radiator

The effectiveness of the used radiator shows the highest performance level at air flow velocity 40 km/h in condition of decontamination state. As compared, after the used radiator is decontaminated, the effectiveness of used radiator is higher than the performance of used radiator during as-it-is condition. The used radiator in contaminated condition shows the lowest percentage of radiator effectiveness. The performance of the used radiator at air flow velocity of 50 km/h, 60 km/h and 70 km/h are lower in sequence of decontaminated condition, as-it-is condition and contaminated condition compared to air flow velocity of 40 km/h.

As observed from Figure 3, the effectiveness of used radiator in decontaminated condition displays 30.16% at 40 km/h and water flow rate of 22 *lpm*. The value is higher than the effectiveness of used radiator at 22 *lpm* in as-it-is condition, 24.91% and at 22 *lpm* in contaminated condition, 21.74%.

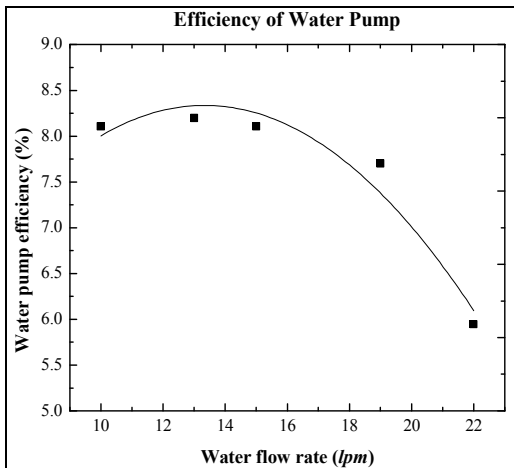


Figure 2: Water pump efficiency against water flow rate

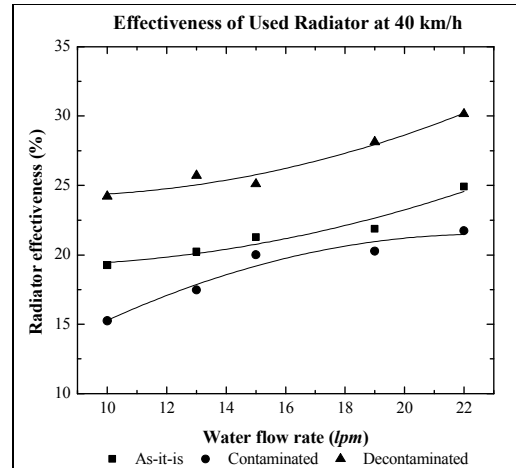


Figure 3: Effectiveness of used radiator at 40 km/h

The effectiveness of new radiator shows the highest performance level at air flow velocity 40 km/h in condition of decontamination state. As compared, after the new radiator is decontaminated, the effectiveness of new radiator is higher than the performance of new radiator during as-it-is condition. The new radiator in contaminated condition shows the lowest percentage of radiator effectiveness. The performance of the new radiator at air flow velocity of 50 km/h, 60 km/h and 70 km/h are lower in sequence of decontaminated condition, as-it-is condition and contaminated condition compared to air flow velocity of 40 km/h.

As observed from Figure 4, the effectiveness of new radiator in decontaminated condition displays 31.42% at 40 km/h and water flow rate of 22 *lpm*. The value is higher than the effectiveness of new radiator at 22 *lpm* in as-it-is condition, 29.79% and at 22 *lpm* in contaminated condition, 28.77%.

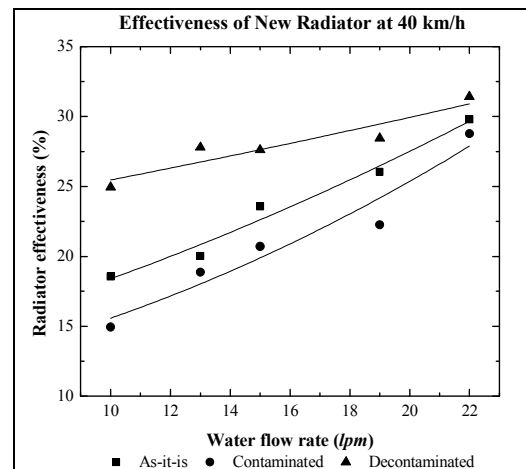


Figure 4: Effectiveness of new radiator at 40 km/h

The effectiveness of new coated radiator shows the highest performance level at air flow velocity 40 km/h in condition of decontamination state. As compared, after the new coated radiator is decontaminated, the

effectiveness of new coated radiator is higher than the performance of new coated radiator during as-it-is condition. The new coated radiator in contaminated condition shows the lowest percentage of radiator effectiveness. The performance of the new coated radiator at air flow velocity of 50 km/h, 60 km/h and 70 km/h are lower in sequence of decontaminated condition, as-it-is condition and contaminated condition compared to air flow velocity of 40 km/h.

As observed from Figure 5, the effectiveness of new coated radiator in decontaminated condition displays 40.48 % at 40 km/h and water flow rate of 22 *lpm*. The value is higher than the effectiveness of new coated radiator at 22 *lpm* in as-it-is condition, 28.55 % and at 22 *lpm* in contaminated condition, 24.40 %.

Overall, it indicates that the treatment of applying multi-enzyme to decontaminate the three radiator and dip-coating layer applied for used radiator and new radiator is effective and practicable in raising the performance of the radiator to better the circulating of cooling system.

3.3 Effectiveness of Radiator Using Different Cooling Fluids

The comparisons between the effectiveness of new decontaminated radiator using different cooling fluids namely used radiator water, tap water and tap water with additive at each air flow velocity are analyzed. The effectiveness of new decontaminated radiator using different cooling fluids at air flow velocity of 40 km/h, 50 km/h, 60 km/h and 70 km/h are displayed in Figure 6, Figure 7, Figure 8 and Figure 9.

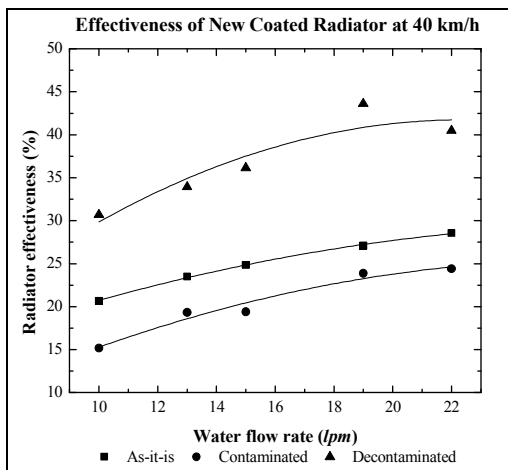


Figure 5: Effectiveness of new coated radiator at 40 km/h

As observed, the effectiveness of the radiator increases with increasing of the water flow rate, but decreases as

the air flow velocity is getting faster. The new decontaminated radiator performs the best at air flow velocity of 40 km/h. Refer to Figure 6, the experiment of new decontaminated radiator with using tap water with additive shows better performance compared to the experiment using cooling fluid of tap water and followed by used radiator water. Selecting tap water with additive as cooling fluid of vehicle cooling system does slightly improve the radiator effectiveness compared to normal cooling fluid which is tap water only.

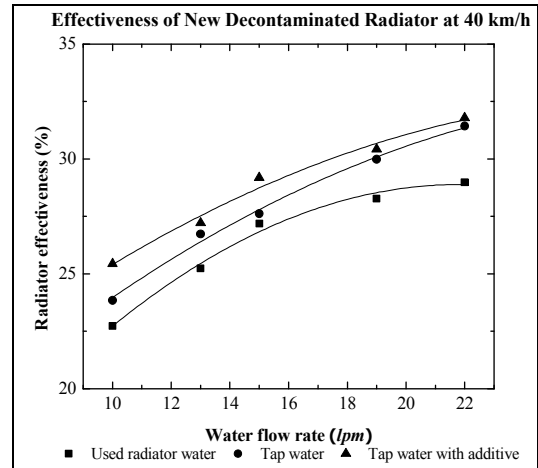


Figure 6: Effectiveness of new decontaminated radiator at 40 km/h

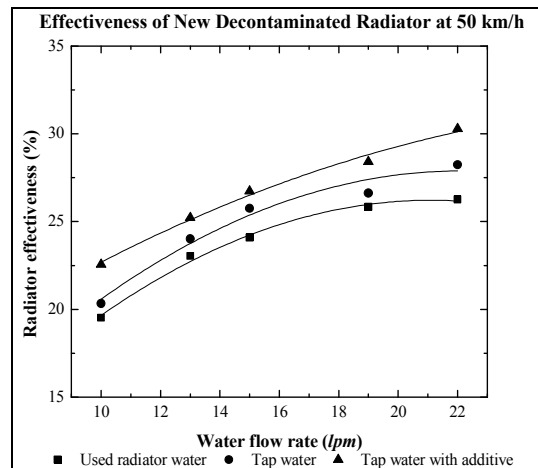


Figure 7: Effectiveness of new decontaminated radiator at 50 km/h

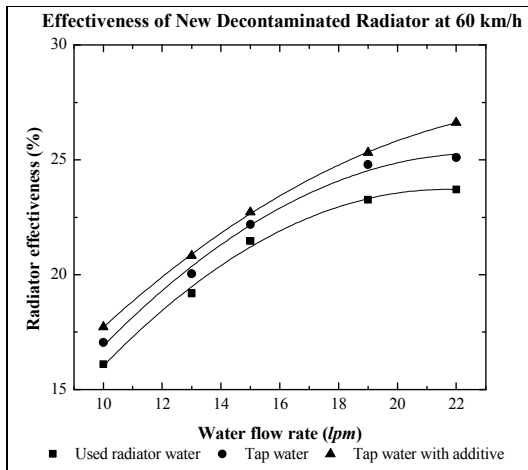


Figure 8: Effectiveness of new decontaminated radiator at 60 km/h

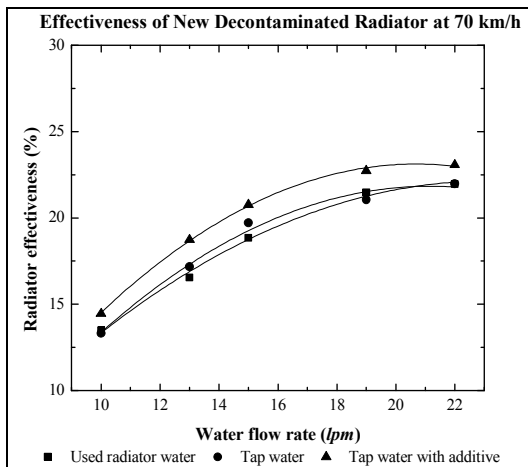


Figure 9: Effectiveness of new decontaminated radiator at 70 km/h

4. CONCLUSION

From the aspect of performance of water pump efficiency, the efficiency of water pump increases with increasing water flow rate until it reaches maximum efficiency which is 8.20%, and then decreases when the water flow rate is increased. The performance of the water pump is following the same trend as for different types of radiators at air flow velocity of 40 km/h, 50 km/h, 60 km/h and 70 km/h. The process of contamination and decontamination on radiator does not give any impact on the efficiency of the pump, in other words the behavior of the water pump remains the same as in as-it-is condition.

For the performance of the radiator in external analysis, the effectiveness of the radiator is better after decontamination treatment than contamination and follow by as-it-is condition. The new coated radiator shows the highest performance, which is 43.60% in decontaminated condition, followed by 28.55% in as-it-is condition, and 24.40% in contaminated condition.

It means that the decontaminants applied on the radiators are effective to increase the performance of the radiator in order to better the vehicle cooling system efficiency.

Overall, the effectiveness of new coated radiator is higher than effectiveness of new radiator and lastly effectiveness of used radiator. In decontaminated condition, the performance of new coated radiator which is 43.60% is higher compared to the performances of new radiator and used radiator which are 31.42% and 30.16%. Each type of the radiator in either condition performs the best at air flow velocity of 40 km/h, and its performance decreases from 50 km/h, 60 km/h and 70 km/h.

For the case of the internal analysis, the effectiveness of new decontaminated radiator using tap water with additive is 31.79%, which is the highest compared to the performances of radiator using tap water and used radiator water which are 31.42% and 28.98%. The effectiveness of the radiator is proved to be higher when the cooling fluid chosen is tap water with additive. The performance of the radiator is lower when tap water is used to be the cooling fluid, and the lowest for used radiator water as coolant. Similarly, the radiator works more effective at air flow velocity of 40 km/h, and its effectiveness drops from 50 km/h, 60 km/h and 70 km/h. In short, the internal treatment additive added into the cooling fluid does increase the performance of the radiator in cooling system.

ACKNOWLEDGMENT

The authors like to convey their thanks and gratitude to Airestec Innovations Sdn. Bhd for their support and assistance with this study and for their appreciation of the benefits to be gained from the research activities.

REFERENCES

- [1] Pang, S.C., et al., A review on air flow and coolant flow circuit in vehicles' cooling system. *International Journal of Heat and Mass Transfer*, 2012. 55(23–24): p. 6295-6306.
- [2] Sathyanarayanan, P.L. and R. Ramprabhu, Study on the effect of different combinations of engine coolant additives on the heat dissipation rate of radiators. *Proceedings of the Institution of Mechanical Engineers, Part D: Journal of Automobile Engineering*, 2005. 219(10): p. 1173-1179.
- [3] Helali, A.B., Effects of water contamination on sub-cooled flow boiling heat transfer. *Energy Conversion and Management*, 2011. 52(5): p. 2288-2295.
- [4] Munson, B.R., et al., *Fundamentals of Fluid Mechanics*. 6th Edition ed. 2009, United States of America: Don Fowley.

[5] Ng, E.Y., P.W. Johnson, and S. Watkins, An analytical study on heat transfer performance of radiators with non-uniform airflow distribution. Proceedings of the Institution of Mechanical

Engineers, Part D: Journal of Automobile Engineering, 2005. 219(12): p. 1451-1467.

A review of Development of Test Rig for Organic Rankine Cycle

M.I. Alhamid^a, Muswar M^b, Nasruddin^c, Budihardjo^d

^aFaculty of Engineering
University of Indonesia, Depok 16424
Tel : (021) 7270011 ext 51. Fax : (021) 7270032
E-mail : mamak@eng.ui.ac.id

^bFaculty of Engineering
University of Indonesia, Depok 16424
Tel : (021) 7270011 ext 51. Fax : (021) 7270032
E-mail : muswar_2000@yahoo.com

^cFaculty of Engineering
University of Indonesia, Depok 16424
Tel : (021) 7270011 ext 51. Fax : (021) 7270032
E-mail : nasruddin@eng.ui.ac.id

^dFaculty of Engineering
University of Indonesia, Depok 16424
Tel : (021) 7270011 ext 51. Fax : (021) 7270032
E-mail : budihardjo@eng.ui.ac.id

ABSTRACT

The development of research equipment for the application of experimental equipment very growing up lately for organic rankine cycle (ORC) moreover from various countries have developed rapidly in the research field of ORC. And need to know that the application of the experimental apparatus of ORC of many kinds of utilization is as experimental ORC in the field of geothermal, ORC field of desalination, ORC field of ocean thermal energy conversion (OTEC), ORC field of refrigeration systems and more application experimental of ORC. This paper will focused on research using experimental equipment ORC as test rig is on the development of the field of refrigeration as power generation and its supporting equipment using its main components include hermetic compressor with using this type of scroll expander, condenser, evaporator and pumps. The working fluid to be used on various types of environmentally friendly such as R134A and pentane. Expected from the development of this experimental device can be used as power plants for remote areas in Indonesia that is not got electricity as a renewable energy that does not use fossil fuels.

Keywords :

Organic rankine cycle, refrigerant, expander, condenser and evaporator.

I. INTRODUCTION

In the days to come the development of the power plant has been developing with naturally follows the desperate need for human life. Because on the other hand the content of oil as fuel for electricity feed will be reduced, would likely be exhausted with unbridled

consumption. Therefore scientist's renewable energy vying finding energy alternatives to replace the fossil energy. On several alternative energy is developed to meet the needs of the adequacy of electricity include nuclear energy, geothermal energy, biomass energy, ocean energy, solar radiation energy, wind energy and other energies. From the author of several alternative energy will focus on alternative energy is energy based on Organic Rankine Cycle scroll compressor as an expander to produce electricity that is designed produce 1-15 kilowatts.

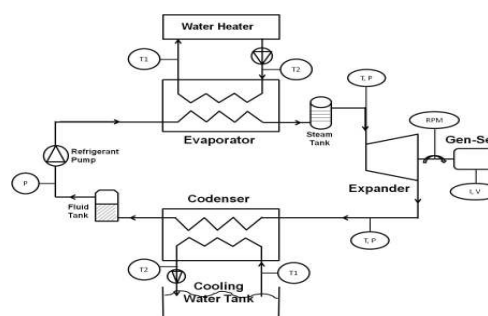


Figure 1. Diagram ORC

For to know's the organic system rankine cycle or ORC need to learn the basic theories that support it, such as the science of heat transfer and thermodynamics. Such knowledge is essential when will the planned system of heat exchanger equipment to be made in a draft. Science of heat transfer include heat transfer by convection, and radiation conductance. Some ways of heat transfer is greatly affect the smooth

working fluid. In addition the system design will be planned will also need to master the basic theory of the cycle rankine as shown in Figure 1 below.

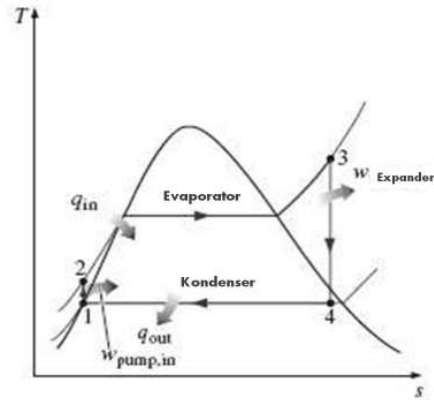


Figure 2. T-s diagram

Ideal Rankine cycle consists of four stages of the

process is :

- 1 – 2 Isentropic compress by pump
- 2 – 3 Isobaric proses in evaporator
- 3 – 4 Ekspansi of isentropic in expander
- 4 – 1 Waste heat in the condenser is isobaric and isothermal

Water enters to the pump 1 as the liquid saturated condition (saturated liquid) and compressed to the operating pressure evaporator. Water temperature will rise during compression isentropic because of decreasing the specific volume of water. Than water enters to the evaporator as a compressed fluid (compressed liquid) on the conditions 2 and will be superheated steam at 3. Where the conditions given by the evaporator to heat water at a fixed pressure. Evaporator and all the parts that produce a refrigerant in a refrigerant called a generator. Superheated steam on 3 conditions, then will enter the expander for isentropic expansion will generate employment and fatherly rotating shaft connected to an electric generator that can produce electricity. Pressure and temperature of the refrigerant will drop during this process towards a situation where the refrigerant will enter the 4 condenser and is usually in the form of saturated steam. This refrigerant will be liquefied at a constant pressure in the condenser and will leave the condenser as saturated liquid that will go to the pump that will complete this cycle. In the ORC system in operation required various types of refrigerant which supports and

various types of major components used include evaporators, condensers, pumps and expander. Expander here serves as a means of turning the generator to produce electricity. Expander is derived from the modification of scroll compressors for air-conditioning cooling machine which has various types that exist in the community, as shown in Figure 2.



Figure 3. Kompresor scroll

Spesification of Scroll Compressor

Parameter	Data
Type	ZR22K3-PFJ (Copeland-Emerson)
Capacity	18200 BTU/hr
Power	1730 watt
EER	10.5 BTU/w.hr
Mass flow	267 Lbs/hr
Electric Rating	220-240 V
Weight	25.9 kg
Height	382.8 mm
Refrigeration Capacity	5330 watt



Figure 4. Heat exchanger

Spesification of Evaporator and Kondensor

Parameter	Data
Type	K070 (Kaori)
Capacity Range	17.58 kW
Max. working temperature	200 °C
Max. working pressure	30 bar
Min. test pressure	43 bar
Max. flow rate (LPM)	240
Max. number of plates (N)	120
Plate Heat Transfer Area (M2)	0.03 m^2
Thickness (mm) – H	10.0+2.38*N
Weight (kg)	1.38+0.134*N



Figure 5. Refrigerant pump

Specification of Refrigerant Pump

Parameter	Data
Type	M 1503-W5 (Sanwa Pump)
Bore	15 mm (suction) x 15 mm (Discharge)
Motor	0.37 kW
Head	10 (12) m
Capacity	24 (6) m
Temp.	100 °C (max) ~-20 °C (min)
Voltage	200/220 V (3 Phase)
Pressure	0.4 MPa

Refrigerant property by Coolpack software

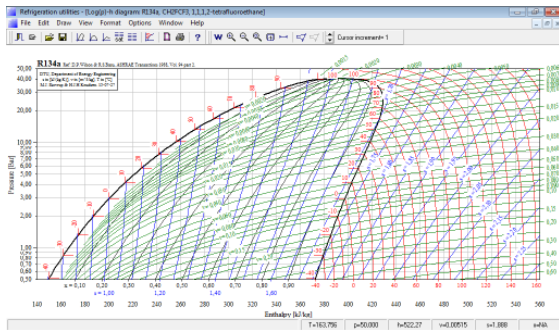


Figure 6. Graph of R-134a by software

Property of R-134a

Parameter	Data
Evaporator inlet temp.	5 °C
Condenser outlet temp.	45 °C
Evaporator pressure	3.48 bar
Condenser pressure	13.221 bar
Mass flow rate	146 kg/hr
Volumetric flow rate	9.11 m ³ /hr
Volumetric capacity	2372 kJ/m ³
Specific pressure drop	578 kPa/m
Pressure ratio	3.79
COP	3.36
COP relative	100 %
Pressure drop relative	100 %
Capacity relative	100 %
Volumetric efficiency	90.2 %

II. BASIC THEORY FOR ORC

Heat transfer can not be avoided between the generation and the surrounding components are ignored to facilitate analysis. Change's of kinetic and potential energy are also ignored. Each component is considered

to be operating at steady state conditions. By using the principle of conservation of mass and energy conservation together with the idealization of it will be developed the equation for energy transfer in each component.

1. Pump

Liquid condensate leaving the condenser at condition 1 is pumped from the condenser into the evaporator so that the pressure rises. By using a control volume around the pump and assuming no heat transfer around, the equilibrium rate of mass and energy is,

$$q - w = h_1 - h_2 + \frac{V_1 - V_2}{2} + g(z_1 - z_2) \quad (1)$$

or

$$q - w_p = h_2 - h_1 \quad (2)$$

Where w_p is the incoming power per unit mass through the pump.

2. Evaporator

The working fluid leaves the pump on condition 2 called water filling, heated to saturate and evaporated in the evaporator. By using the control volume surrounding the tube evaporator and drum drain the water-filling and the condition 2 to condition 3, the equilibrium rate of mass and energy produce,

$$q_{in} = h_3 - h_2 \quad (3)$$

Where q_{in} is the rate of heat transfer from the energy source to the working fluid per unit mass through the evaporator.

3. Expander

Steam from the evaporator at condition 3, which is at a temperature and pressure that have been raised, expanded through the expander to produce work and then discharged to the condenser on the condition 4 with a relatively low pressure. By ignoring the heat transfer with the surroundings, the rate of energy and mass balance for control volumes around expander under mild conditions into,

$$w_e = h_3 - h_4 \quad (4)$$

where m is declared mass flow rate of the working fluid, and w is the rate of work produced per unit mass of vapor through the expander.

4. Condenser

In the case of heat transfer from the condenser to the steam cooling water flowing in separate streams. Condensed steam and cooling water temperature increases. At steady state, the rate of mass and energy

balance for the volume set that covers parts of condensation and heat exchanger is

$$q_{out} = h_4 - h_1 \quad (5)$$

where q_{out} is the rate of energy transfer from the working fluid to the cooling water per unit mass of the working fluid through the condenser. Thermal efficiency measures how much energy into working fluid into the evaporator were converted to net work output.

$$\eta_{T\eta} = \frac{w_t - w_p}{q_{in}} = \frac{(h_3 - h_4) - (h_2 - h_1)}{(h_3 - h_2)} \quad (6)$$

III. SIMULATION OF CALCULATION

After the specification of the main components selected and the data collected then simulation calculations with parameters include temperature, expander power and thermal efficiency as given in the graphic below.

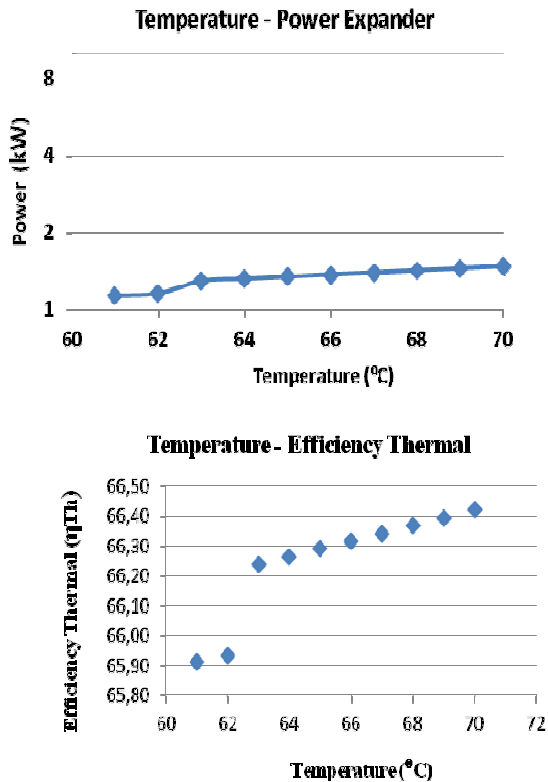


Figure 7. Temperature – Power Expander

Figure 8. Temperature – Efficiency Thermal

IV. CONCLUSION

On the results is that the simulation of calculation for the two parameters at the power expander and thermal efficiency with temperature refrigerant of liquid conditions in the condenser shows graphical trends occur fairly significant increase.

REFERENCES

- [1] M.J. Moran, Howard N. Shapiro, “Fundamentals of Engineering Thermodynamics”, John Wiley & Sons, Inc, 2006.
- [2] S. Declay, S. Qouoilin, L. Guillaume, V. Lemort, “Experimental study on an open-drive scroll Expander integrated into an ORC (organic Rankine cycle) system with R245fa as working Fluid”, Energy, 55 (2013) 173-183.
- [3] S. Quoilin, V. Lemort, J. Lebrum, “Experimental Study and modeling of an organic Rankine cycle Using scroll expander”, Appl. Energy, 87 (2012) 1260-1268.

Investigation into the Selection of an Appropriate Piston Head Geometry for a Spark Ignition Engine Equipped Direct-Fuel Injector

Abdul Rahim Shar Anuar, Mohd Farid Muhamad Said*, Azhar Abdul Aziz, Zulfaqih Lazim

Automotive Development Centre (ADC)
Faculty of Mechanical Engineering
Universiti Teknologi Malaysia
81310, Skudai, Johor, Malaysia
E-mail : mdfarid@utm.my

ABSTRACT

Constructors of gasoline engines are faced with higher and higher requirements as regards to ecological issues and an increase in engine efficiency at a simultaneous decrease in fuel consumption. Satisfaction of these requirements is possible by the recognition of the phenomena occurring inside the engine cylinder, the choice of suitable optimal parameters of the fuel injection process, and the determination of the geometrical shapes of the combustion chamber and the piston head. The aim of the study was to simulate flow in Direct-Injection Fuel engine with different geometrical shapes of piston head. The method of design piston head shapes was referring to existing motorcycle Demak single cylinder 200cc piston size using Solidwork and ANSYS softwarse. The parameter was shallow and deep bowl design on piston head. In term of fuel distribution throughout the combustion chamber, second model that having deeper bowl shows a better fuel distribution than first model as it manages to direct flow the fuel injected towards the location of spark plug. Therefore, second model is chosen as the best model among the two models as it can create a richer mixture around the spark plug.

Keywords:

Direct-Injection, CFD simulation, Piston Head Geometry, Stratification Combustion, Spark-Ignition.

1. INTRODUCTION

The GDI engines are proven to be more advantageous as compared to any other conventional SI engines. The two combustion modes that are homogeneous combustion mode and stratified combustion mode introduced in the GDI engines help to improve the accuracy of Air-Fuel, AF ratio during dynamics and decrease the fuel consumption and CO₂ emission [1-3]. With the

injector installed inside the combustion chamber and its non-throttle operation the engine can achieved higher power output.

Aside from the in-cylinder direct injection, GDI engine has another special feature that is the unique piston top surface shape of the GDI engine. The piston top surface shape plays an important role of determining the behavior of the air-fuel mixture inside the combustion chamber. Commonly, the piston surface of GDI engine is equipped with a piston bowl and the bowl design is mostly determined by its bowl radius, bowl depth, bowl width, bowl location relative to the spark plug [4-5].



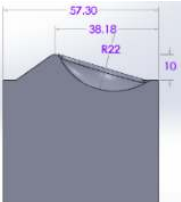

The piston top surface is designed in such way that it will be compatible for both homogeneous combustion mode and also the stratified combustion mode. For the homogeneous combustion mode, the piston top surface plays the role to create a homogeneous mixture of the fuel and air before the combustion. Whereas, for stratification combustion mode, the piston top surface has the responsibility to form a stratified-charge rich fuel cloud around the spark plug [6-7].

2. METHODOLOGY

2.1 Building Models

For this study, a total of two models were built with each of the models is having different types of parameters. The parameters to be varied in this project are mainly focused on the bowl's radius and the bowl's position on the piston top (Table 1). The models were built based on common GDI engine's piston design by using Solidworks software. In term of the piston design measurement, it is adjusted so that the piston will be compatible with the Demak engine with respect of the piston's bore and stroke.

Table 1: Piston design model

Model	Model 1	Model 2
Design		
Measurement		

2.2 Creating flow volume

After combining the piston with the cylinder head, a cavity exist inside the combustion chamber. For the simulation purpose, the cavity inside the combustion chamber has to be replaced with a flow volume first (Figure 1). The flow volume serves as the flow path of the mixture inside the combustion chamber. The flow volume can be created by using the Combine feature in Solidworks software.

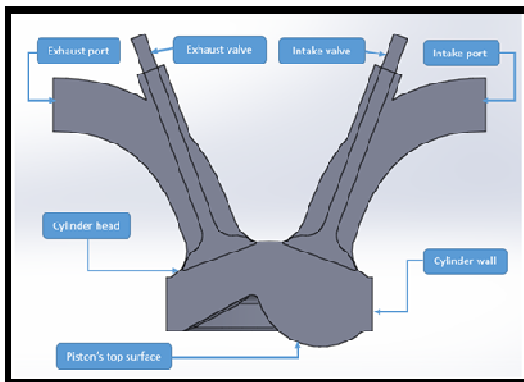


Figure 1: Flow volume and the required parts for the flow volume

2.3 Setting up IC Engine Properties

The engine properties are defined in the ICE properties after IC engine analysis has been selected from the analysis systems toolbox. In the ICE properties, input data such as the simulation type should be included. There are three types of simulation provided for the ICE engine simulation which are cold flow simulation, port flow simulation and combustion simulation. Out of the three simulation types, the combustion simulation is chosen for the simulation type of this project since spray injection has to be included in the study. Basic engine properties such as the engine's

connecting rod length, crank radius, engine speed, minimum valves lift and the valves lift profile should also be defined (Table 2).

Table 2: Basic engine properties

No.	Property	Value
1.	Simulation type	Combustion simulation
2.	Combustion simulation type	Full cycle engine
3.	Connecting rod length	90 mm
4.	Crank radius	30 mm
5.	Engine speed	2000 RPM
6.	Minimum valves lift	0.2 mm

2.4 Decomposing geometry

The flow volume generated is imported to the Ansys Fluent software. The first step before the simulation process is carried out is to decompose the model geometry. When a model is decomposed, the model imported will be divided into smaller volumes where these volumes are compulsory as the mesh requirement in the meshing process. For that, the geometry of the model has to be designed in such way that each small volume can be generated during the geometry decomposition.

Before decomposing the model, some parts of the model need to be defined first such as the inlet, outlet, intake valve, exhaust valve, intake seat and exhaust seat. Since the scope of the study is focused on the fuel injection during the compression stroke, the model is decomposed at 644° CA just before the fuel is injected in the combustion chamber during the compression stroke.

2.5 Meshing

Once the model has been decomposed, meshing process is done. Mesh will be generated individually based on the small volumes of the model geometry created when the model is decomposed. For the analysis, dynamic mesh is conducted.

2.6 ICE Solver setting

ICE solver setting is divided into several parts where in each part, some settings are required for the model. Basically, the ICE solver setting is configured to set the relevant input data required for the simulation. Some example of the input data (Figure 2) are the engine type, fuel type, fuel injection, boundary conditions of the analysis and the type of result required at the end of the simulation (Table 3 & 4).

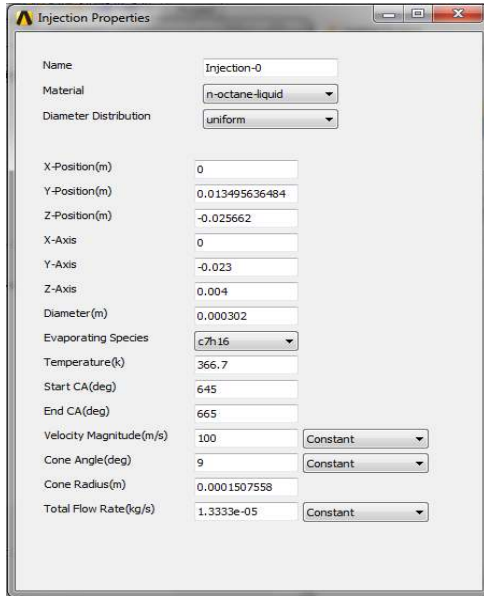


Figure 2: Data input for injection setting [8]

Table 3: Temperature of the combustion chamber wall [8]

Part	Zone	Boundary condition
Head	cyl-head, invalve1-ch, and exvalve1-ch	485 K
Piston	piston	485 K
Liner	cyl-tri	500 K
Exhaust valve	exvalve1-ib, exvalve1-ob, and exvalve1-stem	777 K
Exhaust port	exvalve1-port and exvalve1-seat	485 K
Intake valve	invalve1-ib, invalve1-ob, and invalve1-stem	400 K
Intake port	invalve1-port and invalve1-seat,	313 K

Table 4: Temperature and pressure of the mixture inside combustion chamber [8]

Part	Zone	Pressure	Temperature
Exhaust port	fluid-exvalve-1-port, fluid-exvalve-1-vlayer, fluid-exvalve-1-ib	0.5 MPa	1070 K
Inlet port	fluid-invalve-1-port, fluid-invalve-1-vlayer, fluid-invalve-1-ib	0 Pa	313 K
Chamber	fluid-ch	1 MPa	1070 K

2.7 Running the simulation

ANSYS Fluent will set the relevant number of time-steps and iterations to be calculated for the simulation process to complete. For every one iteration, 30 time-steps are calculated. As an optional choice, to decrease the amount of time consumed in the simulation, the continuity of the calculation is increased to 0.1 and the number of time-step is increased to 1. The total iteration required for the simulation to complete is 3280

iterations where each of the iteration takes a maximum of 50 time-steps. Once every setting is done, the last step is to calculate the simulation. The simulation process can take days to complete depends on the number of iterations provided.

3.0 RESULT AND DISCUSSION

3.1 Swirl ratio

As depicted in Figure 3, Model 1 shows the highest swirl intensity compare to Model 2. This is because Model 2 has higher surface area compare to Model 1 due to its larger piston bowl radius and also the depth of the piston bowl which is deeper than Model 2. This high surface area is creating a high friction to the mixture flow when it comes in contact with the cylinder wall especially at the piston bowl region which in turn resisting the swirl motion inside the combustion chamber of Model 2.

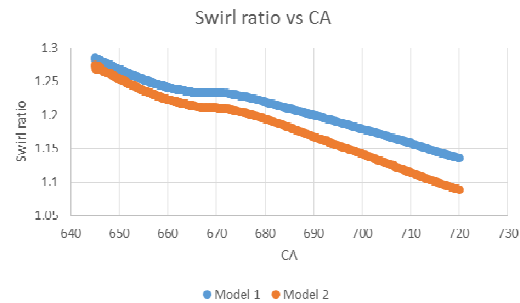


Figure 3: Swirl ratio generated in the combustion chamber of model 1 and model 2

3.2 Tumble ratio

The tumble ratio generated in combustion chamber of all the models tested starts with a negative value and continuously decreasing. However, the negative value does not indicate that the tumble intensity is decreasing but it indicates the direction of the tumble motion of the mixture which is being directed to the exhaust side of the combustion chamber. The figure shows that the intensity of the tumble motion is increasing in a certain direction along the increasing of CA.

The tumble intensity of Model 1 is higher than Model 2 (Figure 4). The major factor that contributes to the turbulent intensity is the piston bowl design where with the right design the piston bowl can help to promote the tumble motion. The right piston bowl design also can help to determine the direction of the mixture throughout the combustion chamber.

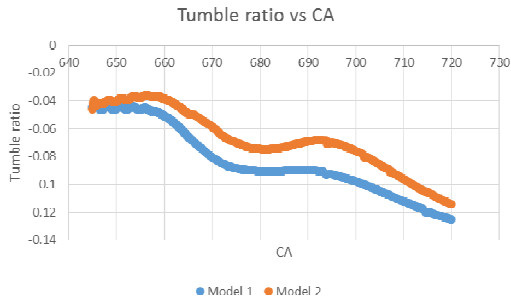


Figure 4: Tumble ratio generated inside the combustion chamber of the Model 1 and Model 2

3.3 Total Kinetic Energy (TKE)

The TKE of Model 2 is the highest among the two models (Figure 5). Due to deeper bowl depth and curvier piston bowl, the piston bowl of Model 2 tends to create vortices with much higher speed than speed of vortices created by piston bowl of Model 1 during the compression stroke. These high speed vortices, in time are colliding against each other to create high turbulent intensity inside the combustion chamber.

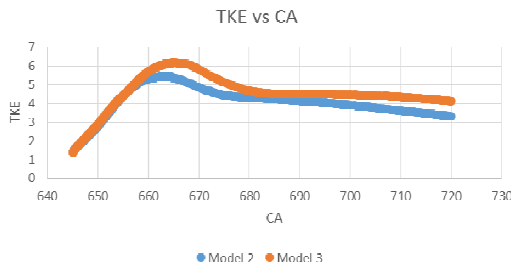


Figure 5: Graph of mass-average of turbulent kinetic energy (TKE) of the two models vs the crank angle

3.4 Pressure

The pressure generated inside the combustion chamber of Model 1 is slightly higher than the pressure in Model 2 (Figure 6). This slight difference is mainly due to the different of compression ratio for both model which is caused by different parameters of the piston models that have different bowl radius and bowl position. Model 1 has a compression ratio of 9 whereby the compression ratio for model 2 is 8.5. The bowl radius is affecting the clearance volume, V_c of both models and thus the compression ratio.

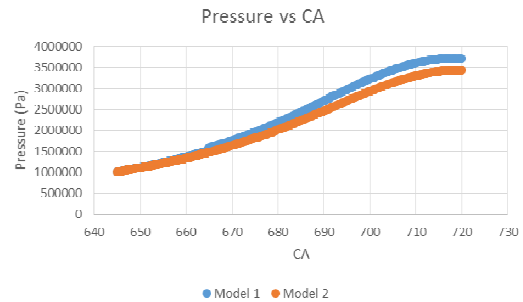


Figure 6: Generated pressure in combustion chamber of Model 1 and Model 2

3.5 Fuel particle traces

Model 1 fails to create rich mixture around the spark plug which is the most important requirement for stratified combustion (Figure 7). Furthermore, this piston design will end up to increase the fuel consumption and produces much lower power output due to unevenly fuel distribution.

For Model 2, when fuel is injected, it travels along the curve part of the piston bowl and in the end it is directed to the center of the combustion chamber where the spark plug is located (Figure 8). This behavior is preferable for stratified combustion since the fuel injected will form a rich mixture around the spark plug. However, there is also a portion of the fuel is being directed back to the intake side. Because of this, the consumption of fuel during combustion cannot be optimized.

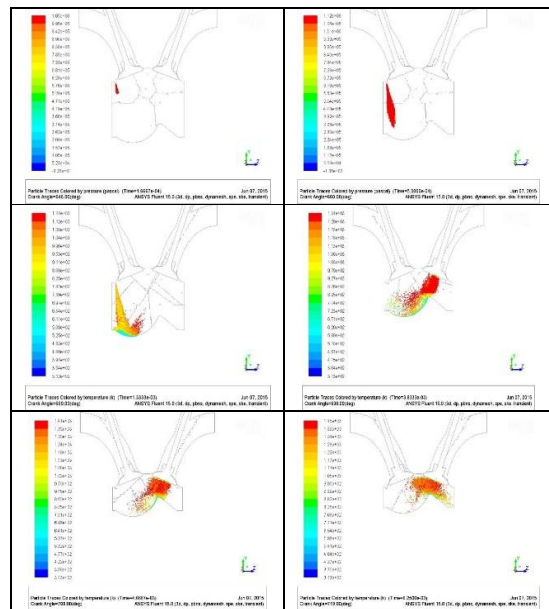


Figure 7: Fuel particle traces of Model 1

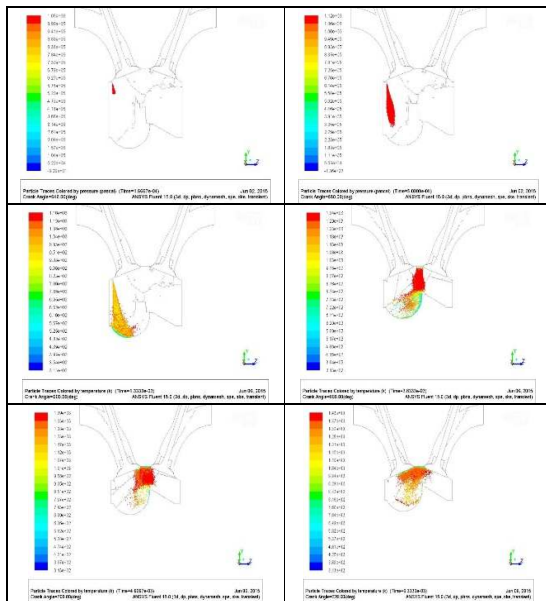


Figure 8: Fuel particle traces of Model 2

4. CONCLUSION

Based on the results obtained from the simulation, both models have their own advantages and disadvantages. For Model 1, the result indicates that it has higher swirl and tumble intensity compare to Model 2 whereas Model 2 has higher TKE value than Model 1. However, the result of swirl ratio, tumble ratio and TKE does not really show a significant difference between the two models. For the fuel distribution throughout the combustion chamber, Model 2 is better than Model 1 since the piston bowl of Model 2 directs the fuel axially towards the center of the combustion chamber where the spark plug is located. This behavior of model 2 design that have deeper bowl is much preferable for stratified combustion mode.

ACKNOWLEDGMENT

The authors acknowledge the financial support from Universiti Teknologi Malaysia (UTM) under the research university grant Q.J130000.2509.08H93 and Automotive Development Centre (ADC).

REFERENCES

- 1) Zhao, H., *Advanced direct injection combustion engine technologies and development*, (1st ed.). Cambridge: Woodhead Publishing Limited, 2010.
- 2) Heywood, J.B., *Internal combustion engine fundamentals*, (1st ed.). United States: McGraw-Hill, Inc., 1988.
- 3) Paul, B. and Ganesan, V., "Flow field development in a direct injection diesel engine with different

manifolds," *International Journal of Engineering, Science and Technology*, 2(1), 80-91, 2010.

- 4) Xu, Z., Yi, J., Curtis, E., Wooldridge, S., "Applications of CFD modeling in GDI engine piston optimization," *SAE Technical Paper 2009-01-1936*.
- 5) Pathak, Y.R., Deore, K.D., and Maharu, P.V., "In cylinder cold flow CFD simulation of IC engine using hybrid approach," *International Journal of Research in Engineering and Technology*, 3(8), 16-21, 2014.
- 6) Priscilla and Meena, P., "A comprehensive study on in-cylinder IC engine due to swirl flow," *International Journal of Engineering Research & Technology*, 2(7), 1156-1161, 2013.
- 7) Abianch, O.S., Mirsalim, M., and Sabet, A.S., "Investigation of swirling and tumbling flow pattern of spark ignition engine," *The Journal of Engine Research*, 14, 27-34, 2009.
- 8) ANSYS Fluent, *Internal Combustion Engine Tutorial Guide*. 2015.

Investigation of Cylinder Deactivation strategies for better fuel consumption using 1-D Simulation Method

Izwan Hamid, Mohd Farid Muhamad Said*, Mohd Fadziel Mohamad Nor, Zulkarnain Abdul Latiff

Automotive Development Centre (ADC)
Faculty of Mechanical Engineering
Universiti Teknologi Malaysia
81310, Skudai, Johor, Malaysia
E-mail : mdfarid@utm.my

ABSTRACT

In order to meet consumer and legislation requirements, big investments on key technology strategies have been made to ensure fuel consumption is reduced. Recent technologies for gasoline engines are lean combustion technologies (including direct injection and homogenous charged compression ignition), optimizing intake and exhaust valve timing with valve lift and also cylinder deactivation system (CDA) have been practised to improve the engine efficiency. In this study, the purpose is to investigate the engine behaviour when running at different cylinder deactivation (CDA) strategies. One-dimensional engine model software called GT-Power is used to predict the engine performances. There are total of five strategies that have been studied which include normal mode, spark plug off mode, cylinder deactivation mode, intake normal with exhaust off mode, and intake off with exhaust normal mode. Engine performance outputs of each strategy are predicted and compared at BMEP of 3 bars with engine speed of 2500 rpm. Also, the effect of CDA strategies on in-cylinder pressure and pumping loss are performed. The study shows that all of these cylinder deactivation strategies are significantly reduce the pumping loss (PMEP) and fuel consumption, furthermore increasing the thermal efficiency of the engine. The results suggest that the most beneficial strategy for activating CDA is for the case whereby both the intake and exhaust valves are kept closed. This strategy successfully reduced the BSFC. It found that most of these cylinder deactivation strategies improve the engine performance during part load engine condition.

Keywords:

Cylinder Deactivation, GT-Power, Intake, Fuel Consumption, Pumping Loss

1. INTRODUCTION

Deactivating cylinders is one of the proven method to reduce fuel consumption in a multi cylinder engine. The fuel improvement that benefit from deactivating

cylinders ranging from 10% to 20% depending on the technological approaches [1-3].

Deactivation means that the cylinder is not producing combustion. There are several ways to deactivate the cylinder. The simplest method is just switching off the ignition. Since the fuel consumption is the main concern, the fuel injector must also be shut off. Other method includes shutting down the intake and exhaust valve from operating. In 1882, Mitsubishi Company tried several techniques of cylinder deactivation on its 1.4L, 4 cylinders Orion MD engine. The techniques are deactivate both intake and exhaust valves, or shut off the fuel supply while supplying fresh air without throttling, or shut off the fuel supply while re-circulating the exhaust gas, or just simply shut off the fuel supply. By doing so, it manage to reduce the fuel consumption up to 42% at certain engine condition [4].

This paper will look into several options of deactivating the cylinders. The methods of deactivating the cylinders will be implemented in a simulation engine model by using GT Power software. Different options of cylinder deactivation should affect the engine performance in different ways. Cylinder deactivation mainly focuses on reducing the pumping loss. Pumping loss is high at part load engine operation due to partially opened throttle valve [5]. This create negative pressure inside the intake manifold. The pumping loss should also be reduced by increasing the intake manifold pressure or by un-throttled operation [6].

Shutting down some cylinders operation will let the working cylinders to do extra work as to produce the same amount of work as if all the cylinders are running. In order to produce more work, the working cylinders need more air. The throttle opening should be opened wider to allow air access to the cylinders. When the throttle opening is open wider, it will increase the pressure in the intake manifold. This will reduce the pumping loss by the engine as the pressure is pushed into the active combustion chambers [7]

If the intake and the exhaust valves are kept shut, there should be air trapped inside the cylinder. The

enclosed air works like a pneumatic spring which is periodically compressed and decompressed without overall pumping work. Therefore, the parasitic losses of the dragged cylinders are reduced [8].

2. METHODOLOGY

2.1 Model Validation

In this study, the strategies to deactivate the cylinders are investigated using 1-D simulation approach. A simulation engine model has been built based on 1.6L Spark Ignition Campro engine. The simulation model is based on one dimensional analysis by using GT Power software. The engine model has been constructed based on actual design, dimensions and parameters. This model has been validated with experimental data as shown in figure 1 [9]. The errors between this simulation model and the actual engine testing are less than 5% which is acceptable to be used as a correlated model. This simulation engine model will be used to run the engine at several different modes.

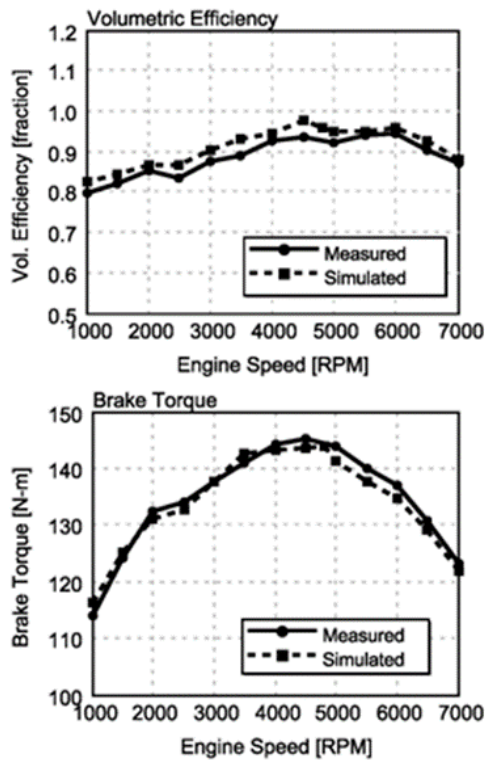


Figure 1: Comparison between Simulated and Measured data [9].

2.2 Parametric Study

For this simulation study, there will be four conditions of cylinder deactivation system to be analyzed. The conditions are based on the active and inactive of these four components which are the intake valve, exhaust

valve, spark plug and fuel injector. The simulation will be run in several modes which are in Normal mode and deactivated cylinders modes. There are four conditions of deactivating the cylinders:

- a) Spark plug off
- b) Cylinder deactivation mode (CDA Mode);
- c) Intake valves close; exhaust valves normal;
- d) Intake valves normal; exhaust valves close;

Normal mode refers to the normal operating conditions without any modifications to the original 4-cylinder engine model. "*Spark plug off*" condition is when only the spark plugs from the deactivated cylinders are switched off as the engine valves are operating in normal condition. "*Cylinder deactivation*" (CDA) mode is when both intake and exhaust valves are switched off. As for the *intake valves close; exhaust valves normal*, the intake valves are switched off by setting the lift arrays to zero while the exhaust valves runs normally and vice versa. Table 1 summarizes the engine operating modes to be simulated. Note that all of these modes only affects cylinder 2 and 3. Cylinder 1 and 4 are allowed to operate normally without any modification. The performance output of the engine in normal and CDA mode are evaluated based on engine speed range between 1000 to 4000 rpm and at specific engine load which is 3 bar BMEP. This operating conditions are selected based on the common driving conditions in Malaysia [10,11].

Table 1: Summary of engine modes to be simulated.

Modes	BMEP (bar)	Intake Valve	Exhaust Valve	Spark Plug	Fuel Injection
Normal mode	3	On	On	On	On
Spark plug off	3	On	On	Off	Off
CDA Mode	3	Off	Off	Off	Off
Intake valves close; exhaust valves normal	3	Off	On	Off	Off
Intake valves normal; exhaust valves close	3	On	Off	Off	Off

3. RESULT AND DISCUSSION

3.1 At Full Load Condition

Comparison of engine brake power for each mode at full load condition is depicted in Figure 2. It shows that by deactivating two cylinders, the power significantly drops to half compared to the power that the normal mode can achieve. The best power curve among the

deactivated modes comes from CDA mode where it produces a slightly higher power compared to other deactivated modes. The highest brake power CDA mode can produce is 32.3kW running at 6500rpm. The least production of power is when *intake normal; exhaust off* mode. This mode provides a steady curve between 4kW to 20kW of power between 1000rpm to 4000rpm.

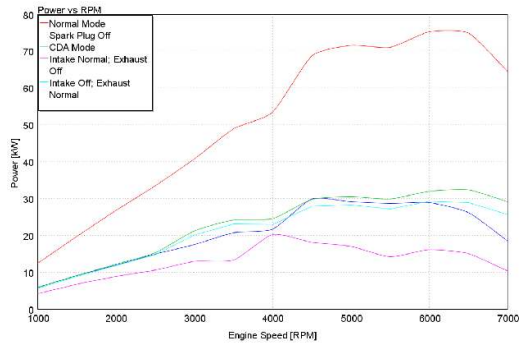


Figure 2: Brake Power versus Engine Speed for all engine modes at full load condition.

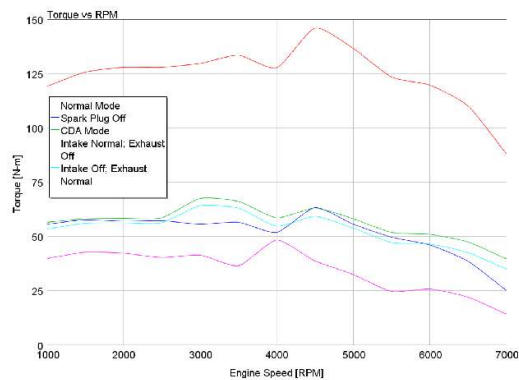


Figure 3: Brake Torque versus Engine Speed for all engine modes at full load condition.

Figure 3 shows the brake torque produced at different engine speeds for all engine modes. Based on the graph, it is obvious that normal mode produced the highest torque among all the modes. The maximum torque generated by normal mode in this simulation is 145.8Nm at 4500rpm. The deactivated mode that produces the highest torque is CDA mode. CDA mode manages to produce a 67.3kW of torque running at 3000rpm. The deactivated modes produce almost half amount of torque of the normal mode. However, these modes are usable and recommended when low torque driving conditions are necessary. Such conditions are during highway cruising just to maintain vehicle speed whereby hard acceleration is not needed.

3.2 At Part Load Condition

This study is to investigate the strategy of deactivating the cylinder especially at part load condition. Thus,

engine simulation model is applied to predict the engine performance at several fixed variables. Such variables are:

- The target engine BMEP for each mode is 3 bar at every engine speed (part load condition).
- The deactivated parameters include the spark ignition, fuel injectors, and intake and exhaust valves.

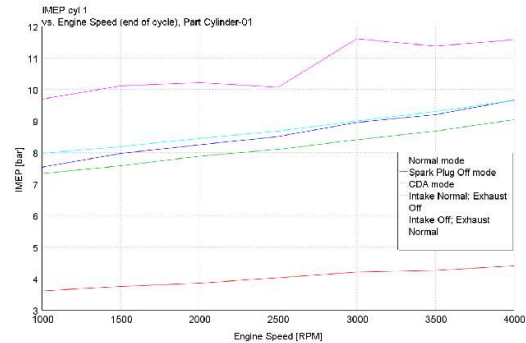


Figure 4: Comparison of Net IMEP per active cylinder versus Engine Speed for different deactivation strategy.

Figure 4 shows the Net IMEP at cylinder #1 for different deactivation mode. The best engine condition to produce high IMEP is when *intake normal; exhaust off* mode is initiated. At 2500rpm, *intake normal; exhaust off* mode manages to produce an IMEP value of 10bar which is 150% increase compared to *normal* mode that only produced 4 bar per active cylinder. *Intake off; exhaust normal* mode manages to produce 8.7 bar IMEP followed by *spark plug off* mode and CDA mode with 8.5bar and 8.1 bar IMEP respectively at 2500 rpm. Each mode contributes more than 100% increase in IMEP when two cylinders are deactivated.

Increase in net IMEP can be related to the reduction in PMEP. The following formula shows the relationship between PMEP and IMEP:

$$\text{Net IMEP} = \text{gross IMEP} - \text{PMEP}$$

By applying cylinder deactivation modes, the amount of PMEP is highly reduced since the intake pressure is increased (Figure 5). Therefore, this produces more positive work to the engine with low pumping work.

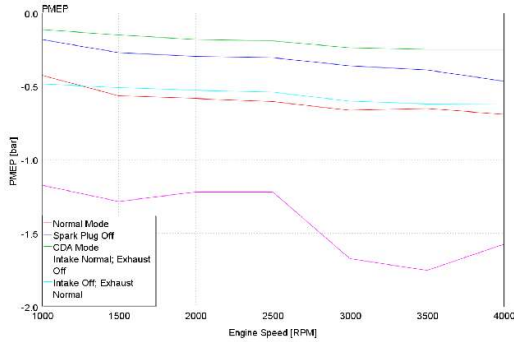


Figure 5: PMEP versus Engine Speed

The main purpose of cylinder deactivation is to reduce pumping work in the engine. Therefore, it is important to evaluate the PMEP of the engine to determine its efficiency in producing positive work.

The engine model that produces the lowest pumping loss is the *CDA mode* where the intake and exhaust valves are both closed (Figure 5). By closing the intake and exhaust valves, the trapped air act like pneumatic spring as the piston move up to compressed it. This will reduce the pumping work done by the engine.

However, the *intake normal; exhaust off* mode shows higher pressure value of PMEP. This indicates that this mode has high pumping loss. It happens due to the working intake valves in this mode while the exhaust valve is closed. Air is sucked into the cylinder during intake stroke, adding fresh air to the existing trapped air inside the cylinder that could not escape due to closed exhaust valve. This caused the pressure in the cylinder to build up and need extra work to compress the air.

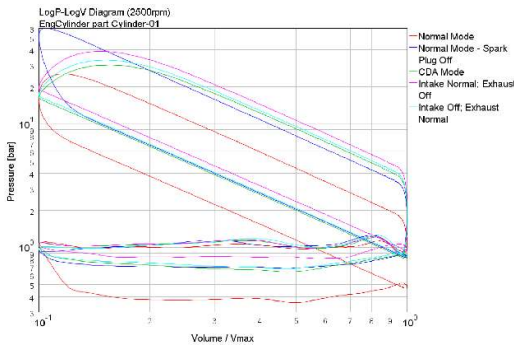


Figure 6: LogP-LogV diagram of all the engine modes (2500rpm; BMEP: 3 bar)

LogP-LogV diagram is plotted for different modes of engine and it is shown in Figure 6. It is clear that all deactivated modes reduce the pumping loss by increasing the pressure in the active cylinders. All the

deactivated modes show significant increase in pressure during compression and power stroke. In terms of positive work, the *spark plug off* mode produced a larger surface area in the graph during compression and power stroke. Therefore, it produced more work compared to the other engine modes. Overall, most of the deactivated modes shows significant reduction of pumping loss and increase of cylinder pressure for combustion.

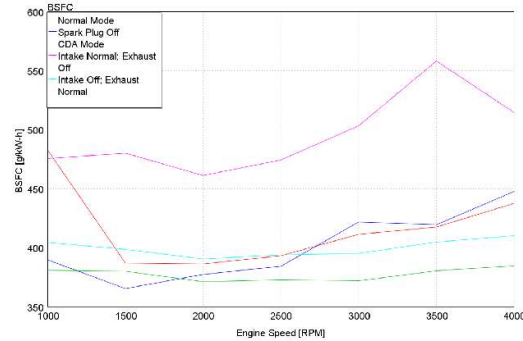


Figure 7: BSFC versus Engine Speed

BSFC is an important parameter in order to identify the fuel efficiency and fuel consumption of the engine. Based on the graph shown in Figure 7, the lowest BSFC recorded is 365 g/kWh at engine speed of 1500 rpm. This happen when the engine operates with only the spark plug at cylinder #2 and #3 are switched off. However, the BSFC increased when higher engine speed are applied.

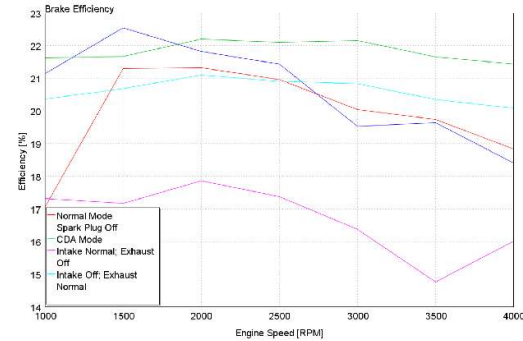


Figure 8: Comparison of engine's brake efficiency for every engine modes

The CDA Mode shows a small fluctuating value of BSFC between 371g/kWh and 384g/kWh. The worst performance in BSFC is when the spark plug, fuel injection, and exhaust valves of cylinder #2 and #3 are switched off while the intake valves operates in normal condition which produced 558 g/kWh at 3500rpm. This can be related with the very high pumping pressure in the cylinder due to the opening of the intake valve which leads to very high fuel consumption to power the engine.

The graph in Figure 8, above shows the brake efficiency of the engine in different engine modes. *Normal* mode starts to increase in brake efficiency from 17% to 21.3% between 1000rpm and 1500rpm. CDA Mode produces steady brake efficiency between 1000rpm to 4000rpm with an average value of 21.8%. CDA mode is clearly the best in brake efficiency among all the modes.

3.3 Summary of the Results

Table 2 shows the results summary between *normal* mode and the *cylinder deactivation* modes. These results are based on part load condition when the engine operates at 2500rpm, BMEP of 3 bar, and AFR of 13.8.

Table 2: Comparison between normal mode and the other cylinder deactivated modes.

Modes Parameter	Normal Mode	Spark Plug Off	CDA Mode	Intake Normal; Exhaust Off	Intake Off; Exhaust Normal
Net IMEP @ cyl 1	4.0	8.5	8.1	10.0	8.7
Net PMEP @ engine	-0.6 bar	-0.3 bar	-0.2 bar	-1.2 bar	-0.5 bar
BSFC @ engine	393 g/kW-h	384 g/kW-h	373 g/kW-h	474 g/kW-h	394 g/kW-h
Brake Efficiency @ engine	21%	21.4%	22.1%	17.4%	21%
Volumetric efficiency @ cyl 1	0.35	0.67	0.65	0.78	0.69
Maximum Cyl. Pressure @ cyl. 1	25.4 bar	59.5 bar	30 bar	38.7 bar	33 bar
Total Fuel Consumption per active cyl @ cyl. 1	13.1mg/cycle	25.5 mg/cycle	24.7 mg/cycle	29.6 mg/cycle	26.1 mg/cycle

Table 3: Percentage differences between normal mode and the cylinder deactivation modes

Modes Parameter	Normal Mode	Spark Plug Off (%)	CDA Mode (%)	Intake Normal ; Exhaust Off (%)	Intake Off; Exhaust Normal (%)
Net IMEP @ cyl. 1	4.03 bar	111.4	101.5	148.8	116.4
Net PMEP @ engine	-0.6 bar	-50.0	-66.7	100.0	-16.7
BSFC @ engine	393 g/kW-h	-2.3	-5.1	20.6	0.3
Brake Efficiency @ engine	21%	1.9	5.2	-17.1	0.0
Volumetric efficiency @ cyl. 1	0.35	91.4	85.7	122.9	97.1
Maximum Cyl. Pressure @ cyl. 1	25.4 bar	134.3	18.1	52.4	29.9
Total Fuel Consumption per active cyl @ cyl. 1	13.1mg/cycle	94.7	88.5	126.0	99.2

4. CONCLUSION

Computer simulation techniques are applied to obtain better understanding in term of cylinder deactivation technology on engine performance. The engine model has successfully predicted engine performance for various of deactivation strategy (mode). The simulation study shows that cylinder deactivation system in various modes does improves the engine in terms of efficiency and fuel consumption. As for reducing pumping loss or PMEP, the mode that is most effective and suitable is CDA mode where both the intake and exhaust valves are closed. CDA mode also has the lowest BSFC and overall fuel consumption amongst the other engine modes.

ACKNOWLEDGMENT

The authors acknowledge the financial support from Universiti Teknologi Malaysia (UTM), Ministry of Higher Education Malaysia (MOHE) under the research university grant Q.J130000.2409.01G53 and also Automotive Development Centre (ADC). Thanks also to Perusahaan Otomobil Nasional Sdn. Bhd for the technical support in this research activity.

REFERENCES

- 1) Kuruppu, C., Pesiridis, A., and Rajoo, S., "Investigation of cylinder deactivation and variable valve actuation on gasoline engine performance," *SAE Technical Paper* 2014-01-1170.
- 2) Leone, T. and Pozar, M., "Fuel economy benefit of cylinder deactivation - sensitivity to vehicle application and operating constraints," *SAE Technical Paper* 2001-01-3591.
- 3) Boretti, A. and Scalco, J., "Piston and valve deactivation for improved part load performances of internal combustion engines," *SAE Technical Paper* 2011-01-0368.
- 4) Fukui, T., Nakagami, T., Endo, H., Katsumoto, T., "Mitsubishi Orion-md - A new variable displacement engine," *SAE Technical Paper* 831007, 1983.
- 5) Shelby, M., Stein, R., and Warren, C., "A new analysis method for accurate accounting of IC engine pumping work and indicated work," *SAE Technical Paper* 2004-01-1262.
- 6) Shiao, Y., & Dat, L. V., "Efficiency improvement for an unthrottled SI engine at part load," *International Journal of Automotive Technology*, 13(6):885-893.
- 7) Watanabe, E. and Fukutani, I., "Cylinder cutoff of 4-stroke cycle engines at part-load and idle," *SAE Technical Paper* 820156, 1982.
- 8) Flierl, R., Lauer, F., Breuer, M., and Hannibal, W., "Cylinder deactivation with mechanically fully variable valvetrain," *SAE Int. J. Engines* 5(2):207-215, 2012.
- 9) Muhamad Said, M., Abdul Aziz, A., Abdul Latiff, Z., Mahmoudzadeh Andwari, A., "Investigation of cylinder deactivation (CDA) strategies on part load conditions," *SAE Technical Paper* 2014-01-2549.
- 10) Zahari, I., Abas M.A., Mat Arishad N.I., Zainal Abidin S.F., and Muhamad Said M.F., "Experimental study to identify common engine part load conditions between Malaysian city driving and NEDC test," *International Review of Mechanical Engineering*, 2013. 7(6): p. 1152-1158.
- 11) Abas, M., Salim, O., Martinez-Botas, R., and Rajoo, S., "Efforts to establish Malaysian urban drive-cycle for fuel economy analysis," *SAE Technical Paper* 2014-01-1159.

Design and Experimental Analysis of Low Temperature Freezer Using Cascade Method

Kasni Sumeru^{a,b}, Azhar Abdul Aziz^b, Henry Nasution^b, Adekunle Moshood Abioye^{c, d}

^a Department of Refrigeration & Air Conditioning
Politeknik Negeri Bandung, Bandung 40012
Tel : (022) 2013789 ext 254. Fax : (022) 2013889
E-mail : sumeru84@gmail.com

^bAutomotive Development Centre
Faculty of Mechanical Engineering, Universiti Teknologi Malaysia, Johor 81310
E-mail : azhar@fkm.utm.my

^cFaculty of Mechanical Engineering, Universiti Teknologi Malaysia, Johor 81310

^dDepartment of Mechanical Engineering, Abubakar Tafawa Balewa University, Bauchi, Nigeria
E-mail : kunleabioye@yahoo.com

ABSTRACT

Typically, a cascade vapor compression refrigeration cycle is applied for low freezer temperature, because single compressor is not effective for this purpose due to low performance and overheating on the compressor. A prototype of freezer using cascade method with R22 for the high pressure stage and R404A for the low pressure state as working fluids has been designed and constructed. The prototype uses two compressor, namely 0.3 HP (225.0 W) and 0.25 HP (187.5 W) for the high and low stages respectively. The evaporator made from copper tube of 3/8 inch (9.5 mm). Designed temperatures of the condenser, intercooler and evaporator are 40°C, -8°C and -62°C respectively. In order to obtain the predesigned temperature, the appropriate length of evaporator and intercooler were determined based on the heat transfer analysis. The results from this analysis, the length of evaporator was 16.201 m. The experimental results showed that the evaporating temperature was higher than that of theoretical model, which is -59.0°C. The coefficient of performance (COP) of a cascade prototype was 1.67. This COP is higher compared with COPs of single stage, namely 1.25 and 0.87 for the same operating conditions, i.e. 40°C and -62°C for the condensing and evaporating temperatures, respectively.

Keywords: Cascade, low temperature, intercooler, evaporator.

1. INTRODUCTION

Compared with other refrigeration systems, vapor compression refrigeration cycle (VCRC) has the highest

coefficient of performance (COP). However, at very low temperature, below -40°C, the COP of VCRC drop significantly. The drawback of the single stage VCRC at very low temperature applications decreases the COP and increases compressor discharge temperature. The increase in compressor discharge temperature increases the compression ratio of the compressor. For instance, the discharge temperature of single compressor system using R22 as working fluid at evaporating and condensing temperature of -50°C and 40°C respectively is approximately 100°C. High discharge temperature tends to increase the rate of lubricating oil breakdown and material fatigue of the compressor.

The compression ratio is ratio between discharge and suction pressures. Due to safety reason, the compression ratio of reciprocating compressors are designed to operate not exceed 12. When a freezer using R22 as working fluid operates at condensing temperature of 40°C, this temperature corresponds to a saturation pressure of 1534 kPa. If the evaporating temperature of -20°C and -40°C, the evaporating pressures correspond to saturation pressures of 245 kPa and 105 kPa, respectively. Furthermore, the compression ratios at the evaporating temperature of -20°C and -40°C are 6.3 and 14.6, respectively [1]. It means that the freezers that operate at -20°C is still safe using single stage compressor, while it do not recommended using single compressor when the evaporating temperature below -40°C, because the compression ratio above 12.

Overheating on the compressor discharge and the high compression ratio result in the evaporating temperature of single stage of VCRC limited, i.e. must be above -40°C. To overcome these limitations, a cascade method

can be applied. In a cascade method, two compressors are utilized and a intercooler applied as a heat exchanger between the condenser of low stage and evaporator of high stage. Besides reducing the overheating and the high compression ratio, the cascade method also increases the COP if compared with single stage which has the same condensing and evaporating temperatures [1-5]. Threlkeld [1] reported that the cascade method increased the COP up to 22% than that of single stage using ammonia as working fluid. Also, numerical simulation carried out by Kim et al. [5-7] reported that the cascade method reduced the input power of the compressor compared to single stage for the same the condensing and evaporating temperatures.

The main scope of this study is to design, construct and investigate experimentally a cascade refrigeration system using two reciprocating compressors. Refrigerant R22 and R404A are used as working fluid in high and low stages respectively. The prototype uses two compressors with capacity 0.3 HP (225.0 W) and 0.25 HP (187.5 W) for the high and low stages respectively.

2. SYSTEM CONFIGURATION

A cascade refrigeration system consists of two compressor, two evaporator, two condensers and two expansion devices, as shown in Figure 1. The figure shows that the high stage of the cascade method uses R22 as working fluid, whereas the low stage uses R404A as refrigerant.

The condenser of the low stage and the evaporator of the high stage are put inside the intercooler. As a result, the released heat from the condenser will be absorbed by the evaporator. In this investigation, the length of the evaporator of the low stage will be calculated.

The cascade cycle in P-h (pressure vs. enthalpy) diagram is shown in Figure 2. According to Figure 2, the COP of the cascade system is,

$$COP_{cs} = \frac{\dot{m}_1(h_1 - h_4)}{\dot{m}_1(h_2 - h_1) + \dot{m}_2(h_6 - h_5)} \quad (1)$$

The cascade COP as shown in Eq. (1) is higher than that of single stage COP for the same the condensing and evaporating temperatures. The single stage COP is determined with Eq. (2).

$$COP_{st} = \frac{(h_1 - h_4)}{(h_6 - h_1)} \quad (2)$$

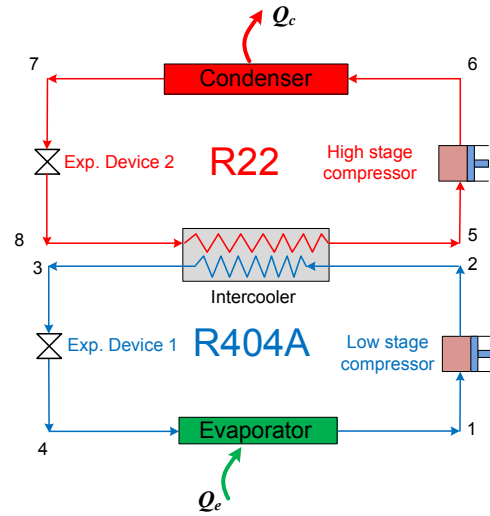


Figure 1: Schematic diagram of a cascade refrigeration system

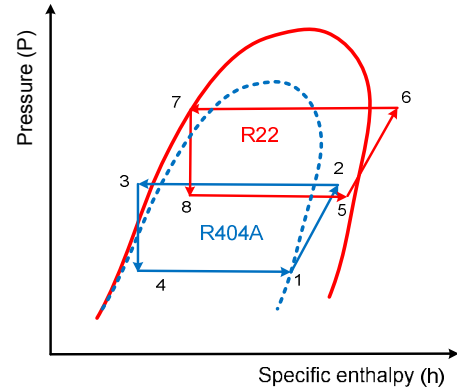


Figure 2: P-h diagram of a cascade refrigeration system

3. EVAPORATOR DESIGN

To achieve desired temperature in the low stage evaporator, the length of the evaporator must be designed accurately. Before designing the length of the evaporator, the design conditions must be determined. Table 1 shows the design condition.

Table 1: Design conditions.

No	Parameter	(°C)
1.	Evaporating temperature	-62
2.	Condensing temp. of high stage	40
3.	Condensing temp. of low stage	-8
4.	Evaporator temp. Different (ETD)	3
5.	Cabin temperature	-57
6.	Ambient temperature	30

There are two ways heat transfer occurs on the evaporator, namely free and forced convections. Free convection occurs between the air in the cabin with the tube surface of the evaporator, whereas the forced convection occurs inside the evaporator tube.

The evaporator is made from copper tube with inner and outer diameters of 0.00870 m and 0.009535 m respectively. The equation to determine the length of the evaporator is,

$$\frac{Q}{L} = \frac{\Delta T(2\pi)}{\frac{1}{h_a r_o} + \frac{\ln(r_o/r_i)}{k} + \frac{1}{h_b r_i}} \quad (3)$$

Due to free convection heat transfer, the convection heat transfer coefficient for “ h_a ” is calculated using Eq. (4).

$$Nu = \frac{h_a \cdot d_o}{k_f} = C (Gr Pr)^m \quad (4)$$

where, Gr = Grashof number and Pr = Prandtl number.

$$Gr.Pr = \frac{g \beta (T_w - T_\infty) d_o^3 Pr}{\nu^2} \quad (5)$$

The air properties are evaluated at film temperature (T_f), where $T_f = (T_w + T_\infty)/2$ and $T_w = T_e + ETD$. As a result, $T_f = ((-62+3)+30)/2 = 14.5^\circ\text{C} = 258.5 \text{ K}$, and $\beta = 1/T_f$ hence $\beta = 1/258.5 = 0.00386/\text{K}$. The air properties at film temperature of 258.5 K are:

$$\begin{aligned} \rho &= 1.373 \text{ kg/m}^3 \\ c_p &= 1.0054 \text{ kJ/kg} \\ Pr &= 0.719 \\ k_f &= 0.02294 \text{ W/m.K} \\ \mu &= 1.64 \times 10^{-6} \text{ kg/m.s} \\ \nu &= 12.05 \times 10^{-6} \text{ m}^2/\text{s} \end{aligned}$$

Hence,

$$Gr.Pr = 14406.323$$

Based on the table [5], for $Gr.Pr = 14406.323$, the values of m and C are 0.25 and 0.480 respectively. As a result, Eq. (4) becomes

$$Nu = \frac{h_a \cdot d_o}{k} = 5.26$$

Then,

$$h_a = \frac{Nu \cdot k}{d_o} = \frac{(5.26) \cdot (0.002294)}{(0.009525)}$$

$$h_a = 12.67 \text{ W/m}^2 \cdot \text{K}$$

Furthermore, the value of “ h_b ” is evaluated using Eq. (6), due to boiling heat transfer inside the evaporator tube.

$$h_b = 0.62 \left[\frac{k_g^3 \rho_v (\rho_l - \rho_v) g (h_{fg} + 0.4 c_p \Delta T_x)}{d_i \mu_v \Delta T_x} \right]^{1/4} \quad (6)$$

The R404A properties at film temperature (for this case the film temperature is 60.5°C) are:

$$\begin{aligned} k_g &= 8.05 \times 10^{-3} \text{ W/m.K} \\ \rho_v &= 2.29 \text{ kg/m}^3 \\ \rho_l &= 1359.4 \text{ kg/m}^3 \\ h_{fg} &= 212.10 \text{ kJ/kg} \\ c_p &= 0.573 \text{ kJ/kg.K} \\ \mu_v &= 8.47 \times 10^{-6} \text{ kg/m.s} \\ d_i &= 0.0087 \text{ m} \end{aligned}$$

Hence, the heat transfer coefficient of h_b is

$$h_b = 3878 \text{ W/m}^2 \cdot \text{K}$$

When “ h_a ” and “ h_b ” insert to Eq. (3), the result is

$$\frac{Q}{L} = 34.720 \text{ W/m}$$

By assuming that the COP of low stage is 3, as a result, the cooling capacity of the evaporator is $3 \times 187.5 = 562.5 \text{ W}$. Hence, the length of the evaporator tube is

$$L = \frac{562.5}{34.720} = 16.201 \text{ m}$$

Based on the numerical results above, the evaporator for low stage is installed in the cascade system.

4. RESULT AND DISCUSSION

The experiment on the cascade system was carried out to validate the numerical results. There two parameters were measured on the system, namely temperature and

pressure. The accuracies of temperature and pressure are shown in Table 2.

Table 2: The accuracies of measuring instrument.

Instruments	Measurement	Accuracy
T-type thermocouple	Temperature	$\pm 0.1^\circ\text{C}$
Pressure gauge	Low pressure	± 0.1 bar
Pressure gauge	High pressure	± 0.5 bar

Based on obtained temperatures and pressures measuring, the results are plotted in P-h diagram as shown in Figure 2, and the results are:

$$\begin{aligned} h_1 &= 198.1 \text{ kJ/kg} \\ h_2 &= 428.2 \text{ kJ/kg} \\ h_3 &= 356.3 \text{ kJ/kg} \\ h_7 &= 181.6 \text{ kJ/kg} \\ h_5 &= 406.2 \text{ kJ/kg} \\ h_6 &= 445.0 \text{ kJ/kg} \end{aligned}$$

Hence the refrigerant mass flow rate in the low stage is

$$\dot{m}_{R404A} = \frac{0.1875}{(428.2 - 383.1)} = 0.00416 \text{ kg/s}$$

$$\dot{m}_{R22} = \frac{0.225}{(445.0 - 406.2)} = 0.00580 \text{ kg/s}$$

Furthermore, the COP of cascade system is determined using Eq. (1),

$$COP_{cs} = 1.87$$

This COP of cascade system is higher compared to the single stage using R22 or R404A. The COPs for ideal single stage using R22 and R404A with condensing and evaporating temperature of 40°C and -62°C , respectively are 1.25 and 0.87, respectively.

The experimental results showed that the COP of designed cascade system was higher than that of single stage at very low temperature. Besides the COP, the evaporator temperature also indicates the performance of the designed system. Figure 3 shows the evaporator temperature during the experiment.

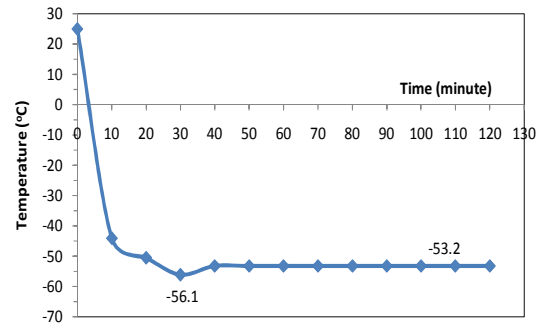


Figure 3: Evaporator temperature of the cascade system

Figure 3 shows that the minimum temperature occurs at 30 minute, that is -56.1°C . Furthermore, the steady state condition occurs after 40 minute with temperature of -53.2°C . Compared to the designed evaporating temperature, i.e., -62°C , the experimental results of the evaporating temperature at the steady state condition is 8.8°C hotter than that of designed temperature. The difference between designed and experiment might be because the designed evaporator is longer than the its ideal length, as a result, causes too high superheating on the suction. This condition increases the evaporator temperature in the cabin. Ideal superheating for low temperature is approximately $2\text{-}5^\circ\text{C}$.

To investigate the superheating, in this experiment, the measuring was also conducted on the inlet and outlet of the evaporator. The inlet and outlet of the evaporator is located at outside of the cabin. The temperatures of inlet and outlet of the evaporator are shown in Figure 4.

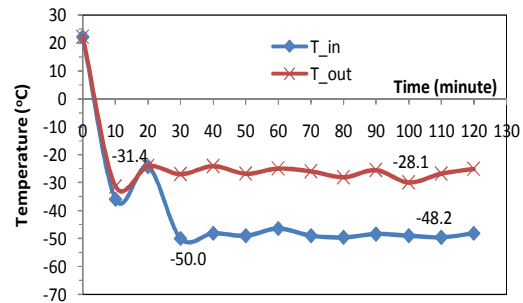


Figure 4: Temperature at inlet and outlet of the evaporator

Figure 4 shows that the minimum temperatures of inlet and outlet are -50.0 and -31.4°C respectively. Meanwhile, the temperature at the steady state conditions for inlet and outlet are -48.2 and 28.1°C respectively. It can be seen that there is a difference of approximately 20°C between inlet and outlet temperatures. If the outlet temperature is compared to the evaporator temperature at the steady state, as shown in Figure 3, the difference is 25.1°C . This difference is

too high, if this is assumed as superheating. This phenomenon might cause the evaporator temperature based on the numerical is hotter than the designed temperature. In other words, the length of the evaporator is longer than the ideal length.

heat pump systems”, *Int. J. Refrig.*, vol. 29, pp. 254-258, 2014.

5. CONCLUSION

The experimental results showed that the methods and the equations used for designing the system were relatively accurate. Inaccurate calculation in the design of the length of the evaporator causes high superheating on the evaporator. Based on the numerical approach, using copper tube with diameter of 3/8 inch (9.5 mm), the length of evaporator tube was 16.201 m. The evaporating temperature based on the experimental was -53.2°C , 8.8°C higher than that of the designed temperature. Also, the cascade freezer prototype had the COP higher than that of single stage freezer at the same working temperatures.

ACKNOWLEDGMENT

This study was supported financially by Ministry of Education, Malaysia under the Research University Grant. The grant was managed by The Research Management Centre, Universiti Teknologi Malaysia. In addition, the authors are also grateful to Politeknik Negeri Bandung Indonesia for facilities and management support.

REFERENCES

- [1] J. L. Threlkeld, *Thermal Environmental Engineering*, 2nd ed. Prentice Hall, Inc., New Jersey, 1970, pp. 63-71.
- [2] D. A. Dokandari and A. S. Hagh, “Thermodynamic investigation and optimization of novel ejector-expansion CO_2/NH_3 cascade refrigeration cycle (novel CO_2/NH_3 cycle)”, *Int. J. Refrig.*, vol. 46, pp. 26-36, 2014.
- [3] T. S. Lee, C. H. Liu and T. W. Chen, “Thermodynamic analysis of optimum condensing temperature of cascade condenser for CO_2/NH_3 cascade refrigeration system”, *Int. J. Refrig.*, vol. 29, pp. 1100-1108, 2006.
- [4] H Park, D. H. Kim and M. S. Kim, “Performance investigation of a cascade heat pump water heating system with a quasi-steady state analysis”, *Energy*, vol. 63, pp. 283-294, 2013.
- [5] H Park, D. H. Kim and M. S. Kim, “An experimental study on the optimal intermediate temperature of a cascade refrigeration system with R134a and R410A”, In Proceeding of the 6th Asian conference on refrigeration and air-conditioning, 2012.
- [6] H Park, D. H. Kim and M. S. Kim, “Thermodynamic analysis of optimal intermediate temperature in R134a and R410A cascade refrigeration system and its experimental verification”, *Appl. Therm. Eng.*, vol. 54(1), pp. 319-327, 2013.
- [7] D. H. Kim, H. S. Park and M. S. Kim, “The effect of the refrigerant charge amount on single and cascade cycle

Flame Propagation and Burning Rates of Methane-Air in a Closed Combustion Vessel

Mohd Suardi Suhaimi, Aminuddin Saat* and Mazlan Abd Wahid

*Department of Thermofluids, Faculty of Mechanical Engineering,
Universiti Teknologi Malaysia, 81310 Skudai, Johor, Malaysia
E-mail: amins@mail.fkm.utm.my

ABSTRACT

The propagation and burning rates of methane-air mixtures were investigated at initial atmospheric pressure with temperature range of 298-302K and equivalence ratio range of 0.8 to 1.3. Experiments were performed in a cylindrical constant volume combustion chamber where the mixture is ignited by centrally located electrodes. The images of spherically expanding flame were observed and recorded using schlieren photography technique with high speed camera system. Analysis of the flame area yield flame radii and further burning rates in term of outwardly flame speed propagation can be calculated. Results shows that smooth spherical flames were observed throughout the flame propagation for all equivalence ratios. The fastest flame propagation was recorded at equivalence ratio 1.0 and 1.2. In addition, flame speed of each equivalence ratio exhibits small fluctuation probably arising from acoustic disturbance. This disturbance becomes more apparent at higher equivalence ratio.

Keywords:

Methane-air, flame speed, schlieren, constant volume

1. INTRODUCTION

The determination of combustion characteristics such as laminar burning velocity is of primary importance as it relevance to both laminar and turbulent premixed combustion. Detailed knowledge from accurate measurement of laminar premixed flames will provide valuable insight on propagation rates, heat release, flammability limits, quenching and emission characteristics. Another useful insight from laminar premixed flame is that it could serve as a preliminary data in understanding a much more complex combustion such as turbulent non-premixed combustion and also combustion process in practical combustor such as internal combustion engine where the initial stage of combustion involves laminar premixed combustion.

Several methods have been used to determine this parameter such as flat flame [1,2], counterflow flame

[3,4] and spherically expanding flame[5-8]. These experiments also enable the study of another parameter which is the stretch that acts on the flame front. This parameter is a combination of curvature and strain rate and is described by Markstein length [9]. For spherically expanding flame, the stretch can be obtained analytically from flame speed and radius. The unstretched flame speed on the other hand could be obtained from linear extrapolation of the flame speed and stretch curve [10]. However it is sensitive to the data obtained from experiment. Earlier work by Taylor [5] involved the differentiation of the spherically expanding flame radius to obtain flame speed, stretch, Markstein length and burning rate. Tahtouh et al [9] compared three different analysis methods namely the polynomial fitting, raw radius differentiation and a new method that involves resolution of Clavin's equation to determine the aforesaid parameters. They reported that each method yield different results.

The objective of this study is to determine the burning rates of methane-air mixture in term of flame speed propagation using images from schlieren photography. Methane is one of the abundant gaseous fuels in nature that also exist in nature as the flammable part of biogas [11]. Schlieren photography is a photography technique that makes use of the density gradient in the vicinity of the object of interest. This is particularly useful in combustion as it generates a region with defined density gradient arising from heat generated. Though the method is not novel, obtaining improved images could improve results from literature. Schlieren photography also permits the exclusion of experiments that produce cellular flame for the purpose of determining flame speed, Markstein length and burning rates [11]. This exclusion is important as the occurrence of cellularity will render the smooth flame front assumption. Comparison with data from literature may also serve as a calibration to the rig setup used in this study.

2. EXPERIMENTAL SETUP

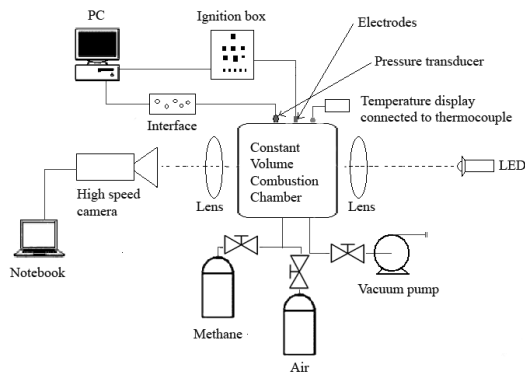


Figure 1. Experimental setup

Figure 1 shows a schematic of experimental setup consisting of a cylindrical constant volume combustion chamber with a volume of 29.3 litre and two 190mm quartz windows, ignition system, Phantom 7.1 high speed camera, collimating and decollimating lens and an LED light source. Ignition was initiated and controlled with Labview 7.1 software that also serves as a data logger recording pressure rise during combustion.

The cylindrical combustor used in his study is equipped a pair of opposing spark electrodes to provide ignition at the center of the combustor. After a vacuum was created in the combustion chamber by a vacuum pump, the chamber was filled with methane and dry air using partial pressure technique which correspond to the desired equivalence ratio. The initial pressure for each experiment was set at atmospheric pressure, while the initial temperature was in the range of 298 to 302K. Ignition was controlled using a desktop computer with LabView 7.1 software connected to the ignition box after the capacitor was charged. The 190 mm windows provide wide optical access and currently limited by the lens used. A pair of collimating and decollimating lens with 150 mm diameter was used. Both lenses have a focal length of 700 mm. The developing flame videos were recorded at 2000 frames per second. A 1.5W LED lamp was used as a light source to illuminate the combustor internal section.

A phantom high speed camera was used to capture the spherically expanding flame at a speed of 2000 frame per second. The recorded cine videos were then converted to image files for further analysis using image processing software. Adobe Photoshop image editing software was used to convert to the images of the spherical flames to binary images. These binary images were then analyzed using a Matlab script file to obtain flame area and later the radius. The obtained flame radii were then tabulated in a spreadsheet file and the flame speed was calculated by differentiating the flame radius with time in a first order fit of five points.

3. RESULTS AND DISCUSSION

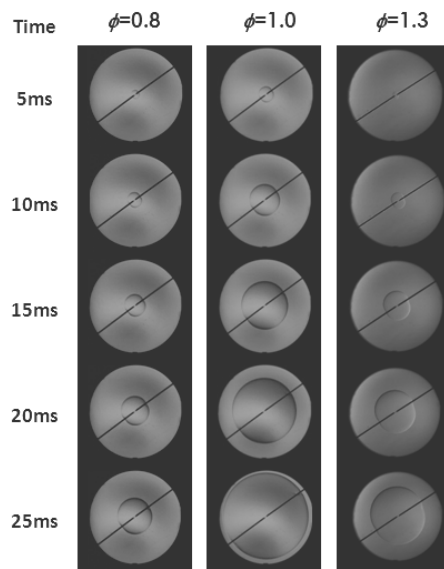


Figure 2. Development of spherical flame propagation of methane-air with central ignition.

Figure 2 shows development of methane-air spherical flame at different equivalence ratio of 0.8, 1.0 and 1.3. The circular boundary represents the size of the optical access windows and the black line crossing in each images is a pair of steel spark electrodes connected to the ignition system to initiate spark from central region. In general, throughout the propagation, all flames developed in a smooth spherical flame. The flame of stoichiometric equivalence ratio developed at a much faster rate compared to the flame at the equivalence ratio of 0.8 and 1.3. This corresponds to the characteristics of combustion where the flame speed tend to be higher at equivalence ratio slightly than stoichiometric and lower in the rich or lean side[12].

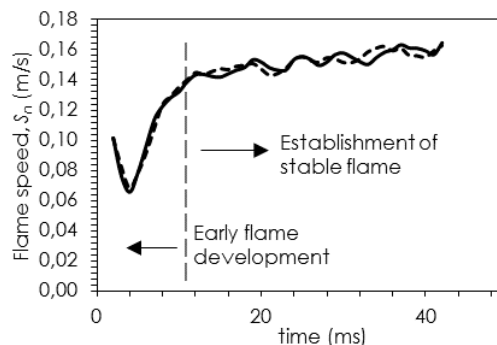


Figure 3. Variation of flame speed of methane-air mixture with time at equivalence ratio of 0.8

Figure 3 shows the variation of flame speed as a function of time at equivalence ratio of 0.8 from two identical experiments. The plot depicts a typical flame

speed progress over time with a sharp decrease from the point of ignition to a certain time where it reaches a minimum pivotal point. This could be attributed to the radicals from the spark that rapidly dissipates until it reaches the minimum point [6]. The spark also creates shockwave that propagates outward, followed by a slower thermal wave. The thermal wave front usually has high initial speed that rapidly decreases over a short period of time [13]. From the minimum point, flame speed start to increase again until it stabilizes with time as the combustion progresses. Within this region normal chemistry predominate combustion as the radicals from the spark diminishes. Flame establishment can be estimated by the linear relation of flame speed against stretch rate which will be discussed later.

Both experiment shows similar trend with a slight variation suggesting good data reproducibility. The percentage of flame speed fluctuation after 15 ms onwards is around 6.3% which is considerably low. The noticeable fluctuation at 19 ms onwards could be linked to acoustic disturbances as observed by Gillespie et al [10]. The flame-acoustic disturbances is caused by an interaction between heat release and acoustic waves [14]. Curved flames (including spherical flame) are more susceptible to acoustic disturbances, where the propagating flame front is stretched and curved by acoustic waves [15]. This disturbance could also be influenced by combustor geometry [16].

Figure 4 shows the comparison of flame speed obtained from different equivalence ratio with respect to time. The trend of the flame speed development displays similar trend with a sudden decrease to a minimum point before it increase again to reach an approximately stable speed with noticeable fluctuation. It is interesting to note that, fluctuation commenced after around 15 ms for each experiment. The percentages of fluctuation are about 12%, 18% and 19 % for stoichiometric, 1.2 and 1.3 experiments, respectively. Apparently, fluctuation is more pronounced at higher equivalence ratio. This might suggest acoustic disturbance, as discussed earlier, is more prevalent at richer side.

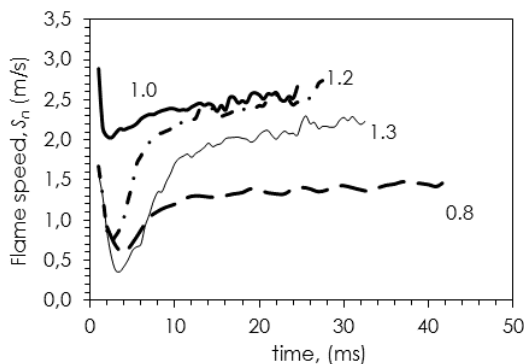


Figure 4. Variation of flame speed of methane-air mixture with time at equivalence ratio of 0.8, 1.0, 1.2 and 1.3.

In terms of trend, the initial flame speed and the point at which the minimum flame speed occurs is different from each condition. This point is highest for flame under stoichiometric condition followed by the flame of 1.2, 0.8 and 1.3. In the early stage of flame propagation, the flame is overcoming the quenching tendency due to high stretch rate arising from curvature effect[17]. Also, the flame speed of 0.8 progressed slower compared other experiments. This is followed by 1.3, 1.2 and lastly 1.0. This indicates the relative speed of the flame under different equivalence ratio. Flames that are either on the leaner or the richer side usually propagates slower than flame under stoichiometric condition. This is due to the disparity in thermal and mass diffusivity magnitude that would affect mass and heat transfer hence the flame propagation; whereas under stoichiometric condition, the magnitude of both thermal and mass diffusivity are equal[18]. The graph also reveals the time at which the flame stabilizes after ignition. The flames of each run took approximately 10 ms to reach an approximately stable flame propagation.

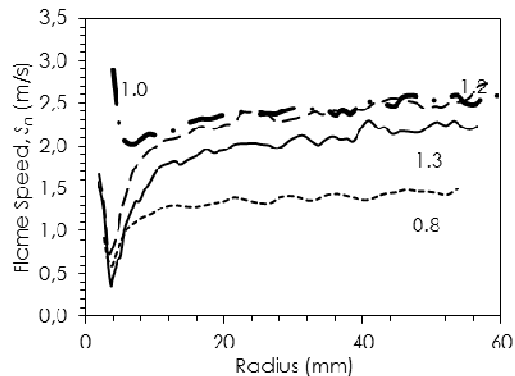


Figure 5. Variation of flame speed of methane-air mixture with radius at equivalence ratio of 0.8, 1.0, 1.2 and 1.3.

Figure 5 shows the plot of flame speed versus radius of methane-air mixture for experiments of 0.8, 1.2 and 1.3 equivalence ratios. The plot shows a periodically scattered data with a trend similar to flame speed variation with time. Fluctuation however is less pronounced in each experiment. At approximately 2 mm radius, the flame reaches its minimum value after ignition. The radius is about 1 mm larger for stoichiometric experiment. From this minimum point onwards, the flame development is due to normal chemistry. Data with radii less than 10mm should be discarded for burning rate calculation, as within this range the flame is significantly influenced by the radicals and shockwave from the spark [17].

Figure 6 shows the variation of methane-air mixture flame speed with stretch. The flame stretch here is defined as the time derivative of the spherical flame area of an infinitesimal element divided by the spherical flame area [10]. With the exception of stoichiometric experiment, the variation of flame speed for three other experiments i.e. for equivalence ratio of 0.8, 1.2 and 1.3 shares some similarities especially the characteristics twist during the early stage of flame propagation. This could be attributed to the effect of ignition energy and also to different stretch rate at the early stage of combustion at earlier stage of flame development [17]. Apparently stretch rate becomes more apparent under lean and rich region. Extrapolating flame speed to a point of zero stretch rate in Figure 6 yields unstretched flame speed, S_b while the slope gives the Markstein length L_b . However, prior to extrapolation, some data especially those represent the early stage of combustion should be excluded as these data are generally affected by ignition spark and could lead to over or underestimation of unstretched flame speed.

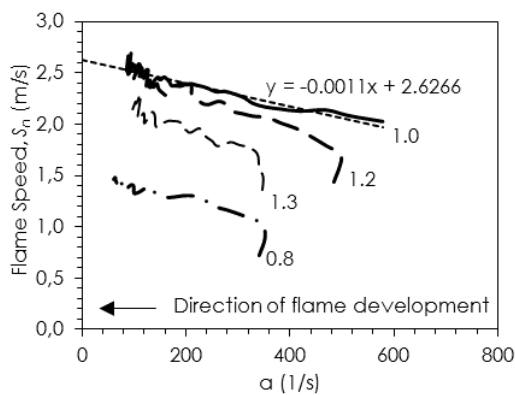


Figure 6. Variation of flame speed of methane-air mixture with stretch rate at equivalence ratio of 0.8, 1.0, 1.2 and 1.3.

The magnitude and signs of Markstein length indicates the effect of stretch on flame propagation. Positive Markstein length indicates that stretched flame speed decreases as stretch rate increases and the flame tend to restrain any disturbance at the flame front leading to flame stability [17]. In this case, the surface convex to the unburned area will be stretched in the opposite direction, and this will suppress flame speed, and the flame stabilizes. On the contrary, negative Markstein length indicates that flame speed increases proportionally with stretch rate, and flame surface will stretch in the same direction, inducing flame front instability in the process. Obviously from Figure 6, Markstein length for each equivalence ratio is positive with different magnitude as indicated by their relative slope. This value is consistent with the smooth flame observation as shown in Fig. 2 for all equivalence ratios.

Figure 7 shows comparison of laminar burning rates of methane-air mixture at different equivalence ratio between previous studies and current study. The laminar burning rates is calculated by multiplying the unstretched flame speed obtained from Fig. 6 with the density ratio of burned and unburned gas which computed under the assumption of adiabatic constant pressure combustion [6]. All plots were obtained by drawing a best fit curve through the data points. The burning rate variation with equivalence ratio shows a quadratic trend with a characteristics peak at equivalence ratio of 1.1. The maximum of burning rates at slightly rich equivalence ratio was probably due to the combined effect of the adiabatic flame temperature and dissociation of combustion products.

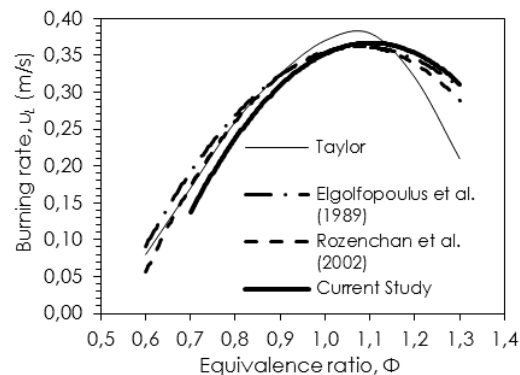


Figure 7. Comparison of methane-air mixture burning rate between present and previous works at equivalence ratio from 0.7 to 1.3.

It is shown that at equivalence ratio of 1.3, the burning rate is higher in this study at 0.31 m/s compared to observations by Rozenchan et al [7] and Elgolfopoulos et al [20] at 0.28 m/s, while Taylor [5] recorded the slowest burning rate at 0.21 m/s. This could be linked to the slightly higher initial temperature for this experiment at 302K. Marginal increase in unburned gas temperature may consequently increase the burning velocity [21]. Different methodology and the quality of data obtained from each study could also lead to different results [9]. This could be observed by results from [21] who used the counterflow methodology to determine the burning rate of methane-air mixture while both [5,7] used recorded schlieren images of spherically expanding flame.

4. CONCLUSION

In the present work, the combustion of methane has been studied by analyzing the spherical propagation flame of methane-air mixture in term of flame development, flame speed and the burning rates. Smooth and stable spherical flames were observed throughout flame development for all equivalence ratio. However, a small fluctuation of the flame speed after the spark influence region suggesting the presence

of acoustic disturbance in the later stage of flame propagation. This fluctuation varies from 7% and up to 19% as equivalence ratio was increased from 0.7 to 1.3, suggesting the influence of equivalence ratio on acoustic disturbance.

The burning rates of methane-air in this study shows a good agreement in comparison with the previous works. Apart from the experimental methodology, the quality of images obtained, image processing and the methods of data analysis could be considered as the source of uncertainties. The largest variation in terms of burning rate could be observed in the case of experiment with equivalence ratio of 1.3. This could be explained by the difference in initial temperature of this particular experiment which is slightly higher at 302K.

ACKNOWLEDGMENT

The authors would like to thank Ministry of Higher Education and Universiti Teknologi Malaysia for supporting this research activity under a Fundamental Research Grant Scheme.

REFERENCES

- [1] Bosschaart, K. J., de Goey, L. P. H. 2004. The laminar burning velocity of flames propagating in mixtures of hydrocarbons and air measured with the heat flux method. *Combust. Flame*. 136: 261–269.
- [2] Konnov, A. A., Dyakov, I. V., De Ruyck, J. 2003. Measurement of adiabatic burning velocity in ethane–oxygen–nitrogen and in ethane–oxygen–argon mixtures. *Exp. Therm. Fluid Sci*. 27: 379–384.
- [3] Chao, B.H., Egolfopoulos, F.N., Law, C.K. 1997. Structure and propagation of premixed flame in nozzle-generated counterflow, *Combust. Flame*. 109: 620–638.
- [4] Jackson, G.S., Sai, R., Plaia, J.M., Boggs, C.M., Kiger, K.T. 2003. Influence of H₂ on the response of lean premixed CH₄ flames to high strained flows. *Combust. Flame*. 132: 503–511.
- [5] Taylor, S. C. 1991. Burning velocity and the effect of flame stretch. PhD Thesis. University of Leeds.
- [6] Gu, X.J., Haq, M.Z., Lawes, M., Woolley, R. 2000. Laminar burning velocity and Markstein lengths of methane–air mixtures. *Combust. Flame*. 121: 41–58.
- [7] Rozenchan, G., Zhu, D. L., Law, C. K., Tse, S. D. 2002. Outward propagation, burning velocities, and chemical effects of methane flames up to 60 atm. *Proceedings of the Combustion Institute*. 29: 1461–1469.
- [8] Hassan, M.I., Aung, K. T., Faeth, G. M. 1998. Measured and predicted properties of laminar premixed methane/air flames at various pressures. *Combust. Flame*. 115: 539–550.
- [9] Tahtouh, T., Halter, F., Mounaim-Rousselle, C. 2009. Measurement of laminar burning speeds and Markstein lengths using a novel methodology. *Combustion and Flame*. 156: 1735–1743.
- [10] Gillespie, L., Lawes, M., Sheppard, C. G. W., and Woolley, R. 2000. Aspects of Laminar and Turbulent Burning Velocity Relevant to SI Engines. Society of Automotive Engineers.
- [11] Hinton, N., Stone, R. 2014. Laminar burning velocity measurements of methane and carbon dioxide mixtures (biogas) over wide ranging temperatures and pressures. *Fuel* 116: 743-750.
- [12] Turns, S. R. 2012. *An Introduction to Combustion: Concepts and Applications*. 3rd edition. New York: McGraw Hill.
- [13] Bradley, D., Lung, K. K. 1987. *Combust. Flame*. 69:71.
- [14] Zhang, Z., Guan, D., Zheng, Y., and Li, G. 2015. Characterizing premixed laminar flame–acoustics nonlinear interaction. *Energy Conversion and Management*. 98: 331–339.
- [15] Shalaby, H., Luo, K. H., Thévenin, D. 2014. Response of curved premixed flames to single-frequency and wideband acoustic waves. *Combustion and Flame*. 161: 2868–2877.
- [16] Movileanu, C., Gosa, V., Razuș, D. 2015. Propagation of ethylene–air flames in closed cylindrical vessels with asymmetrical ignition. *Process Safety and Environmental Protection*. 96: 167–176.
- [17] Bradley, D., Gaskell, P., Gu, X. 1996. Burning velocities, Markstein lengths, and flame quenching for spherical methane–air flames: a computational study. *Combust. Flame*. 104(1–2):176–98.
- [18] Poinso, T., Veynante, D. 2005. *Theoretical and Numerical Combustion*. 2nd edition. Philadelphia: R.T. Edwards.
- [19] Miao, H., Liu, Y. 2014. Measuring the laminar burning velocity and Markstein length of premixed methane/nitrogen/air mixtures with the consideration of nonlinear stretch effects. *Fuel*. 121: 208–215.
- [20] Elgolfopoulos, F. N., Cho, P., and Law, C. K. 1989. Laminar flame speeds of methane-air mixtures under reduced and elevated pressures. *Combustion and Flame*. 76 (3-4); 375-391.
- [21] Bradley, D., Hundy, G. F. 1971. Burning velocities of methane-air mixtures using hot-wire anemometers in closed-vessel explosions. *Symposium (International) on Combustion*. 13 (1): 575-583.

Reduction of NO_x emission using Swirling Flameless Combustion

Raid A. Alwan^{1,a,*}, Mazlan A. Wahid^{1,b}, Mohd Fairus.M.F^{1,c} and Aminuddin Saat^{1,d}

¹ High-Speed Reacting Flow Laboratory, Faculty of Mechanical Engineering
Universiti Teknologi Malaysia, 81310 UTM Skudai, Johor, Malaysia

^araidturbine@yahoo.com

^bmazlan@fkm.utm.my

^cmohdfairus@fkm.utm.my

^damins@mail.fkm.utm.my

* corresponding author: raidturbine@yahoo.com (Raid.A.Alwan)

Abstract

Achieving considerable improvement in the ignition performance via flameless combustion is a big challenge. Obtaining uniform thermal field inside the combustor with ultra-low NO_x and CO emission as well as enhanced combustion stability remain challenging. In the present work, a flameless combustion technique is applied with , the operation and emission of a laboratory scale furnace under the swirling flameless combustion, (SFC) using natural gas. Gaseous fuel is injected in the direction of the combustor axis and air is allowed to enter along the tangential and axial direction of the combustor to create swirling flow with recirculation as well as enhanced mixing of the hot gas near the fuel nozzle. The experimental results of temperature and emission of combustion process are presented. Three cases for SFC are considered which specified the location of entering axial air inside the combustor. The position of the six ports axial air in case 1 and 2 is arranged symmetrically around center with distance half diameter combustor and quarter respectively, while Case 3 use all ports in Case 1 and 2. Case 1 shows the lowest temperature followed by Case 2 and 3. The amount of NO_x and CO emission measured at the outlet is observed to be lowest for Case 3 as a result of the high recirculation effect compared with Case 1.

1. Introduction

In the past, several combustion techniques are developed to reducing the pollutant gases emissions. One of them performed combustion with oxygen concentration below atmospheric levels so that the ignition process is characterized by slower chemical reaction rates, uniform temperature distribution, wider reaction zones and invisible flame [1]. Flameless combustion (FC) possesses invisible flame signatures and considered as flameless (colorless) compared to their conventional counterparts [2, 3].

Flameless combustion in gas turbine combustors are well known for the significant performance improvements in terms of uniform thermal field in the entire combustion chamber (improved pattern factor), ultra-low emission of NO_x and CO, low noise, enhanced stability and higher efficiency [4, 5]. In FC, dilution of oxygen plays a very important role. An oxygen concentration of ~5% in molar fraction is mandatory to prevent flame formation[6], which is considered to be much lower than conventional combustion (~21%). The appropriate oxygen concentration is

achieved using internal recirculation, where air and fuel jets in a confined space entrain combustion products from surroundings. This recirculation can be quantified using a parameter called recirculation factor (K_v) [7]. It is defined as the ratio of the gas mass flow entrained by all jets (\dot{m}_r) to the the sum of air (\dot{m}_a) and fuel mass flows (\dot{m}_f) in the discharge:

$$K_v = \frac{\dot{m}_r}{\dot{m}_f + \dot{m}_a} \quad (1)$$

Figure 1 shows the occurrence of different combustion regimes depending on K_v values and furnace temperature. A recirculation factor higher than 3 and the furnace wall temperature over the auto ignition temperature are prerequisite to obtain the FC regime [8].

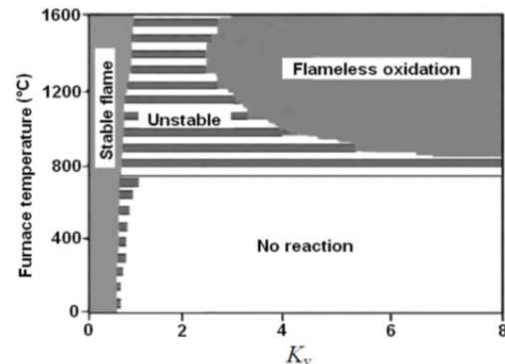


Fig. 1 Furnace temperature and recirculation factor dependent combustion regime [7, 8].

Swirl or vortex flames are not widely explored in a flameless combustion to initiate recirculation and improve the combustion stability. However, swirls are extensively applied, where the flow not only constituted on axial component of velocity but together with tangential and radial velocity. Actually, swirl plays an important role in providing a hot gas recirculation zone for mixing of reactant in a good way. It provides the high resistance of reactant in the toroidal recirculation zone following the compact flame generation that increases the flame stability in various operational conditions [9]. Despite this, the recirculation zone is often formed towards the swirl end. Thus, a reverse flow and the mixing of hot product gases with the incoming stream are observed. The hot mixture supplies the combustion energy towards the fuel its ignition and stabilization.

The significance of recirculation zone generation and the air fuel mixture preparation for ignition cannot be overstated. In this regard, common procedure utilized

for the creation of recirculation and stabilized combustion is the usage of swirl flow. It remarkably affects the recirculation of the hot combustion product that returns towards flame origin. Uniqueness of swirl is crucial for mixing and combustion of these combustor [9, 10]. The recirculation quantity is restricted by raising the mixture temperature, which is composed of air, fuel, and product gases operated at higher auto-ignition temperature. In non-premixed condition, the fuel is inserted at a downward distance to achieve desirable mixing time lower than ignition delay time. The homogeneously mixed fuel/air/product gas suddenly ignited and created a disseminated reaction regime despite thin intense front reaction flame. Thus, the achieved FC is indeed distinct from the conventional flames because it did not require reversal flow or lower velocity stabilization of fuel. The mixing of product gases with the new mixture is performed to enhance the temperature to generate sudden ignition in the whole region than minute regions combustion in conventional flames.

Swirl flows being prospective for efficient combustion are widely used in all types of practical combustion system including gas turbine. Swirl flow experiments are performed ranging from basic isothermal flows to reacting one, which is formed in very complicated swirl combustor geometries [9]. It is established that the uniqueness of swirl flow significantly impacts the flame stability, enhances the combustion effectiveness, and minimize the pollutants emission from the combustion process.

Swirl combustors with peripheral air entry have demonstrated higher swirl intensity. This resulted a reduced emission of NO_x and enhanced the flame stability [11].

In the present work a new configuration of combustor design in term of fuel and air inlet into high momentum injection of the separated fuel and air flows entrain the flue gas through internal recirculation. This further diluting the oxygen concentration in the combustion zone and leads to a more distributed heat release rate of the chemical energy, avoiding high peak temperatures and reducing the thermal formation of NO_x .

2. Geometry and Configurations

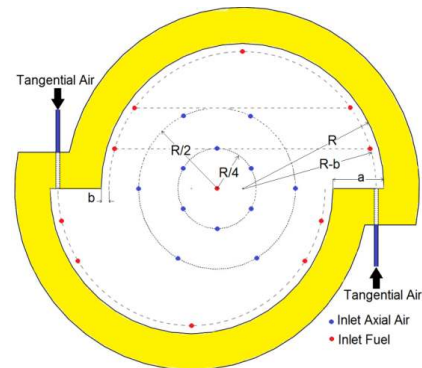
The aerodynamics of swirl flames is expanded to create a strapping swirling field for enhanced flame stability using tangential and axial inlet air as illustrated in Fig. 2. The combustor is run on natural gas, where multiple inlets are used for air and fuel. The test rig is made up of a horizontal combustion chamber formed by a two half steel cylinder with offset displacement (a). Each half of the cylinder contains two inlets for tangential air flow and numerous inlets for axial air as well as for fuel flow. The position of air and fuel inlets is selectively configured to allow the proper mixing of fuel and air within the strong field of forced vortices. Such swirling vortex is created by introducing the air with a full tangential velocity component axial to the combustor.

Table 1 summarizes the three cases depending on location of axial air. The combustion chamber of

volume 0.03 m^3 is made of mild steel that is insulated from the inside with a 40 mm thick refractory material layer to reduce heat losses. The dimensions of the indigenously built experimental asymmetric vortex combustor are: $a = 65 \text{ mm}$, $b = 10 \text{ mm}$, $R = 185 \text{ mm}$ and $L = 300 \text{ mm}$. The fuel and air inlet nozzles diameters are 2 mm and 5 mm, respectively. The combustion chamber is outfitted with circular quartz window on the rear side to perform flame imaging. Air is injected both tangential and axial direction to combustor while the fuel is injected only axially. The gases are extracted at the other end of the combustion chamber through circular hole. Test rig are prepared with several instrumentation systems to record the variables as displayed in Fig. 3. The equivalence ratio is controlled by the mass flow rate of air and fuel at the inlet. The inlet flow rates are measured using flow meters and the temperature along the central line of the combustion chamber is recorded via K-type thermo-couple (TC) at six ports. The first port is placed at 30 mm from the inlet while the other five ports are located at 60, 90, 120, 170, and 220 mm from the burner. The TCs are connected to a data acquisition system through Picolog TC-08, which is equipped with data monitoring software. The NO_x and CO emission is measured inside the exhaust hole with KM9106 Quintox gas analyzer. The accuracy of present gas analyzer is $\sim 5\%$ for the amount of emission more than 100 ppm

Table 1. Location of axial air for the three cases.

Case	Location of Axial Air	Number of ports of Axial Air
1	R/2 from center	6
2	R/4 from center	6
3	R/2, R/4 from center	12



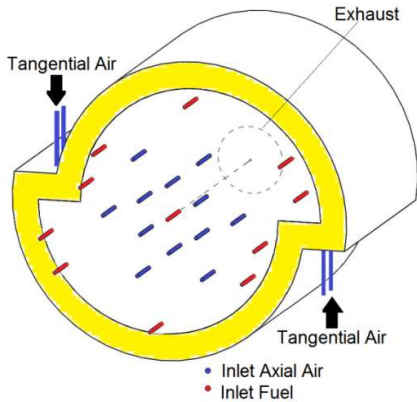


Fig. 2. Schematic diagram of the swirling flameless combustor (a) front view and (b) isometric view.

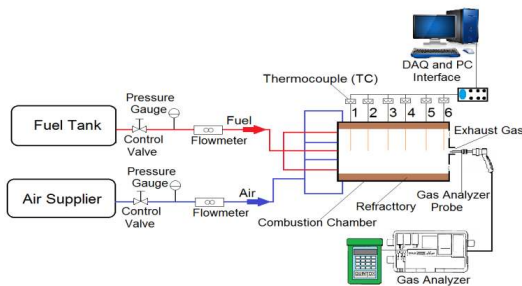


Fig 3. Experimental set up for swirling Flameless combustor.

3.Results and Discussion

The combustor operated for 30 minutes after the warm up and reached a temperature above the auto ignition (flameless mode). Figure 4 to 6 illustrates the temperature distribution along the center burner's length for three Cases. The temperature appeared stable and uniform in each thermo-couple. In all cases the maximum temperature is recorded in thermo-couple three (TC3) at stoichiometric condition, because of the high recirculation in this position. The occurrence of highest temperature for Case 3 than other two cases is attributed to the good mixing and high recirculation for Case 1 and 2.

The NO_x and CO emission levels are measured in every 5 minutes interval. Figure 7 and 8 show the effect of the equivalence ratio on NO_x emissions and oxygen concentration for three cases respectively. The NO_x emission levels in all cases are less than 10 ppm and the oxygen concentration is approximately 3%. NO_x emission being dependent on temperature, oxygen concentration, and recirculation is reduced when the flame temperature is dropped. The low oxygen concentration and high recirculation at lower temperature reduced the NO_x formation. It is clear that the level of NO_x emission for Case 3 is lower than that of Case 2 and 1. Furthermore, the percentages of the oxygen concentration for Case 3 are observed to be lower than that of Case 1 and 2. This caused lower NO_x emission for Case 3 at different equivalence ratio.

Figure 9 shows CO emission with equivalence ratio for three cases. The average CO emission is demonstrated to be lower than 50 ppm in rich and 20 ppm in lean for all cases during FC. The appearance of reduced CO emissions is majorly due to the decreased oxygen concentration within the chamber, which is the characteristic of FC. Generally, CO oxidation is a slow process and hence the residence time has significant effect on its emission. Higher residence time causes more duration for conversion from CO to CO₂ and produce low CO emissions. Thus, the CO emission for Case 3 is observed to be lowest.

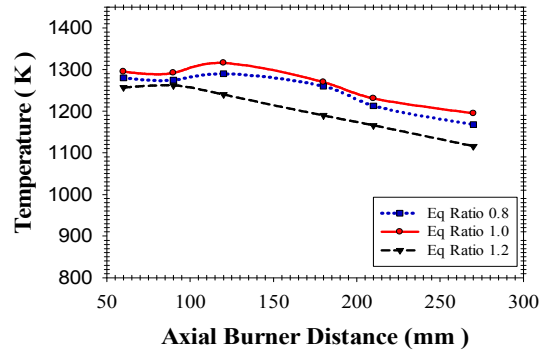


Fig. 4. Temperature distribution along the central axis in case 1.

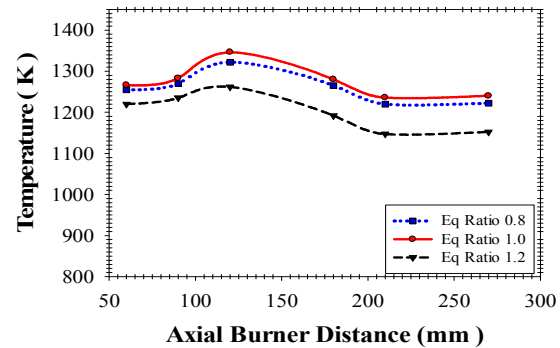


Fig. 5. Temperature distribution along the central axis in case 2

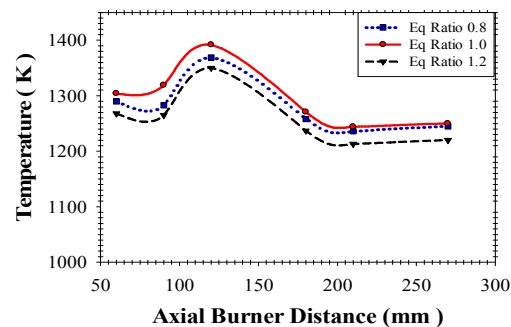


Fig. 6. Temperature distribution along the central axis in case 3.

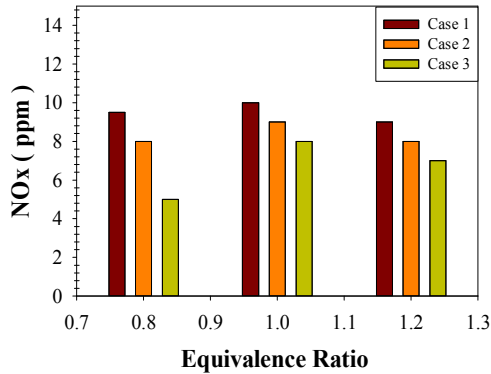


Fig. 7. Average NOx concentrations with equivalence ratio for three cases.

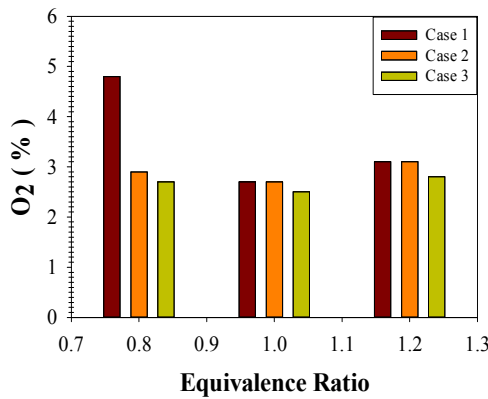


Fig. 8. Average O₂ concentration with equivalence ratio for three cases.

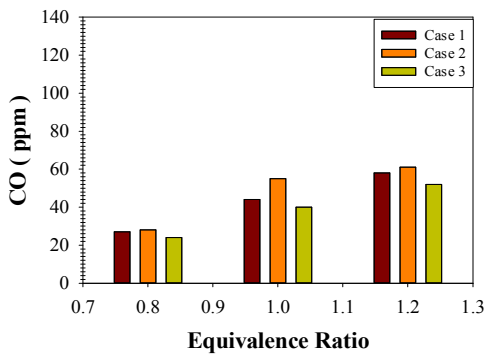


Fig. 9. Average CO concentration with equivalence ratio for three cases.

4. Conclusions

A new combustor configuration is designed to achieve a Flameless combustion without add dilution factor of N₂, CO₂ etc. Experimental is performed to examine the influence of entered air swirling Flameless combustion on diminished NO_x emission. Uniform thermal field in the combustion chamber and ultra-low emission of NO_x is achieved. The air entry along tangential as well as axial direction of the combustor. Significantly higher recirculation of hot gases as well as superior mixing of fuel and air is demonstrated to affect the temperature

distribution and combustion emissions. The pollutants emission in three cases displayed the remarkable role of swirl flow in reducing emissions. A reduction in NO_x emission as much as 50% and CO emission lowering of 25% is achieved for case 3 compared with case 1 at lean condition. The geometry of combustion, air, and fuel entry played a considerable role on the reduction of NO_x and CO emission. Our systematic experimental may constitute a basis for lowering the NO_x emission during combustion and therefore mitigate the global warming.

ACKNOWLEDGMENT

Authors are thankful to Faculty of Mechanical Engineering, Universiti Teknologi Malaysia for providing the technical facility of High Speed Reacting Flow Research Laboratory (HiREF). The authors also would like to thank Ministry of Science (Technology and Innovation), Malaysia for supporting this research activity under Science Grant with registration R.J.130000.7924.4S080 and Universiti Teknologi Malaysia Grant Q.J130000.2525.10H98. Raid is grateful to Iraqi Ministry of Electricity for the financial support and granting the study leave to complete the doctoral degree.

References

- [1] W. Blasiak, K. Narayanan, and W. Yang, "Evaluation of new combustion technologies for CO₂ and NO_x reduction in steel industries," *Advances in air pollution series*, pp. 761-771, 2004.
- [2] A. E. Khalil and A. K. Gupta, "Swirling distributed combustion for clean energy conversion in gas turbine applications," *Applied Energy*, vol. 88, pp. 3685-3693, 2011.
- [3] A. E. E. Khalil, V. K. Arghode, and A. K. Gupta, "Novel mixing for ultra-high thermal intensity distributed combustion," *Applied Energy*, vol. 105, pp. 327-334, 5// 2013.
- [4] A. E. Khalil and A. K. Gupta, "Swirling flowfield for colorless distributed combustion," *Applied Energy*, vol. 113, pp. 208-218, 2014.
- [5] V. K. Arghode, A. E. E. Khalil, and A. K. Gupta, "Fuel dilution and liquid fuel operational effects on ultra-high thermal intensity distributed combustor," *Applied Energy*, vol. 95, pp. 132-138, 7// 2012.
- [6] M. Mancini, P. Schwöppe, R. Weber, and S. Orsino, "On mathematical modelling of flameless combustion," *Combustion and Flame*, vol. 150, pp. 54-59, 7// 2007.
- [7] J. Wüning and J. Wüning, "Flameless oxidation to reduce thermal NO-formation," *Progress in energy and combustion science*, vol. 23, pp. 81-94, 1997.
- [8] C. Lezcano, A. Amell, and F. Cadavid, "Numerical calculation of the recirculation factor in flameless furnaces," *Dyna*, vol. 80, pp. 144-151, 2013.

- [9] A. K. Gupta, D. G. Lilley, and N. Syred, "Swirl flows," *Tunbridge Wells, Kent, England, Abacus Press, 1984, 488 p.*, vol. 1, 1984.
- [10] G. A. Archer S, " Effect of swirl on flow dynamics in unconfined and confined gaseous fuel flames. ," presented at the aerospace sciences meeting and exhibit, 2004.
- [11] R. A. Yetter, I. Glassman, and H. C. Gabler, "Asymmetric whirl combustion: A new low NOx approach," *Proceedings of the combustion institute*, vol. 28, pp. 1265-1272, 2000.

Self-preheated Flameless Combustion

Seyed Ehsan Hosseini*, Mazlan Abdul Wahid

High-Speed Reacting Flow Laboratory, Faculty of Mechanical Engineering, Universiti Teknologi Malaysia, Johor, 81310, Malaysia

*Corresponding author:

Email: seyed.ehsan.hosseini@gmail.com

Abstract

A developed design and test of lab-scale flameless combustion system called self-preheated flameless combustion (SPFC) is presented in this paper. In SPFC system, the flameless chamber is employed as a heater to preheat oxidizer over the auto-ignition temperature of propane (C_3H_8). A helical stainless steel pipe (called self-preheating pipe) is installed inside the chamber to conduct oxidizer from exhaust zone to the burner zone and preheat oxidizer. In the flameless mode, the diluted oxidizer is injected to the self-preheating pipe from the exhaust zone and the preheated oxidizer at the burner zone is conducted to the flameless furnace through a distributor. The most important characteristic of this new flameless combustion design is its simplicity. The very high cost honeycomb-type regenerator as well as quartz balls, which are the most popular heat exchangers, are not employed in SPFC system. Indeed, external heater for preheating oxidizer and external exhaust gas recirculation, which are common methods in flameless achievement, are not utilized. Hence, requirement to the accurate control system and response-switching valve to control the periodical fluctuations of temperature and pressure inside the chamber are eliminated. Heat exchanging between invisible flame and counter-flow oxidizer abates the mean temperature of the furnace in SPFC especially at the end section of the chamber. However, since external heater is eliminated in SPFC design, the thermal efficiency increases.

Keywords: Self-preheat, Flameless combustion, Propane, Burner

Nomenclature:

ϵ : Turbulent eddy diffusivity

δ : Thickness of a premixed flame

ν : Kinematic viscosity

Δh : Excess enthalpy

D_a : Damkohler number

S_L : Laminar flame speed

T_{ad} : Reactants adiabatic temperature

T_{in} : Inlet temperature of reactants

T_{ref} : Reference temperature

T_u : Temperature uniformity inside the chamber

T_i : The measured temperature at the various locations (i)

\bar{T} : The average of all measured temperatures

t_m : Mixing time

t_c : Reaction time

1. Introduction

In order to overcome the conflict of interest between fuel consumption and pollutant formation in the combustion systems, some various methods such as high momentum injection of staging air, application of lean premixed combustion, oxygen enriched combustion, flame cooling with exhaust gas recirculation (EGR) (mixing method) as well as utilization of cooling rods (direct cooling through radiation and convection) in the conventional combustion systems were proposed. During last decade, flameless combustion was developed as a promising combustion technology to protect fossil fuel resources and conserve the environment. Pollutant reduction, energy saving and downsizing the combustion equipment are the main aims of most activities in the flameless combustion field [1]. Based on the temperature of combustion air, Katsuki et al. [2] categorized combustion systems to preheated air combustion (PAC) and highly-preheated air combustion (HPAC). Flameless combustion mode is observed in HPAC where the temperature of oxidizer is higher than self-ignition temperature of the fuel. During the past few years, several experimental and numerical investigations carried out to find various nuance of the flameless combustion technique. Following some advantages of flameless combustion mentioned by various researchers are summarized [3–6].

- Uniform temperature distribution inside the chamber
- Hot spots elimination and low NO_x emission
- Low pollutant formation
- Higher refractory lining lifetime
- Enhancement of burner life time due to lower temperature in burner zone because of combustion propagation
- Flat heat flux distribution
- Fuel consumption reduction
- Low noise combustion
- Possibility of burning low calorific value (LCV) fuel
- Enhancement of exergy efficiency

Heating rate in a chamber is a function of flame shape, flame temperature and its emissivity, wall temperature and emissivity as well as firing rate. It is known that changes of oxygen concentration in the oxidizer impact on the flame emissivity and heat transfer. Moreover, the emissivity of gas components varies with temperature and wavelength. In the combustion phenomenon, reactants and products molecules such as H₂O, CO₂, CO are important to determine gas emissivity. Indeed, in high temperatures, the effects of dissociation and some radicals such as O, H and OH should be considered. Hence, emission and absorption of burned gases occurs in the specific ranges of the spectrum. Enhancement of temperature inside the furnace causes increase of radiation heat transfer by short wavelength. Therefore, O, H and OH radicals are responsible for short wavelength radiation [7]. The mechanism of heat transfer in the flameless combustion with large un-luminous flame volume and low flame temperature is different from traditional combustion. Rafidi et al. [8] investigated the effects of the HiTAC characteristics on the heat transfer intensity and uniformity inside a chamber using different industrial regenerative burners and various flame configurations. They concluded that compared to the traditional combustion, HiTAC flame has a larger reaction zone and more thermal radiation.

2. Heat Recovery in Flameless Mode

Auto-ignition temperature of gaseous fuel varies in different kinds of fuel and various oxygen concentration of diluted air. Due to the development of flameless HPAC, staged fuel supply industrial burners (or high temperature burners (HTB)) operated with highly preheated air, high momentum air injection and advanced low-NO_x technology progressed [9]. In the traditional high temperature air combustion (HiTAC) systems, combustion of high temperature oxidizer and fuel takes place inside the chamber. Recuperative or regenerative heat exchangers are installed outside the chamber to allow the hot exhaust gases transfer part of their enthalpy to the fresh oxidizer, which is called the secondary air. Streams of the exhaust gases and the secondary air alternatively pass through the regenerators with a high frequency [10]. Heat recirculation from exhaust gases to combustible mixture (or so-called heat-recirculating combustion) is considered as an effective method in which reactants are heated prior to the flame zone by heat transfer from exhaust gases without mixing two streams. Theoretically, excess heat of exhaust gases can be transferred to the incoming combustion air using a heat exchanger; however, the practical heat transfer rate is limited by the geometry of heat exchangers and the tolerance of the employed materials. Hence, the maximum achievable temperature of combustion oxidizer depends on the heat-resistance alloys and refractories and the amount of heat losses of the system [2,11]. In order to maximize the enthalpy transmission from flue gases to the combustible oxidizer, recuperative and regenerative heat exchangers were developed. Honeycomb-type regenerators as the most popular heat exchangers were employed in HiTAC system due to their compaction and low thermal inertia [12]. The honeycomb regenerators operate at a very small temperature difference between the exhaust flue gases temperature at the chamber exit and the combustion air

temperature. Hence, further improvement of combustion efficiency as well as fuel consumption minimization are obtainable. Nevertheless, frequently alteration of heat storage and release causes intensive thermal stress, which damages the regenerators and reduces combustion performance. Indeed, an accurate control system and response-switching valve should be employed to control the periodical fluctuations of temperature and pressure inside the chamber, which constrains an extra cost beside expensive ceramic honeycombs [13]. Rottier et al. [14] applied an electrical heater to preheat combustion air over the auto-ignition temperature of the fuel. Cavigiolo et al. [15] used quartz cylinder as a flameless combustor and quartz pellet in the entrance of the oxidizer to maintain the temperature inside the chamber. A self-regenerative burner was employed by Colorado et al. [16] to experiment natural gas and biogas flameless combustion mode.

The experimental results C_3H_8 flameless combustion are presented in this paper, using the flameless chamber as a heater to preheat oxidizer over the self-ignition temperature of C_3H_8 . This new design of flameless combustion furnace has been named self-preheated flameless combustion (SPFC) by the authors. Performance evaluation of C_3H_8 flameless combustion in the new design and compare the results of SPFC by usual flameless combustion (using auxiliary heater for preheating oxidizer) are the most important objectives of this investigation. Flameless stability, the mechanism of burned gas recirculation inside the flameless chamber, temperature distribution inside the furnace and thermal efficiency of the combustion system are parameters that are evaluated in this paper. Various steps of usual flameless combustion were presented by the authors in ref [17].

3. Experimental Setup

A combustion chamber made by carbon steel and equipped with refractory was designed and built in high speed flow rate laboratory (Hiref) in Universiti Teknologi Malaysia (UTM). The length and outlet diameter of the circular flameless furnace are 600mm and 264mm respectively. A high-qualified refractory installed inside the furnace to maintain inside temperature and a helical stainless steel pipe is applied to preheat the fresh oxidizer. To prevent temperature drop in the flameless mode, an insulation wool is applied. K-type thermocouple is employed to measure the temperature of different locations of the furnace and exhaust gases. The 5mm fuel nozzle is at the centre of the burner surrounded by four 5mm nozzles for combustion oxidizer inlet. The distance between fuel/oxidizer inlet jets is 52.5mm. Indeed, the flow rates of fuel/oxidizer are controlled by manual controlled flow meters. Fig2 depicts the configuration of the chamber.

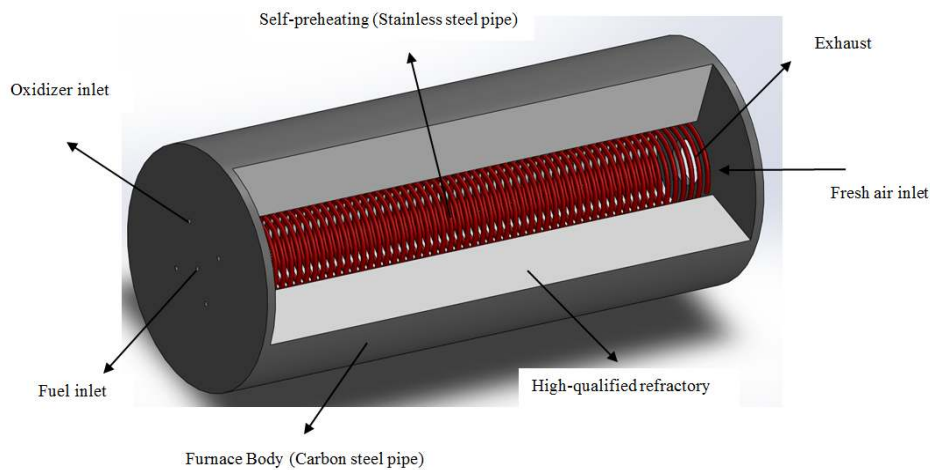


Fig.1. Schematic of the self-preheated flameless furnace

Combustion is started in the conventional flame (heat up step). The present burner is employed in both traditional combustion and flameless mode. In the heat up step, pure C_3H_8 and air are mixed before injection to the burner and the mixture is injected through the fuel nozzle. An electric spark igniter is used in the heat up step to ignite the reactants. In the stoichiometric premixed conventional combustion, air and C_3H_8 flow rates are set 0.002402 kg/m^3 and 0.00154 kg/m^3 respectively. When the mean temperature of the furnace sufficiently increases (around 1200K), combustion system is switched from propane traditional mode to the non-premixed flameless combustion. In the flameless regime,

oxidizer is diluted by nitrogen (7%O₂+ 93%N₂). The diluted oxidizer is injected to the self-preheating pipe from the exhaust zone. The preheated oxidizer at the outlet of this self-preheated pipe (in the burner zone) is conducted to the flameless furnace through a distributor. Propane is injected through the central nozzle of the burner. Exhaust gases are led to the heat exchanger to recover the energy of hot flue gases and preheat the oxidizer. Fig2 and Fig3 illustrate the schematic of the burner and experimental setup respectively.

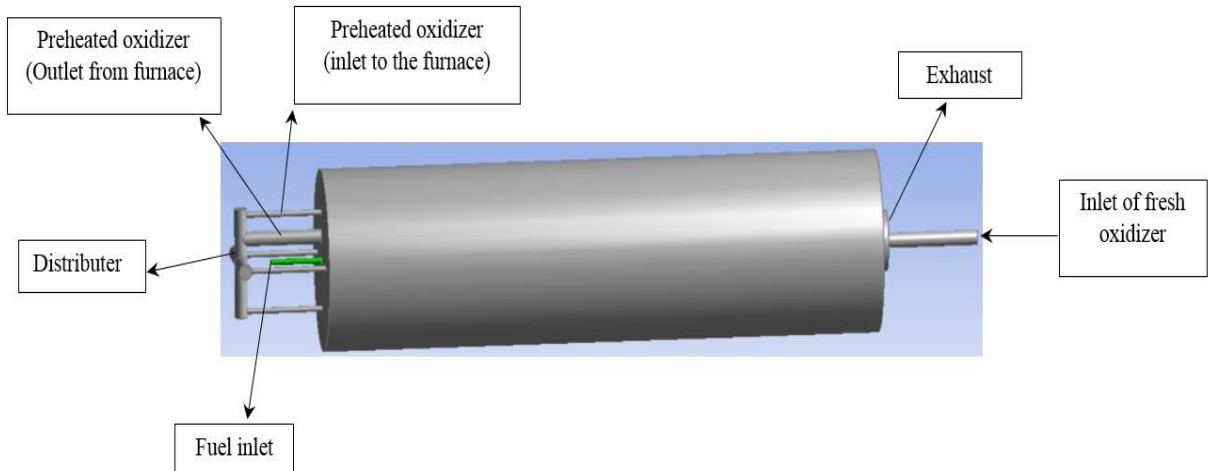


Fig.2. Schematic of the furnace and burner

Due to extremely high temperature inside the chamber (even higher than the self-ignition temperature of the fuel), igniter is not necessary in the flameless combustion and C₃H₈ is burnt spontaneously. A summary of settings in the flameless mode is presented in Table1.

4.Results and Discussion

4.1 Distribution of Temperature inside the Chamber

C₃H₈ is employed in premixed combustion to heat the chamber and the temperature inside the furnace raises conventionally. When the mean temperature of the furnace increases over auto-ignition of C₃H₈, transition from traditional mode to the flameless combustion is started. Hence, the operation of the burner changes from conventional flame to the flameless combustion which is associated with decrease in temperature of the furnace. Fig4 displays the variation of temperature inside the chamber from conventional combustion to flameless mode.

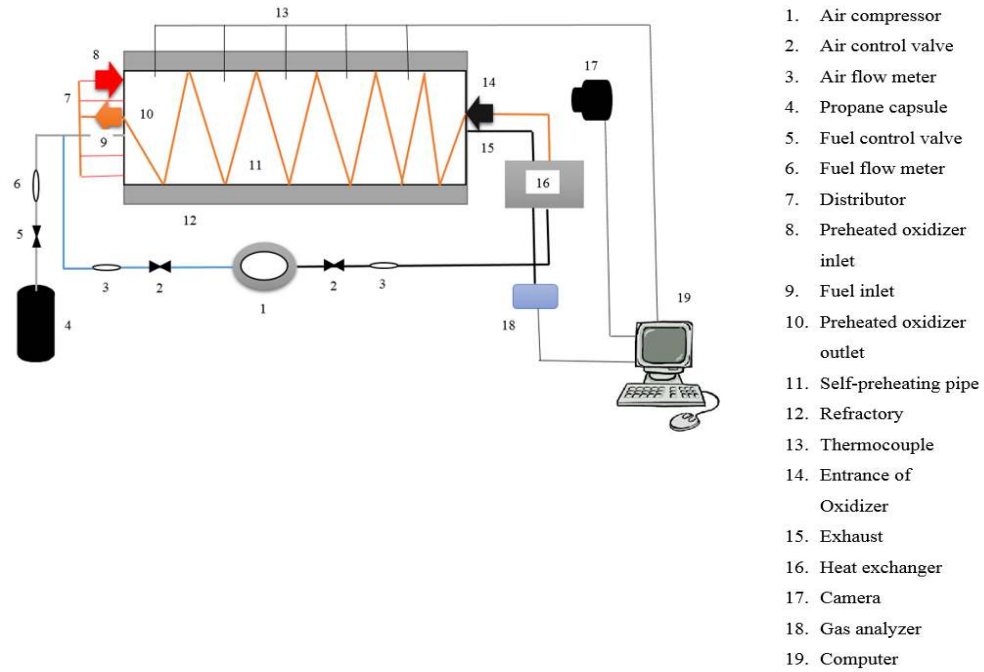


Fig.3. Schematic of experimental setup

Table1. Experimental settings in the flameless mode

Oxidizer inlet	Temperature	uniform, 480K
	Gauge Pressure	0
	Hydraulic diameter	5mm
	Velocity	85 m/s
	Type of diluent	Nitrogen
	Oxygen concentration	7%
	Density	0.383 g/l
	Mass flow rate	0.002402 kg/m ³
Fuel inlet	Temperature	uniform, 300K
	Gauge Pressure	0
	Hydraulic diameter	5mm
	Velocity	26 m/s
	Fuel ingredient	C ₃ H ₈
	Density	1.882 g/l
	Mass flow rate	0.00154 kg/m ³

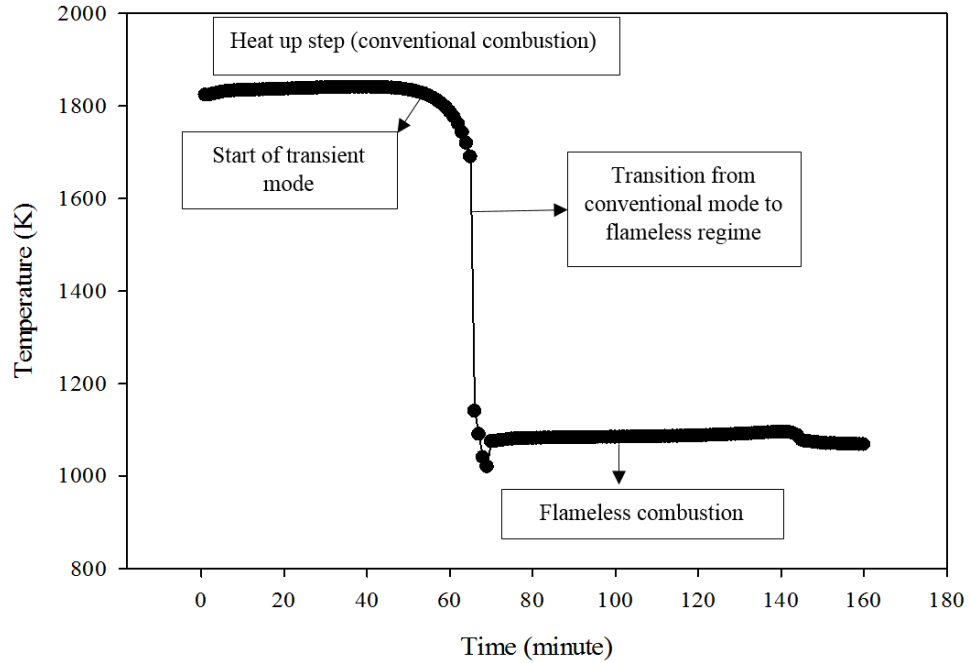


Fig.4. The variation of temperature within the furnace from traditional combustion to flameless

This temperature uniformity (TU) inside the chamber is calculated based on the normalized root mean square value computed from all measured temperatures at different locations [18].

$$T_u = 1 - \sqrt{\frac{1}{N} \sum_{i=1}^N \left(\frac{T_i - \bar{T}}{\bar{T}} \right)^2} \quad (1)$$

where T_u is temperature uniformity in the furnace, T_i is the temperature of various locations (i) and \bar{T} is the average of all temperatures in the different locations in the chamber. In a flameless system, the value of temperature uniformity tends to one, where a complete uniform temperature is found in the chamber. TU were obtained based on the temperature measurements at 15 various locations in the chamber. The values of TU was computed 0.93 in the C_3H_8 flameless combustion mode. Compared to the usual flameless combustion, where auxiliary heater is employed to preheat the oxidizer, it is found that TU in SPFC is lower than usual flameless combustion with 0.97 TU. This discrepancy could be attributed to the constitution of some hot spots in the self-preheating pipe (stainless steel pipe inside the chamber) especially in the burner zone. Indeed, heat exchanging between incoming fresh air (at the exhaust zone) and un-luminous flame especially at the end of combustor, where the temperature variation is high is effective for TU mitigation. Fig5 depicts various regimes of combustion during the experiment.

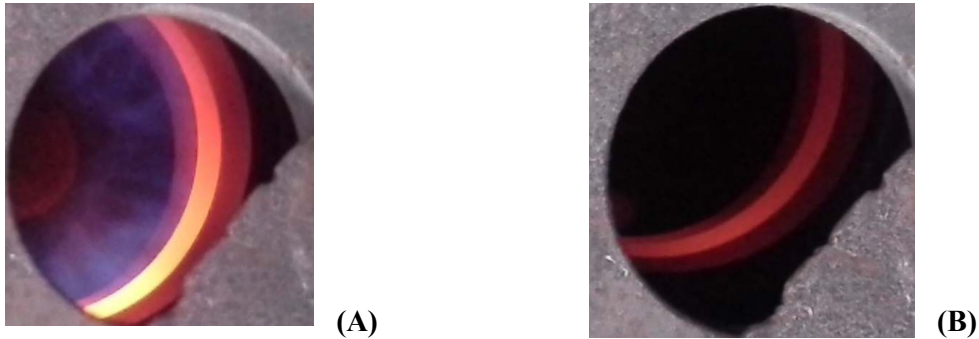


Fig.5. Photos from experiment of SPFC (A) Conventional flame (B) Flameless mode

The temperature of fresh oxidizer is 300K, which is increased to 480K in the heat exchanger (the inlet temperature of oxidizer at point 14 in Fig3). Heat exchanging between un-luminous flame and counter-flow oxidizer (inside the

stainless still pipe) abates the mean temperature of the chamber in SPFC. Fig6 demonstrates the distribution of axial temperature along the flameless furnace.

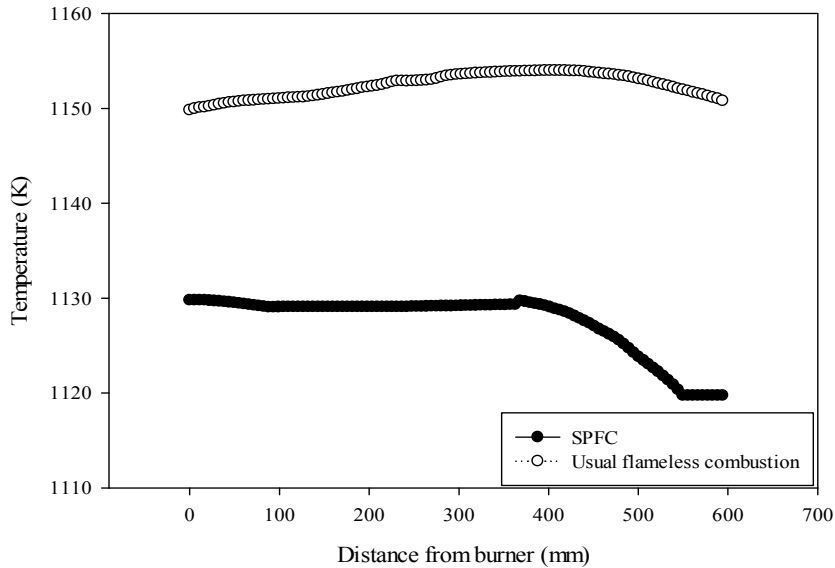


Fig.6. The axial temperature distribution along the chamber

The experiment was implemented for various blends of oxidizer (different combination of N_2 and O_2 in the oxidizer). When oxygen concentration in the oxidizer increases to 10%, the mean temperature of the chamber augmented drastically. However, TU in the combustion chamber in 10% oxygen concentration decreases compared to the 7% oxygen concentration. Fig7 and Fig8 depict the variation of temperature along the furnace and TU inside the chamber with respect to various oxygen concentrations in the oxidizer.

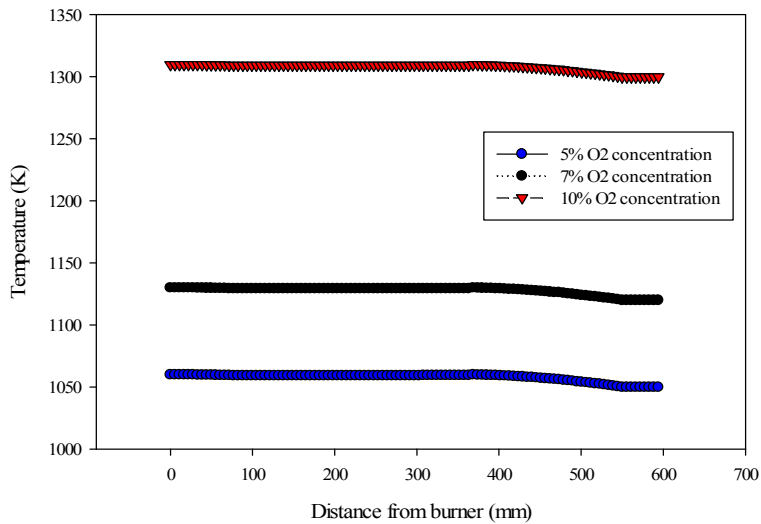


Fig7. The effects of oxygen concentration of oxidizer on the temperature distribution along the chamber

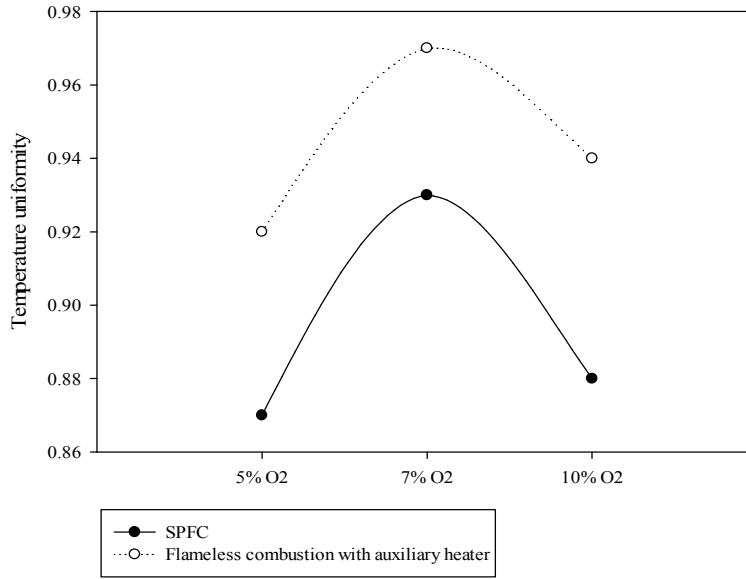


Fig8. Temperature uniformity inside SPFC furnace in various blends of oxidizer

4.2 Burned Gas Recirculation inside the chamber

Combustion phenomenon has been classified to quasi-isothermal combustion and non-isothermal combustion. The maximum available excess enthalpy of the quasi-isothermal combustion which is calculated by Eq (2) is determined by the physical properties of fuel and oxidizer and by the combustion process operating parameters [19].

$$\Delta h = \frac{T_{ad} - T_{in}}{T_{in} - T_{ref}} \quad (2)$$

Where T_{ad} is reactants adiabatic temperature, T_{in} is inlet temperature of reactants and T_{ref} is reference temperature. It has been stipulated that the higher excess enthalpy during the combustion process could be obtained at a lower reactant temperature for combustion over all the oxygen concentration range [19]. As a quantitative parameter, fuel auto-ignition temperature should be taken into consideration for flameless combustion stability. It means, in the flameless combustion mode, stable combustion is achieved when temperature of reactants is maintained over auto-ignition temperature of the fuel. Therefore, in the flameless combustion regime, the maximum excess enthalpy is obtainable by preheating unburned mixture, oxygen concentration reduction in the unburned mixture, enhancement of the heat loss from the flame or flame cooling. In conventional combustion, the flame is onset at the inlet of the chamber (burner zone) and flue gases are extracted at the other end. However, in non-premixed flameless combustion mode, burnt gases flow back to the entrance of the chamber. The distance between fuel inlet jet and preheated oxidizer injection into the furnace results in the fact that the combustion reactants (fuel and preheated diluted air) are mixed with combustion products (burnt gases) before the combustion process occurs. Consequently, a pre-combustion takes place due to the present of low amounts of oxygen in the burnt gases. Indeed, the low level of oxygen concentration in the oxidizer alleviates the maximum temperature of the combustion system. The internal burnt gas recirculation effect could be controlled by the velocity of the fuel/preheated oxidizer and design factors such as the location of nozzles. Higher distance between fuel and oxidizer jets as well as higher injection velocities conduct the combustion system to faster internal flue gas recirculation. As a result, uniform temperature distribution inside the chamber and homogeneous heat flux are achieved [20]. In this experiment, the distance of fuel inlet and preheated oxidizer inlet is 52.5mm and the velocity of the inlet oxidizer is 85m/s, which made excellent circumstance for burnt gas recirculation. Fig9 shows the path line of the particles inside the chamber in flameless combustion regime.

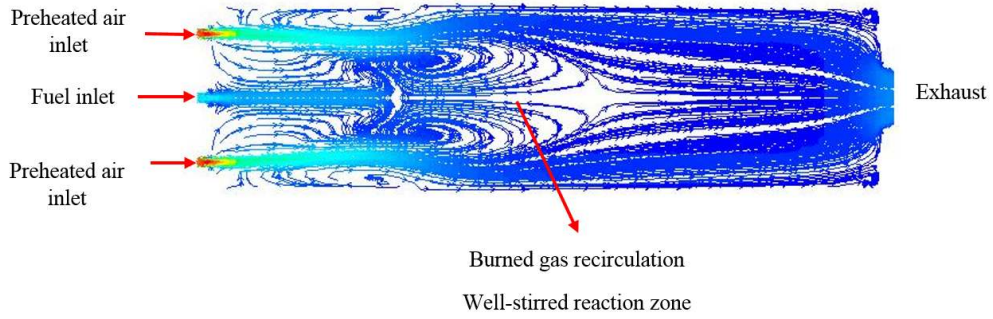


Fig.9. Path line of the particles inside the chamber in flameless mode

Fig9 has been obtained from CFD simulation of propane flameless combustion by ANSYS 14. The simulation settings of biogas flameless mode were presented by the authors in ref [21].

In the flameless combustion mode, invisible flame is expanded in a large volume makes the combustion furnace more like a well-stirred reactor referred to volumetric combustion, causes homogenous and lower temperature of such flame [22,23]. High velocities of oxidizer conduct a majority part of flue gases to the combustion zone. Thus, the concentration of O_2 in the combustion oxidizer rapidly mitigates, which increases reaction time, so that becomes comparable with the mixing time characteristic. In these circumstances, combustion zone is extended over the whole furnace and volumetric combustion appears. Theoretically, when Klimov-William criterion is satisfied, the combustion reaction zone is distributed throughout the chamber. Hence, in one hand the ratio of the root-mean-square velocity fluctuations to the laminar flame speed should be larger than one ($U/S_L > 1$) and in the other hand, Damkohler number (D_a) (the ratio of mixing time scale (t_m) to the chemical time scale (t_c)) should be low enough ($D_a = t_m/t_c < 1$) [24].

$$D_a = t_m/t_c \quad (3)$$

The combustion mixing time is related to the jet length (L) and the turbulent eddy diffusivity (ε) while combustion reaction time is related to the thickness of a premixed flame (δ) and the laminar flame speed.

$$t_m \sim L^2/\varepsilon \quad (4)$$

$$t_c \sim \delta/S_L \quad (5)$$

The eddy diffusivity in an inlet jet is related to the axial velocity and the length of jet ($\varepsilon \sim VL$), and the thickness of a premixed flame is proportional to the kinematic viscosity (ν) and laminar flame speed ($\delta \sim \nu/S_L$). Therefore, for an inlet jet with specific kinematic viscosity and length, D_a number is changed by the square of laminar flame speed directly and the axial velocity inversely.

$$D_a \sim S_L^2/V \quad (6)$$

It implies that by laminar flame speed mitigation and jet velocity augmentation, D_a reduces. Burned gas recirculation in to the entrance of the chamber, which leads to low oxygen concentration in the combustion oxidizer, is crucial for the laminar flame speed reduction. In the flameless combustion regime, the very high-velocity of reactants is large enough in comparison with the laminar speed of the fuel. Furthermore, burned gas recirculation inside the chamber increases reaction time compared to the reactant mixing time. Therefore, high exhaust gases entrainment as well as high turbulence intensity could be fulfilled in high-velocity incoming jets.

4.3 Thermal Efficiency

To calculate efficiency of SPFC, energy balance is considered for the combustion system. To quantify all energy states through the combustion system, the specifications of all bulks entering (such as fuel/oxidizer flow-rates and temperatures) and leaving the boundary were measured. The equation of energy balance for the chamber is expressed as Eq (7) [25].

$$\dot{Q}_{sys} + \sum \dot{m}_i \left(h_i + \frac{u_i^2}{2} + gz_i \right) = \frac{dE_{sys}}{dt} + \sum \dot{m}_o \left(h_o + \frac{u_o^2}{2} + gz_o \right) + \dot{w}_{sys} \quad (7)$$

To solve the energy equation for the SPFC chamber, some assumptions are considered: (i) potential and kinetic energies are not taken into account; (ii) due to long time running of chamber it is considered that $\frac{dE_{sys}}{dt} = 0$; (iii) the reference temperature for moisture free fuel and oxidizer is $TR=300K$; (iv) the latent heat loss of vapor from exhaust is not considered, (v) $Q_{sys} = -Q_{sur}$.

Due to these assumptions, the energy equation changes to the Eq (8).

$$\sum \dot{m}_i h_i = \sum \dot{m}_o h_o + \dot{Q}_{sur} \quad (8)$$

Chemical and physical enthalpy of the fuel and sensible heat in the combustion oxidizer are energy inputs and the sensible heat losses in the flue gases is the system output calculated based on Eq (9).

$$\dot{Q}_{\text{exx}} = \dot{m}_{\text{exx}} \cdot \sum \int_{T_F}^{T_{\text{ex}}} \bar{w}_i c_{p_i} dt \quad (9)$$

\bar{w}_i is the mass fraction of each components

Based on Eq (10) the efficiency of propane SPFC is calculated 64% in this experiment.

$$\eta = \left(1 - \frac{Q_{\text{exx}} + Q_s}{Q_f + Q_A} \right) \times 100 \quad (10)$$

Compared to conventional flameless combustion, the efficiency of SPFC is around 8% higher which could be attributed to the elimination of external heat exchanger and using self-preheated pipe. Low concentration of propane in the exhaust of the furnace corroborates that flameless combustion of propane is more complete in this new design.

4. Conclusion

New design of flameless combustion system called self-preheated flameless combustion was experimented. Flameless stability, the mechanism of burned gas recirculation inside the flameless chamber, temperature distribution as well as temperature uniformity inside the furnace and thermal efficiency of the combustion system were assessed. Although, the mean temperature inside the flameless chamber decreases in this new design (around 20K), the combustion efficiency of SPFC system is higher than the previous design due to elimination of external heater. Enhancement of the distance between fuel injection jet and oxidizer inlet as well as augmentation of oxidizer velocity, increase internal burned gas recirculation. Consequently, a well-stirred circumstance is achieved inside the furnace, which increase the stability of flameless combustion.

References

1. Wüning, J.A., and J.G. Wüning, Flameless oxidation to reduce thermal NO-formation. *Progress in Energy and Combustion Science*, 1997. 23(1): p.81–94.
2. Katsuki, M., and T. Hasegawa, The science and technology of combustion in highly preheated air. *Symposium (International) on Combustion*, 1998. 27(2): p.3135–3146.
3. Tsuji, H., A.K. Gupta, T. Hasegawa, M. Katsuki, K. Kishimoto and M. Morita, High Temperature Air Combustion: From Energy Conservation to Pollution Reduction (Google eBook), CRC Press, , 2002.
4. Hosseini, S.E., and M.A. Wahid, Enhancement of exergy efficiency in combustion systems using flameless mode. *Energy Conversion and Management*, 2014. 86: p.1154–1163.
5. Hosseini, S.E., M. a. Wahid and A.A.A. Abuelnuor, Biogas Flameless Combustion: A Review. *Applied Mechanics and Materials*, 2013. 388: p.273–279.
6. Flamme, M., New combustion systems for gas turbines (NGT). *Applied Thermal Engineering*, 2004. 24(11-12): p.1551–1559.
7. Waal, H. De, and R. Beerkens, NCNG Handboek voor de Glasfabricage. *TNO-TPD-Glastechnologie*, 1997.
8. Rafidi, N., and W. Blasiak, Heat transfer characteristics of HiTAC heating furnace using regenerative burners. *Applied Thermal Engineering*, 2006. 26(16): p.2027–2034.
9. Hosseini, S.E., M. a. Wahid and S. Salehirad, Environmental Protection and Fuel Consumption Reduction by Flameless Combustion Technology: A Review. *Applied Mechanics and Materials*, 2013. 388: p.292–297.
10. Zhang, H., G. Yue, J. Lu, Z. Jia and J. Mao, Development of high temperature air combustion technology in pulverized fossil fuel fired boilers. *Proceedings of the Combustion Institute*, 2007. 31(2): p.2779–2785.
11. Arrieta, C.E., and A.A. Amell, Highly flexible burner concept for research on combustion technologies with recirculation of hot combustion products. *Applied Thermal Engineering*, 2014. 63(2): p.559–564.

12. Kang, K., S.-K. Hong, D.-S. Noh and H.-S. Ryou, Heat transfer characteristics of a ceramic honeycomb regenerator for an oxy-fuel combustion furnace. *Applied Thermal Engineering*, 2014. 70(1): p.494–500.
13. Cao, Z., Thermal and emission characteristics of high temperature air combustion: A technical review, in: 2010 Int. Conf. Mech. Autom. Control Eng., IEEE, p.4010–4014.
14. Rottier, C., C. Lacour and G. Godard, On the effect of air temperature on mild flameless combustion regime of high temperature furnace. *Proceedings of the European Combustion Meeting*, 2009. Vienna, Au: p.1–6.
15. Cavigiolo, A., M.A. Galbiati, A. Effuggi, D. Gelosa and R. Rota, Mild combustion in a laboratory-scale apparatus. *Combustion Science and Technology*, 2003. 175(8): p.1347–1367.
16. Colorado, A.F., B.A. Herrera and A.A. Amell, Performance of a flameless combustion furnace using biogas and natural gas. *Bioresource Technology*, 2010. 101(7): p.2443–9.
17. Hosseini, S.E., and M.A. Wahid, Biogas utilization: Experimental investigation on biogas flameless combustion in lab-scale furnace. *Energy Conversion and Management*, 2013. 74: p.426–432.
18. Cho, E.-S., D. Shin, J. Lu, W. de Jong and D.J.E.M. Roekaerts, Configuration effects of natural gas fired multi-pair regenerative burners in a flameless oxidation furnace on efficiency and emissions. *Applied Energy*, 2013. 107: p.25–32.
19. Blasiak, W., W.H. Yang, K. Narayanan and J. von Schéele, Flameless oxyfuel combustion for fuel consumption and nitrogen oxides emissions reductions and productivity increase. *Journal of the Energy Institute*, 2007. 80(1): p.3–11.
20. Szewczyk, D., A. Kamecki, P. Skotnicki and A. Szydłowski, Copper blast furnace waste gas utilization system as a new field of HiTAC combustion technology, 8 HiTACG 2010, July, 5-7, 2010. *Poznań, Poland*, n.d.
21. Hosseini, S.E., G. Bagheri and M.A. Wahid, Numerical investigation of biogas flameless combustion. *Energy Conversion and Management*, 2014. 81: p.41–50.
22. Yang, W., and W. Blasiak, Flame Entrainments Induced by a Turbulent Reacting Jet Using High-Temperature and Oxygen-Deficient Oxidizers. *Energy & Fuels*, 2005. 19(4): p.1473–1483.
23. Sabia, P., M. de Joannon, S. Fierro, A. Tregrossi and A. Cavaliere, Hydrogen-enriched methane Mild Combustion in a well stirred reactor. *Experimental Thermal and Fluid Science*, 2007. 31(5): p.469–475.
24. Effuggi, A., D. Gelosa, M. Derudi and R. Rota, Mild Combustion of Methane-Derived Fuel Mixtures: Natural Gas and Biogas. *Combustion Science and Technology*, 2008. 180(3): p.481–493.
25. Sonntag, R., and G. Van Wylen, Introduction to thermodynamics: classical and statistical. 1971.